

Electronic transport in quasi-1D atomic wires

Von der Fakultät für Mathematik und Physik
der Gottfried Wilhelm Leibniz Universität Hannover
zur Erlangung des Grades
Doktor der Naturwissenschaften
Dr. rer. nat.
genehmigte Dissertation

von

M. Sc. Frederik Edler

2018

Referent: Prof. Dr. Christoph Tegenkamp (University of Hannover, Germany)
Korreferent: Prof. Dr. Shuji Hasegawa (University of Tokyo, Japan)
Korreferent: Prof. Dr. Wolf Gero Schmidt (University of Paderborn, Germany)

Tag der Promotion: 13.04.2018

Dedicated in loving memory to my grandparents
Anneliese (1934 – 2009) and
Alfred Rapröger (1929 – 2015).

I miss you so much and wish you could be still here with us!

Hey. Don't ever let somebody tell
you, you can't do something. [...]
You got a dream, you gotta
protect it. People can't do
something themselves, they wanna
tell you you can't do it. You want
something, go get it. Period.

*Will Smith alias "Chris Gardener"
in "The Pursuit of Happyness"
(2006)*

Abstract

Atomic wires grown by self-assembly are prototype 1D systems for studying fundamental aspects, e.g. CDW, Peierls instabilities or the dimensional crossover from a Fermi to a Luttinger liquid behavior. In addition, the peculiar interactions between charge, spin and lattice could lead to interesting potential applications in future nanoelectronic devices. In this thesis, three highly discussed atomic wire systems are analyzed by means of a 4pp STM/SEM system.

The first part of the thesis treats the In/Si(111)-(4 × 1) reconstruction which serves as a benchmark system for the understanding of 1D atomic chain reconstructions. It shows strong anisotropic transport properties and a temperature driven MIT. Although being intensively studied for two decades, there are still open questions, like the effect of defects induced by adsorption (e.g. oxygen) in respect to the MIT. It turns out that the sensitivity toward defects can be increased by one order of magnitude by performing the transport experiments on confined areas. Moreover, oxygen adsorption dependent transport studies not only show a reduction of conductivity along the direction of atomic chains but show also a decrease in the perpendicular direction. This was not reported before and reveals an effective interwire coupling between the chains in agreement with additional DFT calculations.

The second part of the thesis focuses on Au-induced wire structures on Si(hhk) substrates. Those attracted recently a lot of attention because of their pronounced magnetic order, which mimics a 2D quantum spin liquid state. The Si(553)-Au and Si(557)-Au surfaces are carefully analyzed during in-situ adsorption of molecular oxygen. In combination with LEED and DFT calculations, the transport in terms of the different structural building blocks (Au chains, Si-Adatom chain, Si-HC edge) is discussed. It is shown, that the cause for the metallic surface bands along the wires are of different origin. Therefore, while the Si(553)-Au surface turns out to be rather immune against oxidation, the Si(557)-Au surface reveals a strong decrease of the conductance due to complete destruction of the Si-adatom ordering along the chains. In addition, the MIT of these systems is investigated. Here, a special focus is set on the Si(553)-Au reconstruction. Within a LEED study it is shown that the ×3 periodicity undergoes structural transition at $T_C = 100$ K, i.e. the ×3 periodicity along the wires vanishes. In contrast, the transport data reveals a residual conductivity along the wires below T_C ruling out a MIT associated with the phase transition of the ×3 reconstruction.

The last part of the thesis analyzes the transport properties of TbSi₂ nanowires grown on vicinal Si(001) substrates. These rare-earth silicide nanowires could generally be very promising for further downscaling of Si based interconnects in CMOS technology because the wires can be grown several micrometer long while they are extremely thin with nanometer widths. A combined STM and transport study shows that the resistivity is strongly depending on the height of wires, which is increased for small heights. The data can be described by a theoretical quasi-classical model considering the surface roughness and lateral surface correlation.

Keywords: atomic wires, electronic transport, quasi-1D

Kurzzusammenfassung

Durch selbstorganisiertes Wachstum entstandene atomare Drähte sind Prototypen von 1D-Systemen zum Studium grundlegender Aspekte, z.B. CDW, Peierls Instabilitäten, oder der Übergang von einem Fermi- zu einem Luttinger Flüssigkeitsverhalten. Darüber hinaus könnten die besonderen Wechselwirkungen zwischen Ladung, Spin und Gitter zu interessanten Anwendungen in zukünftigen nanoelektronischen Geräten führen. In dieser Arbeit werden drei stark diskutierte atomare Drahtsysteme analysiert mittels eines 4-Spitzen STM/SEM Systems.

Der erste Teil dieser Arbeit behandelt die In/Si(111)-(4 × 1) Rekonstruktion, die als Vergleichssystem zum Verständnis von 1D atomaren Kettensystemen dient. Das System zeigt ein stark anisotropes Transportverhalten und einen temperaturabhängigen MIT. Obwohl das System seit zwei Jahrzehnten intensiv untersucht wird, gibt es immer noch offene Fragen, z.B. die Wirkung von durch Adsorption (z.B. Sauerstoff) induzierten Defekten auf den MIT. Es stellt sich heraus, dass die Empfindlichkeit gegenüber Defekten eine Größenordnung erhöht werden kann, wenn die Transportexperimente in endlich begrenzten Gebieten durchgeführt werden. Darüber hinaus zeigt sich in sauerstoffadsorptionsabhängigen Transportmessungen nicht nur eine Reduktion der Leitfähigkeit entlang der Richtung der Atomketten, sondern auch eine Abnahme in der senkrecht Richtung. Über dieses wurde noch nicht vorher berichtet und deutet auf eine effektive *interwire* Kopplung zwischen den Ketten in Übereinstimmung mit zusätzlichen DFT-Berechnungen hin.

Der zweite Teil der Arbeit konzentriert sich auf Au-induzierte Drahtstrukturen auf Si(hhk)-Substraten. Diese Strukturen haben kürzlich eine große Aufmerksamkeit auf sich gezogen wegen ihrer ausgeprägten magnetischen Ordnung, die eine 2D Quanten-Spin-Flüssigkeit nachbildet. Die Si(553)-Au und Si(557)-Au Oberflächen werden sorgfältig während der in-situ Adsorption von molekularem Sauerstoff analysiert. Hierbei wird der Transport in Kombination mit LEED und DFT-Berechnungen in Bezug auf die verschiedenen Strukturbausteine (Au-Ketten, Si-Adatom-Kette, Si-HC-Kante) diskutiert. Es zeigt sich, dass der Ursprung für die metallischen Oberflächenbänder entlang der Drähte unterschiedlicher Natur ist. Während die Si(553)-Au Oberfläche immun gegenüber Sauerstoffadsorption ist, zeigt die Si(557)-Au eine starke Abnahme der Leitfähigkeit entlang der Ketten. Zusätzlich wurde der MIT dieser Systeme untersucht. Hierbei wurde ein besonderer Fokus auf die Si(553)-Au Rekonstruktion gesetzt. Innerhalb einer LEED Messung zeigt sich, dass die ×3-Periodizität einen strukturellen Phasenübergang bei $T_C = 100$ K besitzt, d.h. dass die Periodizität entlang der Ketten verschwindet. Im Gegensatz hierzu zeigen die Transportdaten eine Restleitfähigkeit entlang der Ketten unterhalb T_C , welches einen MIT assoziiert mit der ×3-Rekonstruktion ausschließt.

Der letzte Teil der Arbeit analysiert die Transporteigenschaften von TbSi₂-Nanodrähten, die auf vicinalem Si(001)-Substrat gewachsen wurden. Selteneerden-Silizid-Nanodrähte sind im allgemeinen sehr vielversprechend für die Industrie für eine weitere Herunterskalierung Si-basierten Verbindungen innerhalb der CMOS-Technologie, da die Drähte sehr lang (mehrere μm) und extrem dünn (wenige nm) gewachsen werden können. Eine kombinierte STM- und Transportstudie zeigt, dass der spezifische Widerstand stark abhängig ist von der Höhe der Drähte und dieser erhöht ist für kleine Höhen. Die Daten können durch ein theoretisches quasi-klassisches Modell unter Berücksichtigung der Oberflächenrauigkeit und der lateralen Oberflächenkorrelation beschrieben werden.

Schlagworte: atomare Drähte, elektronischer Transport, quasi-1D

Acronyms

2pp two-point probe	113
4pp four-point probe	129
ARPES angle-resolved photoemission spectroscopy	132
CDW charge density wave	130
DC direct-current	107
DFT density functional theory	129
DOS density of states	111
EBSTD electron beam stimulated selective thermal desorption	52
FIM field ion microscope	17
FWHM full widths at half maximum	93
HC honey comb	130
HCW high coverage wires	69
HHCF height-height correlation function	109
LCW low coverage wires	69
LDA local-density approximation	59
LDOS local density of states	110
LEED low-energy electron diffraction	130
MIT metal-insulator transition	129
ML monolayer	107
PID controller proportional-integral-derivative controller	18
RE rare earth	131
RHEED reflection high-energy electron diffraction	45
SBZ surface Brillouin zone	74
SCL space-charge layer	135
SDW spin density wave	9
SEM scanning electron microscope	129
SPALEED spot profile analysis low-energy electron diffraction	129

SS surface states	76
STM scanning tunneling microscope	129
STS scanning tunneling spectroscopy	110
TEM transmission electron microscope	132
TL Tomonaga-Luttinger liquid	67
TM transition metals	105
UHV ultra-high vacuum	90
XPS x-ray photoemission spectroscopy	44
XRD x-ray diffraction	66

List of Symbols

$\Delta\Theta_{0.48}$	Deviation from the gold coverage of 0.48 ML
Δ_B	Activation energy
Δ	Energy (gap)
ℓ	Electron mean free path
λ_D	Debye length
λ_F	Fermi length
μ_p	Hole mobility
μ	Width-to-height aspect ratio
ρ_{1D}	Resistivity of a 1D circular wire
$\rho_{2D}^{\text{in-line}}$	Resistivity for a collinear equidistant contact spacing of a 2D infinite sheet
$\rho_{3D}^{\text{in-line}}$	Resistivity for a collinear equidistant contact spacing of a 3D semi-infinite material
ρ_{Bulk}	Bulk resistivity
ρ_{Film}	Resistivity of a film
ρ	Electrical resistivity
σ_p	Conductivity of a p-type layer
σ_B	Conductivity attributed to bulk channels
σ_{SCL}	Conductivity attributed to the space-charge layer beneath the surface
σ_{SS}	Conductivity attributed to surface-states
$\sigma_{\parallel, 2D}$	Conductivity of a 2D infinite sheet measured in parallel direction
$\sigma_{\parallel, \text{Mesa}}$	Conductivity measured on a mesa in parallel direction
$\sigma_{\parallel, \text{Mesa}}$	Conductivity measured on a mesa in perpendicular direction
$\sigma_{\perp, 2D}$	Conductivity of a 2D infinite sheet measured in perpendicular direction

σ	Electrical conductivity
$\Theta_{0,1,2}$	Relative fractions of free (0), oxidized (1) and subsequent-oxidized (2) sites
Θ_D	Debye temperature
Θ	Rotation angle
θ	Angle of rotation within rotational square method
A_S	Acceptor states
A	Cross-section of a wire
a	Lattice parameter
D	Oxygen dose
d	Circle diameter
E_A	Acceptor level
E_D	Donor level
E_F	Fermi level
E_i	Intrinsic level
E	Electric field
e	Elementary electronic charge
F_1	Correction factor of finite sample thickness
F_2	Correction factor concerning the alignment of the probes in respect to a sample edge
F_3	Correction factor concerning lateral width of a sample
$F_{3, \text{circle}}^{\text{in-line}}$	Correction factor F_3 for probes aligned in-line within a circle
$F_{3, \text{circle}}^{\text{square}}$	Correction factor F_3 for square arrangement of the probes within a circle
F	Correction factor
$H(x)$	Height-height correlation function
$h(x)$	vertical position of the surface
I_T	Tunneling current
I	Current
J	Current density

k_F	Fermi wave vector
k	Wave vector
L	correlation length
l	side length of a cube
N_A	Acceptor concentration
N_S	Density of states
n_p	hole concentration
n	free elektron density
p	so-called “specular parameter”
Q_{SC}	Space charge
Q_{SS}	Charge of surface states
q	normalized wave vector
R_{contact}	Contact resistance
R_{probe}	Resistance of the contacting probes
R_{sample}	Resistance of the sample
R_{\parallel}	Resistance in parallel direction
R_{\perp}	Resistance in perpendicular direction
R_{2D}	Resistance of a 2D sheet
R_{3D}	Resistance of a 3D semi-infinite material
R	Resistance
r	Radius
s	Probe spacing
T_P	Peierls temperature
T_C	Critical temperature for a phase transition
T	Temperature
t	(Sample) thickness
V_B	Booster voltage
V_T	Tunneling voltage
V	Voltage

Contents

I	Introduction and physical background	1
1	Introduction	3
2	Phenomena in 1D metallic systems	9
2.1	Peierls instability	10
2.2	Quasi-1D	11
2.3	Space-charge layer	13
3	Experimental setup	17
3.1	Setup of the UHV chamber	17
3.2	Standard contacting procedure	19
II	Characterizing electronic transport by a four-point probe technique	23
4	Four-probe methods for isotropic 3D bulks and 2D sheets	25
4.1	Introduction	25
4.1.1	Two-point probe vs. four-point probe measurements	25
4.1.2	Resistivity for a semi-infinite 3D material, infinite 2D sheet and 1D wire	26
4.2	Correction factors for finite isotropic samples	28
4.3	The van der Pauw theorem for isotropic thin films of arbitrary shape	31
5	The 4pp technique on anisotropic crystals and surfaces	33
5.1	Anisotropic semi-infinite 3D bulk and infinite 2D sheets	33
5.2	Rotational square method	35
5.3	Anisotropic finite samples	36
III	Self-assembled atomic-scale nanowires	41
6	In/Si(111)-(4 × 1) reconstruction	43
6.1	Introduction	43
6.2	Atomic and electronic structure	43
6.2.1	Atomic structure	43
6.2.2	Electronic structure	44

6.3	Phase transition	45
6.3.1	Structural properties of the phase transition	46
6.3.2	Electronic properties of the phase transition	47
6.3.3	Role of defects	49
6.4	Electronic transport	50
6.4.1	Finite size effects studied in anisotropic 2D system	51
6.4.2	Adsorption of molecular oxygen	55
6.5	Summary and conclusion	63
7	Au on vicinal Si surfaces	65
7.1	Introduction	65
7.2	Si(557)-Au and Si(553)-Au: An evolution of models	66
7.2.1	Si(557)-Au	66
7.2.2	Si(553)-Au	69
7.3	Electronic transport	74
7.3.1	Sample preparation	74
7.3.2	Transport properties of the pristine surface	74
7.4	Tuning the conductivity of atomic wires by selective chemisorption	76
7.4.1	DFT results	81
7.4.2	Quantitative analysis of the transport data	86
7.4.3	Summary and conclusions on the adsorption process	87
7.5	Probing the phase transition by transport experiments	88
7.5.1	Influence of the space-charge layer	88
7.5.2	Temperature dependence of the Si(553)-Au surface	93
7.5.3	Discussion of the observed structural and electronic transition	101
7.5.4	Summary on the phase transition of Si(553)-Au	103
8	Tb silicide nanowires on Si(001)	105
8.1	Introduction	105
8.2	Formation of TbSi ₂ wires on Si(001)	106
8.2.1	Sample preparation	107
8.2.2	Structural properties of TbSi ₂ wires	107
8.2.3	Electronic properties of TbSi ₂ wires	110
8.2.4	Transport properties of TbSi ₂ wires	112
8.2.5	Resistivity size-effects in TbSi ₂ wires	119
8.3	Summary and outlook	124
9	Summary	129
9.1	Analyzed systems	129
9.1.1	In/Si(111)-(4 × 1) reconstruction	129
9.1.2	Si(hhk)-Au	130
9.1.3	TbSi ₂ nanowires	131
9.2	Outlook	131

IV Appendix	133
A Calculation of the SCL conductance	135
B Two-step adsorption process within the Langmuir adsorption model	137
C Bibliography	139
D Publication list	169
Curriculum Vitae	171
Danksagung	173

Part I

Introduction and physical background

Introduction

Today's advances in technology were paved by the invention of the transistor in 1947 by William Shockley and his colleagues at the famous Bell Laboratories and the subsequent rise of integrated circuits in the 1950s. Today, it seems already somehow natural that there is an ongoing trend resulting in always faster electronics like e.g. PCs, smartphones and tablets year after year and the related benefits resulting from higher computing power are touching nowadays our all daily life in nearly every single aspect. This continuing and evolving advances in technology are mainly achieved by an increasing density of electronic components packed on a chip and have been quantified by the co-founder of Intel Corporation Gordon Moore and his famous law which dates back to 1965 [1]. Based on empirical data, it proposes that the number of transistors on a chip doubles roughly every 18 month [2]. This empirical observation is plotted in figure 1.1 showing the development of transistor density, the used processing technology and the increasing clock rate over the years.

Obviously, to accommodate the ever growing number of electronic components on a chip, the overall dimensions of circuits, electronic interconnects, transistor gates, etc. need to be downsized. While the first chips in the 1970s had a minimum processing size of $10\ \mu\text{m}$, Intel uses currently a 14 nm manufacturing technology [3] which is roughly 6000 times smaller than the thickness of a human hair. Moreover, the International Technology Roadmap for Semiconductors (ITRS) [4] projects in their latest edition 4 nm processing sizes for the year 2020. Since the lattice constant of silicon is $5.430710\ \text{\AA}$ [5], 4 nm will only correspond to approximately 7 times of this value. Thus, in the not so distant future, current silicon based devices are expected to reach their technological limit with respect to the miniaturization [6]. This is not only due to the obvious reasons that a further reduction will reach atomic sizes and that single dopant atoms will heavily change the electronic properties of devices [7]. This is also because miniaturization itself leads to an increased surface to volume ratio and quantum mechanical effects will have to be taken into account. For example, tunneling of charge carriers through a barrier causing a leakage current will play a major role in future designs. In addition, with growing miniaturization progress the general heat dissipation and electromigration is getting more important.

While already the concepts of smaller electronic devices could be proven in laboratory conditions, such as single molecule amplifiers [10] and diodes [11], single layer graphene transistors [12], or as even recently shown single atom transistors based upon a single phosphorus

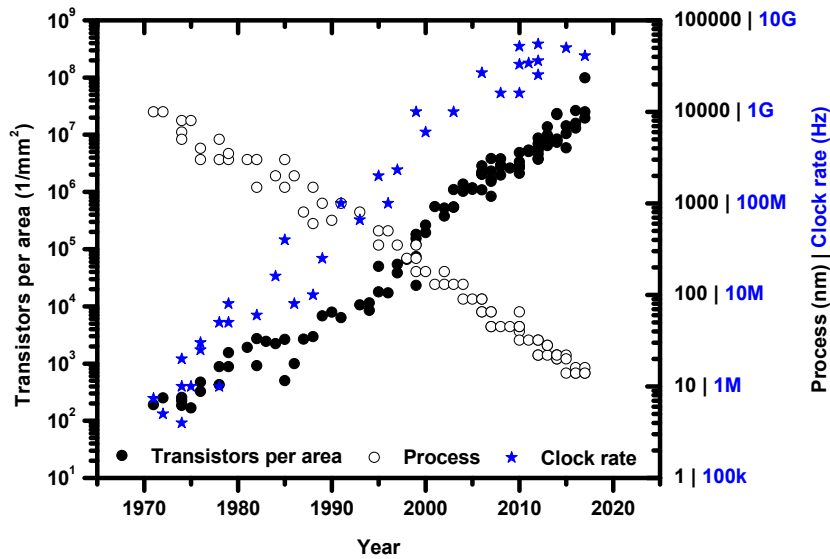


Figure 1.1: Development of the transistor density, processing technology (refers to the smallest structural size that can produced) and clock rate over the years illustrating the “Moore’s law”. Plot based on data published in [8, 9].

atom embedded in a silicon circuit by precision of one silicon lattice constant [13], the interconnects need to be scaled down as well. For this purpose, 1D *atomic wires* or *atomic chains*, respectively, which will be the topic of this thesis, are very promising as active elements in circuits.

These atomic wires are not only striking as simple interconnects from a technological perspective, but they are also highly interesting from a fundamental point of view. In 1D structures, electrons are confined to move only along a particular direction. Thus, the electron interaction and correlation in such systems is of high importance and leads to new physical properties [14, 15]. Most notably, the model of a Fermi liquid can no longer be applied. Instead, such systems need to be described in terms of the Tomonaga-Luttinger liquid theory [16, 17]. Within this theory, a collective excitation leads to a spin-charge separation [18, 19] equivalent to the existence of the so-called quasi-particles spinon and holon which propagate with different group velocities: the spin density wave (SDW) and the charge density wave (CDW). This could lead to further futuristic applications. For example, a spin shift register based on a 1D atomic chain was proposed which could be used as new computer memory devices where the information is encoded in spins [20].

The realization of true 1D atomic chains is still very challenging. For example, atoms can be aligned in a chain by laser cooling and electric and/or magnetic field (cf. exemplarily with references [21–23]). Metallic, free standing atomic chains can be realized using a gold scanning tunneling microscope (STM) tip dipped into a gold cluster and a slow withdrawing [24]. But such realized chains are very unstable, have low life times of a few minutes and short lengths of a few atoms. A more viable approach is the self-assembled growth of metallic atomic chains on vicinal or slightly miscut silicon where the atoms arrange in chains parallel to the step edges. However, by embedding the atomic chains into a 3D environment, strictly

speaking, such prepared systems are not fully 1D but rather “quasi-1D”: There is a coupling with the underlying substrate and an interaction between adjacent chains which can modify the theoretically expected 1D behavior resulting in new effects. For example, PEIERLS [25] already demonstrated in 1930 theoretically that a 1D chain of atoms is unstable with respect to a periodic lattice distortion. Inevitably, a dimerization occurs for half filled bands resulting in the formation of a band gap at $k = \pi/a$, where a denotes the lattice parameter. The embedding of a 1D atomic chain in a 3D environment now results in a stabilizing of the described effect at higher temperatures suppressing the Peierls effect. But on the other hand, additional 1D properties may be modified or even destroyed, and such effects are still largely unexplored from an experimental and a theoretical side.

Therefore, the main focus of this thesis is to further explore and manipulate the transport of atomic chains by an explicit consideration of the environmental embedding.

Structure of this thesis

This thesis is divided into four parts. After this introduction, part I continues in chapter 2 with a brief overview of 1D metallic systems. Chapters 2 and 3 introduces the reader to the experimental setup, the four-point probe (4pp) STM combined with a high resolution scanning electron microscope (SEM), which was used as the main technique for the sample analysis.

In part II transport measurements using a 4pp technique are discussed in detail. Here, chapter 4 first of all motivates the need of 4pp measurements instead of the much easier and maybe more intuitive two-point probe (2pp) technique. Afterwards 4pp measurements in 1D, 2D and 3D are elucidated in general and the differences in respect to the resistivity are highlighted. Experimentally realistic transport problems are always performed on finite sample regions and therefore a later part of the chapter discusses the need of so-called correction factors and under which circumstances it is possible to neglect them, i.e. a sample can be called in good approximation infinite. The chapter ends with a brief introduction of the well known van der Pauw theorem for the measurement of the resistivity of arbitrary shaped samples. Since atomic wire systems are ideally 1D, it is expected that the current is mainly flowing parallel to the wires and nearly no current should flow perpendicular to the wires resulting in a strong anisotropic transport behavior. Chapter 5 is therefore adopting the previously presented 4pp technique used on finite and infinite samples to the case of anisotropic samples. It is pointed out that specific contact geometries are needed to disentangle the parallel and perpendicular components of the resistivity. For this purpose, the reader is introduced to the so-called rotational square method which was used fully throughout the thesis and allows to measure the resistivity components with a high precision by sequentially probing the sample surface while changing the alignment in respect to the chains. The chapter ends with the discussion of correction factors for the case of a square 4pp array inside an anisotropic circular mesa structure and deduces the transition from the finite case (probes align on the periphery of the circular mesa) and the infinite case (probes are in the center with sufficient separation to the edge).

Part III forms the main part of this thesis. In this part three different self-assembled atomic wire systems (In/Si(111)-(4 × 1), Si(hhk)-Au and TbSi₂) are presented. Each system is discussed in its own chapter. The general structure which will be followed for these chapters

is first to introduce the reader within the particular system, followed by the discussion of results obtained from experiments and finally ending with a short summary.

In chapter 6, the In/Si(111)-(4 × 1) reconstruction is investigated. This system has a special status within the atomic wire research community since it was one of the first and up to now most comprehensively studied systems. It is therefore taken commonly as a benchmark system for the understanding of 1D physics in atomic chains. Despite extensive studies over the last two decades, there are still open questions and new observations, e.g. very recently topological defects were detected for this system [26, 27]. Open questions are related to the occurring metal-insulator transition (MIT) and the influence of defects, e.g. it was shown that oxygen increases the transition temperature while the adsorption of hydrogen results in a lowering of the critical temperature T_C . Thus, a special focus of this thesis is set on the effect of defects induced by adsorption of molecular oxygen seen in transport experiments. For a better sensitivity toward defects and in connection with the results of chapter 5, transport measurements are performed in finite areas. It is shown in agreement with recent density functional theory (DFT) results that there is an effective interwire coupling. This finding was not reported in literature before.

In chapter 7 the Si(hhk)-Au system is analyzed. These systems are astonishing because their physical properties can be easily altered by the vicinity of the system and are strongly depending on the structural building blocks (Au chains, Si-atom chain, Si-honey comb (HC) edge). This thesis focuses on the Si(557)-Au and Si(553)-Au systems. The last one attracted a lot of attention recently since a pronounced magnetic order was observed which mimics a 2D quantum spin liquid [28]. Similar to measurements in chapter 6, the transport behavior during the adsorption of molecular oxygen was analyzed. It is shown that depending on the structural building blocks, the Si(hhk)-Au is either rather immune against oxygen adsorption or strongly influenced. This result is further backed up by recent DFT results. In addition, the MIT is revised. Interestingly, a structural phase transition was observed for the Si(553)-Au which at the same time shows still a residual conductivity along the chains. This is in clear contrast with previous reports which showed the formation of a CDW.

The last chapter of part III, chapter 8, treats TbSi₂ nanowires, which were grown on vicinal Si(001) substrates. In contrast to the reconstructions of the In/Si(111)-(4 × 1) and Si(hhk)-Au systems, which form an ensemble of atomic chains, depending on the growth parameters rare-earth silicides form very long, thin and well separated either single or bundled nanowires. These systems are therefore also interesting from an industrial point of view since the self-assembled growth could be used as interconnects in CMOS technology. The transport properties of TbSi₂ nanowires are analyzed in combination with STM revealing a high dependence of resistivity from the surface height and roughness in agreement with the description within a quasi-classical transport model.

Finally, a concluding summary of the content of this thesis and an outlook about future research proposals are given in chapter 9.

Parts of this thesis were already previously published in

- “Interwire coupling for In(4 × 1)/Si(111) probed by surface transport” [29] by EDLER et al. (2015 in *Phys. Rev. B*)
- “The 100th anniversary of the four-point probe technique: the role of probe geometries

in isotropic and anisotropic systems” [30] by MICCOLI, EDLER et al. (2015 in *J. Phys.: Condens. Matter*)

- “Atomic size effects studied by transport in single silicide nanowires” [31] by MICCOLI, EDLER et al. (2016 in *Phys. Rev. B*)
- “Tuning the conductivity along atomic chains by selective chemisorption” [32] by EDLER et al. (2017 in *Phys. Rev. B*)

and will not be separately cited in the text.

Phenomena in 1D metallic systems

Physics usually starts from simple models and implements additional effects step by step while comparing and verifying the outcome of the model with the experiment. Quite often, a simple model is representing a system sufficiently within certain conditions, so that in general one can say a simplification reduces the problem to its essence. Examples in physics are manifold, e.g. the introduction of the center of mass point in classical mechanics. Therefore, it seems to be intuitive to assume that, by reducing the dimensionality of a problem, also a simplification of a physical problem in solid state physics will occur. However, contrary to this expectation, theory and experiments shows that the reduction of the dimension of a metallic solid to 1D results in entirely new effects. Thus, the physical behavior of metals is strongly dependent on the dimension of the system and the electronic properties have to be described differently. The reason is that there is a strong correlation between the electrons of the system.

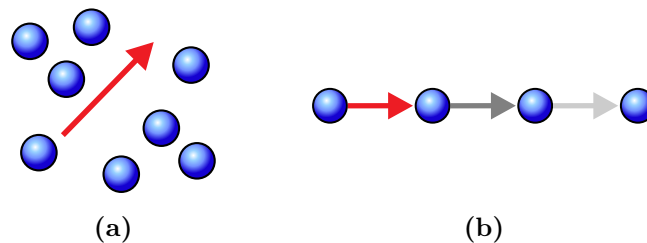


Figure 2.1: Schematic drawing illustrating the excitation of an electron gas in 2D/3D (a) and in 1D (b). The excitation is symbolized by a red arrow. It can be rationalized that only collective excitations (symbolized by the additional gray arrows) are possible for the 1D case.

This can be illustrated as follows in a simple and intuitive model (cf. figure 2.1(a)). Here, a 2D or 3D free electron gas (symbolized by blue spheres) can be excited without interaction with other electron (quasi-free excitation). But for the 1D case (cf. figure 2.1(b)), the excitation of an electron is always associated with the excitation of other electrons, so that only collective excitations exist. As a consequence of the strong electron-electron interaction, various effects occur, which lead to the so-called Peierls instability [25], the splitting of charge and spin into a charge density wave (CDW) or a spin density wave (SDW) [33], and the model of the Tomonaga-Luttinger liquid (TL) [17], leading to a spin-charge separation

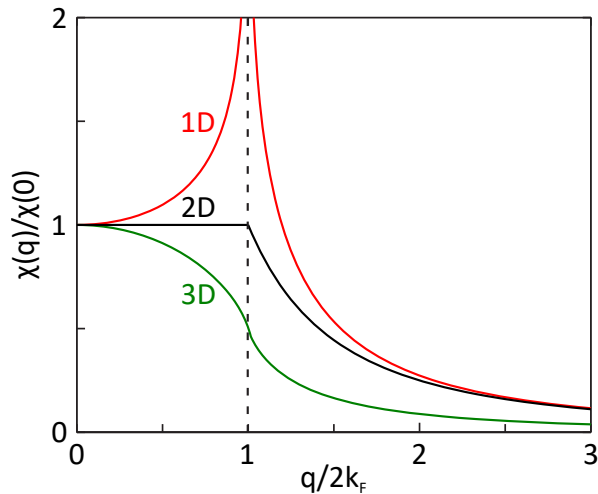


Figure 2.2: Lindhard response function $\chi(q)$ for a one-, two- and three-dimensional free-electron gas at $T = 0$ K [35, 36].

with the two quasi-particles spinon (carrying the spin) and holon (carrying the charge), that can move independently within a 1D system.

2.1 Peierls instability

As written in the introduction, the strong interactions in 1D can lead to a multitude of interesting physical effects. The atomic wire systems examined in this thesis are known to either have a Peierls transition (the In/Si(111)-(4 × 1) reconstruction) or there is the strong debate if the system has a Peierls driven phase transition (the Si(hhk)-Au family). Thus, the following paragraph will give a brief overview of the theory of the Peierls transition.

According to textbook physics (cf. exemplarily the textbooks of GIAMARCHI [14] and GRÜNER [34]) the response of an electron gas to an external perturbation is given by the so-called Lindhard response function which is plotted in figure 2.2. Notably, there is a singularity for 1D at $q = 2k_F$ which has severe important consequences. It implies that any external perturbation leads to a divergent charge redistribution [34]. Because of the diverging Lindhard response function at the wave number $k = 2k_F$ in 1D, an infinitesimal stimulation inevitably results in instabilities which induce lattice distortions due to electron-phonon coupling. This intrinsic instability was first described in theory by PEIERLS [25] in 1930.

The mechanism of the Peierls transition can be illustrated as follows. Above the Peierls temperature T_P the 1D-metallic conduction band of a 1D chain with lattice constant a and one electron per unit cells is filled up to the Fermi level E_F at the Fermi wave vector k_F (cf. figure 2.3(a)). Considering an efficient electron-phonon coupling, the interaction of all electrons with a phonon mode leads with decreasing temperature to an instability of the lattice with an atomic displacement of the periodicity of $2\pi/2k_F$. This introduces a new Brillouin zone at $\pm k_F$ that consequently opens a band gap at E_F as shown in figure 2.3(b). Of course, the system must provide energy for this displacement but at the same time, by changing the lattice periodicity, a band gap Δ opens at the Fermi edge at $\pm k_F$. This results

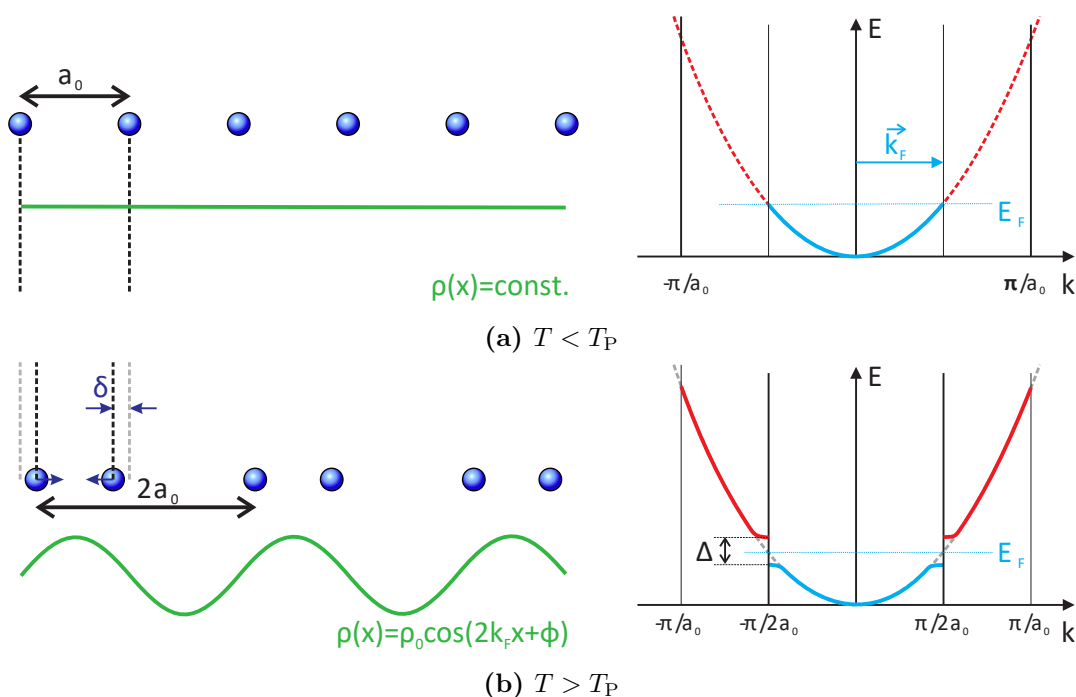


Figure 2.3: Schematic drawing illustrating the effect of a Peierls distortion on a linear chain of atoms occupied with one electron and a half filled band. (a) $T < T_P$: The charge density is constant. The dispersion curve shows a metallic behavior. (b) $T > T_P$: By lattice deformation the edge of the Brillouin zone is reduced to the half value resulting in the opening of an energy gap. The charge density is periodically modulated.

in a higher density of states in the region of the Fermi edge, which leads to an increase in the number of lower energy states that could be occupied by the electrons below the Fermi energy. The overall energy cost in distortion is lower than the gain in electronic energy, making the transition always favorable [34, 37]. By forming an over-structure with said band gap near the Fermi edge, the system transitions from a metallic to a semiconducting state. In the case of a half-filled band, the period of the grid atoms is doubled. A completely filled and an empty subband are formed. As a result of the deflection of the lattice atoms from the equilibrium position, the charge density is modulated with $2k_F$ [35] which is usually called a CDW:

$$\rho(x) = \rho_0 \cos(2k_F x + \phi) \quad (2.1.1)$$

2.2 Quasi-1D

A prototypical representation of 1D systems can be achieved by atomic chains. However, it has to be highlighted that although the term “atomic chains”, which strictly speaking inherently implies the treatment in terms of free atomic chains, is always an idealization since experiments are performed in a 3D environment. Therefore, any real material which comes closest to the 1D concepts, is best described as quasi-1D as there is an inevitable embedding and coupling into our 3D environment. But especially the embedding and related

effects like the coupling to the environment or within an ensemble of wires make these quasi-1D systems very interesting from an experimental and theoretical point of view since new physics can also be explored. For instance, in 1D systems any long-range order is destroyed by thermal fluctuations at finite temperature ($T > 0$ K). Low dimensional structures are stabilized only by a coupling to an environment, enabling access to observe e.g. Peierls driven metal-insulator transition (MIT) at finite temperatures which can be even further tuned by defects [38, 39]. However, up to now, the coupling of 1D systems to their environment and the underlying mechanism are largely unexplored and are still poorly understood [39, 40].

Quasi-1D metallic atomic wires

Metallic atomic wires grown on Si or Ge surfaces can be classified mainly in two groups: the so-called elemental atomic wires and silicide wires. Elemental atomic wires are typically (sub)monolayer structures with metal-induced surface reconstruction. Prominent examples are atomic chains induced by Au, In, or Pb. In comparison, silicide wires are formed from rare earth metals like Y, Dy, Tb, Gd which react with Si and the atomic structure is (mostly) related to bulk silicide properties.

The best understood atomic wire system so far is the In/Si(111)-(4 × 1) reconstruction [41] which consists of an ensemble of wires formed upon room temperature deposition of ca. 0.75 - 1 monolayer (ML) indium on planar Si(111) substrates and subsequent annealing. The structural model was established with great consistency within experiments [42–50] and theoretical calculations [42, 51–58]. Each wire consists of two In zigzag chains within a (4 × 1) surface periodicity which are separated by Si chains. The system shows an interesting temperature-dependent phase transition from the conducting (4 × 1) phase at room temperature to the insulating (8 × 2) structure at temperatures below $T_C = 120 - 130$ K [45, 48, 54, 59–61]. The transition was studied by a plethora of experimental techniques and theoretical studies. After strong debates, inconsistencies in observations could be resolved during recent years. The structure of the low temperature phase could be finally clarified by a combined surface optical-theoretical analysis [62] and was explained by a shear rotation leading to the formation of hexagon like structures with a (8 × 2) [63, 64]. The transition was finally explained as a Peierls-like first order phase transition [65–67] forming a CDW accompanied by a band gap opening of 0.1 - 0.3 eV [45, 46, 48, 59]. However, the environmental effect of defects like adsorbates is still puzzling, e.g. while many adsorbates (H, Cs, Na, ...) decrease the MIT temperature T_C , the adsorption of oxygen leads to an increase of T_C [39].

Another prominent atomic wire system formed by self-assembly, which builds ensemble structures, is the Si(hhk)-Au family [68]. In comparison to preparations on planar surfaces as for the In/Si(111)-(4 × 1), highly stepped Si(111) surfaces share a common set of structural motifs which open the possibility for tuning the physical properties (e.g. interchain coupling) by variation of the terrace width. While the structural models of Au induced atomic wire systems on Si(hhk) seem to be clarified and understood in recent years [69], e.g. all known reconstructions have an Si-honey comb (HC) at the step edge and the terrace hosts depending on the width either single or double Au chains, the discussion about possible phase transitions in these systems is not settled yet. For example, earlier scanning tunneling microscope (STM)/scanning tunneling spectroscopy (STS) studies reported Peierls-like CDW instabilities and transitions into an insulating state below 200 K in the Si(553)-Au and Si(557)-

Au systems [38, 70] which was partly supported by surface transport measurements [71]. However, later simple Peierls-like transitions were disproven [41, 72], since the observed band fillings do not match the required nesting conditions and observed periodicity doubling in STM was strongly depending on tunneling parameters. Thus, the structural transitions observed are not connected with the formation of CDW but the spin order found along the terrace edge plays a major role so a transition could be explained by an order-disorder effect. But just like for the In/Si(111)-(4 × 1), the role of doping and other defects, which may change the interchain coupling drastically, is still not understood.

In contrast to the mentioned elemental wire systems, which form ensemble structures of wires, single or bundled silicide wires consisting of rare earth (RE) metals grow on silicon. As shown, e.g. for Y, Dy, Gd on various Si substrates the interchain interaction of silicide wires is of less relevance [73–76]. Since the growth of silicide wires is uniaxial along one crystallographic direction and selflimiting with built-in Schottky barrier to the substrate, in addition to the physical effects in 1D, silicide wires are interesting from a technical point of view since they could be easily integrated in current nanotechnology setups. So far, only very few transport studies have been performed on RE silicide wires. Interestingly, transport measurements on silicide nanowires showed a similar dependence on defects and interwire related effects as ensemble wire structures. Exemplarily, transport measurements on GdSi₂ [77] wires on Si(100) showed a MIT on isolated nanowires, while a robust metallic state was obtained for wire bundles. This behavior was explained for the isolated wires by defects, which lead to electron localization, while the interwire coupling is stabilizing the structure and metallic states in the wire bundles [73]. Similar effects are to be expected on other materials like, e.g. Tb which will be used in this thesis.

Summarizing the three presented atomic wire systems, defect and doping related effects play a major role in understanding the physical properties of atomic scale nanowires and especially the inter- and intrawire coupling is far from being completely understood. The inter- and intrawire coupling can be best explored experimentally by surface transport experiments. Here, the following main questions arise which shall be covered within the thesis: *How do environmental and embedding related effects alter the atomic chains and transport? How do defect structures influence the inter- and intrawire coupling? How important is the interwire coupling for the transport? How are defects and interwire coupling related to the phase transition?*

2.3 Space-charge layer

Concerning transport and environmental effects, it is known that near the surface space-charge layer (SCL) regions are formed on semiconductors like Si or Ge. In general within transport experiments, the measured conductivity σ is always the sum of the contributions of three different current channels

$$\sigma = \sigma_{\text{SS}} + \sigma_{\text{SCL}} + \sigma_{\text{B}}, \quad (2.3.1)$$

where σ_{SS} is the contribution of the surface-state bands of the topmost atomic layer, σ_{SCL} is the isotropic surface SCL beneath the surface and σ_{B} is the contribution from the bulk. Naturally, for the surface transport the contribution of the surface-state bands σ_{SS} is interesting. Thus, further questions are *how relevant are the parasitic transport channels σ_{SCL}*

and σ_B for the surface transport and its interpretation? Can the channels be disentangled? This section will give additional insights to the formation of SCLs and the band structures. In the experimental chapters of part III the influence of the SCL on transport experiments will be discussed further.

Depending on the Fermi level at the surface of a semiconductor and the type of surface states (SS) (acceptors or donors, i.e. some electrons are transferred from the bulk into the SS which charge them negatively or electrons are donated from the SS into the bulk, respectively), the SS carry a charge Q_{SS} (positive charge for donors and negative charge for acceptors), which is screened by an equivalent charge the so called space charge Q_{SC} within the semiconductor bulk material. In order to maintain the charge neutrality, i.e.

$$Q_{SS} = -Q_{SC}, \quad (2.3.2)$$

the bands bend in the sub-surface region. The bands bend upward (downward) to induce excess holes (electrons) for counterbalancing the SS charge Q_{SS} , when acceptor (donor)-type SS form [78].

The band bending, near the surface is given by the deviation of the intrinsic level E_i from the Fermi energy E_F :

$$\Phi(z) = \frac{1}{e}(E_F - E_i(z)). \quad (2.3.3)$$

The theoretical description of SCLs consists basically in solving the Poisson's equation

$$\frac{d^2\Phi(z)}{dz^2} = -\frac{\rho(z)}{\epsilon_0\epsilon_B}, \quad (2.3.4)$$

where ϵ_B is the relative permittivity of the semiconductor bulk and $\rho(z)$ the charge density, which is depending on the density of ionized acceptors N_A and donors N_D , and the concentration of the electrons $n(z)$ and conduction holes $p(z)$, respectively (e is the electric charge):

$$\rho(z) = e(N_D - N_A + p(z) - n(z)). \quad (2.3.5)$$

However, since

$$n(z) = n_i \exp(e\Phi(z)/(k_B T)), \quad \text{and} \quad p(z) = n_i \exp(-e\Phi(z)/(k_B T)), \quad (2.3.6)$$

where $n_i = \sqrt{p \cdot n}$ is the intrinsic carrier concentration given by

$$n = N_{\text{eff}}^C \exp(-(E_C - E_F)/k_B T), \quad (2.3.7)$$

$$p = N_{\text{eff}}^V \exp(-(E_F - E_V)/k_B T) \quad (2.3.8)$$

are itself a function of $\Phi(z)$ (N_{eff}^C and N_{eff}^V are the effective densities of states of the conduction and valence band, respectively), solving the Poisson's equation is a tedious task and a general analytical solution can not be given [79].

The spatial extent of the space charge Q_{SC} is characterized by the so-called Debye length which is given by [80]

$$\lambda_D = \sqrt{\frac{\epsilon_0\epsilon_B k_B T}{e^2(N_D + N_A)}}, \quad (2.3.9)$$

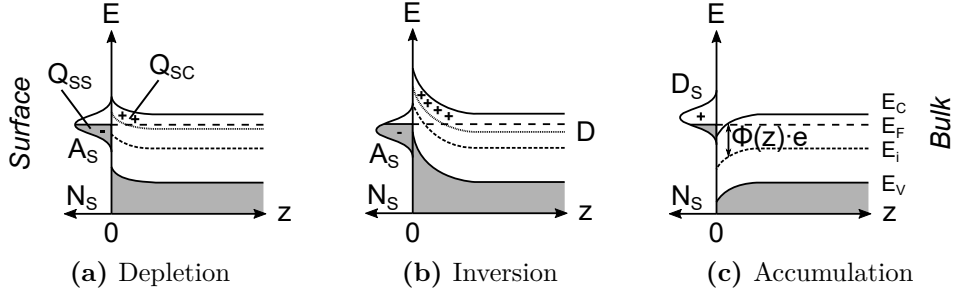


Figure 2.4: Band diagrams of a n-type semiconductor showing schematically the (a) depletion-, (b) inversion-, and (c) accumulation-SCL at the surface. E_C , E_V are the conduction and valence band edges, E_F the Fermi energy and E_i the intrinsic energy. A_S , D_S denotes surface acceptors and donors, respectively. Bulk donors are labeled by D . N_S is the density of states. Q_{SS} is the charge of the surface states which is compensated by the space charge Q_{SC} . $\Phi(z)$ is the potential variation, i.e. the band bending.

where ϵ_0 is the permittivity of the vacuum, ϵ_B the permittivity of the bulk, e the elementary charge, and N_D and N_A are the bulk carrier densities, respectively. If $N_A \ll N_D$ equation (2.3.10), is simplified to

$$\lambda_D \approx \sqrt{\frac{\epsilon_0 \epsilon_B k_B T}{e^2 N_D}}. \quad (2.3.10)$$

Based on the band bending, three different types of the SCL have to be distinguished which are related to an depletion, inversion and accumulation of mobile carriers at the surface. The SCLs for a n-type semiconductor are schematically drawn in figure 2.4. The situation is correspondingly reversed for a p-type semiconductor.

In the case of a *depletion layer* an upward bending of the bands near the surface occurs. This allows the SS band to cross the Fermi level which leads to a SS charge density Q_{SS} . For the same reason, the bulk donor states are raised above the Fermi level and thereby emptied of electrons. This builds up a positive space charge Q_{SC} of ionized donor centers (E_D). The fact is very important for the later interpretation of transport experiments presented in chapter 7, section 7.5.1 since the fixed ionized background leads to scattering in transport experiments. The SCL is called depletion layer since free conduction-band electrons (majority carriers) are pushed away from the surface, and their density is lowered with respect to the bulk density [79].

For an even stronger upward band bending by higher densities N_S of surface acceptor states (A_S), the SCL is called an *inversion layer*. The situation is exemplarily depicted in figure 2.4(b). For this case, the intrinsic level E_i at the surface is above the Fermi level E_F and density of holes, i.e. the minority carriers, is greater than the intrinsic carrier density below the surface. By this, the type of carrier at the very surface is inverted with respect to the bulk forming a p/n junction. This is important for the In/Si(111)-(4 × 1) and the Si(hhk)-Au systems treated in part III. According to angle-resolved photoemission spectroscopy (ARPES) measurements [81, 82], the bulk valence-band maximum at surface is located at around 120 meV below Fermi for the In/Si(111)-(4 × 1) and around 250 meV for the Si(hhk)-Au systems which indicates an inversion type SCL for an n-type Si wafer [83]. The p/n junction ensures that the system is electronically isolated from the bulk and no probing current is

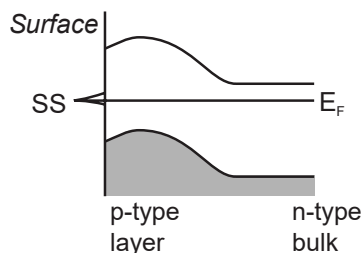


Figure 2.5: Schematic drawing of the band bending of a n-type semiconductor with a p-type layer near the surface due boron or carbon diffusion into the bulk during flash annealing. Image adapted from [84].

penetrating into the bulk. Thus a parasitic contribution of the bulk σ_B can be neglected in the transport experiments of those systems.

The last case shown in figure 2.4(c) is called an *accumulation layer*. An accumulation layer occurs when there are donor-type surface states which are located at high energies and carrying a positive surface charge Q_{SS} . The positive surface charge Q_{SS} is compensated by a negative space charge Q_{SC} within the bulk leading to the accumulation of free electrons in the conduction below the surface. Thus, the band bending in the case of an accumulation layer is a downward bending.

The conductivity of the SCL which is measured as an isotropic, parasitic contribution in the transport experiments arises from the accumulation of mobile minority carriers. In the case of a depletion and inversion layer these are excess holes whereas electrons for the case of an accumulation layer [78].

Following the arguments outlined in [78], the space charge contribution can be numerically expressed. For example, in the case of a n-type Si material with a resistivity of $\rho = 1700 \Omega\text{cm}$, the SCL contribution is calculated to be below $1 \mu\text{S}$ at room temperature. A detailed description of the calculation is given in appendix A.

Formation of p-type layer on low doped (n-type) samples

The preparation of clean and long-range ordered surface structures demands high temperature ultra-high vacuum (UHV) annealing of the Si templates. However, systematic surface sensitive transport experiments revealed irreversible surface-near changes of the doping in terms of the type, concentration and distribution [84–86]. It was shown for n-type bulk semiconductors that boron [85] or carbon [84] diffuse into the surface by flash annealing which leads to the formation of a p-type surface layer as exemplarily shown in figure 2.5. This effect is especially severe on low doped samples. Due to the p-type layer, close to the surface there is a downward band bending depending on the the Fermi-level position [84]. Therefore, high temperature annealing steps with temperatures $> 1150^\circ\text{C}$ were not done while performing experiments in this thesis. Nonetheless, in order to maintain long-range ordered chain structures, the lower temperatures were compensated by multiple flash cycles.

As it will be shown in the experimental part in chapter 7, even lower flash annealing temperatures lead to the formation of a p-type layer near the surface and this effect can not be hindered. Thus, chapter 7 will discuss in detail how this SCL feeds back to the transport.

Experimental setup

All transport experiments of this thesis were carried out by means of a commercially available four-point probe (4pp) scanning tunneling microscope (STM)/scanning electron microscope (SEM) system from the Omicron NanoTechnology GmbH. The following sections will briefly explain the main components of the system.

3.1 Setup of the UHV chamber

To minimize the influence of defect adsorption, experiments were carried out in an ultra-clean environment under ultra-high vacuum (UHV) conditions. The typical base pressure of the system was below 3×10^{-10} mbar. A schematic overview of the UHV chamber is given in figure 3.1. The chamber is separated into two parts: a preparation and an analysis chamber. Additionally, for every chamber part there are load lock chambers which allow the exchange of samples as well as the replacement of tips without compromising the UHV conditions.

The preparation chamber part hosts several components for sample treatment. Samples can be heated either via direct current or via a backside filament. All samples investigated in this thesis were first degassed by direct current heating for at least five hours at 700 °C. Additionally, samples can be cooled to 140 K on a separate stage using liquid nitrogen. The temperature is controlled by an infrared pyrometer (LUMASENSE IG 140, accuracy in probed temperature region ± 5 °C) and the emissivity coefficient is calibrated in feedback controlled manner with respect to a Si substrate. Currently, up to three evaporators can be used for thin film deposition. In addition, the preparation chamber hosts a gas inlet system and H₂ cracker for further preparation steps. A first characterization of the sample preparation can be performed by means of a spot profile analysis low-energy electron diffraction (SPALED) system. A sample garage allows the storing of up to six samples.

For the transport experiments, the samples were transferred into the analysis chamber, which is separated from the preparation chamber by a gate valve allowing elevated pressures during processing of samples. The main part of the analysis chamber is formed by a multi-tip STM in combination with a high resolution SEM, which allows the exact positioning of STM tips and contacting of nanostructures in the nm ranges. In addition, the chamber hosts a mass spectrometer, which allows the characterization of the residual gas composition, and a field ion microscope (FIM). For high precision measurements the chemical composition of the

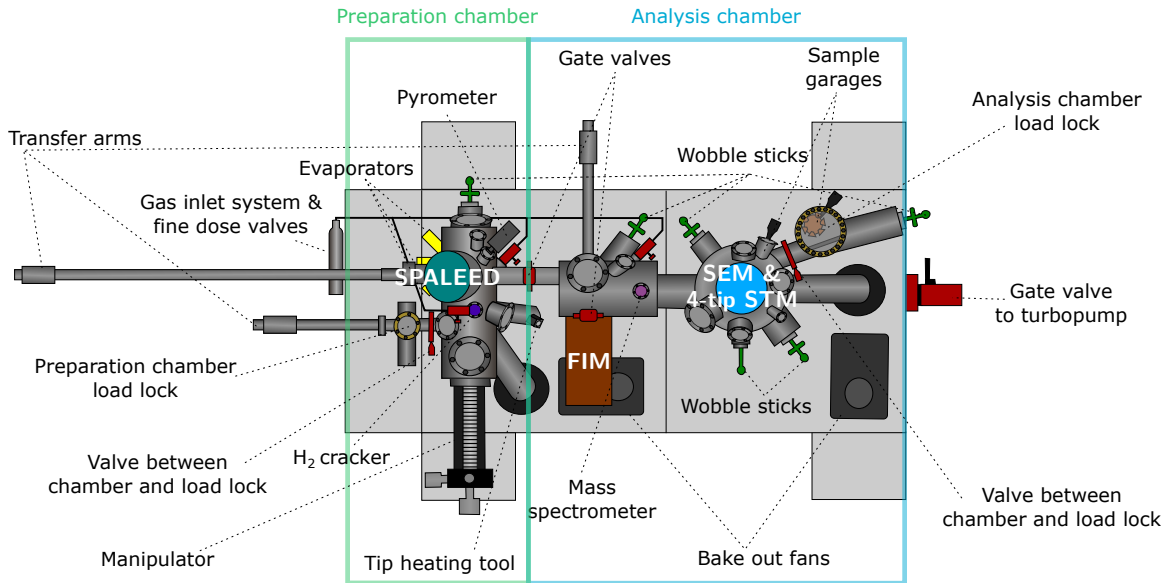


Figure 3.1: Schematic drawing showing the UHV chamber used for the transport experiments. The chamber is divided into two parts: The preparation chamber and the analysis chamber which hosts the 4pp STM in combination with a SEM.

tip apex can be characterized by FIM [87] or even tuned by field evaporation to form single atom tips as recently demonstrated by WOOD et al. [88]. During transport measurements the sample stage can be cooled with liquid helium to a temperature of 25 K. The tips can not be cooled directly and only cool while they are in tunneling or ohmic contact (cf. discussion of effects related to this limitation in section 3.2). By means of a proportional-integral-derivative controller (PID controller) the sample stage can be counter heated by filament for exact stabilization of temperature. Just like the preparation chamber, up to ten samples or replacement tips, can be stored in a garage within the analysis chamber.

High resolution SEM in combination with multi-tip STM

A schematic overview of the high resolution SEM and multi-tip STM setup is shown in figure 3.2. The SEM is a Gemini® type SEM of the Carl Zeiss AG. The electrons get extracted by a strong electrostatic field applied to a sharp tip which is heated at around 1200 K by hot field emission. In comparison to the cold field emission, much higher emission currents and beam stability can be achieved resulting in an increased image quality at lower accelerating voltages. A further improvement of the image quality – especially compared to other SEMs – is achieved in this type of SEM by an additional voltage, the so called booster voltage (cf. V_B in figure 3.2(a)). This additional voltage maintains a high beam energy throughout the whole column. The electrons are decelerated to the chosen primary beam energy only shortly before hitting the sample. By this, aberration is minimized and the beam diameter is only of a few nm. The aberration correction is especially important because of the relative large working distance of around 1.5 cm needed for operating the multi-tip STM. Using this setup,

the Gemini® type SEMs are certified to have a maximal resolution of 4 nm.

The multi-tip STM setup consists of four individual STM scanners of two different types. A schematic drawing of the setup is shown in figure 3.2. The three so called standard scanners are mainly used just for transport experiments. In contrast, the design of the high resolution scanner provides a better protection against vibrations which can be used to resolve sample surfaces with atomic precision. The four individual, feedback controlled STMs scanners are necessary in order to move the tips on the sample surface on a nanometer scale and to gently contact the surface during transport measurements. All the tips used in transport experiments and STM as well as scanning tunneling spectroscopy (STS) measurements are homemade, electrochemically etched tungsten tips using a well established standard recipe [91]. Before first usage, every tip is treated by voltage pulses for cleaning purpose between 10 - 20 V for 1 - 50 ms and in addition tested on a graphene reference sample.

3.2 Standard contacting procedure

Sourcing and probing of currents and voltages is done by means of a Keithley sourcemeter. Unless stated otherwise, transport investigations are carried out in the following way. First, the tips are navigated to their desired position while controlling the movement by the SEM. Then, the tips are approached by the STM feedback loop to the specified tunnel current. For transport measurements, the feedback loop is turned off and the tips are brought in contact to the sample surface in 0.1 nm steps. If the substrate is conductive, a voltage (10 mV) is applied between the sample ground and the tip which is getting approached. Reliable contacts are realized as soon as the measured current jumps from 10^{-10} A (i.e. the noise level with blanked SEM beam) to about 10^{-7} A. In the case of not conductive substrate material and only a conductive nanostructure, the same approach is used with the difference that two tips are approached simultaneously while measuring the current flow. The characterization of electronic transport by 4pp technique in general is shown in detail in part II.

Probe induced heating effects

As written before in section 3.1, the four probes of the system can not be cooled directly like the sample stage and they are only cooled while they are in (tunneling) contact. This means that there is inevitably a heat transfer between sample and probes as long as the system is not in equilibrium. Obviously, until the tip and sample have not reached an equilibrium state in terms of heat transfer, stable tunneling conditions can not be acquired. Thus, when the system is being cooled down, tips in tunneling contact are constantly shrinking and the corresponding STM piezo is expanding. Vice versa, when the system is heating up, tunneling tips are elongating while the STM piezo is decreasing in length. Depending on the initial temperature difference between tip and sample, typically two to three hours are needed for stable tunneling conditions.

Additionally, an equilibrium of heat transfer of the tip and sample is heavily changed when a probe contacts the surface. For obvious reasons, contacting of a cooled sample with a probe warmer than the sample temperature leads to a heat transfer from tip to the sample resulting in a local heating of the surface. At the same time the length of tips can shrink which eventually leads to a loss of contact if the tips are contacting for a long time. Thus, to

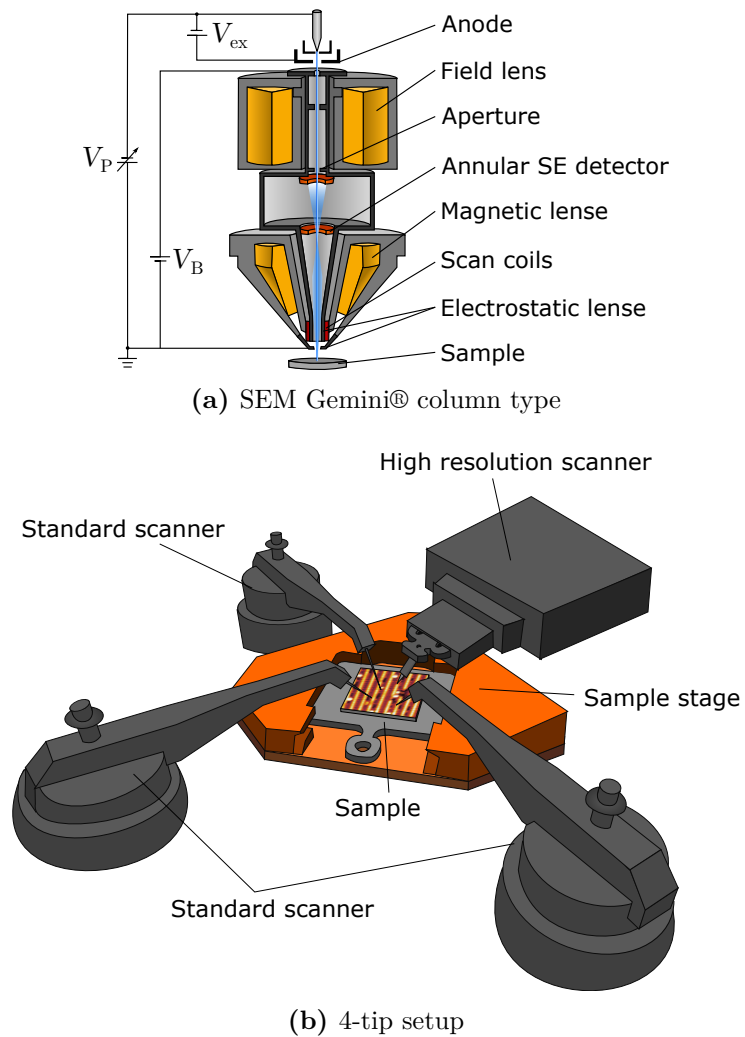


Figure 3.2: (a) Cross sectional view of the principal setup of the Gemini® SEM type (adapted from [89]).
(b) Schematic overview of the 4pp STM setup used for the transport experiment (adapted from [90]).

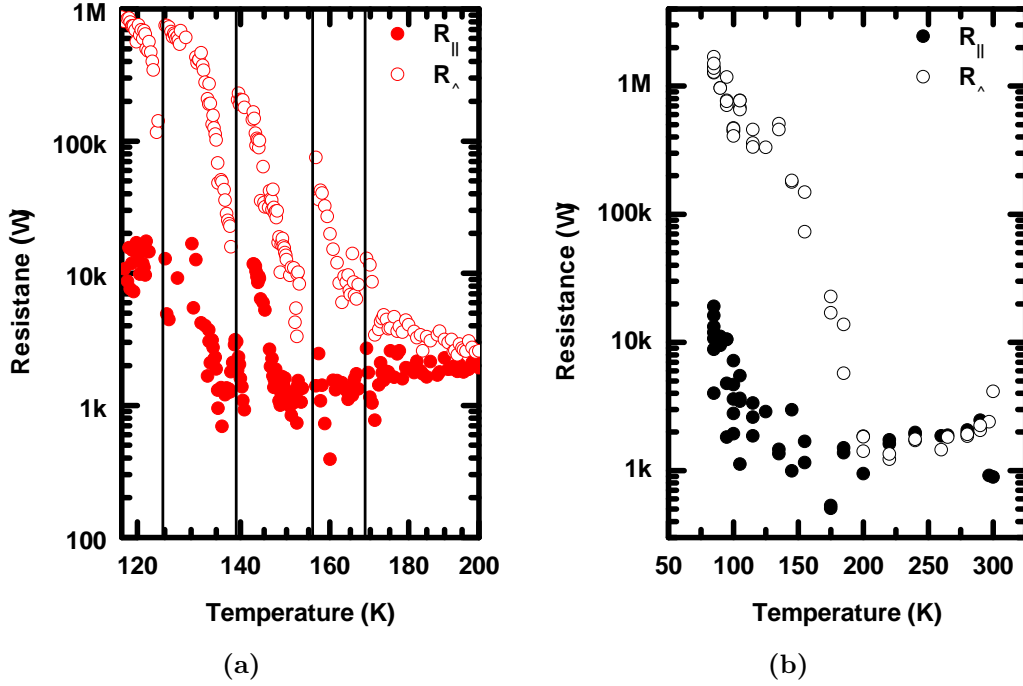


Figure 3.3: Temperature dependence of the Si(557)-Au measured by a 4pp approach in square configuration. (a) Multiple phase transitions seem to be induced after every new contacting of the sample (indicated by black vertical lines) and are explained by heat transfer from tip to sample (cf. explanation in text). (b) The transition measured with reduced heat transfer.

overcome shrinkage and for stable contacts, the tips are usually approached several additional nanometers¹ after an ohmic contact is observed in $I(V)$ curves.

It turns out in experiment that the contacting time and corresponding heat transfer between tip and sample is not negligible which can lead to a wrong interpretation of data. This effect is exemplarily illustrated in figure 3.3(a) showing temperature dependent measurements of the resistance parallel (R_{\parallel}) and perpendicular (R_{\perp}) to chains on Si(557)-Au.

Highlighted by black vertical lines, figure 3.3(a) shows sharp resistance drops of several orders at around 125 K, 140 K, 155 K and 170 K which could be interpreted as *apparent multiple* metal-insulator transitions (MITs). But, a careful analysis of the data and comparison to the measurement protocol reveals that at the mentioned temperatures the tips were moved to another position on the sample surface. Therefore in conclusion, the onset of a MIT at different temperatures is related to a local temperature increase on the sample surface by heat transfer. This is schematically shown in figure 3.4. The transition to a conducting state occurs when the heat transfer to the surface was sufficient to heat up the sample area above T_C to form a percolated current path between the four probes.

An accurate modeling of the heat transfer between sample and probes using an approach

¹E.g. one can roughly estimate, that for a temperature change from room temperature to 100 K, a tip with a typical apex length of $100 \mu\text{m}$ will contract by 70 nm (assuming a thermal expansion coefficient of $4 \cdot 10^{-6} \text{K}^{-1}$) [92, 93].

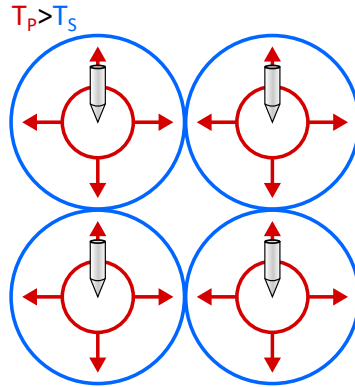


Figure 3.4: Simplified outline illustrating the heat spreading out from the four probes (symbolized by red color, temperature of probe is T_P) on a sample surface below T_C . If the local surface temperature T_S is below T_C the 4pp will measure an insulating behavior as long as the heat transfer to the surface was not enough to form a percolated current path between the areas heated above T_C (red circle expanded so much that the diameter is greater or equal than the blue circle).

based on Fourier heat equations[94, 95] is not straight forward and very complex and tedious. For example, one problem is the not exactly known contact area size during experiment which in addition is changing all the time due to shrinkage of tips. Secondly, the heat transfer on the surface reconstruction and the contribution of the bulk and coupling of surface/substrate is not known.

The effect of local heating of the sample is reduced when the tips are immediately retracted and brought back into tunneling contact after the acquisition of each single temperature dependent data point. This approach was used consistently in the whole thesis. Figure 3.3(b) depicts the temperature dependence of such approach measured on the same sample but another preparation. Clearly, a single sharp transition is visible at around 200 K. Notably, the envelope function of the data shown in figure 3.3(a) which takes into account only the very first data points after the contacting is in very good agreement with the data presented in figure 3.3(b). Small deviations are explained by differences in contacts which always inevitably come with a mechanical impact leading to a local alteration of the surface by defects (cf. additional discussion in chapter 8 section 8.2.4) which can increase the measured resistance.

Part II

Characterizing electronic transport by a four-point probe technique

Four-probe methods for isotropic 3D bulks and 2D sheets

The following chapters describe in detail the key aspects of the four-point probe (4pp) technique used for the transport measurements within this thesis. They are summarizing parts of the work “The 100th anniversary of the four-point probe technique: the role of probe geometries in isotropic and anisotropic systems” [30] by MICCOLI, EDLER et al. previously published in *J. Phys.: Condens. Matter* in 2015. For a detailed presentation which includes derivations of shown formula, the reader is referred to the mentioned publication.

4.1 Introduction

From a fundamental point of view, the resistance R of a material in the diffusive transport regime is closely related to its electrical resistivity ρ and the conductivity is $\sigma = 1/\rho$, respectively. In general, the resistivity of a material is defined as the ratio of the electric field E to the current density J

$$\rho = E/J. \quad (4.1.1)$$

Experimentally, only the resistance R , depending on the ratio of applied voltage V and current I , can be measured while the resistivity ρ is an intrinsic property of the system. It can be calculated when the geometry of the examined system is well-known, as it is shown in the following sections.

4.1.1 Two-point probe vs. four-point probe measurements

In order to measure the resistance of a sample, a two-point probe (2pp) measurement seems to be intuitive. However, as shown in the following, this method has serious disadvantages. Instead, 4pp measurements are recommended to measure the resistance. A schematic representation of both measurements is depicted in figure 4.1.

Two-point probe measurements

For the case of a 2pp measurement (cf. figure 4.1(a)), a defined current I is impinged by two probes and the corresponding voltage drop V is measured. But the measured resistance R as

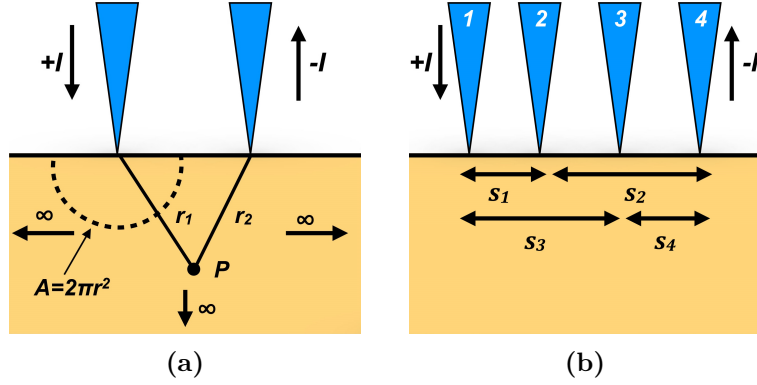


Figure 4.1: Schematics drawing of (a) 2pp and (b) a 4pp measurement in collinear arrangement with equidistant contact spacing.

the ratio of voltage V and current I is not only the resistance of the sample R_{sample} itself. It is intrinsically including the resistance of the probes R_{probe} as well as the contact resistance R_{contact} . Hence, the overall resistance is given by

$$R = \frac{V}{I} = 2R_{\text{probe}} + 2R_{\text{contact}} + R_{\text{sample}}. \quad (4.1.2)$$

Therefore, for determining the resistance R_{sample} in a 2pp measurement, the knowledge of the exact values R_{probe} and R_{contact} is required. Something which can only be estimated in 2pp experiments because the contact resistances of probes is not know and different for every contacting.

Four-point probe measurements

In contrast to the 2pp case, 4pp measurements of the sample resistance R_{sample} do not include contributions of the contact and the probes resistance because not all probes serve as current injecting and voltage measuring probes at the same time. As exemplary shown in figure 4.1(b) for a collinear 4pp arrangement, two probe are injecting a current I through the sample while the voltage V drop is measured simultaneously with the other two probes. Considering that the impedance of a voltmeter is usually much higher compared to contact resistances, the current flowing through the voltage measuring probes is practically zero. Hence, the measured resistance as the ratio of the voltage drop V and applied current I is equal to R_{sample} .

4.1.2 Resistivity for a semi-inifinite 3D material, infinite 2D sheet and 1D wire

It can be easily shown that for the ideal case of a 3D semi-infinite material, the resistivity in collinear 4pp setup $\rho_{3D}^{\text{in-line}}$ with equidistant contact spacing s (cf. figure 4.1(b)) is given by [96]

$$\rho_{3D}^{\text{in-line}} = 2\pi s \frac{V}{I}, \quad (4.1.3)$$

where V is the measured voltage drop between the two inner probes, I the current flowing through the outer pair of probes.

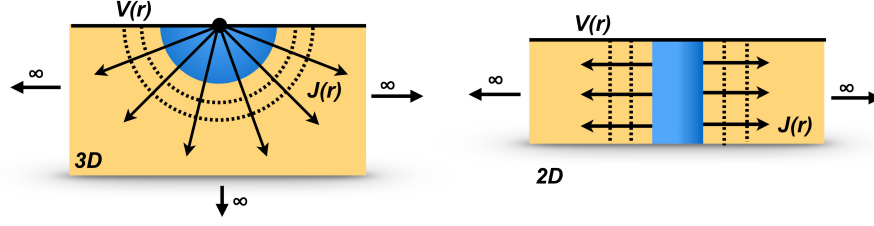


Figure 4.2: Comparison of the voltage $V(r)$ and current density $J(r)$ profiles of a semi-infinite 3D material and an infinite 2D sheet.

Equation (4.1.3) is not valid if the sample thickness t is small ($t \ll s$) compared to the probe spacings s . In this case, the semi-infinite 3D material can be treated as an infinite 2D sheet. Within this approximation the current impinged by the probes can be assumed to spread cylindrically instead spherically inside of the material (cf. figure 4.2). Similar calculations as for equation (4.1.3) lead to the resistivity

$$\rho_{2D}^{\text{in-line}} = \frac{\pi t}{\ln 2} \frac{V}{I}. \quad (4.1.4)$$

In comparison to equation (4.1.3) it stands out that the resistivity and therefore the resistance of a 2D sheet is not dependent on the probe distance ($R_{2D} \propto \rho \cdot \ln 2 = \text{const.}$), while the resistance of a 3D semi-infinite material is decreasing with increasing probe spacing ($R_{3D} \propto \rho/s$). Hence, measuring the probe distance dependence of a system during transport experiments is a good way to characterize the dimensionality of a system. The probe spacing independence of a 2D infinite sheet in comparison to a 3D material can be explained by the schematics shown in figure 4.3 for a linear arrangement of probes. While an increase of probe distances lead to an increase of the paths of the electric charges which should lead to an increase of resistance, the resistance remains constant due to the compensation effect of current spreading additionally perpendicular to the probes. In the 3D case this effect is overcompensated by an additional spreading of the current into the bulk of the sample causing the s^{-1} dependence of the resistance.

For the case of a 1D wire, the current density is constant and independent of the distance s from the probes injecting the electric current. In respect to the conclusions drawn from the schematics shown in figure 4.3, it is obvious that the resistance of an 1D wire is proportional to the probe spacing s . Using the same approach as for the 3D and 2D case one can easily deduct the resistivity of a 1D wire. For a circular wire with a radius r much smaller than the probe spacing ($r \ll s$) this leads to a resistivity of

$$\rho_{1D} = \frac{\pi r^2}{s} \frac{V}{I}. \quad (4.1.5)$$

As summarized in table 4.1, the resistivity is strongly dependent on the dimensionality of the system. For reasons discussed in the following chapter 5, it is often useful to place the probes in a non-linear arrangement. Therefore, table 4.1 additionally includes the case of a square arrangement of the probes, which can in comparison even lead to a slightly higher

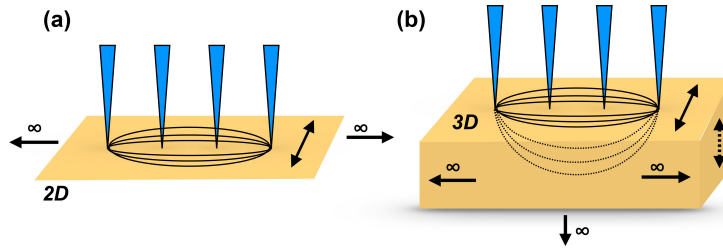


Figure 4.3: Schematics showing the current paths for (a) an infinite 2D sheet and (b) a semi-infinite 3D material.

sensitivity of up to a factor of two. One should keep in mind, that all the previously shown cases are only valid in the extreme case of (semi)-infinite samples which is only valid for real specimens within limits. Therefore, correction factors are needed for finite geometries which is the scope of the following sections.

4.2 Correction factors for finite isotropic samples

As it was shown in the previous section, the resistivity strongly depends on the dimension of the investigated material. It is important to note that the expressions for the resistivity given in the previous section (cf. table 4.1) are only valid in the limit of infinite large samples. They need to be corrected for finite geometries by so called *correction factors*. Equivalently, correction factors also become necessary if the probes are placed close to the boundaries of a sample or if the probe spacings are comparable to the size of the investigated sample itself. Introducing a correction factor F , the resistivity can in general be expressed as

$$\rho = F \frac{V}{I} \quad (4.2.1)$$

For many applications, the correction factor F is usually written as the product of three different factors ($F = F_1 \cdot F_2 \cdot F_3$) which are taking into account the finite thickness of the sample (F_1), the alignment of the probes in respect to a sample edge (F_2) and the finite lateral width of the sample (F_3). The correction factors reduce to 1 as they approach the

Table 4.1: Resistivity ρ depending on the dimensionality of the system for the case of linear and square arrangements of four probes on a semi-infinite 3D material, an infinite 2D sheet and an 1D wire.

Sample shape	in-line	square
3D bulk	$2\pi s \frac{V}{I}$	$\frac{2\pi s}{2-\sqrt{2}} \frac{V}{I}$
2D sheet	$\frac{\pi t}{\ln 2} \frac{V}{I}$	$\frac{2\pi t}{\ln 2} \frac{V}{I}$
1D wire	$\frac{\pi r^2}{s} \frac{V}{I}$	—

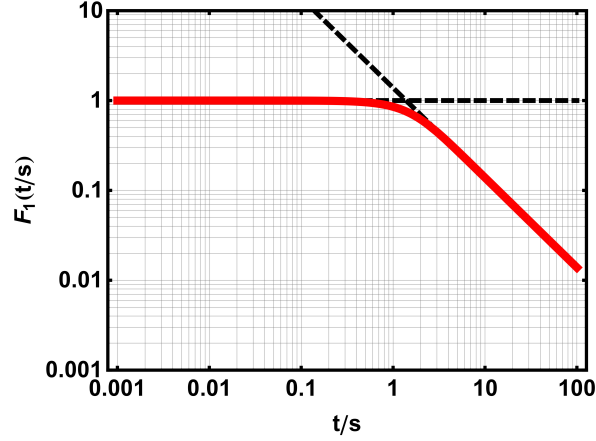


Figure 4.4: The correction factor F_1 vs normalized sample thickness (t/s , where t is the wafer thickness and s is the probe spacing).

limit of infinite large samples. The following sections will briefly discuss the correction factors $F_{i=1,2,3}$ separately for different geometric configurations and probe arrangements. Additional correction factors are needed for special cases of finite geometries or anisotropic samples which will be discussed in section 4.3 and chapter 5.

The thickness dependent correction factor $F_1(t/s)$, where t is the wafer thickness and s the probe spacing, was first derived by VALDES [96]. For the case of a collinear 4pp arrangement on an infinite sheet of thickness (electrically decoupled from a substrate) with equal probe spacing s , the correction factor is given by [97]

$$F_1^{\text{in-line}} = \frac{\ln 2}{\ln\{\frac{\sinh(t/s)}{\sinh(t/2s)}\}} \quad (4.2.2)$$

A graphical representation of the correction factor F_1 is shown in figure 4.4. Using this correction factor, one can demonstrate that for thick samples with $t/s \gg 1$ the curve can be approximated by $F(t/s) \approx 2 \ln 2(s/t)$. Then, the resistivity term

$$\begin{aligned} \rho \cdot F_1^{\text{in-line}}(t/s \gg 1) &= \frac{\pi t}{\ln 2} \frac{V}{I} \cdot 2 \ln 2(s/t) \\ &= 2\pi s \frac{V}{I} = \rho_{3D}^{\text{in-line}} \end{aligned} \quad (4.2.3)$$

is leading to the expression of semi-infinite 3D specimen as listed in table 4.1. On the other hand, for thin samples with $t/s \ll 1$ the term $\sinh(t/s)$ can be approximated by t/s . In this case F_1 becomes unity and equation (4.2.3) is equal to the expression of an infinite 2D sheet $\rho_{2D}^{\text{in-line}}$ as listed in table 4.1. As a remark, one can calculate with an approximation error of $\epsilon \approx 1\%$ that for $t/s < 1/5$ ($t/s > 4$) real semiconductors with a finite thickness t can be considered as a quasi-2D sheet (semi-infinite 3D specimen).

The correction factor F_2 takes into account the impact of the position of probes in respect to the proximity of an edge on a semi-infinite sample. It was first described by VALDES [96] using the method of images [98] which is exemplarily shown in figure 4.5(a) for the

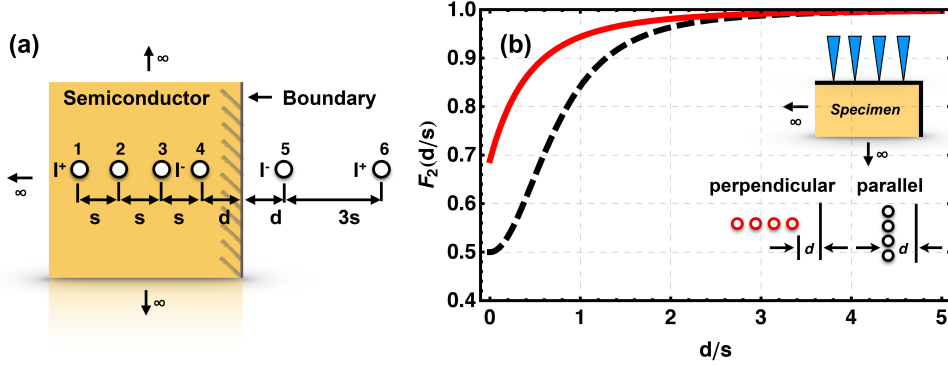


Figure 4.5: (a) Schematic drawing illustrating the method of images. An array of equally spaced probes (probe distance s) is aligned perpendicular in-line to a non-conducting boundary of a semi-infinite 3D specimen by a distance d . Probes 5 and 6 are the mirrored, imaginary charges. (b) The correction factor F_2 versus the normalized edge distance d/s for the cases of perpendicular and parallel alignment of the probes.

example of a collinear probe alignment of a non-conducting boundary. Figure 4.5(b) depicts the correction factor F_2 depending on the normalized edge distance (d/s) calculated for an in-line alignment parallel and perpendicular to an edge. It is easy to calculate that the correction factor F_2 reduces to unity (with an error of around $\epsilon \approx 1\%$) if the probe distance from the wafer boundary is at least four times the probe spacing. Another remark has to be taken into account regarding the minimum of $(F_2)_{\min} = 1/2$ when the 4pp array is aligned parallel along the sample edge. In this case the effectively measured resistance R can increase by up to a factor of two compared to the case of a semi-infinite 3D sample which is providing a higher sensitivity for the measurements. Qualitatively, in comparison to the image shown in figure 4.2, this can be easily rationalized since the current paths are restricted to one half of the semi-infinite 3D sample.

The correction factor F_3 considers the entire effect caused by all lateral boundaries of the sample in respect to the overall probe alignment. Two exemplary cases of 4pps aligned in a collinear as well as a square alignment centered on a finite circular slice are shown in figure 4.6. The plotted correction factors F_3 shown in figure 4.6 can be calculated using the method of current images as shown by [99] and [100] to

$$F_{3, \text{circle}}^{\text{in-line}} = \frac{\ln 2}{\ln 2 + \ln \left\{ \frac{[(d/s)^2 + 3]}{[(d/s)^2 - 3]} \right\}} \quad (4.2.4)$$

$$F_{3, \text{circle}}^{\text{square}} = \frac{\ln 2}{\ln 2 + \ln \left\{ \frac{[(d/s)^2 + 2]}{[(d/s)^2 + 4]} \right\}}. \quad (4.2.5)$$

For a ratio of $d/s > 25$ the corrections factors can be approximated by 1 (within an approximation error of $\epsilon \approx 1\%$). As a rule of thumb, a finite sample may be considered as infinite when the overall width is at least one order of magnitude larger than half of the probe spacing. It is worth noting that the correction factors reach a minimum of $1/2$ when the external current probes lie on the sample circumference ($d = 3s$ for the linear and $d = \sqrt{2}s$ for a quadratic arrangement, respectively). In other words, the measured resistance increases by

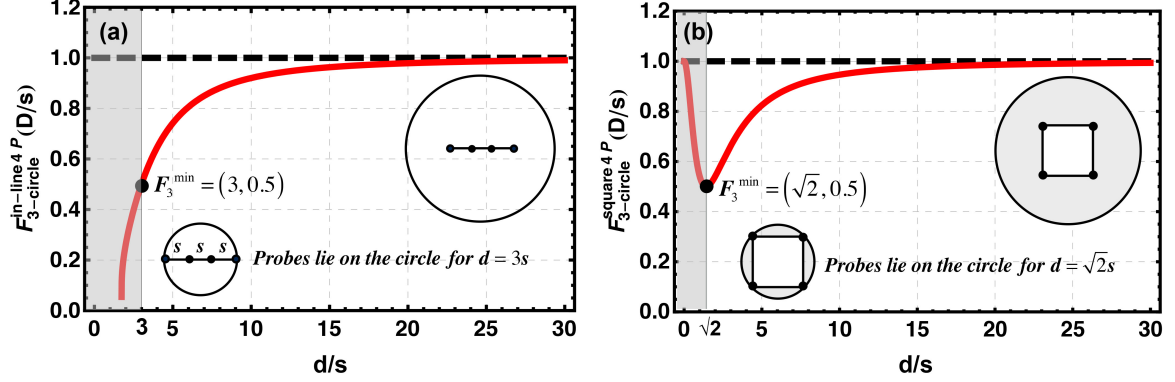


Figure 4.6: Correction factor F_3 versus normalized wafer diameter (d/s) for the special case of probes aligned in a (a) collinear respectively (b) square configuration centered on a finite circular slice.

a factor of two when the 4pp array is moved from the center to the sample periphery (see additionally section 5.3 for the anisotropic case as well as section 6.4.1 in a later chapter demonstrating this effect in experiments) increasing the sensitivity of measurements.

4.3 The van der Pauw theorem for isotropic thin films of arbitrary shape

Of great importance for resistivity measurements using 4pp and commonly used is the so called van der Pauw method. It generalizes the calculation of the correction factor F_3 introduced in section 4.2 for samples of arbitrary shape as long as the 4pps are placed around the perimeter of the sample. Additionally, the van der Pauw method requires the following assumptions:

- (i) the samples are homogeneously thin (i.e. $t/s < 1/5$: $F_1 = 1$),
- (ii) isotropic,
- (iii) and singly connected, i.e. solid without holes.

An arbitrary shaped sample contacted within the van der Pauw method is shown in figure 4.7(a). Here a current I_{AB} is flowing between the contacts A and B and a voltage drop V_{AB} between contacts C and D is measured. The acquired resistance is then given by $R_{AB,CD} = V_{CD}/I_{AB}$. Equally, for a different contact configuration one can obtain $R_{BC,DA} = V_{DA}/I_{BC}$. It was shown by VAN DER PAUW [101] that the resistances then fulfill the following condition

$$\exp\left(-\pi \frac{t}{\rho} R_{AB,CD}\right) + \exp\left(-\pi \frac{t}{\rho} R_{BC,DA}\right) = 1. \quad (4.3.1)$$

The resistivity in general is expressed by [101, 102]

$$\rho = \frac{\pi t}{\ln 2} \frac{R_{AB,CD} + R_{BC,DA}}{2} \cdot f, \quad (4.3.2)$$

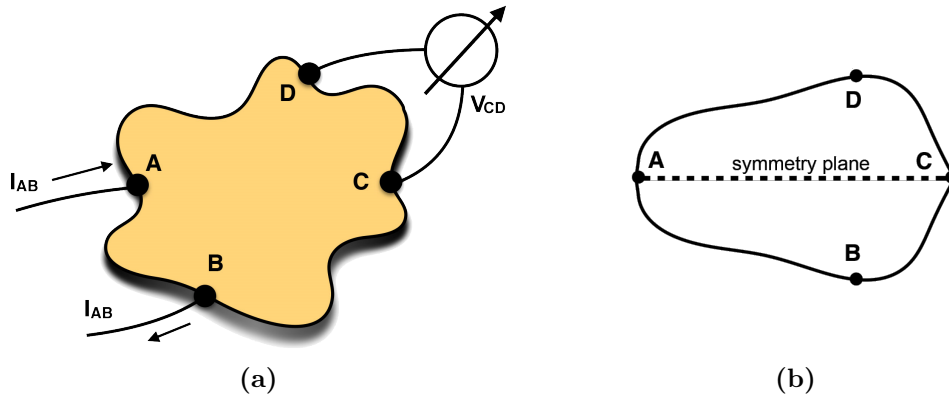


Figure 4.7: (a) Schematic drawing of an arbitrary shaped sample contacted by the van der Pauw method. (b) Schematics of a sample with probes aligned in respect to the symmetry plane.

where f is a function depending of the ratio $R_{AB,CD}/R_{BC,DA}$ satisfying the relation

$$\cosh \left\{ \frac{\ln 2}{f} \frac{R_{AB,CD}/R_{BC,DA} - 1}{R_{AB,CD}/R_{BC,DA} + 1} \right\} = \frac{1}{2} e^{\ln(2)/f}. \quad (4.3.3)$$

In the special case of probes aligned with respect to a symmetry plane (two probes placed on the symmetry line and the other two probes symmetrically to this line, see figure 4.7(b)), the so-called reciprocity theorem is valid ($R_{AB,CD} = R_{BC,DA} = R$) and equations (4.3.2) and (4.3.3) are simplified to

$$\rho = \frac{\pi t}{\ln 2} \left(\frac{V}{I} \right) \quad (4.3.4)$$

which is half of the term one would get for a semi-infinite 2D sheet (cf. table 4.1) in square configuration and in accordance to the comments given to factor F_3 for the special case of probes placed on the circumference of the periphery.

The 4pp technique on anisotropic crystals and surfaces

The previous chapter was depicting main aspects of the four-point probe (4pp) technique for characterizing samples by the resistivity ρ , which is an intrinsic quantity of the system, and the measured resistance R , respectively. But within this thesis measurements were also conducted on anisotropic samples. Therefore, the following section will discuss how to expand the previously introduced methods on anisotropic samples, necessary for the interpretation of measurements shown in part III.

For the case of anisotropic solids the resistivity ρ is no longer a scalar. Instead, it is a symmetric second-rank tensor $\hat{\rho}$, whose components ρ_{ij} represents the resistivities along different directions of the solid. Thus, the Ohm's law in equation (4.1.1) needs to be adopted as

$$\begin{pmatrix} E_x \\ E_y \\ E_z \end{pmatrix} = \begin{pmatrix} \rho_{xx} & \rho_{xy} & \rho_{xz} \\ \rho_{yx} & \rho_{yy} & \rho_{yz} \\ \rho_{zx} & \rho_{zy} & \rho_{zz} \end{pmatrix} \begin{pmatrix} J_x \\ J_y \\ J_z \end{pmatrix}, \quad (5.0.1)$$

where E_i and J_i are the electric field and the current density along the i th direction. As shown by SMITH [99], depending on the crystallographic symmetries, the number of components ρ_{ij} of the resistivity tensor $\hat{\rho}$ required for describing a physical system are reduced. For example, a crystal with no symmetry is described by six components, while a twofold symmetry axis reduces the amount to four independent components. In the case of highly symmetric cubic crystals as for an isotropic material, only one resistivity parameter is needed.

The following sections will describe the case of anisotropic systems with resistivities $\rho_x = \rho_{xx}$, $\rho_y = \rho_{yy}$ and $\rho_z = \rho_{zz}$ orientated along the x -, y - and z -axes of samples (i.e. the case of an orthorhombic crystal), focusing on anisotropic 2D systems.

5.1 Anisotropic semi-infinite 3D bulk and infinite 2D sheets

The main idea of handling anisotropic materials with different resistivities ρ_i ($i = x, y, z$) along the x -, y - and z -axes is to transform the coordinates of an anisotropic cube with dimension l onto an isotropic parallelepiped of resistivity ρ and dimensions l'_i (cf. schematic

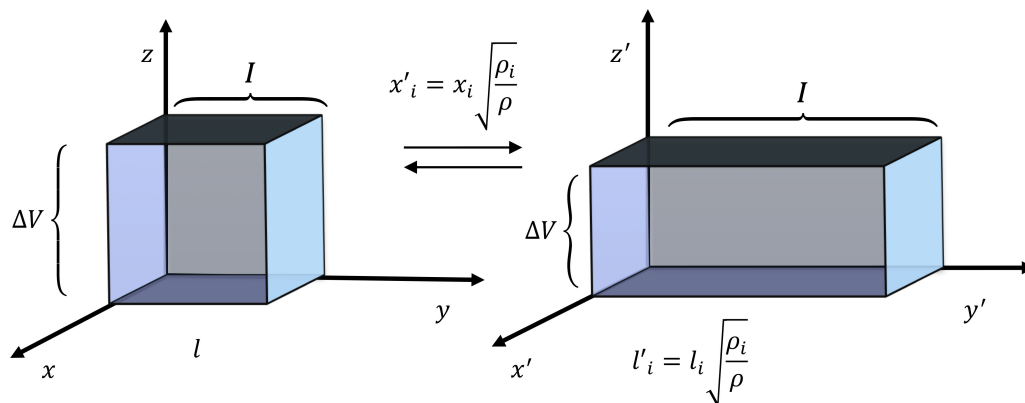


Figure 5.1: Schematic drawing illustrating the mapping procedure of an anisotropic cubic sample into an equivalent isotropic parallelepiped.

drawing in figure 5.1) by

$$l'_i = \sqrt{\frac{\rho_i}{\rho}} l \quad \text{with} \quad \rho = \sqrt[3]{\rho_x \cdot \rho_y \cdot \rho_z}. \quad (5.1.1)$$

WASSCHER [103] showed that these transformations preserve voltage V and current I – thus, they do not affect the resistance R . Using this approach, the isotropic cases discussed in section 4.1.2 can be easily updated for the anisotropic samples as shown in the following.

For the case of 4pp aligned along the x -axis of an anisotropic material, according to equation (5.1.1) the probe distances can be transformed to $s'_x = \sqrt{\rho_x/\rho} s_x$. Since V_x and I_x are preserved, the resistivity in comparison to the isotropic case shown in equation (4.1.3) is given by

$$\rho = 2\pi \sqrt{\frac{\rho_x}{\rho}} s_x \frac{V_x}{I_x}, \quad (5.1.2)$$

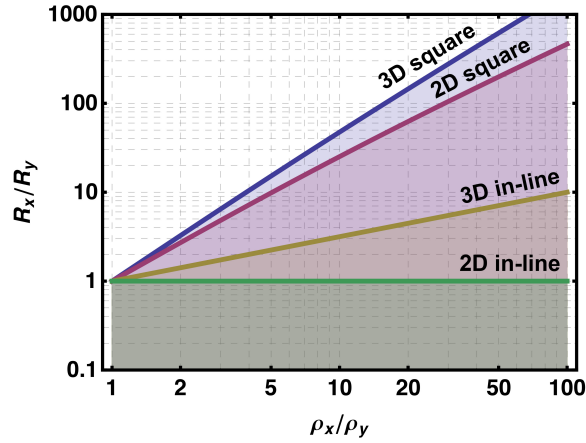
which can be rearranged to $R_x = \frac{1}{2\pi s_x} \sqrt{\rho_y \rho_z}$. Thus, the resistance measured by a 4pp in-line arrangement along one axis is the geometric mean of the resistivity components of the other two axes. The remaining cases shown in table 4.1 are calculated in a similar way leading to the formulas shown in table 5.1. The equations reported in table 5.1 can be used to fully determine the resistivity tensor of 3D and 2D samples. For 3D samples three distinct measurements are necessary, while for 2D samples only two are sufficient.

Table 5.1: Resistance R_x for the cases of linear and square 4pp arrangements on an anisotropic semi-infinite 3D material and infinite 2D sheet

Sample shape	in-line	square
3D bulk	$\frac{1}{2\pi s} \sqrt{\rho_y \rho_z}$	$\frac{\sqrt{\rho_x \rho_z}}{\pi s} \left[1 - \left(1 + \frac{\rho_x}{\rho_y} \right)^{-1/2} \right]$
2D sheet	$\frac{\ln 2}{\pi t} \sqrt{\rho_x \rho_y}$	$\frac{\sqrt{\rho_x \rho_y}}{2\pi t} \ln \left(1 + \frac{\rho_x}{\rho_y} \right)$

Table 5.2: Resistance ratio R_x/R_y for the cases of linear and square 4pp arrangements on an anisotropic semi-infinite 3D material and infinite 2D sheet

Sample shape	in-line	square
3D bulk	$\sqrt{\frac{\rho_x}{\rho_y}}$	$\frac{\sqrt{1+\rho_x/\rho_y}-1}{\sqrt{1+\rho_y/\rho_x}-1}$
2D sheet	1	$\frac{\ln(1+\rho_x/\rho_y)}{\ln(1+\rho_y/\rho_x)}$

**Figure 5.2:** Electrical resistance ratio R_x/R_y versus the resistivity anisotropy degree ρ_x/ρ_y for the case of infinite 3D half plane and 2D sheet depending on the adopted 4pp geometric configuration (in-line vs. square).

Comparing table 5.1 with the results of table 4.1 it is worth noting that the measured resistances still decrease when increasing the probe distance on a semi-infinite half plane, while they remain constant for the case of an infinite 2D sheet since the current spreading (cf. figure 4.3) in the direction normal to the probe array and into the sample is not changed by anisotropy. In order to reveal information about the anisotropy either the current/voltage probes need to be exchanged or the 4pp geometry needs to be rotated. The anisotropy ratio of the resistivities R_x/R_y is summarized in table 5.2 and plotted in figure 5.2 as a function of the anisotropy ratio ρ_x/ρ_y . It is evident that in the case of an infinite 2D sheet, the anisotropy cannot be determined by an in-line arrangement. Additionally, the ratios R_x/R_y show that a higher sensitivity can be achieved by a square arrangement compared to an in-line geometry. As pointed out for the isotropic case, it can be deduced that the impact of finite boundaries is negligible if the sample size is by one order of magnitude larger compared to the probe spacing.

5.2 Rotational square method

The equations of table 5.1 are only valid as long as the probes are aligned accurately along the principal axes of the anisotropic surface. If the contact geometry is not aligned in that way a

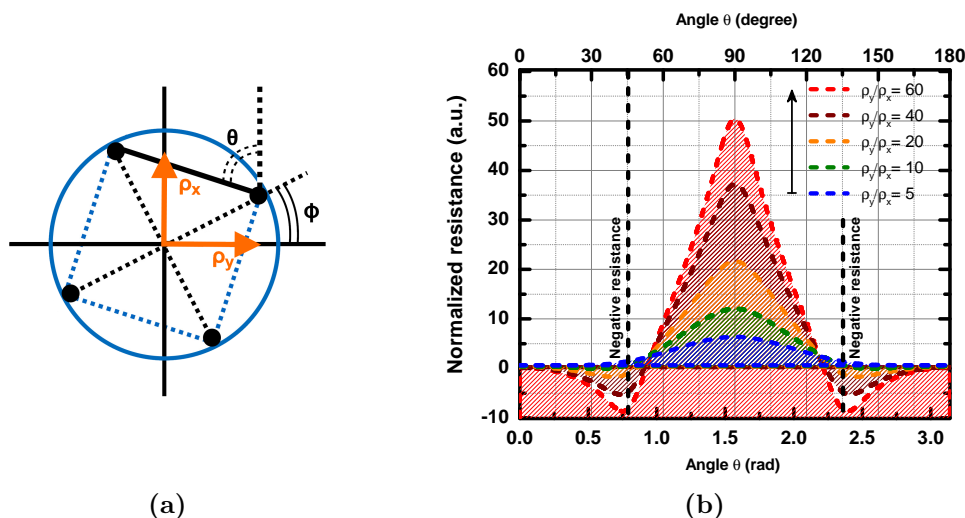


Figure 5.3: (a) Schematic drawing of a square probe configuration rotated by an angle $\theta = \phi + \pi/4$. θ is the angle in respect to the orientation of the resistivity directions ρ_x, ρ_y . (b) Angle θ dependence of the electrical resistance $R(\theta)$ for an anisotropic infinite 2D sheet for various anisotropy degrees (expressed in ρ_x/ρ_y ratios).

correct interpretation of the data will be very difficult or even impossible. Thus, for the case of unknown orientation of the anisotropic resistivity components, the correct alignment can be retrieved by the so called rotational square method first proposed by KANAGAWA et al. [83]. A square 4pp array is rotated on an anisotropic 2D sheet by an arbitrary angle θ with respect to the two orthogonal resistivity components (cf. figure 5.3(a)). The resistance can then be expressed as a function of the angle θ (see [30] for a detailed derivation):

$$R(\rho_x, \rho_y, \theta) = \frac{\sqrt{\rho_x \rho_y}}{2\pi t} \ln \sqrt{\frac{\left(1 + \frac{\rho_y}{\rho_x}\right)^2 - 4 \cos \theta \sin^2 \left(1 - \frac{\rho_y}{\rho_x}\right)^2}{\left(\sin \theta + \frac{\rho_y}{\rho_x} \cos^2 \theta\right)^2}} \quad (5.2.1)$$

Figure 5.3(b) plots the expected resistances for various resistivity anisotropy ratios depending on the rotation angle θ . The highest anisotropy is measured when the square is aligned in respect to the resistivity components ($\theta = 0, \pi$ and $\theta = \pi/2$). Additionally, a negative resistance is prominent at some θ for extremely anisotropic materials, i.e. $\rho_y/\rho_x > 5 + 2\sqrt{6} \approx 9.9$. This feature is explained by a deformation of the electrostatic potential in the case of very large anisotropies and was first observed by KANAGAWA et al. [83] while studying transport properties of indium chains on Si(111) (see also discussion of these transport measurements in part III). Another explanation was recently given in [104] explaining the negative resistances by submicrometer-size whirlpools/viscous electron backflow in the electron current direction.

5.3 Anisotropic finite samples

Up to now, the resistivity of finite anisotropic materials is calculated in literature by two methods introduced by MONTGOMERY [105] and by WASSCHER [106]. The following will

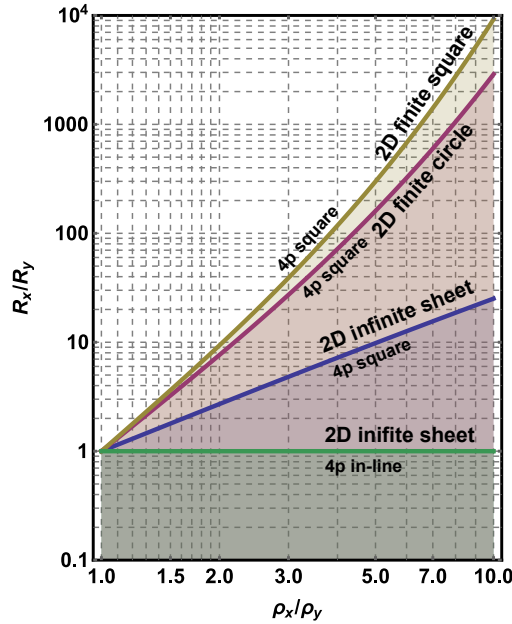


Figure 5.4: Electrical resistance ratio R_x/R_y versus the resistivity anisotropy degree ρ_x/ρ_y for the case of an infinite 2D sheet, a finite circular and square sample size depending on the adopted 4pp geometric configuration (in-line vs. square).

cover the method of WASSCHER because it allows the direct comparison between the infinite and finite regimes of anisotropic thin films (cf. section 5.3). Basically, WASSCHER showed that an anisotropic rectangular or circular thin sample can always be mapped on an isotropic semi-infinite sheet where the van der Pauw equations are valid. The demonstration is not trivial and uses both the coordinate transformation of equation (5.1.1) and the conformal mapping theory in the complex field. The problem is then solved by using the methods shown in section 4.1.2 and finally the result is transformed back to the original anisotropic starting situation.

The expected theoretical electrical resistance ratio R_x/R_y versus the resistivity anisotropy degree ρ_x/ρ_y for finite circular and square geometries is shown in figure 5.4. It is obvious that the restriction to finite area increases the resistance ratio R_x/R_y for a given resistivity anisotropy degree ρ_x/ρ_y . Thus, much higher sensitivity of several orders magnitude can be easily achieved when the sample size becomes comparable to the probe distance.

Correction factors for a square 4pp array inside an anisotropic circular area

It is assumed in the following that the finite area has the shape of a circle. Additionally, the components of resistivities are aligned with respect to two orthogonal diameters as well as a square 4pps array with probe spacing s is placed in the center of the circular shape with diameter d (cf. schematics in figure 5.5(a)). In the context of the Wasscher method, it is assumed further that both the probe size and the sample thickness are small with respect to the probe spacing. By applying the Wasscher transformation equation (5.1.1), the anisotropic

circle is first transformed into an electrically equivalent isotropic ellipse, while the square 4pp assembly is simultaneously stretched into an electrically equivalent rectangular 4pp assembly which is then mapped by conformal mapping to a unit circle in the complex field to solve the problem (cf. schematics in figure 5.5(b) and (c)).

It can be shown that the resistance anisotropy ratio R_x/R_y is then given by

$$\frac{R_x}{R_y} = \frac{\ln(1 + r(d/s, \rho_x, \rho_y)^{-2})}{\ln(1 + r(d/s, \rho_x, \rho_y)^2)}, \quad (5.3.1)$$

where $r = a/b$ is the aspect ratio (with $a = \overline{A''D''}$ and $b = \overline{A''B''}$, cf. figure 5.5(c) of the rectangle mapped on the unit circle. For a complete description of the mapping and the solution in the complex field, the reader is referred to MICCOLI et al. [30]. An exemplary graphical illustration of equation (5.3.1) for several anisotropy degrees ρ_x/ρ_y is shown in figure 5.6. It is apparent that the measured electrical resistance ratio R_x/R_y rises exponentially as the 4pp square array is moved from the center ($d \gg s$) to the circle periphery ($d = \sqrt{2}s$). As expected, the values for the extrema $d \gg s$ (infinite 2D sheet) and for $d = \sqrt{2}s$ (probe on circle circumference) match the values plotted in figure 5.4.

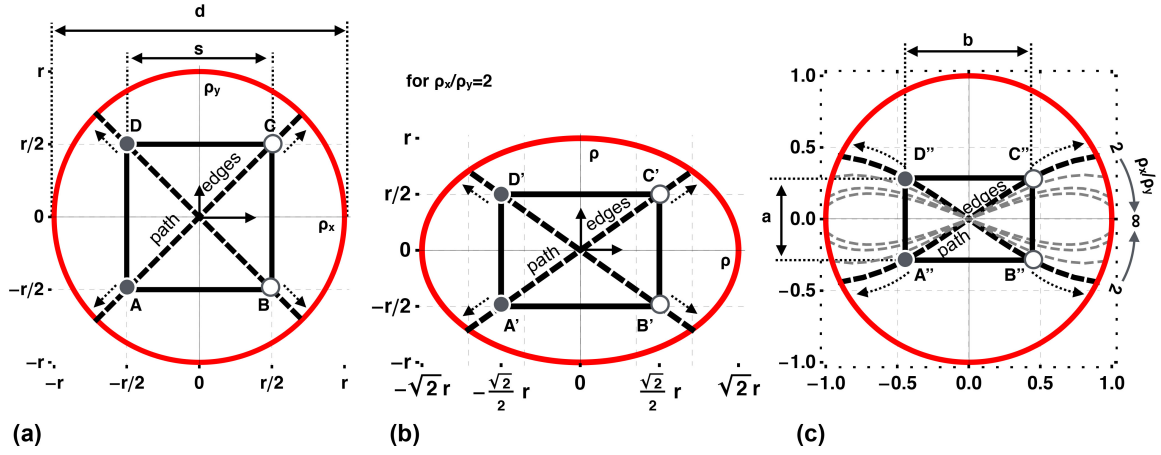


Figure 5.5: (a) Schematic drawing of a 4pp square array with probe spacing s placed in the center of an anisotropic circular sample of diameter d . The probe array is aligned parallel to the resistivity components ρ_x and ρ_y . (b) Transformed anisotropic square array to an electrically equivalent elliptical isotropic sample. The aspect ratio is depending on the resistivity anisotropy degree. (c) Subsequent mapping onto an unit circle.

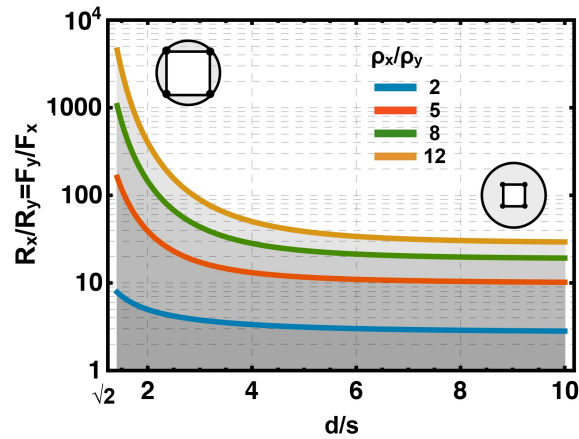


Figure 5.6: Theoretical electrical resistance ratio R_x/R_y versus the normalized wafer diameter d/s for a 4pp array placed in the center of an anisotropic circle plotted for various anisotropy degrees ρ_y/ρ_x .

Part III

Self-assembled atomic-scale nanowires

In/Si(111)-(4 × 1) reconstruction

6.1 Introduction

The adsorption of indium on silicon Si(111) produces a wide range of surface reconstructions and was studied for more than 50 years starting from the low-energy electron diffraction (LEED) studies of LANDER et al. [107]. The various reconstructions were first studied in detail and summarized in the form of a phase diagram by KAWAJI et al. [108] in 1979, and later revised hereafter several times [109–111]. Due to its unique quasi-1D structure, which can be used as a prototypical model system for studying the peculiar electronic properties of 1D systems, the In/Si(111)-(4 × 1) reconstruction is the most studied reconstruction of indium on silicon until today. Pioneering were the works of the HASEGAWA GROUP which showed for the first time in transport measurements a metal-insulator transition (MIT) of quasi-1D structure using a four-point probe (4pp) setup. Up to now, the system has been comprehensively characterized by various experimental techniques as well as *ab initio* theory, as recently reviewed by SNIJDERS et al. [41] and SCHMIDT et al. [112]. But still there are a lot of ongoing discussions related to the phase transition or the influence of surface defects.

The following sections will first briefly summarize and discuss the current state of In/Si(111)-(4 × 1) system research and then connect these with recent results obtained within the scope of this work. Here, parts of the results were published in “The 100th anniversary of the four-point probe technique: the role of probe geometries in isotropic and anisotropic systems” [30] by MICCOLI, EDLER et al. and “Interwire coupling for In(4 × 1)/Si(111) probed by surface transport” [29] by EDLER et al. and will not be separately cited.

6.2 Atomic and electronic structure

6.2.1 Atomic structure

The In/Si(111)-(4 × 1) phase forms on well prepared Si(111)-(7 × 7) reconstructions and was found for absolute coverages of 0.6-1.2 monolayer (ML) [108, 111, 113]¹ indium and subsequent tempering at 400-500 °C. Due to the high symmetry of the (7 × 7) reconstruction of the Si substrate, domain growth is observed in three distinguished directions, namely

¹1 ML corresponds to one Si atom per 1 × 1 unit cell on the Si(111) surface, i.e., $\sim 7.8 \cdot 10^{14}$ atoms/cm².

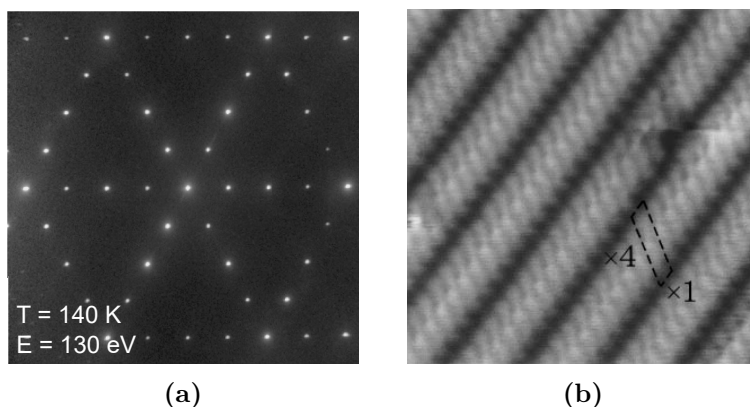


Figure 6.1: (a) SPALEED image showing the three domains of the (4×1) reconstruction [117]. (b) STM image of the 4×1 reconstruction showing a ridges like structure [45].

$[\bar{1}10]$, $[10\bar{1}]$, $[01\bar{1}]$ (cf. spot profile analysis low-energy electron diffraction (SPALEED) image in figure 6.1(a) showing a perfect triple domain (4×1) reconstruction). Depending on the substrate miscut angle and orientation, single domain growth can be triggered. STEVENS et al. [114] observed triple domain growth for the $[11\bar{2}]$ direction, while a single domain growth was seen for a miscut along the $[\bar{1}\bar{1}2]$ direction. Typically, the miscut angles in literature vary between $1^\circ - 4^\circ$ [82, 114–116] towards the $[\bar{1}\bar{1}2]$, i.e. the surface exhibits between 5 - 20 steps per $10 \mu\text{m}$.

First STM studies performed by NOGAMI et al. [118, 119] showed that the (4×1) reconstruction consists of parallel ridges like structures (cf. exemplary low-resolution STM image in figure 6.1(b)). The basic structure of these ridges – which is generally accepted nowadays – was proposed first by BUNK et al. [120] in 1999 based on the analysis of surface x-ray diffraction (XRD) data. In accordance to observations in LEED [42, 43], x-ray photoemission spectroscopy (XPS) experiments [44] and STM studies [45–50], a structural model was developed over the years by first-principle total energy density functional theory (DFT) calculations [42, 51–58]. In this model the adsorption of In on Si(111) leads to parallel self-assembled In nanowires separated by 3.8 \AA . Each nanowire consists of two zigzag chains of In atoms which forms the uppermost layer on the surface reconstruction. It is shown that the outer zigzag chains are slightly protruding the inner chains. Additionally, the nanowires itself are separated by zigzag Si chains resembling the π -bonded chains of the clean Si(111)- (2×1) surface placed on a lower site in comparison to the In atoms. A schematic drawing of this structural model compared to a high resolution STM scan is shown in figure 6.2.

6.2.2 Electronic structure

Highly important for the discussion of the transport properties is the electronic structure of the system itself. It was shown in various angle-resolved photoemission spectroscopy (ARPES) experiments [45, 47, 82, 122] and later proved in concluding DFT calculations [51–55, 57, 58, 123, 124] that the In/Si(111)- (4×1) reconstruction represents in fact a *quasi-1D metal* with three metallic In surface bands in the fundamental gap of the bulk Si substrate. Those surface-state bands are commonly denoted as the m_1 , m_2 and m_3 bands (cf. figure 6.3

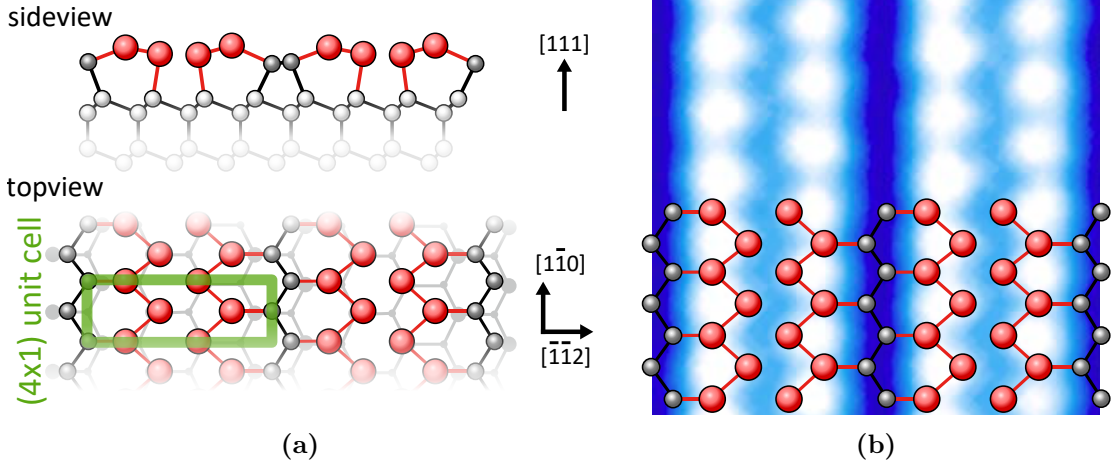


Figure 6.2: (a) Schematic top and side view of the structural model of the In/Si(111)(4 × 1) reconstruction showing the zig-zag shape structure along the $[1\bar{1}0]$ direction. Red spheres symbolize the indium atoms whereas the gray/white ones are symbolizing the silicon atoms of the surface/bulk. The (4 × 1) unit cell is indicated by the green square. Drawing adapted from [52, 120, 121]. (b) High-resolution STM image ($5 \times 5 \text{ nm}^2$, -0.15 V and 20 pA) with superimposed structure model depicted in (a). STM image taken from [48].

for an exemplarily ARPES dataset parallel to the chains). The bands are almost parabolic along the direction of the wire, centered at the X point of the surface Brillouin zone and cross the Fermi level E_F at 0.75 , 0.54 and 0.41 \AA . The band fillings calculated by integrating over the first Brillouin zone are 0.11 ($m1$), 0.38 ($m2$) and 0.50 ($m3$), respectively. DFT calculations indicate that $m1$ and $m2$ are mostly originating from the p_z orbitals of the In atoms while $m3$ can be attributed to the Si-In bonds [58]. The three bands make almost straight Fermi lines. A small wiggling of the Fermi contours as seen in figure 6.3(b) and most notably visible for the $m1$ band, indicates a weak coupling in the direction normal to the In atom wires [41]. The anisotropy of the band structure expressed by the transfer integrals t_{\parallel}/t_{\perp} is high (72 for $m3$) and the half-filled $m3$ appears to be almost perfectly nested [47], as expected for a Peierls like instability. Indeed, a structural and electronic phase transition was observed upon cooling of the system to $\sim 120 \text{ K}$ which is discussed in detail in section 6.3.

6.3 Phase transition

The In/Si(111)-(4 × 1) reconstruction is not only interesting due to the peculiar properties measured at room temperature. The reconstruction is also of special interest due to a phase transition upon cooling to a critical temperature $T_C \sim 120 \text{ K}$. A reversible phase transition was first reported within a combined study by YEOM et al. [45] using ARPES, STM and reflection high-energy electron diffraction (RHEED). It was shown, that the In/Si(111)--(4 × 1) reconstruction transforms around 120 K first of all into a (4 × 2) and gradually converts into a (8 × 2) structure (cf. SPALEED image in figure 6.4(a) in comparison to figure 6.1(a) illustrating the period doubling upon cooling). Later it was concluded by additional ARPES measurements [47, 59] that the $m3$ band is exactly half filled below 120 K while the $m1$ band

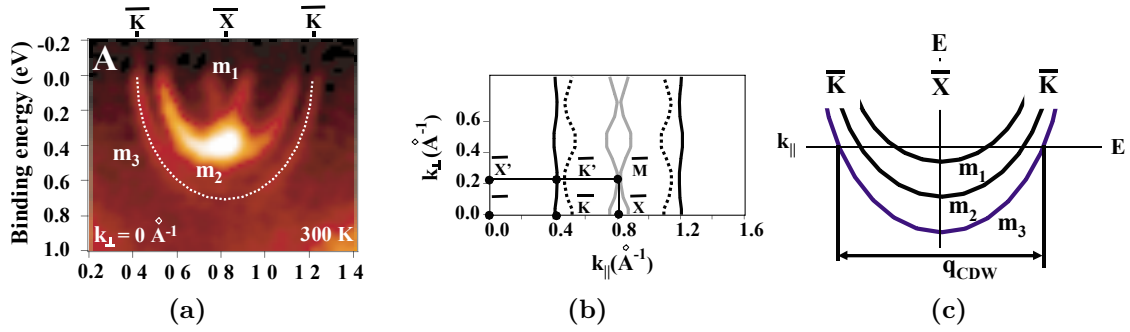


Figure 6.3: (a) Band dispersions of the (4 × 1) reconstruction measured along the chains at room temperature as seen in ARPES data. (b) Schematic of the surface Brillouin zone and the experimentally determined Fermi contours at room temperature. (c) Illustrated surface-state band structure at room temperature [47].

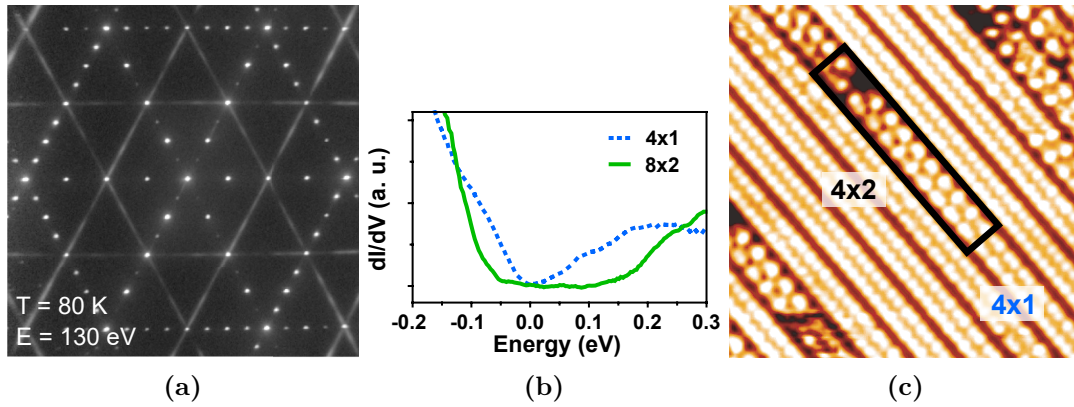


Figure 6.4: (a) SPALEED image showing the three domains of the (8 × 2) reconstruction [117]. (b) STS spectra of the (4 × 1) and (8 × 2) reconstruction highlighting the insulating character of the (8 × 2) phase. Spectra taken from [48]. (c) STM showing domain fluctuations (4 × 1) ↔ (4 × 2) of the filled-states of several In wires at $T = 135$ K. STM image with tunneling conditions ± 0.15 V and 20 pA taken from [48].

disappears completely indicating a charge transfer from m_1 to the m_2 surface-state band [41] which backfolds around the K point. Thus, by perfect nesting of the half-filled m_3 band, the phase transition was attributed to a charge density wave (CDW) instability with insulating band gap ~ 300 meV (cf. also scanning tunneling spectroscopy (STS) spectra in figure 6.4(b) and discussions in section 6.3.2).

6.3.1 Structural properties of the phase transition

For a long time, the details of the (4 × 1) ↔ (8 × 2) phase transition were subject to intense debate. Temperature dependent STM measurements [49, 50, 125] show that 1D striped domains of the (4 × 2) phase nucleate around 135 - 145 K [49]. Additionally, it is noticed that these 1D stripes change their position or length or even appear/disappear abruptly with each STM scan which was attributed to fluctuating CDWs. Around T_C the domains coalesce into the (8 × 2) phase. The (4 × 1) and (8 × 2) coexist over a wide range from 105 to 135 K [41,

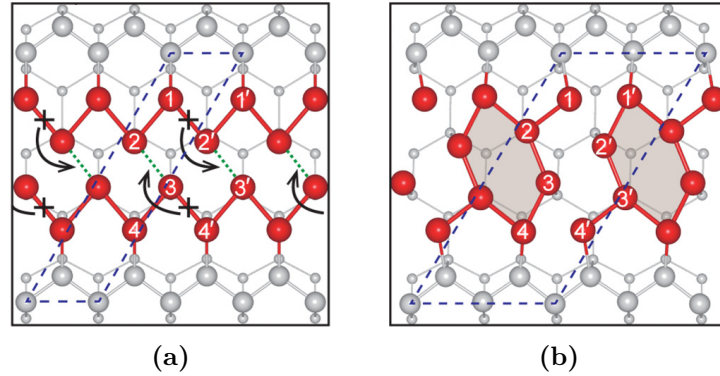


Figure 6.5: Schematics of the $\times 1$ (a) to $\times 2$ (b) phase transition illustrating the formation of hexagon like structures below T_C . Red and gray spheres represents indium and silicon atoms, respectively. Drawings taken from [64].

49]. The domain fluctuations are illustrated exemplarily by the STM image in figure 6.4(c) taken at 135 K. The structural transition to a (8×2) transition is completed at around 85 K [49].

The basic structural model of the phase transition – which is nowadays well established – was first proposed by GONZÁLEZ et al. [54] in 2006 on the basis of DFT calculations. It was concluded that the structural building block of the (8×2) phase consists of a hexagonal In structure (cf. illustration in figure 6.5). Nevertheless, the microscopic mechanism of hexagon formation and the driving force of phase transition was under heavy debate for a long time. It was discussed that either the leading mechanism could be induced by a Peierls dimerization [27, 45] or a shear distortion induced by soft phonon modes [63] stabilized by van der Waals interactions [126] or by an exothermic reaction with consecutive bond breaking and making [64]. Recently, it was concluded that the mechanism could only be explained by soft shear phonon modes as proposed by the SCHMIDT GROUP [63] (cf. section 6.3.2).

6.3.2 Electronic properties of the phase transition

The structural transition from the (4×1) to the (8×2) reconstruction as presented in the previous section 6.3.1 is additionally accompanied by an electronic transition, namely a MIT. The MIT in the In/Si(111) system is the result of a balanced intra- and interwire coupling [47, 63, 126, 127]. For instance, the MIT is correlated with the appearance of the $\times 8$ diffraction spots, i.e. with ordering between adjacent wires. This underlines a notable interwire coupling, which is also reflected by the conductivity components measured at room temperature (cf. the following discussions within section 6.4). The MIT was first observed in transport experiments using a linear 4pp alignment by TANIKAWA et al. [46] in 2004 and was reevaluated several times within the last decade [39, 128, 129]. As depicted in figure 6.6(a), TANIKAWA et al. [46] saw that the resistance for the (4×1) phase prepared on a n -type substrate is almost constant up to a $T_C \sim 120$ K. For temperatures below that critical temperature T_C the resistance follows a steep trend and increases by three orders within an interval of 30 K. Contrary, for p -type substrates no MIT was observed in transport measurements. Puzzlingly, simultaneous RHEED observations showed a transition from the (4×1) to the (8×2) reconstruction.

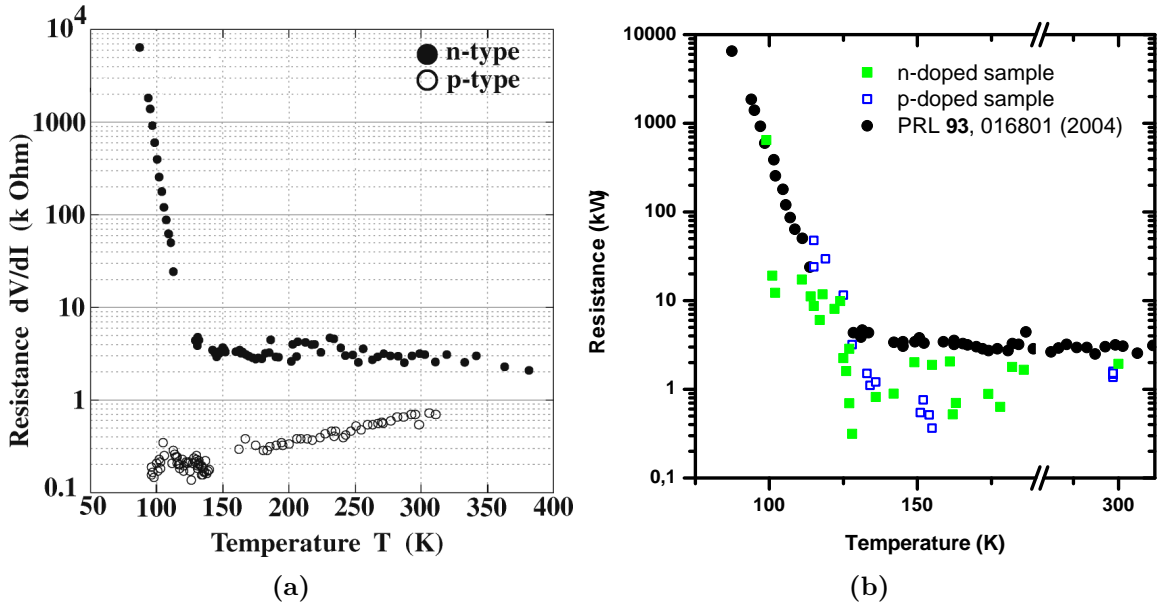


Figure 6.6: (a) The metal-insulator transition $(4 \times 1) \leftrightarrow (8 \times 2)$ measured by linear probe arrangement (probe spacing $8 \mu\text{m}$) [46]. Measurements were performed on a n -type (bulk resistivity $\rho = 1 - 10 \Omega\text{cm}$) and p -type ($\rho = 1 - 30 \Omega\text{cm}$) substrates (both 1.8° miscut toward $[11\bar{2}]$). (b) MIT observed in this thesis measured by linear probe arrangement on n - and p -type substrates in comparison to [46]. The n -type substrate was P doped ($\rho = 500 - 800 \Omega\text{cm}$) with a nominal miscut of 1° towards the $[\bar{1}\bar{1}2]$ direction. The p -type sample was B doped ($\rho > 1800 \Omega\text{cm}$) planar Si(111) showing triple domain 4×1 structures in SPALEED. Probe spacings were $30 \mu\text{m}$ for the n -type substrate and $9 \mu\text{m}$ for the p -type substrate.

The difference between n - and p -type substrates was attributed to the difference in band bending beneath the surface by TANIKAWA et al. [46]. ARPES measurements [82, 83] show that preparations on n -type substrates host an inversion layer [46, 83] (cf. section 2.3). The inversion layer is separated from the n -type bulk by a depleting layer which hinders current penetrating into the n -type bulk, so that the bulk contribution σ_B can be neglected within transport measurements [83]. Therefore, the transport measurements are surface sensitive. For substrates without that inversion layer as it is for p -type material, there is a nearly flat band situation. Thus, the measuring current spreads into the bulk. This means, the measured values for this case are mainly due to the bulk contribution. The gradual change of the resistance is assigned to the temperature dependence of the carrier mobility.

Figure 6.6(b) shows the MIT measured in a linear 4pp configuration within the scope of this thesis in comparison to the measurements of TANIKAWA et al. [46]. The sample substrates were low doped n -type (P doped, $\rho = 500 - 800 \Omega\text{cm}$) and p -type (B doped, $\rho > 1800 \Omega\text{cm}$) and sample preparation was the same as in [46]. The n -type material was with a miscut of 1° towards the $[\bar{1}\bar{1}2]$ direction while the p -type sample was a planar Si(111) showing triple domain (4×1) structures in SPALEED. As obvious, a MIT could be observed for both substrate types. The slight scattering of the data is mainly caused by probe induced heating effects as a limitation of the used measurement setup (cf. section 3.2 for a detailed discussion

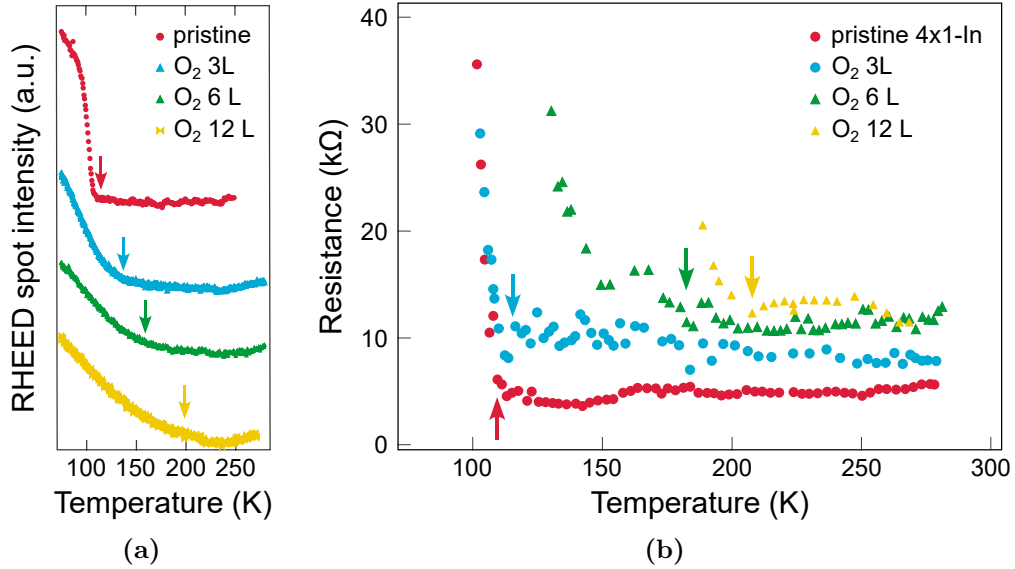


Figure 6.7: Change of the transition temperature by O₂ adsorption as observed by (a) RHEED and (b) by 4pp transport measurements. In contrast to other defect materials (e.g. H, In), the transition temperature for the structural and electronic transition increases both upon adsorption. Adopted from [39].

of this effect). Following the argumentation of [46], the contradicting behavior of the p -type substrate is attributed to nearly three orders higher resistivity hindering a large contribution from the bulk crystal in general maintaining the surface sensitivity.

There was a long lasting discussion about the nature of the electronic transition. The transition was either attributed to a Peierls instability [63, 112] or some order-disorder [49, 54, 61, 130] behavior. It was just shown very recently by KLASING et al. [117] within ultrafast time resolved RHEED measurements and 4pp transport measurements by HATTA et al. [67] through observations of a robust hysteresis signal during temperature sweeping around T_C that the phase transition is a first order grand canonical transition [65] where the hysteresis is an evidence for an energy barrier of around 40 meV between two phases.

6.3.3 Role of defects

The phase transition becomes even more puzzling and fascinating when defects are taken into account. Multiple studies showed that the transition temperature can be tuned by various adsorbates [39, 60, 131–133]. As introduced in the previous two sections, it is important to distinguish between the structural transition (4×1) \leftrightarrow (8×2) and the electronic MIT. Exemplarily, a comprehensive study by SHIBASAKI et al. [39] showed that the temperature for the occurrence of a structural transition can be decreased by adsorption of H or In adatoms and transport measurements revealed a shift of the insulating phase to higher temperatures. An exception seems to be the adsorption of O. Here an increase of the temperature for the structural as well as the electronic transition was observed [134] (cf. measurement depicted in figure 6.7).

The different temperature behavior for the structural transition and the MIT may be ex-

plained as follows [39]. First of all, it needs to be understood what happens when a pristine (4 × 1) is cooled down. As described in section 6.3.1, 1D CDWs with (4 × 2) periodicity along the chain start to form. However, these 1D CDWs are fluctuating and thus metallic conducting paths are still available for electron transport. Upon further cooling, these fluctuations form rather stationary 2D island of insulating (8 × 2) phase. When 2D islands of the (8 × 2) phase have grown sufficiently and coalesce so that the current path through the metallic (4 × 1) phase gets cut, the surface-state resistance increases steeply. Therefore, the temperatures for the structural and electronic transition are nearly the same for the pristine phase. If there are defects added to the surface (e.g. H or In), the CDWs get pinned upon cooling and can not fluctuate. Upon further cooling defect-pinned CDWs without having the ×8 periodicity get connected. Again as in the pristine case, when these insulating islands without (8 × 2) order become the dominant phase, the resistance will increase steeply. The temperature for the occurrence of MIT is higher in comparison to the pristine phase because of the suppression of fluctuations [39]. Regarding the lowered temperature for the structural transition by defects SHIBASAKI et al. [39] propose that “this is probably because the pinning effect by randomly distributed defects [...] is much stronger than the interchain coupling on the pristine surface which favors the ×8 periodicity.” Therefore, the temperature must be lower considering the entropic contribution in the free energy. While this model can explain qualitatively the effect of H and In defects, it fails to provide an explanation of the peculiar behavior of oxygen defects which is up to now still under heavy debate (see for example the recent STM and DFT study by OH et al. [135]).

6.4 Electronic transport

As it was motivated in the previous section, the impurities and their related effects are still not completely understood. Surface transport experiments offer a unique way to probe the intra- and interwire coupling, which will also give further understanding into defect related effects.

Unless stated otherwise, the samples in all the following experiments of this chapter were prepared as follows. Samples of Si(111) substrate (n-type, P doped, $\rho = 500 - 800 \Omega\text{cm}$) with a nominal miscut of 1° towards the $[\bar{1}\bar{1}2]$ direction were used. The samples were outgassed in ultra-high vacuum (UHV) by direct-current heating at 700°C for several hours. Subsequent flash annealing under UHV conditions to maximum temperatures of 1150°C was used for cleaning of the surface, while maintaining a pressure below 7×10^{-10} mbar. Finally, single domain In (4 × 1) structures were grown at 400°C by deposition of one ML of indium. The overall quality of both the substrate and the In phase as well as the orientation were controlled by SPALEED. An exemplary SPALEED image is shown in figure 6.8(a) depicting clearly single domain In wires with (4 × 1) symmetry running along the $[1\bar{1}0]$ direction.

The samples were contacted in a feedback controlled manner as described in section 3.2 avoiding irreversible damages to probes and surface. The contacting is exemplarily demonstrated in SEM images shown in figure 6.8(b). Using the 4pp rotational square method (cf. section 5.2), the resistance in dependence of the orientation in respect to the In chains was probed by evaluation of the corresponding $I(V)$ curves (cf. figure 6.8(c)). The outcome of such measurements is depicted in figure 6.8(d). The resistance anisotropy degree for the In/Si(111)-(4 × 1) system grown onto unstructured area is around $\left(R_{\perp}/R_{\parallel}\right)_{2\text{D}} \approx 2.6$. The

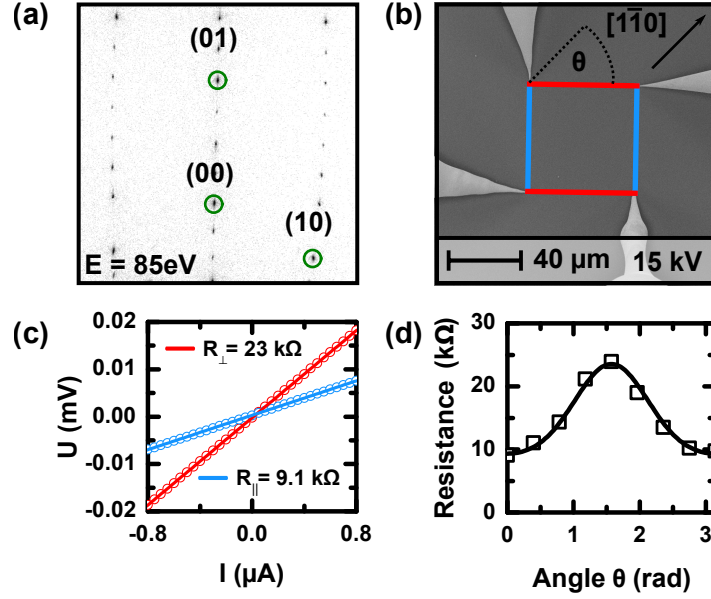


Figure 6.8: (a) Exemplary SPALeED image of the 4×1 reconstruction on the prepared samples demonstrating the growth of a long range ordered single domain structure. Image of LEED pattern was taken at 300 K and 85 eV. (b) SEM image of four W-tips placed in a square configuration on In-(4×1) on Si(111). (c) $I(V)$ -curves obtained for the two distinct configurations (current along the red and blue lines, respectively) (d) The resistance measured in a square 4pp geometry at room temperature as a function of the angle zero along the direction of the In wires.

solid line is a fit to the data by using equation (5.2.1) leading to conductivity values of $\sigma_{\parallel, 2D} \approx 10 \mu\text{S}/\square$ and $\sigma_{\perp, 2D} \approx 5 \mu\text{S}/\square$.

Table 6.1 lists the different anisotropy ratios $\sigma_{\parallel}/\sigma_{\perp}$ and conductivity values as published in literature over the years as well as those obtained within this thesis using the 4pp rotational square method. While the measured conductivity values within this thesis are one order lower than the values reported in literature, the conductivity ratio is close to the most recent study. But, it is evident that the overall high deviation in the list of the values must be related to further surface effects not taken into account, e.g. the pre-treatment of the Si sample. In addition, from potentiometry and transport measurements it is known that monatomic steps significantly increase the resistance [136–138], thus the vicinality of the Si(111) surface should have an effect on the In/Si(111) anisotropy.

6.4.1 Finite size effects studied in anisotropic 2D system

As it was shown in part II in sections 4.2 and 5.3, any constriction of current paths can significantly increase the measured resistance resulting in an apparently higher anisotropy. Thus, in order to get a higher sensitivity towards defects and to correlate such imperfections with transport properties, In/Si(111)-(4×1) wires were also prepared on spatially restricted structures. For this purpose, the advantages and disadvantages of three different approaches were investigated:

Table 6.1: Experimental anisotropy ratio $\sigma_{\parallel}/\sigma_{\perp}$ listed in literature at 300 K. The substrate miscut is given towards the $\langle\bar{1}\bar{1}2\rangle$ direction.

$\sigma_{\parallel}/\sigma_{\perp}$	σ_{\parallel} [$\mu\text{S}/\square$]	σ_{\perp} [$\mu\text{S}/\square$]	substrate miscut [$^{\circ}$]	reference
60	720	12	1.8	KANAGAWA et al. [83], 2003
17	310	18	1.8	OKINO et al. [115], 2007
7	220	33	between 1 and 2	UETAKE et al. [129], 2012
2	10	5	1	this thesis, EDLER et al. [29], 2015

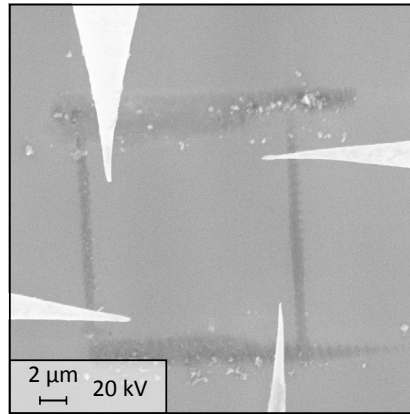


Figure 6.9: Quadratic window with $15\ \mu\text{m}$ side length made via scratching of one of the STM tips. The debris of scratching process is visible as white spots.

- direct STM manipulation of surface structures, i.e. SEM-guided scratching of the quasi-infinite 2D-phase
- UHV compatible in-situ lithography by electron beam stimulated selective thermal desorption (EBSTD)
- ex-situ preparation of mesa structure by optical lithography

SEM-guided scratching of the quasi-infinite 2D-phase Since the hardness of tungsten is higher than the one of silicon [139], W-STM-tips can be easily used to scratch the surface. The method was investigated in detail in the master thesis [140] which was supervised by the author of this thesis and a produced structure is exemplarily shown in figure 6.9. While it turned out that this method can be used in principal to restrict the current paths, which resulted in a higher sensitivity, the scratching process itself is difficult to control and is heavily accompanied by defects from the scratching debris. In addition, it could not be guaranteed that the scratching only removed the adlayer while the Si-template remains intact. Otherwise bulk-states may be involved in the transport easily.

UHV compatible in-situ lithography by EBSTD An UHV compatible lithography on silicon can be achieved by the so-called EBSTD mechanism. This mechanism was first described

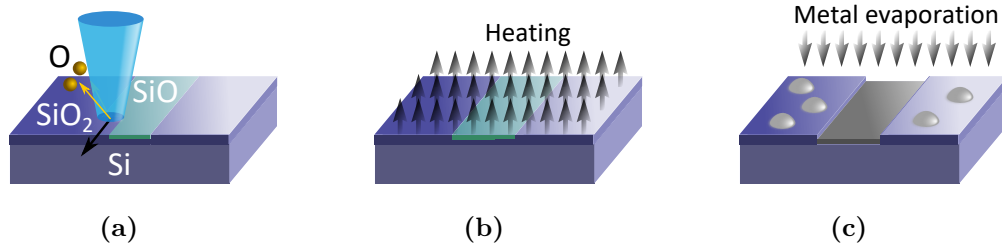


Figure 6.10: Schematic sketch of the EBSTD lithography process shown step-by-step. (a) The e-beam of the SEM induce a local reduction of $\text{SiO}_2 \rightarrow \text{SiO}$. (b) SiO is desorbed at temperatures around 700°C . (c) Metal evaporation resulting in metal epitaxy only in the written fields.

by the group of ICHIKAWA in the late 1990s (cf. [141–143]). The process steps are in principal similar to the traditional, “standard” ex-situ lithographic methods. A schematic sketch of the process steps is depicted in figure 6.10. Basically, instead of using a photoresist, a monolayer thin silicon dioxide SiO_2 layer is used as the “light” sensitive material for patterning. Structures of arbitrary size are fabricated after local e-beam exposure. This leads to a local reduction of $\text{SiO}_2 \rightarrow \text{SiO}$ which can be selectively desorbed at elevated temperatures around 700°C .

First results using this technique on the $\text{In}/\text{Si}(111)-(4 \times 1)$ system are shown in figure 6.11. Here, figure 6.11(a) shows the SEM image of a fabricated structure while figure 6.11(b-e) shows the STM images inside and outside of such structure. Such prepared (4×1) reconstructions show a lot of defects in comparison to a perfect (4×1) (cf. inset in figure 6.11(e)) and the quality needs to be improved before future transport measurements (cf. comparison in figure 6.11(e)). Nevertheless, the approach is promising for measuring the local transport on spatially restricted wire ensembles with defined control of the size and number of steps allowing in combination with STM a better understand of the role of local defects.

Ex-situ preparation of mesa structure by optical lithography For this purpose, half of the samples were in addition structured by circular mesa structures of different sizes with diameters ranging from 15 to $40 \mu\text{m}$. The mesa structuring was performed ex-situ by standard optical lithograph and reactive ion etching technique using an etching depth of 500 nm . Before inserting the samples into UHV, these were first further cleaned through a vigorous chemical treatment including standard RCA-1 etching [144] in air for removing any residuals of resist used for the optical lithography. To preserve the lithographic structures and reduce refacetting, flash annealing temperatures of maximum 1000°C were used for cleaning of the surface. As it will be shown in the following, the avoidance of high annealing temperatures only affects the defect density along the wires and results in slightly lower σ_{\parallel} values which are nonetheless still comparable to literature.

The surface was characterized as in the unrestricted area by the 4pp rotational square method (cf. section 5.2) as shown in figure 6.12(a). Notably, in comparison to the unrestricted sample area much higher resistances were measured, i.e. the resistance anisotropy for $\text{In}/\text{Si}(111)-(4 \times 1)$ measured on the circular mesa surface was $(R_{\perp}/R_{\parallel})_{\text{Mesa}} \approx 27.2$ instead of 2.6 measured on the unstructured area. This result is of importance, because it directly

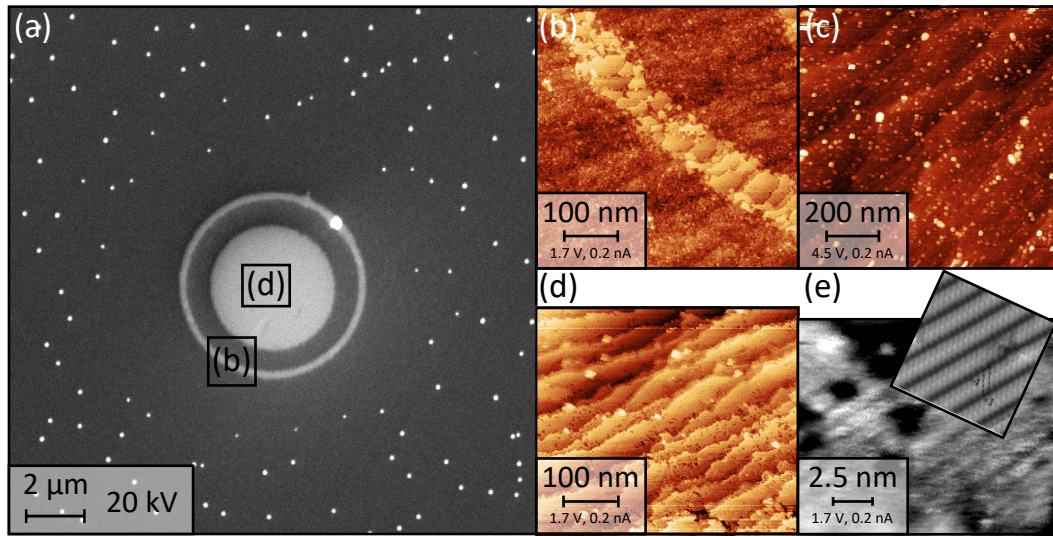


Figure 6.11: (a) SEM image of oxidized Si(111) surface after writing of a circle and coaxial annular ring by EBSTD and deposition of 1 ML of indium. White spots are indium droplets which do not stick efficaciously on SiO_2 . The annular ring was used in order to limit the indium diffusion from the surroundings inside the written structure. (b-e) STM images showing (b) the annular ring, (c) a region outside the written structure and (d,e) the circular region in two different magnifications. The inset in (e) is taken from [45].

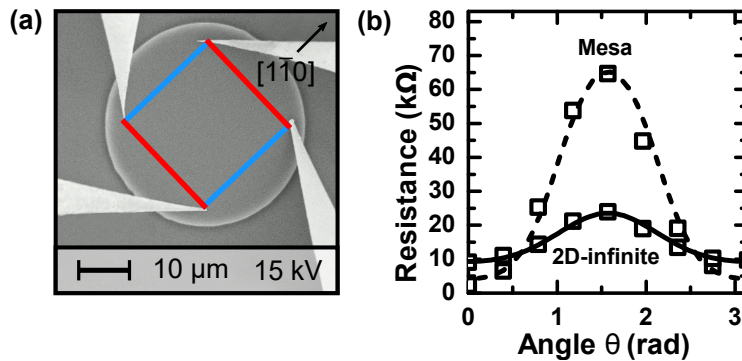


Figure 6.12: (a) Exemplary SEM image of four W-tips placed in a square configuration on a circular In/Si(111)-(4 × 1)-mesa structure (40 μm diameter). (b) The resistance measured on a mesa structure (15 μm diameter) in a square 4pp geometry at room temperature as a function of the angle zero along the direction of the In wires. In addition, the resistance measured on quasi-infinite area (probe distance 15 μm). An angle of 0° refers to a parallel orientation of the current probes. The resistance anisotropy measured on the spatially restricted area is significantly higher than for the quasi-infinite 2D case.

confirms that a much higher sensitivity (of one order of magnitude or more) can be easily achieved when the sample size becomes comparable to probe distance and validates both theoretical models introduced for the description of infinite and finite regimes in part II.

As for the infinite case, the conductivity values were calculated using equations (5.2.1). Here, solid and dashed lines in figure 6.12(b) show the best fit to the data. The calculated conductivity values are $\sigma_{\parallel, 2D} \approx 10 \mu\text{S}/\square$ and $\sigma_{\perp, 2D} \approx 5 \mu\text{S}/\square$ for the unconfined and $\sigma_{\parallel, \text{Mesa}} \approx 16 \mu\text{S}/\square$ and $\sigma_{\perp, \text{Mesa}} \approx 6 \mu\text{S}/\square$ for the finite case. It needs to be highlighted, that both shown measurements were performed on the same sample at different sites with same probe distance. Therefore, it is expected that the conductivity components (2D/Mesa) are the same. This is almost the case, as seen for the σ_{\perp} values, showing that the average step density along the $[\bar{1}\bar{1}2]$ direction has not changed significantly. The slight increase of the conductivity anisotropy is probably accounted by an increased conductivity value σ_{\parallel} for In wires grown on Si-mesa templates. The finite size of such a template may favor step straightening and thus trigger growth of extended In wires with an increased electronic mean free path. An influence of stress for tuning the step morphology is known from other investigations [145]. Additionally, in comparison to the values reported in literature as listed in table 6.1 it is noticeable that the anisotropy ratio $\sigma_{\parallel}/\sigma_{\perp}$ is slightly lower. The difference is most likely due to the lower annealing temperature during sample preparation in order to preserve the mesa structures. This leaves a higher concentration of surface defects behind which is responsible for the larger measured resistance.

The measured increase of sensitivity towards defects due to finite size effects is modeled by theory (cf. discussions in section 5.3). Figure 6.13(a) illustrates the theoretical development of a 4pp square array placed in the center of a finite circular anisotropic structure as a function of the ratio d/s of structure diameter d and probe spacing s and rotation θ for a sample preparation with conductivity values as listed in figure 6.12. Here, a ratio of $d/s \rightarrow \sqrt{2}$ corresponds to the case of probes placed on the circular periphery (finite case) while for $d \gg s$ the finite case can be probed. As shown in the figure 6.13(b) for measurements on two different circular mesa structures, the ratio decreases exponentially like from a value of $R_{\perp}/R_{\parallel} \approx 11$ with the tips at about $1 \mu\text{m}$ from the circular border down to a minimum value of $R_{\perp}/R_{\parallel} \approx 3.5$ when the probes are at a distance of only $3 \mu\text{m}$. The solid curve is the best-fit by using equation (5.3.1) and yields a resistivity-anisotropy of $\rho_{\perp}/\rho_{\parallel} = 2.5 \pm 0.1$ which perfectly agrees with the values determined with the rotational square 4pp. A very low scattering of the data points with respect to the fitting curve is caused most likely due to uncertainties regarding the positioning of the tips or possible inhomogeneities within the In-reconstruction on the Si(111)-mesa itself.

6.4.2 Adsorption of molecular oxygen

In respect to the puzzling influence of oxygen adsorption towards the structural and electronic phase transition (cf. section 6.3.3), an investigation of the transport properties with adsorbed oxygen is of high interest. For this purpose, the 4×1 reconstruction was prepared on spatially restricted areas to increase the sensitivity towards surface defects as it was shown in the previous section 6.4.1. Using this approach, the oxygen adsorption on the In-(4×1) phase was carefully investigated. All oxygen dose experiments were done via a leak valve using a background pressure of 3×10^{-7} mbar.

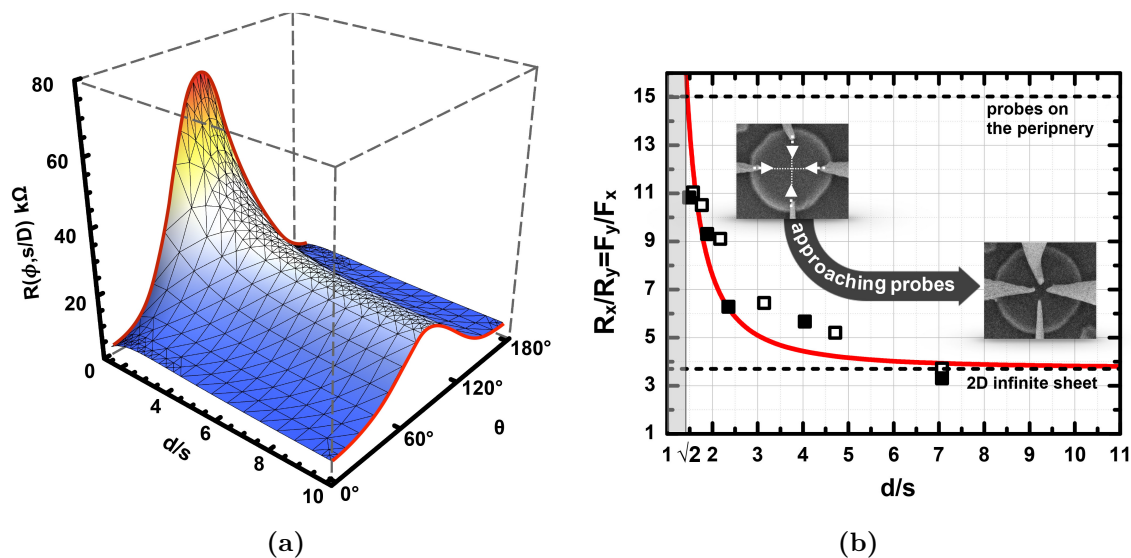


Figure 6.13: (a) Calculated theoretical development of the resistance for a 4pp square array placed in the center of a finite anisotropic structure as a function of the ratio d/s of structure diameter d and probe spacing s and rotation θ in respect to the directions of anisotropy. The plot uses conductivity values corresponding to figure 6.12 (e). (b) Experimental electrical resistance ratio $R_x/R_y = R_{\perp}/R_{\parallel}$ versus normalized wafer diameter d/s measured on (4×1) -In wire system grown on a Si(111) mesa structure ($d = 20 \mu\text{m}$). The empty and filled symbols refer to two different mesas measured on the same sample preparation. The solid line is the best fitting curve of the experimental data using equation (5.3.1) as demonstrated in part II.

Figures 6.14(a) and 6.14(b) show the different conductivity components of the In-(4 × 1) phases measured on quasi infinite 2D or mesa structures grown on differently prepared Si surfaces in terms of the flash annealing temperature as a function of oxygen dose. Each series of measurements itself was performed using the same probe distance on the quasi infinite as well as mesa structured area. For every oxidation step, the conductivity components were determined by appropriate fits using the rotational square method (cf. discussion of figure 6.12 in the previous section 6.4.1).

One may argue that the adsorption of oxygen is severely influenced by the initial defect density of the pristine In phase. Compared to the transport experiments performed on high temperature annealed and on higher miscut Si(111) surfaces [83], the conductivity values in figure 6.14 along the wires are lower by one order of magnitude, i.e., relying on defect-induced transmission coefficients of 50% [146], the defect concentration along the wires must be approximately four times higher. As deduced from STM images of the pristine In phase, the (intrinsic) defect concentration is of the order of $1 \times 10^{12} \text{ cm}^{-2}$ [115]. This means that the intrinsic defect concentration for the measurements is around $5 \times 10^{12} \text{ cm}^{-2}$, which is equivalent to a dosage 1 – 2 L of O_2 . Therefore, as the gradual decrease of conductance along both directions is seen even for higher dosages, the findings are not limited by the structural imperfections, but are more likely due to the modification of the In-(4 × 1) itself.

Before the effect of oxygen adsorption seen in the measurements is discussed in detail,

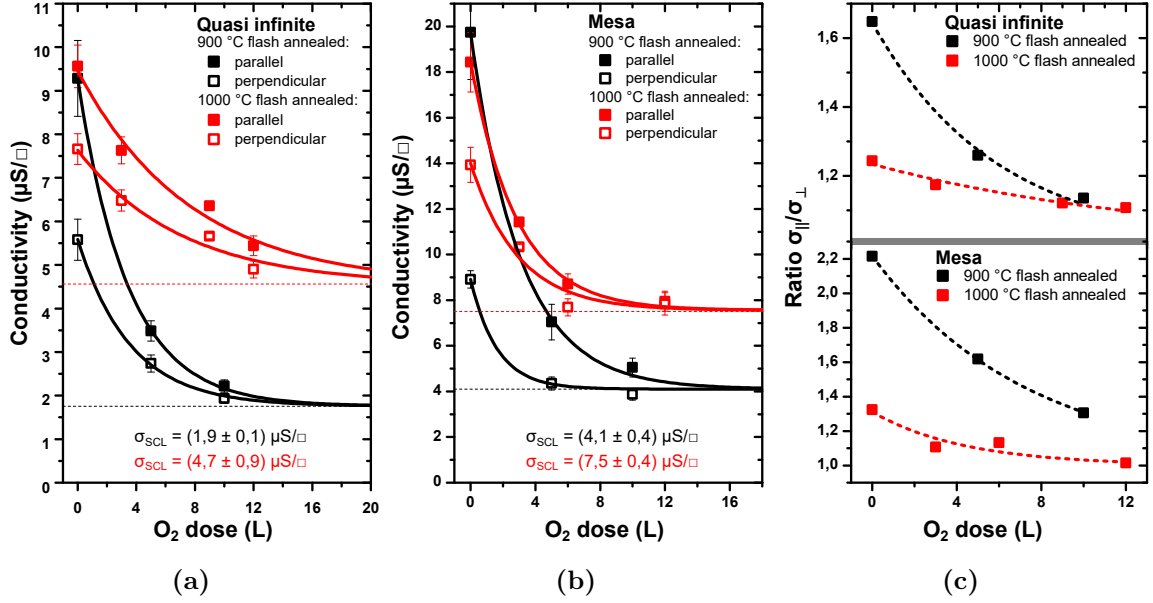


Figure 6.14: Transport measurements on In-(4 × 1) phase performed on (a) quasi infinite 2D and (b) mesa structure as a function of the O₂ dose and flash annealing temperature. The isotropic background refers to a contribution of the space charge layer σ_{SCL} . The associated decrease of the anisotropy $\sigma_{\parallel}/\sigma_{\perp}$ as function of the O₂ dose is shown in (c).

the effect of the sample preparation by thermal annealing at 900 °C and 1000 °C prior to adsorption of In should be highlighted. Higher flash temperatures were not considered, since otherwise the mesa-structures became irreversibly damaged. Obviously, the absolute conductivities and anisotropies are influenced by the pre-treatment of the Si sample. While annealing at 900 °C yields larger anisotropy ratios (cf. figure 6.14(c)), higher annealing temperatures primarily increase σ_{\perp} . These effects come along with the gradual increase of an isotropic background. Indeed, it was recently shown by UETAKE et al. [129] that the σ_{\perp} component correlates with the flash annealing temperature used for cleaning and preparation of the Si(111) surfaces. Apparently, high temperature flash annealing in vacuum leads to formation of a p-type epi-layer [84]. The associated flat band condition in this area gives rise to an isotropic σ_{SCL} background in addition to contributions from surface states. However, higher annealing temperatures tend to result in cleaner and long-range ordered surfaces. Therefore, increased σ_{\parallel} values are expected as a function of increased annealing temperature, which is only to some extent visible in case of the quasi 2D-infinite sample (cf. figure 6.14(a)). Apparently, the miscut angle of the sample, i.e. the step-step interaction, is a further critical parameter, which not only influences the growth of single domains but also determines the average lengths of the wires.

Upon adsorption of oxygen both σ_{\parallel} and σ_{\perp} for the quasi infinite case as well as for the case of mesa structures decrease with increasing dose D of molecular oxygen. The results show unambiguously that both the intra- and the interwire couplings are affected by adsorption. Furthermore, both components saturate at a finite value, i.e. the surface state mediated transport channels are superimposed by an isotropic background. This background is robust against further adsorption of oxygen, thus reminiscent of a buried transport channel, e.g. of

a space-charge layer (SCL), as already pointed out by UETAKE et al. [129]. Thus concluding from the shown experimental data, the measured conductivity σ for both components is the sum of the contributions of the σ_{SS} (the contribution of the surface-state bands of the topmost atomic layer) and the σ_{SCL} (the isotropic surface SCL beneath the surface):

$$\begin{aligned}\sigma_{\parallel} &= \sigma_{\text{SS},\parallel} + \sigma_{\text{SCL}} \\ \sigma_{\perp} &= \sigma_{\text{SS},\perp} + \sigma_{\text{SCL}}.\end{aligned}\tag{6.4.1}$$

Quantitatively, the conductivities measured as a function of the O₂ dose D can be described by

$$\sigma_{\parallel,(\perp)}(D) = \sigma_{\parallel,(\perp)}(0) \cdot \exp\left(-D/D_{0,\parallel(0,\perp)}\right) + \sigma_{\text{SCL}}.\tag{6.4.2}$$

The SCL contributions of the quasi infinite area found for annealing the Si-substrate to 900 °C and 1000 °C are 1.9 $\mu\text{S}/\square$ and 4.7 $\mu\text{S}/\square$, respectively, and are in nice agreement with the trend reported in [129]. For the quasi infinite 2D case the decay along the wires for 900 °C is $D_{0,\parallel} = 3.4 \text{ L}^{-1}$. For the perpendicular case, the decay of the conductivity along the interwire direction is slightly weaker ($D_{0,\perp} = 3.6 \text{ L}^{-1}$), but generally similar, showing that oxygen affects both transport channels in the same way. $D_{0,\parallel}$ in good agreement with previous studies [115, 129], where molecular oxygen and the residual gas were used in a long-term experiments. However, a change of the σ_{\perp} was not reported or not directly obvious due higher conductivity in the parallel direction [115, 129].

Comparing the results of the quasi infinite area with the In phase on the Si(111) mesa structures, the increased σ_{SCL} background on the mesa structure by a factor of 1.9 ± 0.2 compared to the data presented in figure 6.14(a) sticks out. Assuming that the mesa structure with a nominal height of 500 nm reveals entirely p -type character, the thickness of p -type region within the quasi infinite regime is around 550 nm, which is in reasonable agreement with estimations given by UETAKE et al. [129]. As obvious from figure 6.14(b), in the saturated regime the electronic transport occurs via the SCL, i.e. in the case of the Si-mesa structure the currents are not necessarily restricted any longer to the mesa itself implying that possibly different correction factors are needed. Therefore, in case of the anisotropic transport regime different correction factors are probably mandatory, e.g. for the finite 2D scenario, assumed here for clean surface which is justified as long as the surface state contribution dominates the transport signal, and the 2D infinite scenario (saturated regime). However, after dosage of 15 L the R -ratio is unity, i.e. the conductivities measured with the used tip geometry for the alleged confined regime and 2D infinite case reveal the same conductivities [30]. It has to be highlighted that such considerations are not necessary for the quasi 2D infinite case as discussed in context of figure 6.14(a), i.e. the general conclusions will not be affected by the different SCL implications in case of the Si-mesa structure.

To summarize, the performed experiments of this thesis have confirmed the presence of a SCL contribution and that its magnitude depends on details of the pretreatment of the Si sample. Secondly, it is also shown that σ_{\perp} is affected by adsorption of oxygen, in other words also the In-induced surface states now contribute to the transport channel in the direction across the wires.

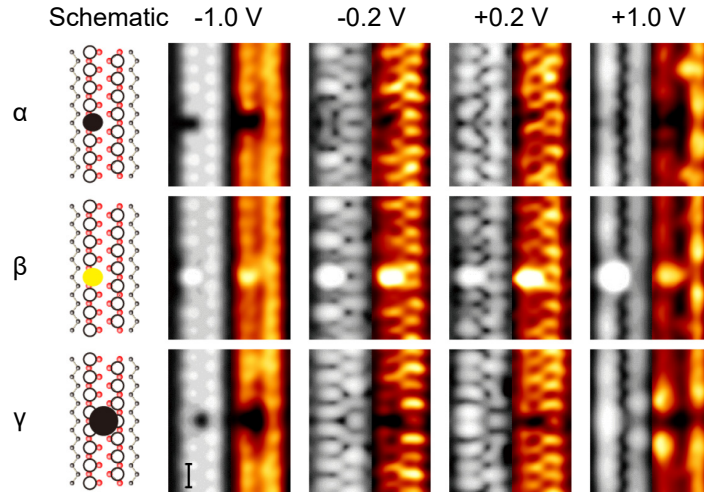


Figure 6.15: Bias-dependent STM images (colored part experiment, gray scaled simulation) of the three defect structures (α, β, γ) induced by O on In/Si(111)-(4 × 1) as classified by OH et al. [135]. Classification by OH et al. [135] of the three defect structures (α, β, γ) induced by O on In/Si(111)-(4 × 1). The typical population ratio is $\alpha : \beta : \gamma = 10 : 3 : 1$ [135]. [135]. The schematic drawing shows the 4 × 1 structure model with the defect. Here a depression (protusion) of the oxygen-induced defects is represented with black (yellow) circles. The In and Si atoms are represented by red and gray balls. Image is taken from [135].

DFT calculations

In two recent studies, the oxygen adsorption sites were determined by high resolution STM measurements and were confirmed by DFT calculations [135] (cf. figure 6.15). According to these studies, oxygen prefers to adsorb on-top within a threefold coordinated position in one of the two zig-zag In chains (so-called α -type defect) [135, 146, 147]. With a probability of around 30 % other adsorption sites were found, where the oxygen adsorbs at the Si/In interface (β -defect) or between the two zig-zag In chains (γ -defect), respectively. The statistical analysis of STM images revealed further [135] that a dose of 3 L at room temperature results in defect concentrations of $8 \times 10^{12} \text{ cm}^{-2}$ (cf. (intrinsic) defect concentration of pristine surface is $4 \times 10^{12} \text{ cm}^{-2}$ [115]). This corresponds to a defect concentration of around 4 % with respect to the (4 × 1) unit cell. The ARPES measurements have shown that the overall electronic structure of the In surface bands are not drastically altered. The band filling factors are increased by around 7 % after dosing 10 L O₂, i.e. oxygen injects electrons [148]. For low oxygen coverages, the band filling factors and band structure are almost unchanged. Therefore, a change of the conductivity measured at room temperature is expected to be mainly related to the electronic mobility, i.e. to the scattering times.

In order to rationalize and interpret the experimental findings of the experiments in this thesis, in cooperation with the university of Paderborn (SCHMIDT GROUP) DFT calculations within the local-density approximation (LDA) were performed utilizing the structural models recently obtained in [135] for oxygen adsorption on the In/Si(111)-(4 × 1) phase. Within this analysis and by following the arguments given by OKINO et al. [115] an influence of the

oxygen atoms towards the SCL has been neglected, as both spectroscopic investigations as well as calculations revealed rather a modification of the surface states upon adsorption [146, 148]. The subtle energetics of the In/Si(111) systems has been shown to be very sensitive with respect to the details of the exchange-correlation functional used [52, 126] and even with respect to relativistic and spin-orbit coupling effects [149]. However DFT-LDA provides meaningful total energies, atomic structures as well as vibrational and optical properties for In/Si(111) [62, 63].

In particular, quantum transport calculations were performed using the scattering approach proposed by JOON CHOI et al. [150] and SMOGUNOV et al. [151] as implemented in the PWCOND module [152] of the QUANTUM-ESPRESSO-package [153]. This allows determining the coherent transmission coefficients \mathfrak{T} through the oxygen contaminated indium wires. The transport system setup is depicted in the following paragraph for the two relevant transport directions along and perpendicular to the wires. The setup used in the theoretical calculations consists of two parts: (i) the ideal contacts, which are followed up periodically to semi-infinite contacts and (ii) the enclosed scatter region which contains the impurities. In order to make the parameter-free solution of the scattering problem feasible for the large adsystems, the silicon substrate in the super cell is modeled with a single double-layer saturated with hydrogen. This affects the most transport relevant In bands only marginally compared to a supercell with three double-layers Si substrate and leads to a numerical error bar of the calculated transmittance \mathfrak{T} of less than 10%. The Brillouin zone of the (4 × 1) unit cell was sampled with a 16 (intrachain) × 4 (interchain) × 1 Monkhorst-Pack mesh of special \mathbf{k} points [154]. Equivalent \mathbf{k} point meshes have been used for larger unit cells. Other technical parameters were chosen as in previous In nanowire studies [135, 149].

LDOS and transmission functions

DFT calculations of the local density of states (LDOS) at E_F show that oxygen atoms severely affect the electronic structure of the In wire they adsorb on, see also [135]. Interestingly, it is found that the LDOS is perturbed not only in the immediate vicinity of the adatom, but ranges several lattice constants along the wire direction. In addition to this, there is also a cross talk with the neighboring In wire, which should affect the transport in the direction across the wires. Figure 6.16 shows the difference of the LDOS (integrated over ± 0.1 eV around E_F) with respect to the perfect (4 × 1) phase. As obvious, the adsorption of oxygen changes the density of states (DOS) at E_F also on the neighboring In chain and the tiny fractions of a local increase in the DOS are overcompensated by areas with a reduced DOS (marked in red).

In order to quantify the influence on transport of the most common oxygen defect (α -type) onto the quantum transport properties of the indium nanowires, a coherent transport model is applied along and perpendicular to the indium wires. Therefore, a 4 × 4 surface unit cell is used that contains a single oxygen adatom which is roughly comparable to the dosage 15 L of O₂ in the experiment. This unit cell is sandwiched between ideal contact elements as depicted in figure 6.17.

For the configuration shown in figure 6.17(a) the transmittance decreases to around

$$\mathfrak{T}_{\parallel}(15\text{L})/\mathfrak{T}_{\parallel}(0\text{L}) \approx 0.65 \quad (6.4.3)$$

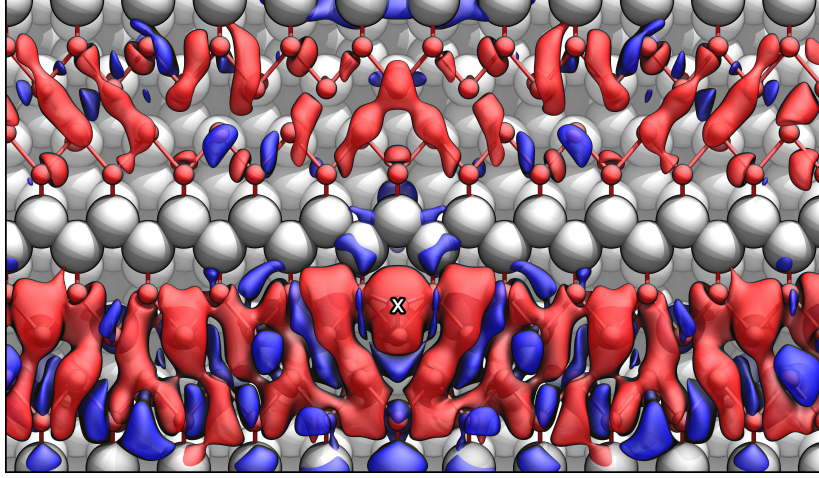


Figure 6.16: Difference of LDOS within a 8×12 unit cell integrated within an interval of ± 0.1 eV centered at E_F around an α -type oxygen defect (marked by a cross) compared to ideal, defect-free wires. The increase (decrease) of the LDOS is colored in blue (red). The corresponding iso-values are set to 1×10^{-5} and -7.5×10^{-5} , respectively.

in the parallel (*intrachain*) direction. This agrees quantitatively with previous transport calculations based on a Green function formalism [146] where it has been shown that oxygen strongly affects the conductivity along the wires mainly due to the combination of two effects: On the one hand, O adatoms form a potential well that effectively scatters the electrons, thus reducing the transmittance. On the other hand, oxygen adsorption leads to geometric deformations of the In nanowires that reduce its conductance. Relying on the configuration shown in figure 6.17(b), the transmission across the direction of the wires has been investigated as well. The calculation reveal for one oxygen defect per 4×4 unit cell a ratio of

$$\mathfrak{T}_{\perp}(15 \text{ L})/\mathfrak{T}_{\perp}(0 \text{ L}) \approx 0.45, \quad (6.4.4)$$

i.e., the coherent transport perpendicular to the wires is even slightly more affected than the parallel transport.

Moreover, it should be considered that the realization by semi-infinite perfect In-units underestimates the effect of the oxygen defect within the 4×4 unit cell, i.e. the effective defect concentration in the calculation is lower. In order to investigate the effect of higher defect concentrations and mimic to some extent the experimental situation of a diffusive transport regime, calculations considering two subsequent scattering units were also performed. Interestingly, the additional transmittance decrease along the wires is stronger than in interwire direction, which is in qualitative agreement with the experimental findings (cf. with figure 6.14). Relying on the fact that the conductivity along the wire is higher compared to the $[\bar{1}\bar{1}2]$ direction, as correctly modeled within an effective mass tensor calculation [112], the trend seen for the direction-dependent transmittance factors in this study would finally result in an isotropic electronic transport in accordance with the experiments.

Nonetheless, comparing the present calculations to the measured findings, one should consider further that the effect of realistic contacts, i.e. their scattering behavior, as well as

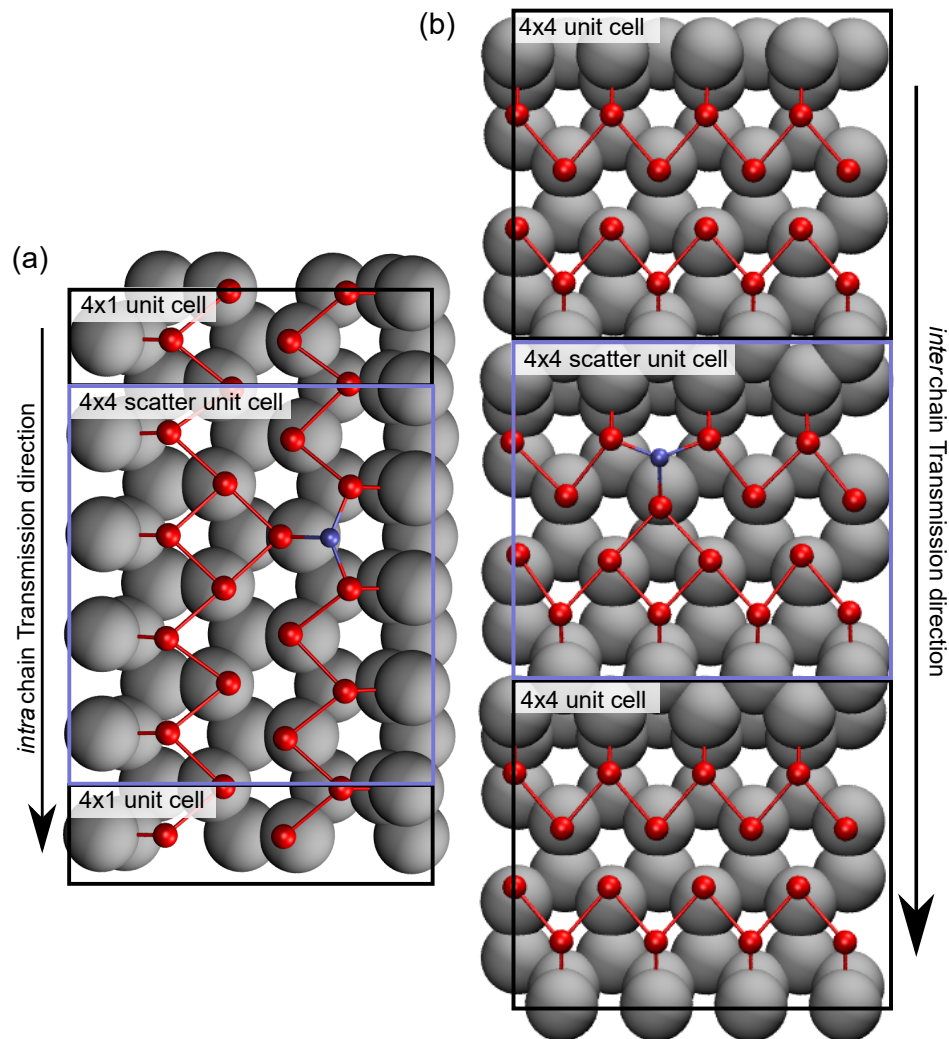


Figure 6.17: Schematic setup of the transport calculations for the intrachain (a) and interchain (b) direction. The 4×4 unit cell containing the O scatterer (purple frame) is sandwiched between ideal wire segments that model semi-infinite ideal contacts (black frame).

thermal dissipative scattering due to phonons at finite temperature are not included in the simulations. Despite these limitations, the coherent-transport calculations describe well the oxygen-induced conductance modifications observed experimentally. Most importantly, they show clearly that oxygen defects affect the conductance perpendicular to the In wire direction.

6.5 Summary and conclusion

In this chapter the electronic transport of the atomic chain system In/Si(111)-(4 × 1) was investigated and discussed within the context of current literature. It was shown that the properties of the system are highly influenced by defects. In addition, as presented in the theoretical chapter II, a higher sensitivity towards defects could be achieved by a spatial restriction. By this, the effect of defects was studied by adsorption of molecular oxygen at room temperature. Here, it was seen that the contributions of the surface states are gradually reduced by adsorption at room temperature. Notably it was observed that the conductivity σ after adsorption is not only decreased in parallel but also perpendicular direction to the atomic chains which is in clear contrast to previous findings [115, 129]. This effect was further quantified and verified in cooperation with the SCHMIDT GROUP by quantum-conductance calculations. Thereby, the decrease of σ_{\perp} with increasing oxygen dose underlines the interwire coupling in this alleged quasi-1D system.

Au on vicinal Si surfaces

7.1 Introduction

The adsorption of submonolayers of gold on the silicon surface results in plethora of reconstructions. Among them, the reconstructions on vicinal, high index Si(111) substrates (Si(hhk) in the following) are highly interesting. Here, the narrow terraces of the substrate lead to well ordered arrays of atomic gold chains parallel to the stepped substrate by self-assembly. Starting from the work of JAŁOCHOWSKI et al. [155] in 1997, up to now, four stable Au induced atomic wire systems were observed: namely the reconstructions on Si(553), Si(557), Si(335) and Si(775) [81].

Depending on the cutting angle, the terrace width of the Si(hhk) surfaces varies according to the Miller index which results in different wire reconstructions. One can even go one step further generalizing the Si(hhk) surface as a template material since all observed Si(hhk)-Au reconstructions share a set of reoccurring structural building blocks: The step-edge is always formed by a honey comb (HC) chain while the terraces host – depending on their width – either a single or double atomic Au chain strand. In addition, some Si(hhk)-Au surfaces also host an additional silicon adatom row. These systems are thus very interesting due to the possible tuning the inter-chain coupling and the related physical phenomena like Peierls instabilities and MIT. Furthermore, recently it was seen that some Au-induced arrays of wires on Si(hhk) give rise to spin polarized surface bands due to their strong spin-orbit coupling. In case of Si(553)-Au even spin-ordering phenomena are reported to yield a spin liquid behavior [28, 156].

In this thesis the focus was set on the Si(553) and Si(557) surface (cf. schematic drawing of side cutaway of the Si crystal lattice in the $(1\bar{1}0)$ plane in figure 7.1) and their corresponding gold chains reconstructions. It was shown in recent reviews by SNIJDERS et al. [41] and DUDY et al. [69], the understanding of these systems is complex, still not completely settled and models describing them were vividly discussed and changed a lot over the last decade. Thus, the following sections will first briefly summarize and discuss the current state of research on gold induced atomic wires on vicinal Si(553) and Si(557) surfaces. The chapter then follows on connecting these with the results obtained within the scope of this thesis. Some parts of the results were previously published in “Tuning the conductivity along atomic chains by selective chemisorption” [32] by EDLER et al. [32] and will not be cited separately.

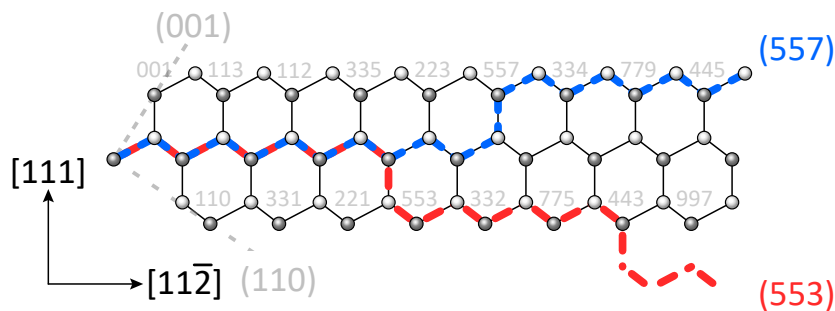


Figure 7.1: Schematic sketch showing a side cutaway of the Si crystal lattice in the $(\bar{1}\bar{1}0)$ plane, which is perpendicular to (111) surface. The examined vicinal surfaces Si(553) and Si(557) are highlighted in red and blue.

7.2 Si(557)-Au and Si(553)-Au: An evolution of models

The atomic and electronic structural models of the gold chains (especially for the Si(553)-Au reconstruction) on vicinal silicon underwent multiple revisions over the years depending on the outcome and interpretation of experimental results. The evolution of models nicely illustrates how the collaboration of experimental and theoretical physicists leads to a refined understanding. Up to now, the models are still – especially concerning the interpretation of phase transitions – not completely settled and under discussions. Thus, the following sections will briefly recapitulate the evolution and drawbacks of models and end with the most present accepted model.

7.2.1 Si(557)-Au

Atomic and electronic structure

The vicinal surface Si(557) is tilted by 9.5° away from the Si(111) plane towards the $[\bar{1}\bar{1}2]$ direction. A deposition of a submonolayer gold¹ on these surfaces results in multiple coverage depending facets [157]. Of special interest is the coverage of 0.18 ML Au (referenced in the following as Si(557)-Au). At this coverage, as first observed in 1997 by JAŁOCHOWSKI et al. [155] in electron diffraction experiments (cf. exemplarily spot profile analysis low-energy electron diffraction (SPALED) pattern in figure 7.2(a) revealing a highly ordered, anisotropic, structure), the gold deposition results in the growth of atomic gold chains aligned parallel to the step edges. The scanning tunneling microscope (STM) images as exemplarily shown in figure 7.2(b) showing regular arrayed terraces of $5\frac{2}{3}a_{[\bar{1}\bar{1}2]} \approx 19.07 \text{ \AA}$ where $a_{[\bar{1}\bar{1}2]} = 3.32 \text{ \AA}$. Additionally, two atomic wires per unit cell are found. Here, one of these wires has a corrugated $\times 2$ periodicity in empty state images while the other shows for the same conditions nearly no corrugation but is dominant in filled state images.

The structural model, which is nowadays generally widely accepted, has evolved over the years taking into account x-ray diffraction (XRD) studies [159], first principle theory total-energy calculations [81, 160–163] and STM experiments [157, 164–166]. A schematic drawing of the structural model is presented in figure 7.3. Notably in comparison to the Si(553)-Au

¹Where 1 ML corresponds to $\sim 7.8 \times 10^{14}$ atoms/cm² of Si atoms in the Si(111) plane.

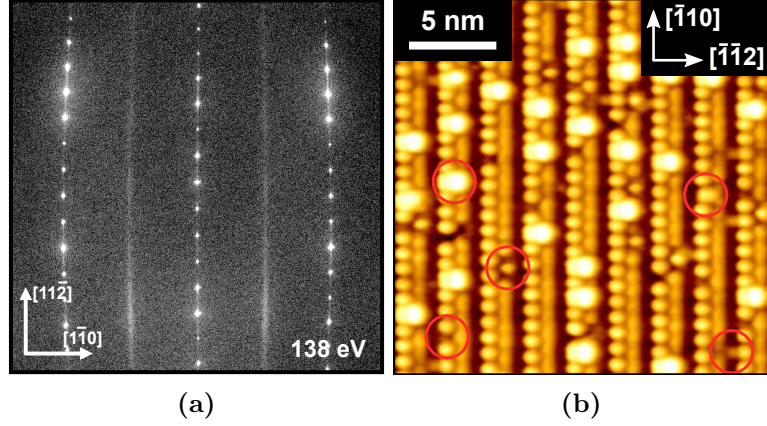


Figure 7.2: (a) SPALEED pattern of the Si(557)-Au reconstruction taken at room temperature. The spot splitting of 17.4%SBZ is in perfect agreement with former studies (cf. discussion in text). (b) Exemplary STM image (taken from [158] at room temperature) of a Si(557)-Au surface reconstruction ($V_T = 1$ V, $I_T = 50$ pA). KANG et al. [158] identified on Si(557)-Au five different reoccurring defect types which are highlighted by red circles.

reconstruction, as shown in the upcoming section, every terrace incorporates one single Au atom in the middle of the terrace forming a single gold chain. Moreover, it needs to be highlighted that the Si(557)-Au surface hosts further Si-atom chain surrounded by the so-called rest-atoms (cf. also discussion in section 7.4). Additionally, silicon atoms near the step edge perform a rebonding to a stable HC like structure.

In contrast to the atomic structure, the electronic structure of the Si(557)-Au reconstruction is still not well established. The band structure of Si(557)-Au was first reported by SEGOVIA et al. [167] in angle-resolved photoemission spectroscopy (ARPES) measurements in 1999. They found a spectrum of a one-dimensional half-filled metallic band dispersion along the wire direction crossing the Fermi level E_F with a band splitting into two bands over a wide energy range which seemed to merge into a single peak at E_F . Additionally, as expected for a 1D character, this state did not disperse in the direction perpendicular to the wires. This was interpreted as a property of separate charge and spin energy excitations and the branches of the dispersion related to spinon and holon excitations as predicted by Tomonaga-Luttinger liquid (TL) theory for 1D electron gases [167].

However, in further photoemission measurements with higher resolution [68, 164, 165, 168] (cf. figure 7.4) it was seen that the two bands are not merging at E_F . Contrary, there are two closely separated almost half filled bands S_1 and S_2 with band fillings of around $S_1 = 0.49$ and $S_2 = 0.42$ [81]² just below the Fermi level E_F , which are having a finite density of states (DOS) at the Fermi level E_F [164], invalidating the idea of a TL. The bands are separated at E_F by $\Delta k_{\parallel} = 0.06 \text{ \AA}^{-1}$ [169]. The transfer integrals based on tight-binding calculations [81] for the bands is $t_{\parallel}/t_{\perp} > 60$ underlining a highly anisotropic character as expected for a quasi-1D system.

Calculations by density functional theory (DFT) confirmed two metallic bands associated

²The reported band fillings deviate slightly in literature presumably attributed to slightly different coverage rates [41].

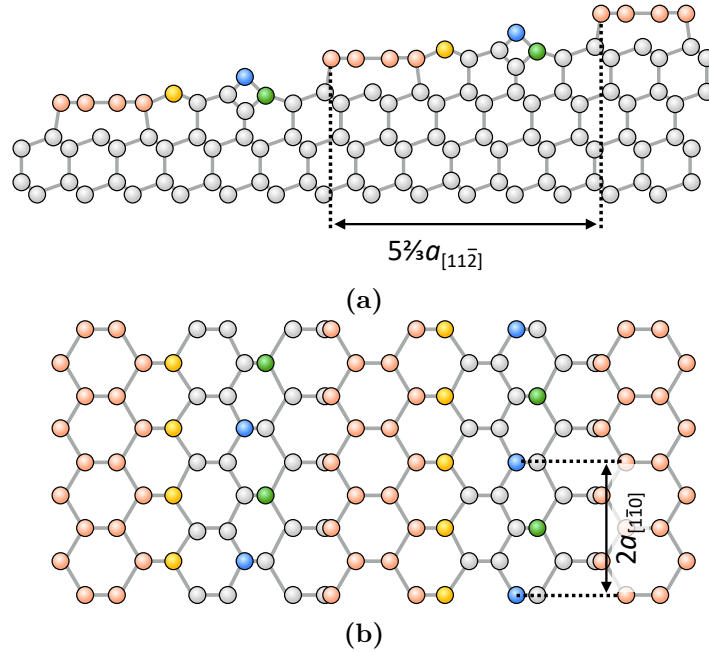


Figure 7.3: Side (a) and top view (b) of the 0.18 ML Au reconstructed Si(557)-Au surface. The Si bulk atoms, Si-honeycomb chain atoms, Au atoms, Si adatoms and the so-called “restatoms” (cf. also discussion in section 7.4) are symbolized by gray, light red, yellow, blue and green spheres, respectively. Structural model adapted from [81].

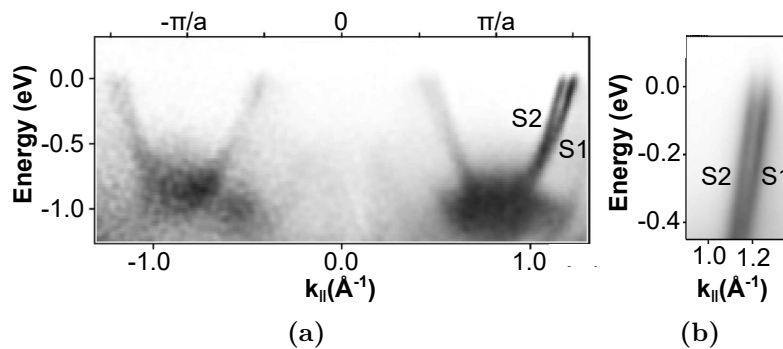


Figure 7.4: (a) ARPES of the full Brillouin zone showing the band dispersion of the Si(557)-Au surface states along the $[1\bar{1}0]$ direction parallel to the chains. (b) Zoomed-in ARPES data for the S1 and S2 band. STM image in (b) taken from [158]. ARPES data in (a) and (b) taken from [168] and [68]. The data was taken at 150 K.

with Au-Si bonds [160]. Additionally, theoretical calculation proposed that these bands originate from the same band and are spin-orbit split due to the Rashba effect associated with a 1D band of the gold chains [160, 162] which was later confirmed experimentally [170, 171]. It was shown that the origin of spin-orbit interaction is the hybridization of the row of Au atoms with the neighboring Si atoms on the terrace [162]. Since the states in $S1$ and $S2$ are found to be spin polarized with opposing spins, the band situation becomes quite complicated which could be one of the reasons for the incomplete debate on a phase transition.

Phase transition

The very first temperature dependent ARPES and low-energy electron diffraction (LEED) measurements of the system between 60 and 300 K [167] in 1999 reported no clear dependence on the temperature. However, proceeding experiments by AHN et al. [165] in 2003 showed a metal-insulator transition (MIT) in ARPES for the $S1$ band at around a temperature of $T_C \sim 270$ K (while the $S2$ band remained insulating) accompanied by a periodicity doubling seen in STM while the adatom attributed chain remained unchanged. These findings were later confirmed in a following combined STM/scanning tunneling spectroscopy (STS) study [172] by the same group showing at low temperatures a band gap of 80 – 100 meV and was explained in terms of a traditional Peierls transition in the $S1$ band due to its near-perfect nesting conditions [41, 172]. However, the data [165, 172] within a simple model of a Peierls like transition could not be independently confirmed. Exemplarily, SAUTER et al. [173] and KIM et al. [169] could not reproduce any evidence of a temperature dependent changed periodicity within a STM study (cf. figure 7.5). In addition, HAN et al. [174] showed in a high resolution STM study that the change of periodicity is (also) attributed to the tunneling conditions, i.e. a $\times 2$ modulation becomes more prominent while increasing the tunneling current. Furthermore ARPES measurements showed that the room temperature gap previously observed for the $S2$ band could not be confirmed independently as well [169]. Noteworthy, a nearly identical metallic behavior of the two bands $S1$ and $S2$ was reported for $83 \text{ K} \leq T \leq 300 \text{ K}$ [169], well below previously stated T_C values. However, SAUTER et al. [173] showed a temperature dependent gap that becomes “considerably small” at room temperature for both, the adatom and HC related structure elements, summarizing and suggesting that for a proper understanding of the phase transition, it is mandatory to take finite-size effects of the 1D segments into account. Moreover, it was shown in transport experiments by OKINO et al. [71] that the temperature dependent conductivity of the Si(557)-Au is better explained in terms of an activation-type nearest-neighbor-hopping insulating behavior which shows no clear T_C .

Nevertheless, while the nature of the phase transition as well as the exact temperature of occurrence is not completely understood up to now, the onset of a phase transition is generally accepted in literature for the Si(557)-Au system.

7.2.2 Si(553)-Au

A Si(111) wafer miscut of 12.5° along the $[11\bar{2}]$ direction results in vicinal Si(553) surfaces. In contrast to the Si(557)-Au surface, the Si(553) can host two different chain configurations depending on the gold coverage: The so called high coverage wires (HCW) and low coverage wires (LCW). The later one was just very recently discovered in 2015 by SONG et al. [175]

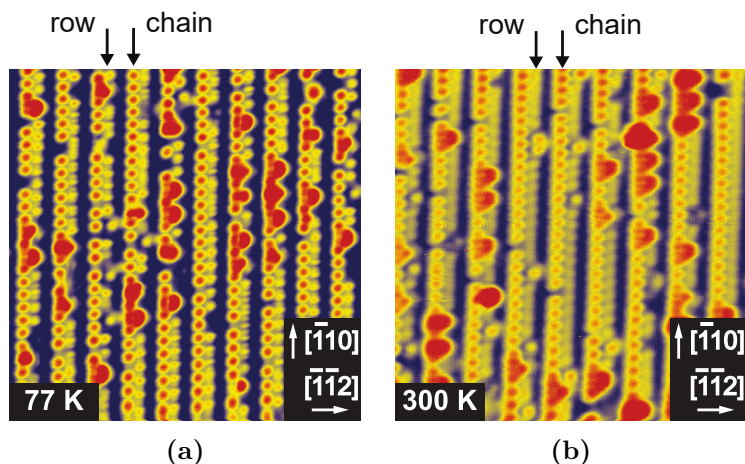


Figure 7.5: STM images of the Si(557)-Au reconstruction at (a) 77 K [173] and (b) 300 K [173]. Both images were acquired with a bias voltage of 1 V and a tunneling current of 0.1 nA. *Row* is attributed to Si atoms forming the HC step edge while *chain* is attributed to a chain of Si adatoms. Images are taken from [173].

within a combined STM, STS, ARPES study in addition with first principle calculations. In comparison to the HCW, only every second terrace is filled with HCW like Au structure while in between there is an intermittent empty terrace of $5\frac{1}{3}a_{[11\bar{2}]}$. This hosts a $\times 5$ superstructure along the terrace resulting in an interwire distance of 32.7 Å. Notably, despite the structural difference, the ARPES spectra are very similar (Only the $S1$ is shifted down by approximately 200 meV). The following sections and the presented experiments will only concentrate on the HCW phase.

Atomic and electronic structure

The HCW phase was first observed by CRAIN et al. [68] in 2003 within a combined STM and ARPES study. For a Au coverage rate of 0.48 ML (referenced in the following as Si(553)-Au), an ordered array of atomic wires parallel to the $[\bar{1}10]$ direction is formed. Figure 7.6 shows exemplarily the reconstruction in STM and SPALEED images. ARPES measurements show a band structure consisting of three bands [68] (cf. ARPES spectra in figure 7.7 showing the three bands $S1$, $S2$ and $S3$ as well as the corresponding Fermi contour plot), a doublet band structure ($S1$ and $S2$) similar to the two bands observed for the Si(557)-Au reconstruction with a band filling of 0.56 and 0.51, respectively, and a third band with fractional filling of 0.27. All bands have parabolic shape and their minimum is at the M point of the Brillouin zone. Notably, as for the Si(557)-Au, the $S1$ and $S2$ band cross at the minimum and the branches separate with increasing wave vector. At the Fermi energy E_F the separation of the bands is $\Delta k_{\parallel} = 0.04 \text{ \AA}^{-1}$ [68]. The slight wiggling of the Fermi contour plot indicates a weak coupling in the direction normal to the atomic wires. The $S1$ and $S3$ bands are metallic while the $S2$ shows an energy gap of 40 meV below E_F [38] at room temperature. Further analysis in ARPES by BARKE et al. [170] in 2006 revealed that - like for the Si(hhk)-Au - the doublet band structure of the $S1$ and $S2$ is a result of the Rashba effect due to spin-orbit coupling.

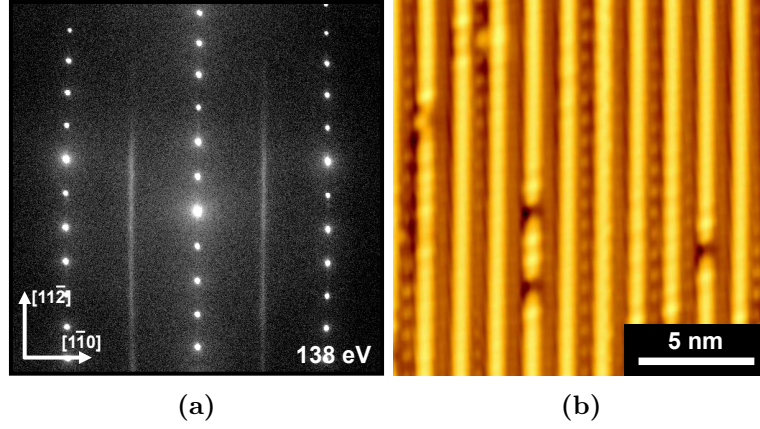


Figure 7.6: (a) SPALEED pattern of the Si(553)-Au HCW reconstruction. (b) Typical STM image of a Si(553)-Au HCW surface reconstruction at room temperature ($V_T = 0.2$ V, $I_T = 50$ pA). STM image taken from [176].

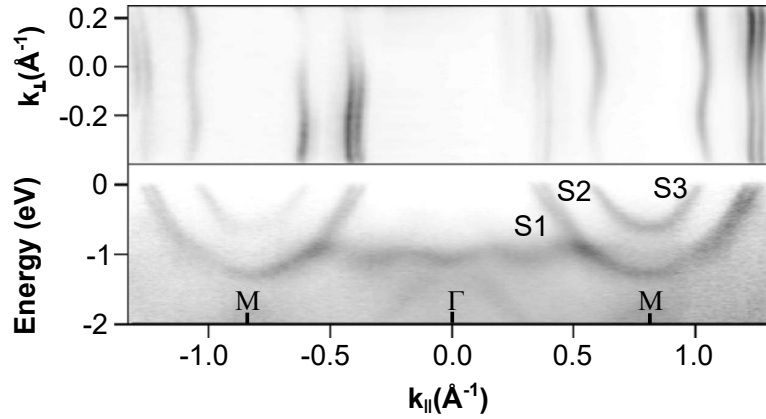


Figure 7.7: ARPES of the full Brillouin zone showing the band structure of the Si(553)-Au HCW phase. The top shows the Fermi surface while the bottom shows the band dispersion. ARPES spectra adapted from [68].

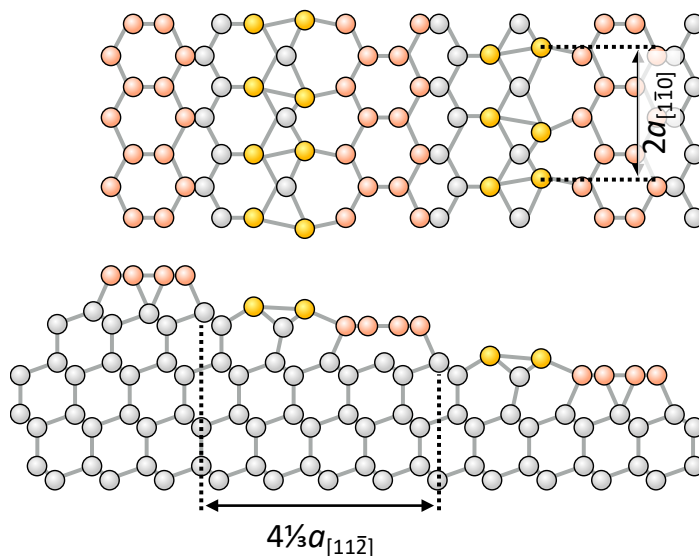


Figure 7.8: Structural model for the Si(553)-Au HCW phase reconstruction. Drawing based on calculations by [180]. The Si bulk atoms, Si-honeycomb chain atoms and Au atoms are symbolized by gray, light red and yellow spheres, respectively.

As a side mark, in the very first structural model proposed by CRAIN et al. [68] based on ARPES, LEED and STM measurements, the surface reconstruction consisted of a single Au chain replacing one Si row at the center of the terrace. This model was very similar to the Si(557)-Au but without any stabilizing Si-honeycomb chain atoms. Consequently the first publications reported an erroneous coverage value of 0.24 ML. The currently accepted model (cf. schematic drawing of the structural model in figure 7.8) and correct Au coverage is based on XRD experiments by GHOSE et al. [56] and VOEGELI et al. [177] and further ab initio DFT calculations by ERWIN et al. [28], RIIKONEN et al. [178], and KRAWIEC [179].

In this model, the HCW phase consists of a dimerized double-strand Au atom chain row with a $\times 2$ periodicity. For the Si(557)-Au reconstruction the step edges are stabilized by a Si honeycomb chain structure. Additionally, ERWIN et al. [28] showed in their DFT calculations that an additional spin polarization of the Si HC structure is energetically favorable and needs to be taken into account. Thus, every third Si step edge atom of the honeycomb structure has a half-filled electron orbital and is spin polarized, whereas the other atoms have a negligible polarization [28].

Phase transition

Upon cooling below ≈ 100 K the Si(553)-Au HCW phase undergoes a structural as well as an electronic phase transition. The transition itself is still under debate and the interpretation is not completely settled (cf. remarks in the recent review by [69] and the discussion of results obtained within this thesis as shown in section 7.5).

At low temperatures AHN et al. [38] first observed in 2005 a structural transition in a STM and LEED study. The onset of this transition was later independently proved by several

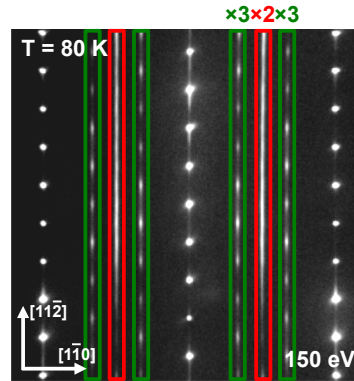


Figure 7.9: SPALEED pattern of the Si(553)-Au surface taken at 80 K and 150 eV. Highlighted in red are the $\times 2$ streaks and in green the $\times 3$ spots. Image adapted from [156].

other groups [156, 181, 182]. Their experiments show at low temperatures ($\sim 70 - 80$ K) a threefold ($\times 3$) periodicity along the steps, in addition to the twofold ($\times 2$) periodicity visible at room temperature (cf. figure 7.9).

Moreover, ARPES and STS measurements revealed a gradual gap opening at low temperatures [38, 70] which led to the interpretation of the transition in terms of a Peierls distortion along the wires. However, the explanation of the structural transition in terms of a Peierls transition is questionable. Indeed, one of the arguments against such a scenario concerns the fractional band fillings [68] in the Si(553)-Au system [41] which do not match the conditions for nesting required for the observed two- and threefold periodicities. Additionally, it was reported in 2013 by POLEI et al. [183] that the periodicity of the chains change reversibly from a $\times 3$ periodicity to a $\times 2$ by charge injection from a STM tip. Currently, the $\times 3$ periodicity is explained by the formation of a charge-ordered spin chain with a frustrated spin texture at every third Si-edge atom as shown by spin-dependent DFT calculations [28, 180, 184] and within STM studies [72]. Thus, the $\times 3$ periodicity is only an increased density of unoccupied states on every third step edge atom and not a Peierls distortion. The $\times 3$ reconstruction vanishes at sufficiently high temperatures when the spin sites fluctuate like a random walker while for sufficiently low temperatures this hopping freezes out [180]. It was also initially reported that the interaction between neighboring spin-polarized Si atoms along the step is anti-ferromagnetic. Furthermore, ERWIN et al. [28] showed that the spin-polarized Si atoms are lowered by 0.3 \AA in respect to their non spin-polarized neighbors which results in a $\times 3$ periodicity of the step edges and a $\times 6$ periodicity by including the spin-polarization. But, very recently HAFKE et al. [156] in 2016 disproved this anti-ferromagnetic ordering in high resolution temperature dependent LEED, STM and additional DFT calculations. It was shown that there is a significant correlation between adjacent spin chains. In particular, this leads to a magnetically frustrated situation with suppressed magnetic ordering since it was found that the spacing between adjacent spin sites is equivalent suggesting a spin-liquid system which also disproves a $\times 6$ superstructure present in the system as suggested before [28, 72].

7.3 Electronic transport

As pointed out in the introduction, one of the open research topics for the Si(hhk) systems is the phase transition and the influence of defects. Transport measurements will give an insight into the inter- and intrawire coupling, their dependence on defects, which deepens the understanding of the phase transition.

First of all, section 7.3.1 will present the sample preparation used for all the following experiments. In section 7.3.2 the transport characteristics of pristine Si(553)-Au and Si(557)-Au surfaces will be discussed. Section 7.4 will show in detail a systematic study of the transport characteristics and structural changes of the Si(553)-Au and Si(557)-Au surface during the adsorption of molecular oxygen at room temperature. The adsorption process will be discussed in combination with a SPALEED and DFT study. Finally, in section 7.5 the phase transition will be reinvestigated by transport experiments. A special focus will be set on the conductivity components and the corresponding T_C of the Si(553)-Au surface in respect to structural changes observed in a LEED analysis.

7.3.1 Sample preparation

All experiments presented in the following were performed with low-doped (with phosphorus) Si crystals cut in the appropriate (557) and (553) directions and with a bulk resistivity of $\rho = 1700 \Omega\text{cm}$ at room temperature, unless otherwise stated. The ex-situ cleaning, degassing and flashing procedure is the same as already described in chapter 6. The Au atomic chains were prepared on Si(553) and Si(557) surfaces by evaporating of 0.48 ML and 0.20 ML Au at 650°C , respectively, using a flux-controlled e-beam heated evaporator. After Au deposition, the direct-current (DC) heating was turned off and samples were immediately cooled down to room temperature. The successful growth of long-range ordered Au-induced chain structures on Si(553) and Si(557) surfaces is nicely demonstrated by the LEED patterns shown in figures 7.10(a) and 7.10(b), respectively. The patterns taken at 300 K nicely reflect the atomistic details of the crystallographic structures shown in figures 7.3 and 7.8. For Si(553)-Au, the step-step distance along the $[11\bar{2}]$ -direction is

$$\delta_{[11\bar{2}]}^{553} = 4\frac{1}{3}a_{[11\bar{2}]} / \cos \phi = 14.7 \text{ \AA}, \quad (7.3.1)$$

where $a_{[11\bar{2}]} = 3.32 \text{ \AA}$ and $\phi = 12.5^\circ$ is the miscut angle with respect to the (111)-orientation. In perfect agreement with the experiment, this correlated step-step structure gives rise to a spot splitting in reciprocal space along the $[11\bar{2}]$ -direction, which amounts to $2\pi/d = 0.42 \text{ \AA}^{-1}$ or, equivalently, 22.2% surface Brillouin zone (SBZ), if normalized to the reciprocal lattice vector of the Si(111) surface. Similarly, the Si(557) surface yields a step-step distance of

$$\delta_{[\bar{1}\bar{1}2]}^{557} = a_{[11\bar{2}]} / (5\frac{2}{3}a_{[11\bar{2}]} / \cos 9.5^\circ) = 21.9 \text{ \AA}, \quad (7.3.2)$$

which refers to a spot splitting of 17.4% SBZ, consistent with previous studies [175, 185–187].

7.3.2 Transport properties of the pristine surface

Using the four-point probe (4pp) rotational square method (cf. part II, section 5.2), the parallel and perpendicular conductivity components are deduced with high precision by gradually

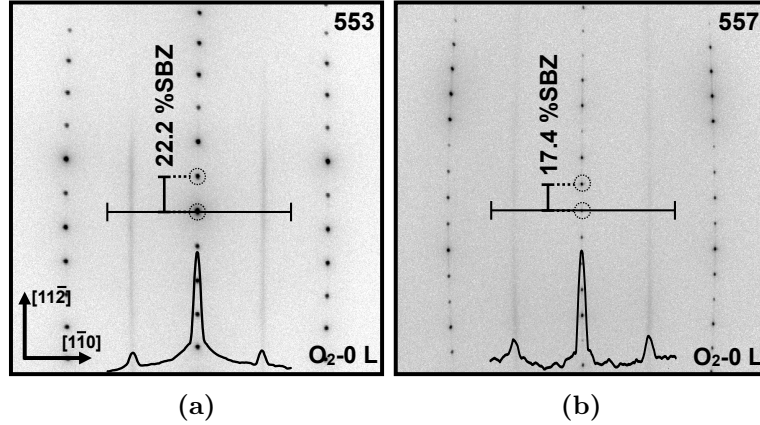


Figure 7.10: SPALEED patterns of pristine Si(553)-Au and Si(557)-Au directly after preparation (Electron energy 138 eV). Horizontal lines indicate where the line scans, shown at the bottom, were taken. The $\times 2$ streaks are clearly visible for both configurations.

varying the orientation angle θ of the setup with respect to the crystallographic directions of the surfaces (cf. figure 7.11(a) and (b) illustrating exemplarily the contacting of a Si(553)-Au surface in scanning electron microscope (SEM) and the corresponding IV curves). The different slopes of the IV curves, i.e. different resistances R , shown in figure 7.11(b) already nicely reflect the anisotropy of the conductivity components of the surface.

The result of an angle dependent transport measurement is shown in figure 7.11(c). Applying equation (5.2.1) of the rotational square method to the plotted data, the best-fit for the Si(553)-Au with a sample doping of $\rho = 1700 \Omega\text{cm}$ yields conductivity values of $\sigma_{\parallel} = 239 \mu\text{S}/\square$ and $\sigma_{\perp} = 186 \mu\text{S}/\square$ leading to a ratio of $\sigma_{\parallel}/\sigma_{\perp} \approx 1.3$ at 300 K (cf. green curve in figure 7.11(c)). Similar conductivity values and ratios were also obtained for the Si(557)-Au surface using the same analysis method and sample doping. Figure 7.12 shows the outcome of such an analysis. The conductivity measured parallel to the chains has a value of $\sigma_{\parallel} \approx 99.7 \mu\text{S}/\square$ while for the perpendicular direction a conductivity of $\sigma_{\perp} \approx 51.9 \mu\text{S}/\square$ was obtained. The conductivity ratio is about $\sigma_{\parallel}/\sigma_{\perp} \approx 1.9$. Notably, the absolute resistance values for the data shown in figure 7.12 are slightly higher than the resistances shown in figure 7.11. The absolute resistance values vary from one preparation to the other and are related to the contributions of the isotropic space-charge layer (SCL). This effect will be further discussed in section 7.5.1. Nevertheless, the anisotropies at 300 K measured on multiple Si(553)-Au and Si(557)-Au samples were ranging for all sample preparations between 1.3 and 1.9. These values are slightly smaller than the ones typically measured for the Si(111)-(4 \times 1)-In system [29, 129] (cf. also chapter 6), but in close agreement with previous investigations of the Si(hhk)-Au systems reported in literature [71, 188] as it will be discussed in the context of figure 7.21(b) in section 7.5.1.

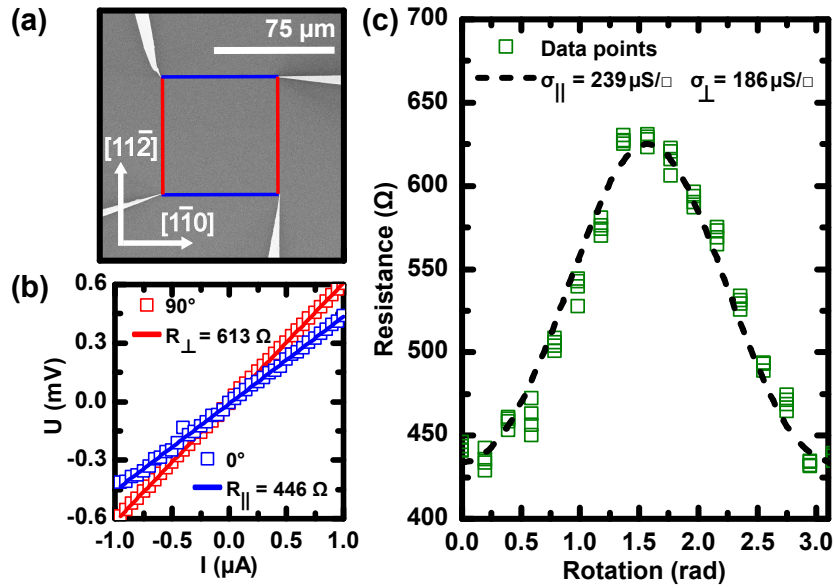


Figure 7.11: (a) SEM image of the four STM-tips used for transport measurements showing exemplarily the used characteristic square geometry. (b) IV curves obtained for two distinct configurations (current along the red (perpendicular direction) and blue lines (parallel direction), respectively). From the slopes the resistances are determined and plotted as a function of the orientation of the squared arrangement with respect to the crystallographic directions of the surface. Measurements were performed on low n-doped Si(553)-Au samples with $\rho = 1700 \Omega\text{cm}$. (c) Resistances measured using the rotational square method ($\pi/2$ refers to current along the $[11\bar{2}]$ -direction, i.e. perpendicular to the chains) measured Si(553)-Au ($\rho = 1700 \Omega\text{cm}$). The four data points visible at each angle correspond to the possible permutations of probes applying voltage and the direction of the current. The dashed line is a fit to the experimental data and allows to derive the conductivity along (σ_{\parallel}) and across (σ_{\perp}) the array of wires.

7.4 Tuning the conductivity of atomic wires by selective chemisorption

As emphasized in the introduction, the Si(hhk)-Au systems share similar structural motifs. But up to now, a systematic investigation of the influence of adsorbates and related defects on the surface states (SS) is missing. In the following, the structural building blocks and their behavior towards adsorption is analyzed in detail on the example of molecular oxygen adsorption.

For the interpretations of this section, the following important difference in the structural models between the Si(553)-Au and Si(557)-Au (cf. figures 7.3 and 7.8) should be emphasized once again: The Si(553)-Au surface consists of a double row of Au atoms, which substitute Si surface atoms and form a HC-like chain of Si reconstruction at the step edge. Si(557)-Au has a very similar structure except that the Au chain is formed by a single row of atoms. Most importantly, the Si(557)-Au surface hosts a further Si-atom chain surrounded by rest-atoms. As a result, the metallic surface states probed by surface transport are of different origin. Thus, as a consequence of these structural peculiarities, the intensity streaks

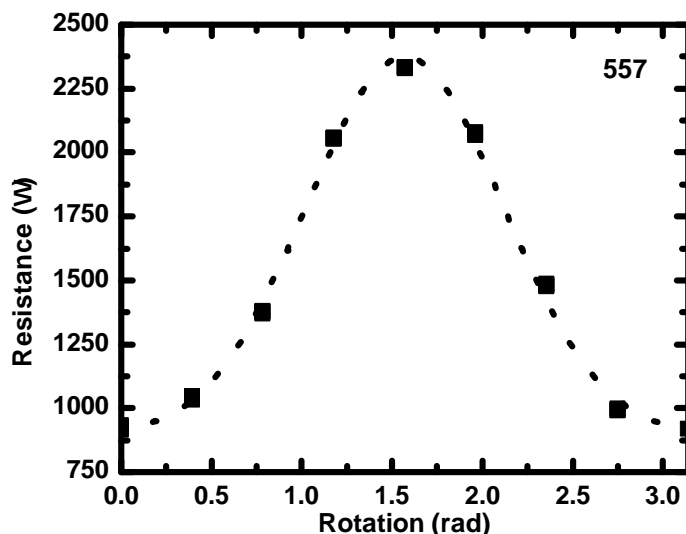


Figure 7.12: Resistances measured on the Si(557)-Au using the rotation square method. Measurements were performed on low n-doped samples with $\rho = 1700 \Omega\text{cm}$. The dashed line is a fit to the experimental data leading to a conductivity value of $\sigma_{\parallel} = 99.7 \mu\text{S}/\square$ parallel to the wires and $\sigma_{\perp} = 51.9 \mu\text{S}/\square$ ($\sigma_{\parallel}/\sigma_{\perp} \approx 1.9$).

along the $[11\bar{2}]$ -direction of the Si(557)-Au and the Si(553)-Au surface are due to a different origin in the LEED images. The $\times 2$ -streaks for the Si(553)-Au are ascribed to the double periodicity within the gold chains along the $[1\bar{1}0]$ -direction [179, 186], whereas the $\times 2$ -streaks seen for Si(557)-Au surface originate from the Si-adatoms [28, 162, 189]. It will be shown in the following sections that the additional Si-adatom chain has severe impact on transport properties in combination with surface defects.

Though the transport characteristics of the Si(553)-Au and Si(557)-Au are very comparable for the pristine surface, and despite the structurally similar building blocks, the surfaces Si(553)-Au and Si(557)-Au behave very differently upon the adsorption of molecular oxygen. The oxygen dosage experiments presented in the following were performed at a background pressure of 5×10^{-9} mbar at 300 K. The cross-section for electron-beam induced dissociation by the electron beams of LEED and SEM turned out to be so low that no effect was detected, as explicitly tested separately by adsorption experiments performed with blanked beams.

Figure 7.13 shows the LEED patterns of pristine Si(553)-Au and Si(557)-Au before (a,c) and after (b,d) the adsorption of 20 L. For both substrates the periodicity of the step train is unchanged upon adsorption. Remarkably, however, the $\times 2$ streaks induced by the dimerization of the Au chains on Si(553)-Au, are very little affected by oxygen adsorption, while these streaks in case of Si(557)-Au have completely vanished, as demonstrated by figure 7.14, which shows the normalized peak intensity of the $\times 2$ -spot as a function of the oxygen dose. Already after a dosage of 5 L the long-range order along the Si-adatoms is entirely destroyed. Assuming that the ordering for LEED is effectively destroyed if every second Si-dimer is occupied

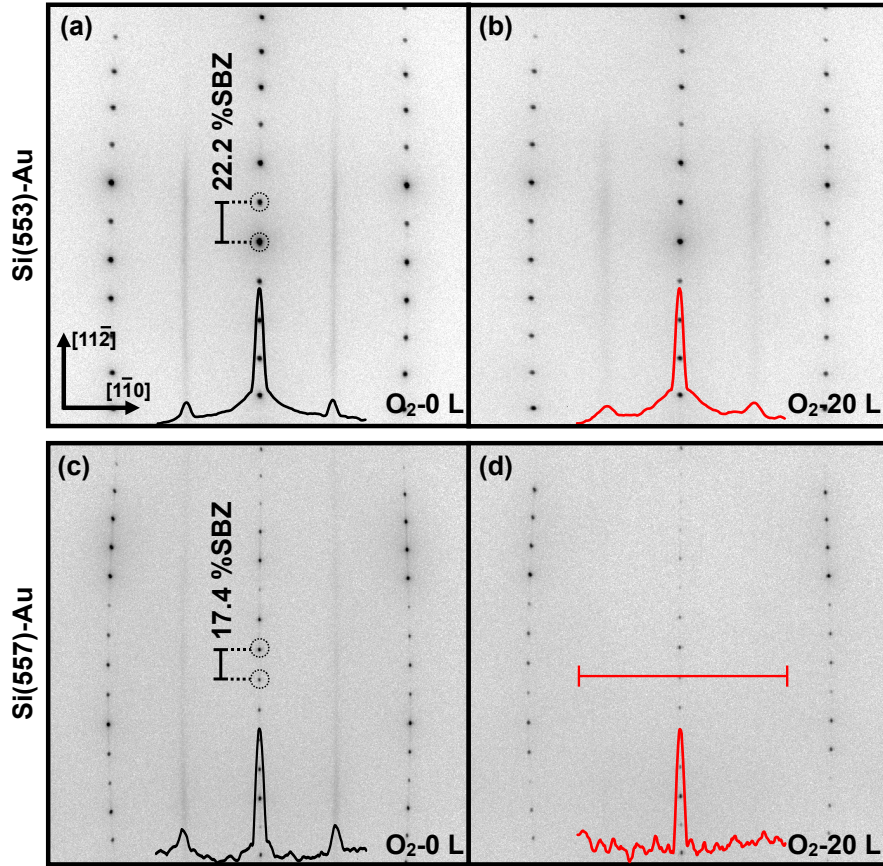


Figure 7.13: SPALEED patterns of Si(553)-Au and Si(557)-Au surfaces before (a,c) and after (b,d) exposure to 20 L of molecular oxygen (Electron energy 138 eV). Horizontal lines indicate where the line scans, shown at the bottom, were taken.

(on average), it can be deduced that the sticking coefficient is in the order of 10-20 %. Within the data acquisition time for LEED, the dose is around 0.2 L, i.e. five events of chemisorption take place within the transfer width of the used LEED system. The linear increase of the background, also shown in the inset, is indicative for a random adsorption. The fact, that the background increases even further shows that other sites become occupied by oxygen as well ³.

Figure 7.15 now shows the two conductivity components (σ_{\parallel} , σ_{\perp}) as a function of the oxygen dose for the Si(553)-Au (a) and Si(557)-Au (b) reconstruction. Apparently, the conductivity along the atomic chains is affected by O_2 adsorption more strongly than σ_{\perp} . Moreover, while σ_{\parallel} for Si(553)-Au is reduced only by 5 % after 30 L, leaving the sample anisotropy almost intact, the parallel conductivity of Si(557)-Au decreases by 20 % after the same exposure, and makes the initial transport anisotropy disappear.

Before the decay mechanisms along the wires is analyzed in more detail, the σ_{\perp} component

³As presented later in this section, additional DFT calculations confirm that the dissociative adsorption of molecular oxygen takes place selectively at the Si-adatom and rest-atom sites which has direct consequences for the electronic transport.

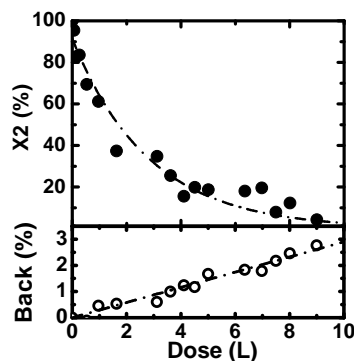


Figure 7.14: The oxygen induced gradual decrease of the $\times 2$ peak intensity and the linearly increasing background as a function of oxygen dose.

will be briefly discussed. This part of the conductivity for the Si(553)-Au system remains constant (cf. figure 7.15(a)), at least within the scatter of the data. In contrast, the corresponding component for Si(557)-Au reveals a small conductivity drop of around 3% of the overall background signal until an O_2 -dose of 2.5 L is reached, before the conductivity slowly recovers towards its original value. This tiny but measurable effect is ascribed to a modification of band bending upon oxidation and consequently of σ_{SCL} , which is strongest upon adsorption of roughly half of the reactive adsorption sites. For higher coverages the effect starts to be compensated due to competing adsorbate-adsorbate interactions. Within this simple model, the 2.5 L would nicely corroborate the saturation dose of around 5 L seen in LEED for the annihilation of the $\times 2$ reconstruction on Si(557)-Au.

Based on the separation of isotropic (bulk-like) and anisotropic surface contributions, the procedure previously described in section 6.4.2 of chapter 6 about the analysis of oxygen adsorption on In/Si(111)-(4 \times 1) is adopted. Thus, the change of the conductivity as a function of the oxygen dose D is well described via equation (6.4.2). Using this approach, the transport through the bulk is covered by σ_{SCL} , which is almost constant during the dosage with molecular oxygen. In contrast, $\sigma_{\parallel}(0)$ denotes the surface transport along the wires. Thereby, both adsorption-induced changes of the band structure as well as changes of the lattice periodicity, giving rise to hopping transport, are subsumed by this contribution. Albeit this is a simple approach, it rather well describes the transport findings, i.e. that the Si(hhk)-Au surfaces comprise differently reactive sites.

It will be shown in the following by DFT calculations that the oxygen adsorption alters the band structure. In principle, defect-mediated transport across defects could be considered as well. However, the transport in the direction across the wires is rather independent to the adsorption, thus oxygen induced hopping across the wires can be neglected. From figure 7.15(a) it is obvious that the impact of oxygen on Si(553)-Au for the conductivity along the wires is quite small. Extrapolating the data with the above mentioned approach yields an approximate value of $D_0 \approx 200$ L. The same approach used for Si(557)-Au (cf. with black dashed line in figure 7.15(b)) is only able to fit at best the behavior in the high dosage regime (≥ 10 L). The fitting curve obtained for $\sigma_{\parallel,(553)}$ is also plotted in figure 7.15(b) in order to show that the high dosage regime indeed reveals a similar dependence of conductance on oxygen exposure for both surfaces, possibly to due the reaction of oxygen at common

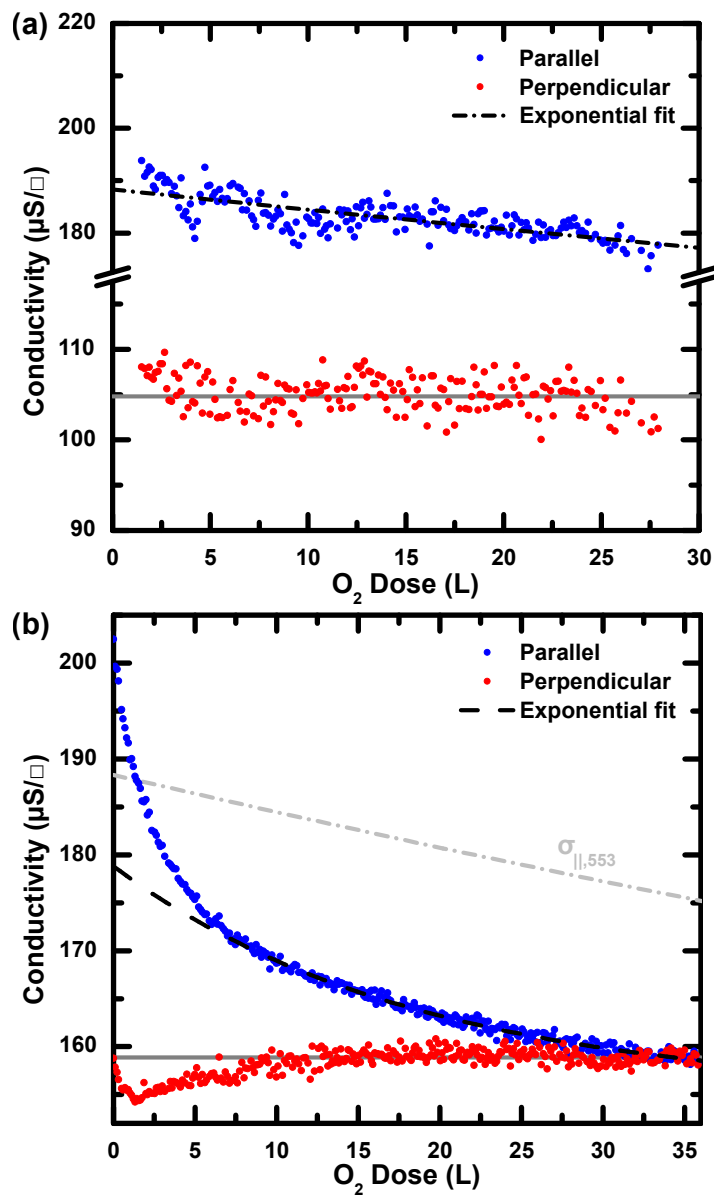


Figure 7.15: Conductivity along (σ_{\parallel} , blue) and perpendicular (σ_{\perp} , red) to the wire directions as a function of the O_2 dose D for Si(553)-Au (a) and Si(557)-Au (b). The dashed and dashed-dotted curves are exponential fits to the conductance on the Si(557)-Au and Si(553)-Au surfaces, respectively.

structural motifs, e.g the Si-HCs. Noticeably, the initial part of $\sigma_{\parallel,(557)}$ cannot be described by such an ansatz. Thus, as it will be shown in the following discussion, this deviating behavior is due to the presence of the Si-adatoms on Si(557)-Au and the oxygen reaction with them.

7.4.1 DFT results

In order to rationalize and interpret the experimental findings, in cooperation with the university of Paderborn (SCHMIDT GROUP) DFT calculations were performed within the generalized gradient approximation (GGA) using the PBE functional [190]. The electron-ion interaction was modeled within the projector augmented wave (PAW) method [191] as implemented in the Vienna Ab initio Simulation Package (VASP) [192]. An energy cutoff of 410 eV and a k -point mesh of $2 \times 9 \times 1$ were utilized to determine the structurally relaxed ground-state configurations. The Si surfaces were modeled within periodic super cells, which contain a material slab of six essentially bulk-like Si bilayers plus a surface layer containing Si and Au surface atoms as well as adsorbed O species. The opposite side of the slab was terminated with atomic hydrogen. The lowest two bilayers were fixed in ideal bulk positions during the structural relaxation, while all other atoms were allowed to relax. The adsorption energies were calculated by positioning O₂ molecules in various starting configurations on specific lateral surface sites of the relaxed Si(hhk)-Au surface. Thereby the system was relaxed under the constraint that the lateral position of one oxygen atom remained fixed. Subsequent calculations for the energetically most stable adsorption sites on the potential energy surfaces without any structural constraints were used to determine the most favorable O adsorption geometries. These calculations provided the input for band structure calculations that allow for an interpretation of the experimental data. Figure 7.16(a) and (c) show the adsorption energies for molecular oxygen adsorbed dissociatively on clean Si(557)-Au and Si(553)-Au at various lattice sites, respectively. In total 90 and 72 different sites within the unit cells of Si(557)-Au and Si(553)-Au were probed.

It turns out that O adsorption at the Au sites is unfavorable for both surfaces. This is particularly pronounced in case of Si(553)-Au. Oxygen clearly prefers to attack the Si-adatom and the Si-HC sites. This site-specific adsorption behavior for oxygen already explains the changes of the LEED patterns and disappearance of the $\times 2$ diffraction spots for Si(557)-Au upon adsorption, discussed in context with figure 7.13. Comparing the different Si adsorption sites on Si(557)-Au, the Si-HC site is less favorable by around 250 meV compared to Si-adatoms. The corresponding adsorption geometries for these two preferred adsorption sites are shown in figure 7.17(a) and (b). The detailed analysis of seven different geometries in total showed that the configuration shown in panel (a) is energetically most favorable but nearly equivalent to a scenario, where the oxygen occupies slightly different adsorption sites around the Si-adatoms. Concluding, a site-specific reaction of oxygen with the Si(557)-Au surface at the Si-adatoms is seen in DFT, but with randomly oriented SiO-complexes destroying long-range order of the former Si-adatom structure.

The following part will concentrate specifically on the oxidation of Si(557)-Au surface in terms of the possibility of subsequent oxidation processes. Figure 7.16(b) shows the corresponding potential energy surface for a second step of oxidation (for guidance, the initial configuration of the pre-oxidized Si-adatom sites is superimposed). Compared to the pristine

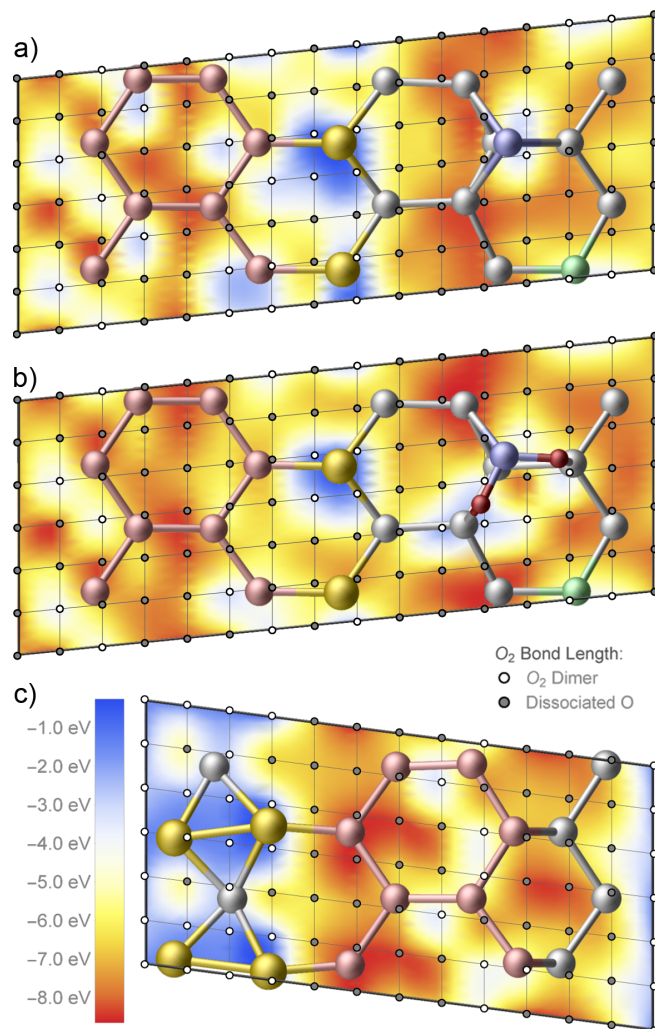


Figure 7.16: Calculated adsorption energies for O₂ adsorption within the unit cells of Si(557)-Au (a) and Si(553)-Au (c). The adsorption energies in (b) for Si(557)-Au were determined with initial oxygen precoverage on the Si adatoms, indicated by red balls (see text). Tested adsorption sites of O₂ are shown as small circles. Filled circles on the grid indicate where dissociative adsorption occurs spontaneously. The superimposed crystal structures refer to the structures of the clean (a,c) and pre-oxidized surfaces (b) and illustrates the preferred adsorption sites. Au, O, Si-HC, and Si- adatoms are marked by yellow, red, orange and blue colors, respectively. The color coding of the energies is obtained by nonlinear bicubic interpolation.

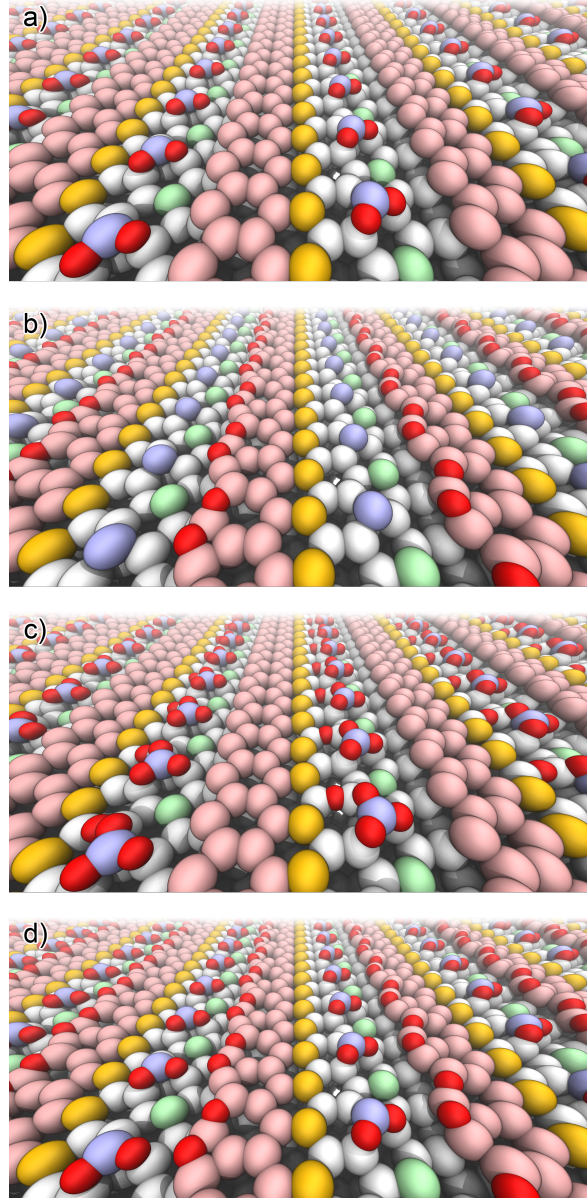


Figure 7.17: Different models for the dissociative adsorption of molecular oxygen on Si(557)-Au. (a) Oxygen (dark red balls) bound to the Si-atom (light blue) and rest-atom sites (light green). (b) Oxygen adsorption at the step edge of the Si-HC structure (light red). (c) Further oxidation of the configuration shown in (a), where oxygen is now adsorbed next to Si rest-atoms (green). (d) Alternative model for a two-fold oxidation process, which is energetically less favorable by around 500 meV compared to (c). However, in contrast to (c), both transport channels are affected by oxygen adsorption.

Si(557)-Au surface, the barriers for further adsorption at the Si-HC site, in proximity to the oxidized Si-adatoms, is slightly increased. A likely configuration is shown in figure 7.17(c) and energetically favored by at least 500 meV compared to configurations, where the two oxygen atoms of a molecule bind to different Si-sites, e.g. to Si-adatoms and Si-HCs, as shown in figure 7.17(d).

The corresponding band structures for Si(557)-Au in comparison to Si(553)-Au are shown in figure 7.18. Panels (a/b) and (e/f) show the surface bands for the respective clean surfaces. As obvious, there are two bands crossing the Fermi energy E_F . Thereby, the green-colored band is induced by the Si rest-atoms while the redish-colored band stems mainly from the Si-HC step edge atoms. The Si-adatoms give rise to the dispersing unoccupied band shown in blue. In figure 7.18(c), the Si(557)-Au band structure after oxidizing the Si-adatoms and rest-atoms is shown (cf. corresponding schematic 3D sketch in figure 7.17): The former band of the Si-adatoms (blue) shows strong admixtures of oxygen orbitals, coming along with localization. Additionally, the metallic band originating from the Si rest-atoms is slightly shifted to higher energies and the electron effective mass at the Fermi energy increases by 13%. Thus the conductivity along the wire direction should be reduced. The electronegativity of the oxygen atoms obviously depopulates the bands associated with the rest-atoms. Redistribution of charges associated with the oxidation process are the reason for formation of further surface dipoles which change the work function, as discussed in context of σ_{\perp} for Si(557)-Au (cf. figure 7.15(b)). In contrast, the band originating from the Si-HC shows a weak anti-crossing feature, but remains essentially unchanged. It should be highlighted that the calculations were performed in the high coverage regime, where each of the Si-adatoms and Si-restatoms sites are covered by oxygen. Therefore, particularly in the low oxygen coverage regime, the mobility along the wires is expected to be further reduced by scattering at oxygen defects.

The band structure after the second step of oxidation depends crucially on details of the adsorption geometry. For instance, the bands for the energetically most favorable geometry, shown in figure 7.17(c), look rather similar to those obtained after the first oxidation step. In contrast, the scenario presented in figure 7.17(d) shows the strongest modifications in the band structure by opening an electronic gap of around 100 meV at E_F . Of course, if the conductivity along the surface band channels is entirely disabled the anisotropy should vanish, similarly to the situation shown in figure 7.15(b). Albeit the theoretical calculations for the ideal surfaces revealed that the configuration shown in figure 7.17(d) is slightly less favorable than the geometry of panel (c), a reaction of these sites could be effectively triggered by surface defects. For instance, in case of water adsorption, STM revealed the occupation of Si-HC sites [158].

Obviously, the oxygen-modified electronic band structures discussed above describe only part of the influence of oxygen on the electron transport properties. For example, potential-well scattering can be expected to play an important role as well [146]. Nonetheless, the DFT analysis showed that the Si(557)-Au and Si(553)-Au surfaces host differently reactive adsorption sites. Moreover, the Si(557)-Au provides two reactive transport channels made up by Si-atoms. For comparison, the metallic bands for the Si(553)-Au surface stem mainly from the Au-atoms [28]. The Si-HC band in this system is energetically slightly below E_F , similarly to the result obtained for Si(557)-Au, shown in figure 7.18(a). Therefore, oxygen adsorption at the Au sites is expected to yield the largest impact on transport in this system. However, since the Au-strands are chemically inert, oxidation should have only a small influence on

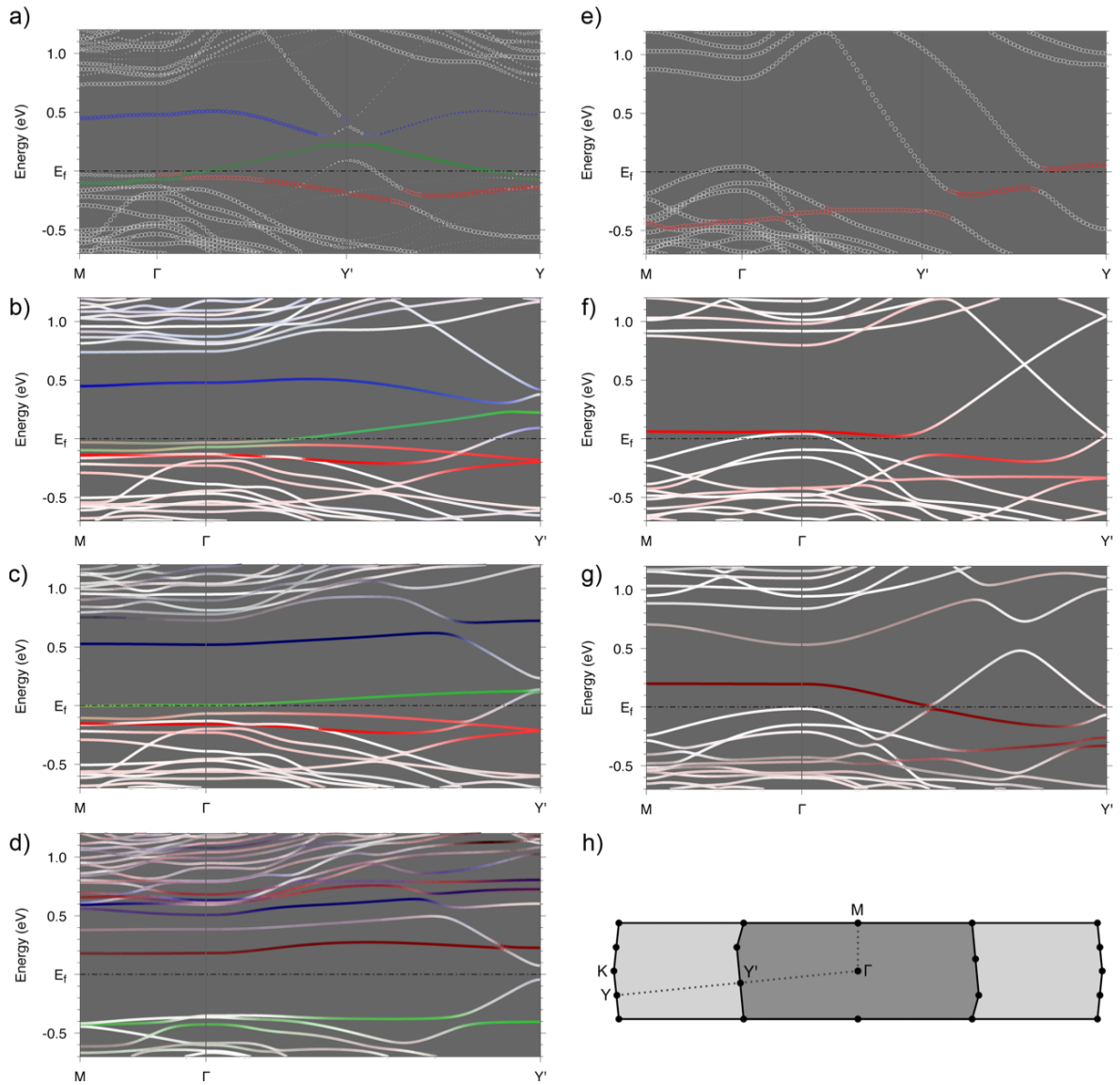


Figure 7.18: Band structures for Si(557)-Au and Si(553)-Au. Unfolded/folded ($\times 2$) band structures for clean Si(557)-Au and Si(553)-Au surfaces are shown in (a/b) and (e/f), respectively. The point sizes in the unfolded bands structures (a) and (e) indicate the (5×1) character of the respective state, cf. [193]. Band structures for oxidation of Si(557) Si-atom sites (cf. figure 7.17(a)) and Si-atom and rest-atom sites (cf. figure 7.17(d)) are shown in (c) and (d), respectively. The band structure of Si(553)-Au, where oxygen is built into the Si-HC site, is shown in (g). The notation of the high-symmetry points is explained in (h). The colors of the surface bands denote their spatial localization: Si adatom (blue), Si rest-atom (green), Si step-edge atoms (red). Dark blue (b,c) denotes the admixture of oxygen orbitals upon adsorption.

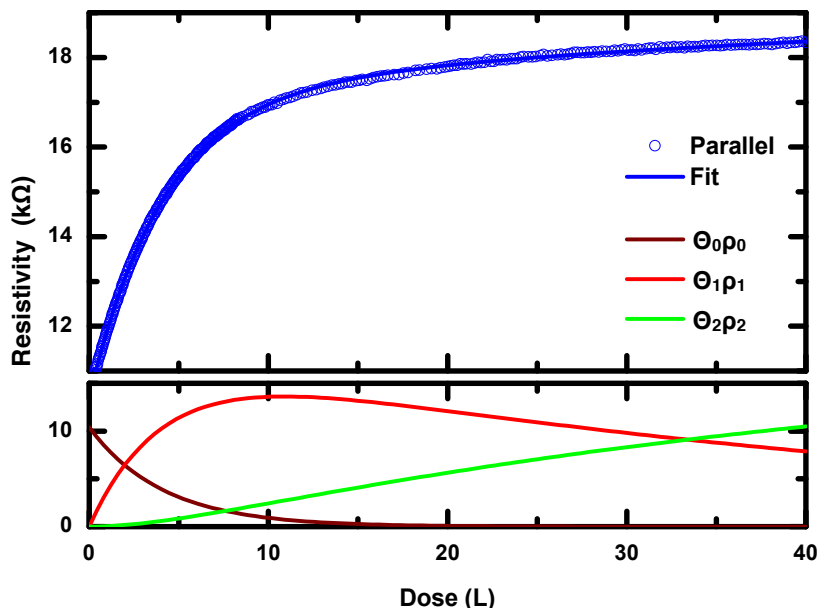


Figure 7.19: Resistivity along the wires for Si(557)-Au as a function of oxygen dose. The solid line is a fit to the data. The lower part shows the weighted contributions of the uncovered (brown curve, $\Theta_0\rho_0$), oxidized (red, $\Theta_1\rho_1$) and subsequent-oxidized fraction (green, $\Theta_2\rho_2$).

transport. In fact, the calculated band structures in figure 7.18(f) and (g) show that oxidation of the Si-HC site at the Si(553)-Au surface essentially shifts the Si step edge states by about 0.1 eV, but has only a minor influence on the strongly dispersive Au states. Also in case of Si(557)-Au it is found that the effect of the oxidation is stronger for the Si than for the Au states. Since the Si-atom chain, that does not exist on Si(553)-Au, is also metallic on Si(557)-Au, the largest change in transport is due its oxidation.

7.4.2 Quantitative analysis of the transport data

It was shown before, especially the Si(557)-Au is rather sensitive to adsorption of molecular oxygen. DFT revealed two transport channels, which originate primarily from different Si-atom reconstructions. The reduction of the surface state conductivity is mainly described by the change of the conductivity in each of the channels. Nonetheless, from an energetic point of view, theory showed that the oxidation of the Si-atom chain influences the adsorption energy of the Si-HC site, which may give rise to a subsequent oxidation procedure.

In the following, a model will be briefly presented for describing the shown transport data. For a full derivation, the reader is referred to the appendix B. Notably, although theory showed that the energy differences are small compared to the adsorption energies, this effect is included into the modeling. Therefore, the relative coverages on each of the transport channels are not entirely independent.

In the following, Θ_0 , Θ_1 and Θ_2 denote the relative fractions of free, oxidized and subsequent-oxidized sites on the Si(557)-Au surface, respectively. Additionally, it is assumed that the subsequent-oxidation step occurs only if Θ_1 is already nonzero. If the background pressure

p of oxygen (mass m) is kept constant during the experiment, the increase of subsequent-oxidized sites per time is given by $\dot{\Theta}_2 = C_1\Theta_1$. Accordingly, the rate for the increase of the singly-oxidized states reads

$$\dot{\Theta}_1 = C_0\Theta_0 - \dot{\Theta}_2. \quad (7.4.1)$$

The C_i 's are constants and comprise details about the sticking coefficients. Within the model of Langmuir adsorption, assuming first order adsorption kinetics, i.e. no diffusion of the oxygen atoms after dissociation, the constants read

$$C_i = c_i \exp(-E_a^i/k_B T) \sqrt{p/2\pi m k_B T}, \quad (7.4.2)$$

where the c_i 's and the E_a^i 's denote the condensation coefficients and energy barriers for adsorption, respectively [79, 194, 195]. The combination of both rate equations leads to a second order linear differential equation. Based on this subsequent oxidation model the number of doubly oxidized sites follows

$$\Theta_2(t) = \frac{C_0 - C_0 \exp(-C_1 t) + C_1(\exp(-C_0 t) - 1)}{C_0 - C_1}. \quad (7.4.3)$$

Finally, based on the above mentioned equations, also $\Theta_0(t)$ and $\Theta_1(t)$ can be determined.

Assuming that during each oxidation step the initial resistivity ρ_0 is sectionally modified, the overall resistivity ρ along the wires can be described via

$$\rho = \Theta_0\rho_0 + \Theta_1\rho_1 + \Theta_2\rho_2, \quad (7.4.4)$$

where the resistivity for the clean surface and the resistivities after the first (ρ_1) and second step of oxidation (ρ_2) are weighted by the number of available sites. Figure 7.19 shows the change of the resistivity as function of the oxygen dose. In addition, also the individual components are plotted. While the contribution $\Theta_0\rho_0$ gradually decreases the other two oxidized states mutually increases. Thereby, the first oxidation dominates the initial increase of the resistivity, while the high dose regime is dominated by the subsequent oxidation.

According to this model the increase of the resistivity due to oxidation at beginning of the dosing experiment can be approximated by (time t equivalent to dose D if $p = \text{const.}$)

$$\Theta_1\rho_1 \approx 1 - \exp(-C_0 D). \quad (7.4.5)$$

The value of $D_0 \equiv 1/C_0 = 4.1 \text{ L}^{-1}$ is in good agreement with the decay constant found independently in the LEED experiment for the $\times 2$ -reflexes. The corresponding contribution to the resistivity for an independent oxidation in the high coverage regime was shown and discussed by the dashed line in context of figure 7.15(b).

7.4.3 Summary and conclusions on the adsorption process

The SPALEED, transport and DFT study on Si(553)-Au and Si(557)-Au elaborated in detail the effect of oxygen adsorption. Most strikingly it was shown that the origin for the metallic surface bands along the wires are of different origin. While the Si(553)-Au surface turned out to be rather inert against oxidation, the Si(557)-Au surface revealed a strong decrease of the conductance, which comes along with the complete destruction of the Si-adatom ordering

along the chains. The DFT calculations were performed in the limit of high oxygen coverage and showed the reduction of charge carrier density and an increase of the effective masses – and unambiguously confirmed – the different orbital characters and reactivity of the transport channels. Any additional effects, e.g. due to disorder, were not covered by the calculations. Moreover, by high resolution transport measurements a subsequent oxidation for Si(557)-Au was resolved. However, as motivated in section 7.5.1 the surface transport comes along with a strong isotropic bulk contribution, which depends on the preparation and is limited by the resolution of the technique. Thus, high resolution STM experiments should be performed in future in order to support the structural models for adsorption further and to elucidate in more detail any subsequent oxidation steps on these heterogeneous surfaces. Nonetheless, the investigation showed that the 1D transport channels, realized by Si(hhk) surfaces with quite similar structural elements, have different origins. But utmost, it remains difficult to generalize the impact of other adsorbates.

7.5 Probing the phase transition by transport experiments

The Si(hhk)-Au reconstructions show a structural phase transition in temperature dependent measurements. As motivated in the introduction of this chapter and in chapter 2, those transitions are of special interest and still not completely understood until now. The structural phase transitions of Si(553)-Au and Si(557)-Au were observed in multiple experimental studies. However, questions arise *how this is linked to the electronic transport?* and *how defects will feedback to the transition?*. All previous temperature dependent transport studies in literature [71, 188] on Si(hhk)-Au were performed using a *co-linear* 4pp approach. As it was discussed in chapter 5, such transport experiments on anisotropic samples always average the conductivity components and thus no direct conclusion can be drawn for transport behavior along the chains. Hence, in view of the contribution of an isotropic SCL, anisotropic surface states and possibly a close entanglement of intra- and interchain interactions, further directional-dependent measurements of the structural and electronic behavior, which are sensitive to defects, are necessary using a 4pp square configuration. Therefore in this section, the temperature dependence will be investigated using the 4pp rotational square method which allows the correlation of the temperature details of the phase transition with the conductivity components along and perpendicular to the atomic wires. A special focus is set on the Si(553)-Au surface. In addition, the structural transition will be characterized in detail by high resolution SPALEED.

Since, the contribution of the SCL and the understanding of its influence within measurements is crucial for the interpretation of the following temperature dependent transport data, this section will first of all discuss SCL related effects before describing the measured phase transition in detail.

7.5.1 Influence of the space-charge layer

ARPES data, as exemplarily shown in figures 7.4 and 7.7, reveal quasi-1D Fermi surfaces. Hence large anisotropy values are expected only if surface bands provide the transport channels [81]. It was motivated before in chapter 6 that the finite resistance measured along the $[11\bar{2}]$ -direction perpendicular to the atomic chains must be triggered by defect-induced

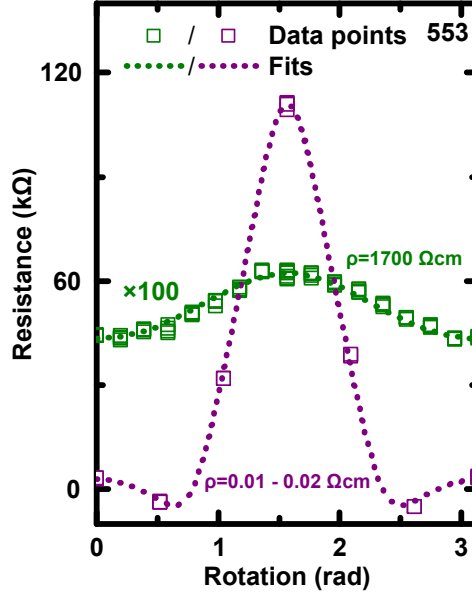


Figure 7.20: Comparison of measured resistances using the rotational square method. Purple data points correspond to measurements performed on high n-doped samples with $\rho = 0.01 - 0.02 \Omega\text{cm}$ while the green data corresponds to measurements performed on samples with $\rho = 1700 \Omega\text{cm}$ as shown before in figure 7.11. Dashed and dotted lines are the corresponding fits.

modifications of the Si bulk bands.

As it turns out by the measurements of this thesis, the influence of the SCL on the transport data can not be neglected for the Si(hhk)-Au systems. Figure 7.20 shows the transport data of a rotational square measurement performed on a Si(553)-Au reconstruction. Here, the purple data shows the resistance of the Si(553)-Au reconstruction measured on a highly doped ($\rho = 0.01 - 0.02 \Omega\text{cm}$) sample in comparison to transport data measured on low doped sample ($\rho = 1700 \Omega\text{cm}$). It needs to be highlighted that LEED revealed completely identical surface reconstruction for both measurements in figure 7.20. Thus, the difference in resistances has to be related to the sample doping, i.e. SCL. Notably, a negative resistance is measured for certain angles which is expected for high anisotropic surfaces and generally explained by a deformation of the electrostatic potential contours (cf. further remarks in section 5.2). The dotted purple line is the best fit using (5.2.1) and reveals a conductivity of $\sigma_{\parallel} = 15 \mu\text{S}/\square$ along the chains and $\sigma_{\perp} = 0.97 \mu\text{S}/\square$ in perpendicular direction. It is striking that in comparison to the data in figure 7.11, which was measured on a low doped sample, the conductivity components of the highly doped samples are of 1-2 orders lower than the values for the low doped samples. They are also showing a higher conductivity ratio of $\sigma_{\parallel}/\sigma_{\perp} \approx 15.4$. Further transport studies [71, 115, 188] on Si(hhk)-Au systems performed on samples with an intermediate doping ($\rho = 1 - 10 \Omega\text{cm}$) are revealing conductivities following the trend of previously reported values. The apparent relation between measured conductivities and sample resistivity or the conductivity ratio, respectively, is illustrated in figures 7.21(a) and 7.21(b).

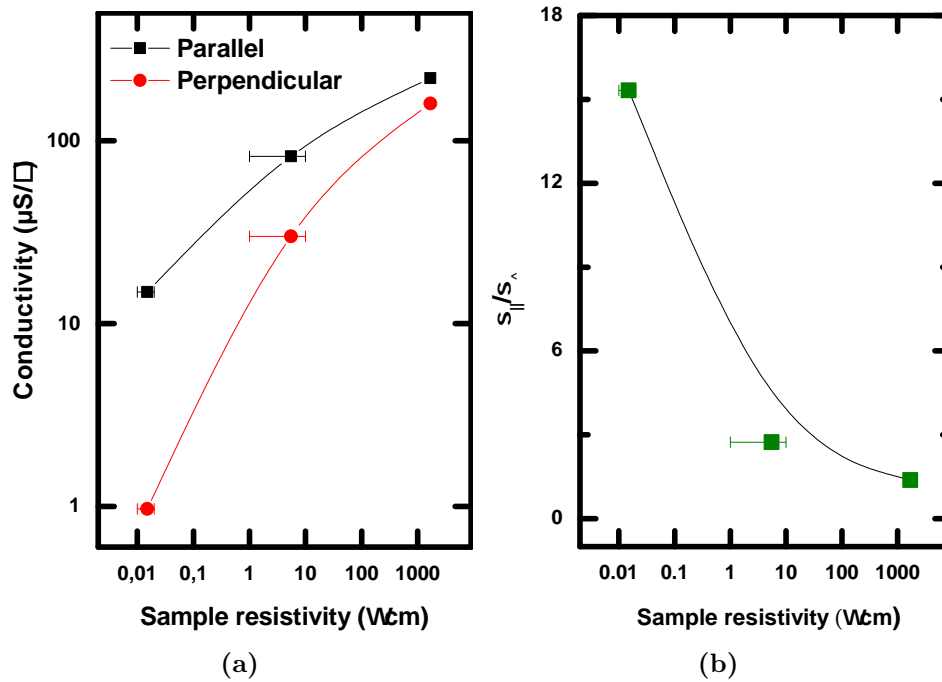


Figure 7.21: (a) Conductivity σ_{\parallel} and σ_{\perp} of the Si(553)-Au as a function of the sample resistivity (n-doped by phosphor). (b) Typical anisotropy ratios as a function of the sample resistivity (n-doped by phosphor). Values for a resistivity of 1 – 10 Ωcm were taken from [71, 115, 188]. The lines are a guide to the eyes.

At first glance, it may seem to be puzzling that the conductivity in both components decreases as the doping of the bulk increases. However, this effect can be qualitatively rationalized as follows. A SCL forms due to Fermi-level pinning by the surface state (cf. the introduction to the formation of SCL in section 2.3). Moreover, it is known from literature [84–86, 129] that flash annealing of n-doped semiconductors leads to irreversible changes of the doping in terms of type and concentration at the surface resulting in the formation of a p-type layer at the surface which is especially severe for low doped samples. The formation of the p-type layer below the surface (cf. figure 2.5) is attributed to be either a B diffusion (coming from Borosilicate parts in ultra-high vacuum (UHV) components or from glass beakers in the Si cleaning process [85]) or C contaminations, which are resulting in interstitial defects [84]. This effect is especially distinct and effective for high flash annealing temperatures greater than 1150 °C resulting in an increase of the SCL contribution [129]. Therefore, high temperature annealing steps were not applied and all the samples were prepared with maximum flash annealing temperatures of 1150 °C. Nonetheless, even by reduced temperatures a change of the SCL by every flash annealing step can not be inhibited as shown in the following.

The increase of the SCL as a result of the flash annealing times is exemplarily shown in figure 7.22. In this figure, the conductivity perpendicular to the atomic chains, which is mainly given by the SCL contribution, is plotted for five different samples as a function of the total flash annealing cycles during sample preparation. The plot shows that the perpendicular conductivity increases in average by 2.6 $\mu\text{S}/\square$ per flash annealing for low doped

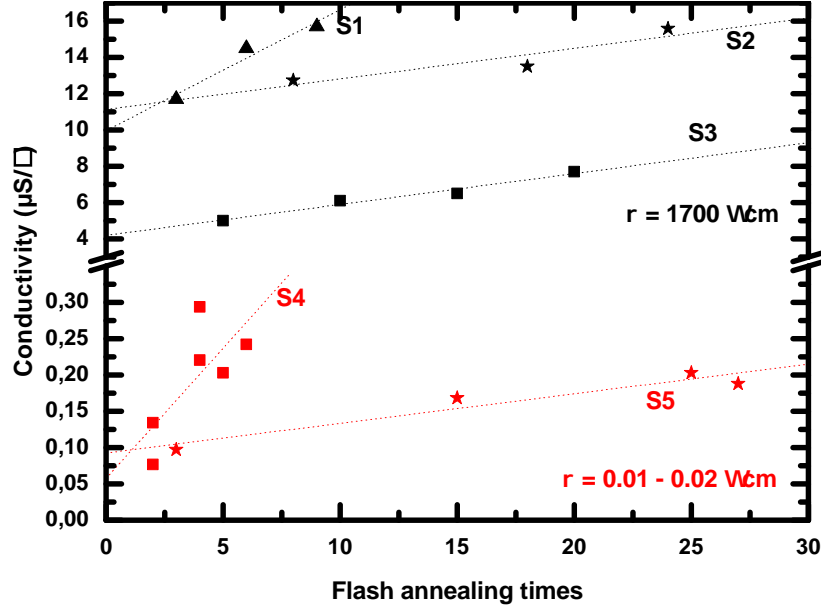


Figure 7.22: Conductivity (σ_{\perp}) measured along the $[1\bar{1}0]$ direction as a function of the flash annealing cycles. Different symbols refer to different samples. Data points in black color were measured on samples with $1700 \Omega\text{cm}$ while red data points refer to samples with $\rho = 0.01 - 0.02 \Omega\text{cm}$. The dotted lines are fits to the data. The averaged (over S1, S2 and S3) increase of conductivity per flash annealing step was on the low doped ($\rho = 1700 \Omega\text{cm}$) samples $2.6 \mu\text{S}/\square$. The averaged (over S4 and S5) increase on the highly doped ($\rho = 0.01 - 0.02 \Omega\text{cm}$) samples was $0.9 \mu\text{S}/\square$ per flash annealing step.

samples ($\rho = 1700 \Omega\text{cm}$) and just by $0.9 \mu\text{S}/\square$ per flash annealing for highly doped ones ($\rho = 0.01 - 0.02 \Omega\text{cm}$). It seems apparent that low doped samples are much more sensitive to high temperature in-situ flash annealing cycles.

As motivated in section 2.3, the spatial extent of a SCL is characterized by the so-called Debye length λ_{D} (cf. equation (2.3.10)). The dopant concentration for the low doped ($\rho = 1700 \Omega\text{cm}$) samples is $N_{\text{D}} \approx 3 \cdot 10^{12} \text{cm}^{-3}$. In contrast, the dopant concentration for the highly doped ($\rho = 0.01 - 0.02 \Omega\text{cm}$) samples is $N_{\text{D}} \approx 5 \cdot 10^{18} \text{cm}^{-3}$. The corresponding Debye lengths for this idealized scenario are $2.4 \mu\text{m}$ and 1.8nm , respectively⁴. Due to the high dopant concentration in the highly doped samples and a comparatively small Debye length, the electrons are confined in a very small near-surface area as schematically depicted in figure 7.23(a). Thus, they are more affected by scattering at ionized bulk donors within transport than for the case of low doped samples with a large λ_{D} resulting in overall lower conductivities. Notably, there is a difference of two orders of magnitude in the perpendicular direction to the chains while comparing the conductivity of the low and highly doped samples. However, there is only one order magnitude difference for the parallel direction which leads to high anisotropy ratios $\sigma_{\parallel}/\sigma_{\perp}$ for the highly doped samples. The conductivity perpendicular to the chains is mostly attributed to the SCL. Nonetheless, perpendicular to the chains there are also surface steps. The large anisotropy ratio for the case of highly doped samples

⁴Assuming a relative permittivity of the semiconductor bulk of $\epsilon_{\text{B}} = 11.8$.

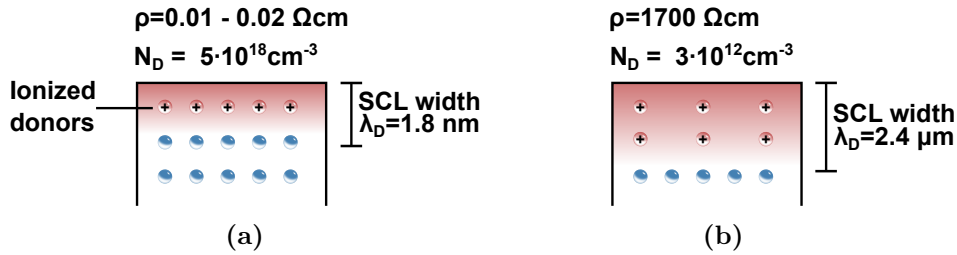


Figure 7.23: Schematic drawing of the SCL illustrating the different dopant concentrations ((a) highly doped sample vs. (b) low doped sample).

is explained by the strong confinement of the electron gas near the surface steps which increases the scattering of the electron gas at the step edges. Correspondingly, for the low doped samples the confinement is three orders less and thus the electrons suffer less scattering.

One result of chapter 4 was that it is possible to distinguish the dimensionality of an electron gas by the probe distance behavior (see exemplarily the distance dependence in table 4.1). Another result of section 4.2 was that a layer with a finite thickness can be approximated by a quasi-2D sheet as long as the probe distance is approximately one fifth of the layer thickness. Hereby, it is possible to roughly estimate the thickness of the SCL by varying the probe distance. Figure 7.24 depicts the distance dependence of the resistance perpendicular to the chains measured on two equally prepared low doped ($\rho = 1700 \Omega\text{cm}$) samples. For probe spacings larger than $30 \mu\text{m}$ no variation of the resistance is observed. The resistance is constant as expected for the transport behavior of a 2D sheet. The absolute values for the two samples differ slightly due to different flash annealing cycles and defect concentrations. Notably, there is a sharp drop observable for probe distances $< 30 \mu\text{m}$. Thus, the thickness of the SCL is roughly estimated by results of section 4.2 to be at least $6 \mu\text{m}$ for the samples with $\rho = 1700 \Omega\text{cm}$ ⁵. Unfortunately, the expected 3D behavior for smaller probe spacings, which is presumed to start after the drop of resistance, could not be resolved during the measurements with the probes available. The guide of the eye in figure 7.24 depicts the expected trend.

The thickness of the SCL, which was estimated from the experiment, deviates by 25 % from the calculated Debye length. However, as pointed out before, flash annealing of low doped n-type samples leads to a strong transformation of the doping to a p-type layer for areas near the surface. Apparently, at least up to $6 \mu\text{m}$ a p-doped area is formed which contributes to the SCL (cf. also discussion of the temperature dependence in transport experiments in section 7.5.2).

Further interpretation of figures 7.21 and 7.22 lead to the conclusion that it is better to perform transport measurements on highly doped samples rather than on low doped ones, since the contribution of the SCL is reduced and since there is a larger difference in the conductivity values for the parallel and perpendicular direction and the highly doped samples are less affected by flash annealing cycles. However, it turns out during the experiments of this thesis that samples with a small SCL and confined p-type layer suffer a lot from scattering and defects in the atomic chains. To achieve reliable (linear) IV curves is a very tedious task in contrast to measurements on low doped samples with a larger SCL contribution.

⁵This approximation assumed a linear probe alignment. The correction factor of a square probe alignment [196] is approximately two times bigger than the linear case which lead to a slightly bigger estimate.

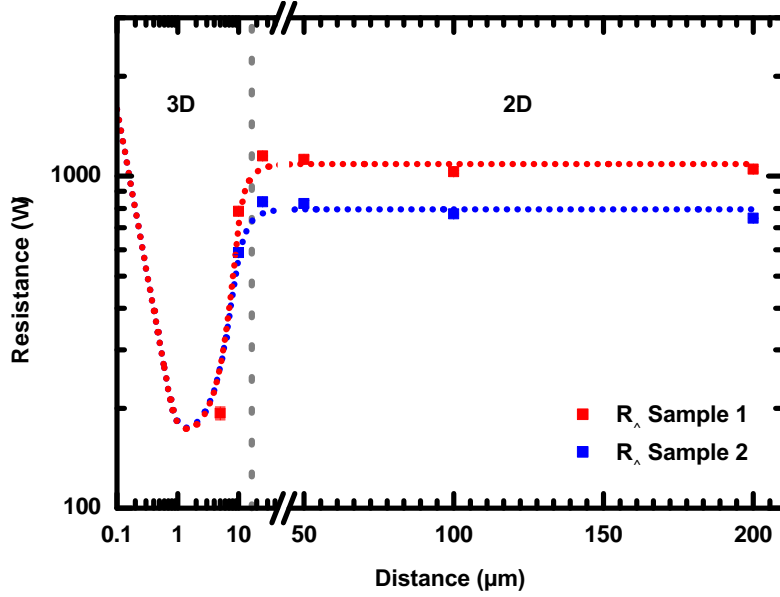


Figure 7.24: Resistance (R_{\perp}) as a function of the probe distance measured on low doped samples. The resistance is constant for probe distances of $s \geq 30 \mu\text{m}$. For measurements using a smaller probe spacing a strong dependence is observable. The vertical dashed line indicates the beginning of the sharp drop in resistance. The dotted curves are a guide of the eye. The trend for distances $< 1 \mu\text{m}$ was estimated from the expected resistances for a 3D bulk based on the resistivity value [30].

Therefore, all the temperature dependent experiments in the following were performed on low doped samples with special care of the SCL contribution.

7.5.2 Temperature dependence of the Si(553)-Au surface

Structural phase transition

Cooling of the samples was performed using LHe while the temperature was monitored with a Pt100 resistance mounted on the manipulator close to the Si-sample. The high resolution LEED pattern at 40 K shown in figure 7.25 reveals clearly the step train and the half-order diffraction spots along the $[1\bar{1}0]$ direction stemming from the surface vicinality and the $\times 2$ reconstruction along the Au strands, respectively (cf. structure model introduced in section 7.2.2). In comparison to the LEED pattern at room temperature (cf. figures 7.6(a) and 7.13) the LEED exhibits the $\times 3$ reconstruction which vanishes upon annealing. This absence of the $\times 3$ spots at room temperature is indicative for a long-range ordering along the wires, i.e. a defect free surface preparation.

Further details about the structural phase transition are exemplarily depicted in figure 7.26. Here, figure 7.26(a) shows three line scans taken along the $[1\bar{1}0]$ direction at different temperatures. The peak intensities and full widths at half maximum (FWHM) for the $\times 2$ and $\times 3$ reconstructions were deduced from the fits and were plotted versus the temperature as shown in figure 7.26(b). Clearly visible is a sudden increase of the FWHM of the $\times 3$ reconstruction

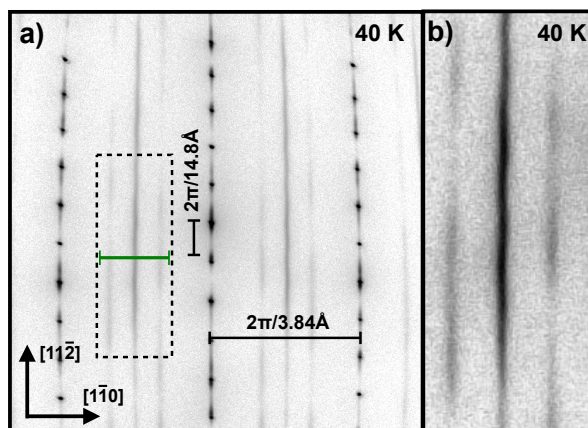


Figure 7.25: SPALEED pattern of the Si(553)-Au taken at $T = 40$ K and $E = 138$ eV. The area marked by a dashed rectangle is shown in (b) in greater detail. The green marked line denotes the position of the line scan analysis shown in figure 7.26.

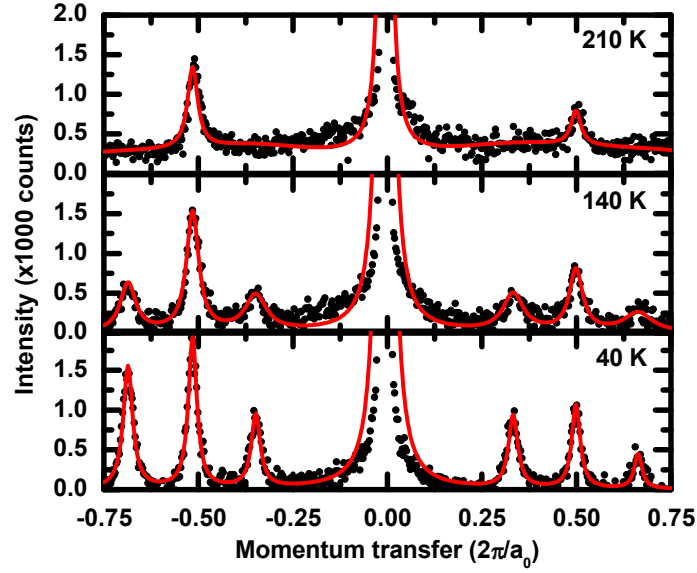
at a critical temperature of $T_C = 100$ K, which marks the onset of the phase transition. Additionally, also the corresponding peak intensity shows a stronger decrease at 100 K, which is superimposed onto the decrease induced by the Debye-Waller effect.

Contrary to the analysis of the $\times 3$ at low temperatures, the FWHM of peaks from the $\times 2$ -periodicity along the Au-chains remains almost constant and the corresponding peak intensity shows only the Debye-Waller related exponential decrease over the entire temperature regime in figure 7.26(b). The Debye-Waller effect related decay of the intensity $I(T)$ in LEED may be approximated by [197]

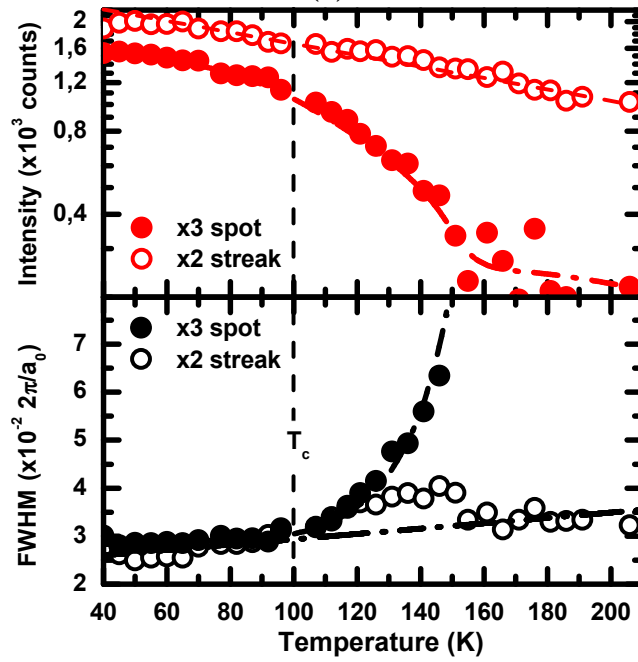
$$I(T) = I_0 \exp \left(\underbrace{-\frac{24m_e(B \cos^2 \vartheta + U)T}{m_a k_B \Theta_D^2}}_{-\frac{24m_e(B \cos^2 \vartheta + U)}{m_a k_B} := X} \right) = I_0 \exp \left(X \frac{T}{\Theta_D} \right), \quad (7.5.1)$$

where m_e and m_a are the electron mass and atomic mass respectively. B is the electron beam energy, U the inner potential (in average between 5 and 15 meV [198]) and ϑ the detection angle. Using equation (7.5.1) as a fitting function, a surface Debye temperature of $\Theta_D \approx 115$ K is estimated from the decay of the diffraction intensity of the $\times 2$. To mimic the Au-Si bond strength adequately for the lattice fluctuation, the averaged mass of a Au- and Si-atom was used. The corresponding fit is shown in figure 7.27.

For temperatures above 160 K the $\times 3$ diffraction spots are completely vanished. Since surface defects are able to stabilize this reconstruction [70, 180], the temperature window of this order-disorder transition may vary from sample to sample. Indeed, it turned out within the experiments of this thesis, that the freeze-out temperature for the transition of the $\times 3$ is highly depending on the defect concentration and that pinning of the $\times 3$ reconstruction significantly increases the transition temperature. It could be shown that defective Si(553)-Au HCW phases, which were intentionally induced during preparation by evaporating up to 12% less than the necessary 0.48 ML Au, even showed $\times 3$ characteristics at room temperature.



(a)



(b)

Figure 7.26: (a) Line profiles taken along the $[1\bar{1}0]$ direction for three different temperatures as indicated in figure 7.25. The solid lines denote fits in order to deduce the peak intensities and FWHMs. (b) Peak intensity (top) and FWHMs (bottom) of the $\times 3$ - and $\times 2$ -spots as a function of the temperature.

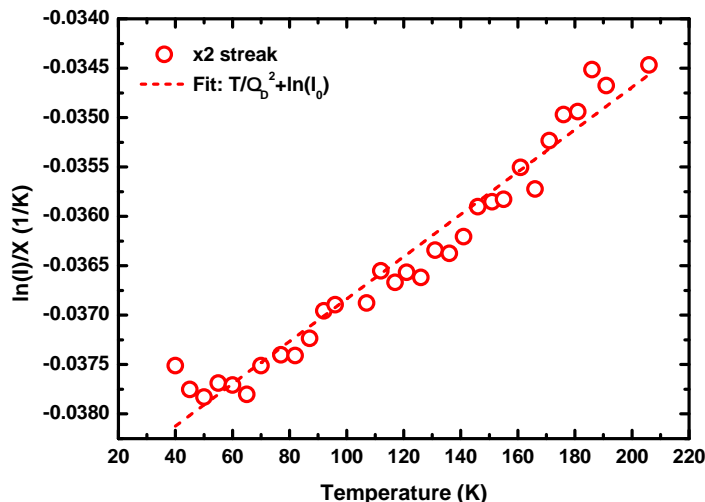


Figure 7.27: Logarithmic peak intensity of the $\times 2$ streaks as a function of the temperature. Using equation (7.5.1) as a fitting function, a Debye temperature of $\Theta_D \approx 115$ K was estimated. X was defined in equation (7.5.1) and summarizes the constants of the equation.

The correlation between total Au coverage and the normalized intensity of the $\times 3$ spots and $\times 2$ streaks is shown in figure 7.28(a). It is obvious that the intensity of the $\times 3$ spots increases exponentially, while the intensity of the $\times 2$ streaks decreases with reduced Au coverage and more defective surfaces.

Summarizing, the LEED data clearly reveals that only the Si-edge undergoes a 1D order-disorder phase transition, which contrasts with previous measurements [38].

Modeling T_C as a function of the Au coverage As pointed out before, the FWHM of different profiles is not influenced by temperature. Any change is only related to the Debye-Waller effect. Thus, the change of T_C as a function of the defect concentration and deviation $\Delta\Theta_{0.48}$ from the necessary gold coverage of 0.48 ML can be estimated as illustrated in the following. The transition temperature T_C for $T < 300$ K is obvious from temperature dependent line scan analyses as exemplarily shown in figure 7.26(b). For the data measured at room temperature as shown in 7.28(a) an error of 20 K around $T_C = 300$ K was assumed. From the analysis of the data presented in figure 7.28(a) the relation between the FWHM of the $\times 3$ and the Au coverage was deduced. By this the deviation $\Delta\Theta_{0.48}$ for the data with $T < 300$ K was calculated. Since the $\times 3$ periodicity corresponds to the long-range ordering of the Si step edge atoms perpendicular to the steps with $a_0 = 3.84$ Å [156] and assuming that a “perfect” preparation with exactly 0.48 ML has 0 defects, the number of point defects per cm was calculated whose overall trend reasonably explains the observed $\times 3$ at room temperature. The outcome of the described analysis is shown in figure 7.28(b).

Electronic phase transition

Figure 7.29 shows the resistance components R_{\parallel} and R_{\perp} of the $[1\bar{1}0]$ - and $[11\bar{2}]$ -direction, respectively, measured on three different samples. All preparations were prepared with an

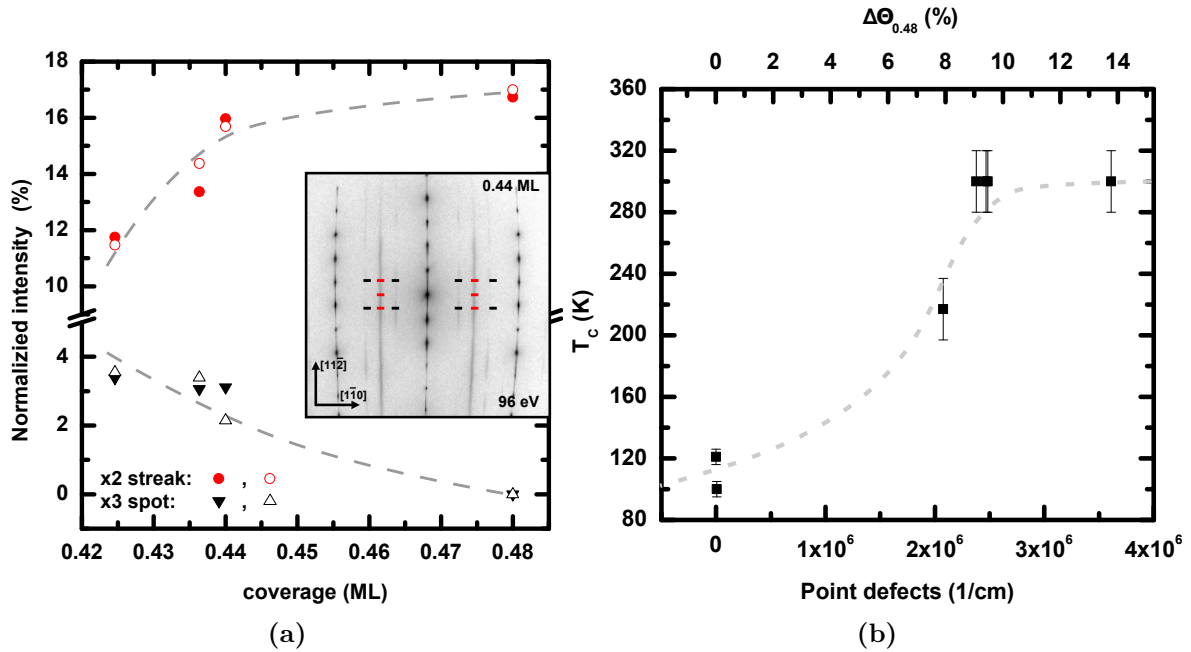


Figure 7.28: (a) Intensity of the $\times 2$ streak and $\times 3$ spot calculated from line profiles taken along the $[1\bar{1}0]$ direction as a function of the sample Au coverage (normalized in respect to the 00 spot of the sample). The visibility of the $\times 3$ even at room temperature is explained by a defect mediated pinning of the low temperature $\times 3$ reconstruction which results in an increased transition temperature for the occurrence of the $\times 3$. The dashed line is a guide to the eye. The inset shows exemplarily a SPALeED pattern of a 0.44 ML prepared sample surface with clearly visible $\times 3$ spots. All the LEED patterns for the analysis were taken at room temperature. Highlighted by black and red lines are the position used for the analysis of the $\times 2$ streak and $\times 3$ spot which was performed on multiple samples.

(b) Phase transition temperature T_C as a function of the estimated point defects and deviation $\Delta\Theta_{0.48}$ from the necessary gold coverage of 0.48 ML. The phase transition temperature T_C for $T < 300$ K was derived from the analysis of temperature dependence of the FWHM as exemplarily shown in figure 7.26(b). See text for further remarks how the point defect concentration or relative coverage was estimated. The gray line is a guide of the eye to the data.

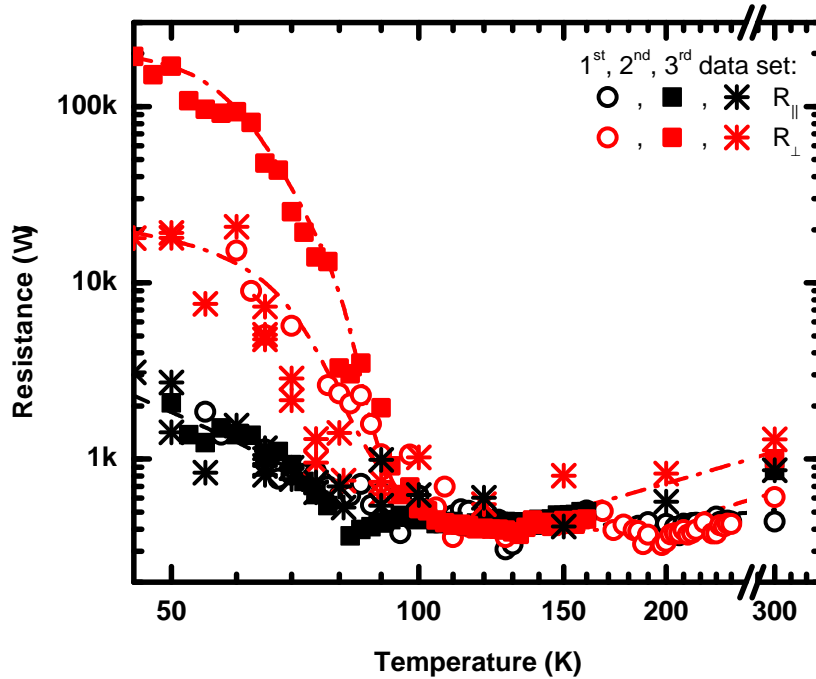


Figure 7.29: Three different data sets of temperature dependent resistance measurements shown on a log-log scale. Notably, all data sets see a drastic change of resistance occurring at around 100 K and all parallel resistances $R_{||}$ follow the same trend.

gold coverage of $\Theta = 0.48$ ML and only showed the $\times 2$ reconstruction in LEED at room temperature. For temperatures above 100 K the resistance values and anisotropy factors are comparable to the measurements presented in section 7.4. This changes drastically upon cooling to lower temperatures, where the anisotropy induced by the surface fully emerges. Coming from high temperatures, R_{\perp} increases all of a sudden at 120 K by around 2 - 3 orders of magnitude. $R_{||}$ along the wires increases also, however, by only one order of magnitude. Notably, $R_{||}$ of all the data sets follow the same trend, while R_{\perp} differ slightly for every preparation which is corresponding to SCL contributions as motivated in the previous section. Moreover, both branches show a saturation behavior for $T < 60$ K. Since ARPES [68, 81, 199] reveals unambiguously that metallic surface bands are present only along the $[1\bar{1}0]$ direction (i.e. the direction of the wires) and that weak interchain coupling manifests by a faint wiggling of the Fermi lines, the observed R_{\perp} -contribution is not related to the surface state bands and must be related to transport across the Si-bulk.

Figure 7.30 shows the conductivity of the data points presented in figure 7.29. The bulk contribution was modeled by an n-doped SCL model (as motivated in section 2.3) as well as by a parasitic Si-bulk effect related to a p-type SCL resulting from flash annealing. As obvious from figure 7.30, the contribution can not be explained by a simple space charge model based on an n-type doping while a reasonable explanation is given by a parasitic p-type surface effect related to flash annealing (as motivated before in section 7.5.1).

In the following, the details of the modeling of that p-type layer are briefly summarized. The hole mobility μ_p was estimated using the empirical derived model by ARORA et al. [200],

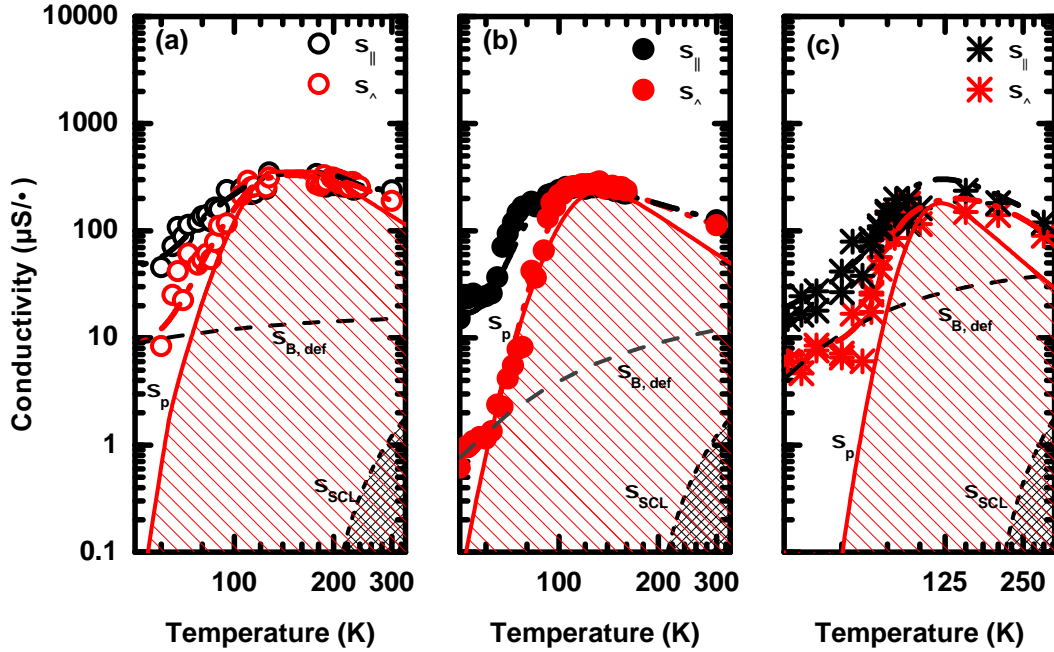


Figure 7.30: Conductivity vs. sample temperature (log-log plot) measured along and perpendicular to the wire direction. The solid lines are guides to the eyes. Apparently, the transport in the atomic wire systems is strongly governed by parasitic bulk channels. Two band scenarios, i.e. the SCL effect (σ_{SCL}) and the p-doped layer contribution (σ_p) are shown. In addition, an activated contribution (dashed-dotted line) is also plotted.

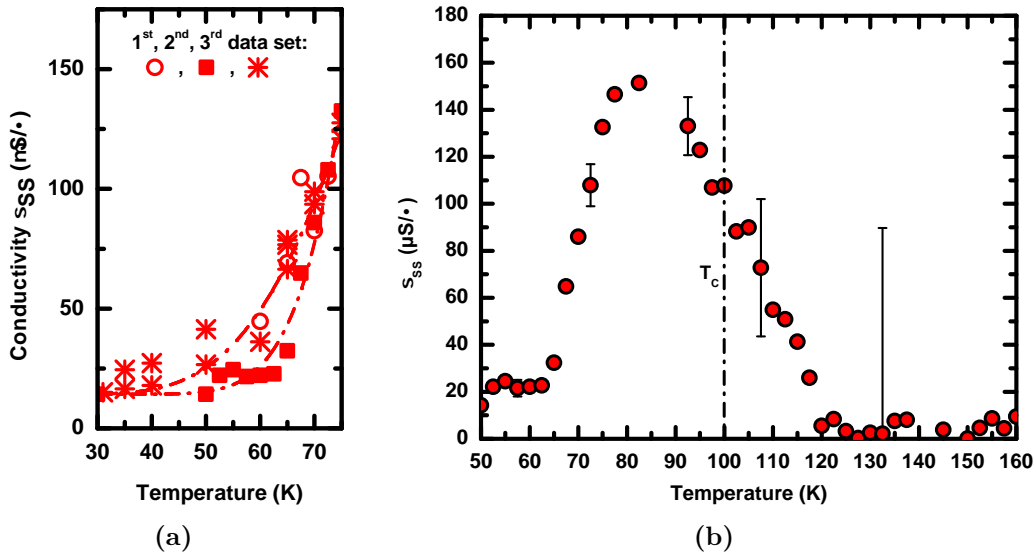


Figure 7.31: (a) Surface conductivity σ_{SS} along the wires obtained after subtraction of the perpendicular transport component. The fits revealed activation energies between $\Delta_S = 30$ meV and 60 meV. (b) σ_{SS} showing the full low temperature range of data set 2 (data set with lowest scattering). The T_C observed in figure 7.26(b) is indicated by a dash-dotted line. The error bar is drawn in selectively for the different temperature regimes.

while the hole concentration n_p was calculated using the model by LI [201] with

$$n_p(T, N_A) = \frac{N_A}{1 + [4 + 2 \exp(-\Delta/k_B T)] \exp((E_A - E_F)/k_B T)}, \quad (7.5.2)$$

where E_A is the acceptor energy level and depends on the acceptor concentration N_A and Δ is an empiric constant ($\Delta = 0.0438$ eV for boron contaminations [85] and $\Delta = 0.07$ eV for interstitial-carbon defects in Si [84]). The conductivity of the p-type layer was then fitted to the data by

$$\sigma_p(T, N_a) = e\mu_p n_p(T, N_A). \quad (7.5.3)$$

The best fits were obtained for the data presented in figure 7.30(a,b) for an ionization energy of around 71 meV fitting to a parasitic p-layer by interstitial-carbon defects[84], an acceptor concentration in the range of $N_A = (1 - 10) \cdot 10^{15} \text{ cm}^{-3}$ and a SCL thickness of around $8 - 10 \mu\text{m}$, which is comparable to the rough estimation in section 7.5.1. The fit of figure 7.30(c) revealed an acceptor concentration of one order less ($N_A \approx 3 \cdot 10^{14} \text{ cm}^{-3}$) with a SCL thickness of around $20 \mu\text{m}$. However, it should be noted that the fitting routine is very sensitive to the scattering of the data which is prominent in the low temperature range for this data set. Thus, the deviation from the values of figure 7.30(a,b) are rationalized in terms of the higher scattering of the data set, especially since data set 1 and 3 in figure 7.29 follow the same trend. On the other hand, the deviation could also be explained by slight differences in sample preparations (deviation in flash annealing temperature and amount of flash cycles as discussed before in section 7.5.1).

Importantly, this interface transport channel is spatially extended compared to atomic distances, i.e. details of atomic structure at the surface are irrelevant, hence this transport channel is expected to be isotropic with respect to the directions of the atomic wire structure. Besides this p-type layer mediated transport, also activated transport via bulk defects was included. The isotropic bulk-related hopping channel was modeled via a Boltzmann term ($\sigma_{\text{B, def}} \propto \exp(-\Delta_{\text{B}}/k_B T)$) and is shown by the dashed line in figure 7.30. The details of the temperature dependency of this background are difficult to quantify as it covers the entire temperature range. The average activation energy of all plots is $\Delta_{\text{B}} \approx 6 \pm 4 \text{ meV}$ ⁶. This is rather low and the large uncertainty might be indicative for the formation of various shallow defect states upon the high annealing steps.

The previous discussion showed that the temperature dependency of the $\sigma_{\perp} \equiv 1/\rho_{\perp}$ component is explained by considering (isotropic) bulk contributions. Thus, if scattering of charge carriers in between the surface and bulk channels are of minor relevance, the contribution of the Au-induced surface states along the $[1\bar{1}0]$ direction is calculated by

$$\sigma_{\text{SS}} = \sigma_{\parallel} - \sigma_{\perp}, \quad (7.5.4)$$

where $\sigma_{\perp} = \sigma_p + \sigma_{\text{B, def}}$, which is depicted in figure 7.31.

Two conclusions are drawn from figure 7.31: Notably, there is a finite conductivity below $T_C = 100$ K deduced from the structural transition observed in LEED. Furthermore, it needs to be highlighted, that at least down to 30 K the system remains metallic. This excludes the formation of a charge density wave (CDW), as previously reported [38, 115]. Figure 7.31(b) shows the full low temperature range of data set 2 which showed the lowest

⁶ $\Delta_{\text{B}} = 2 \pm 1 \text{ meV}$ for data set 1, $\Delta_{\text{B}} = 10 \pm 5 \text{ meV}$ for data set 2 and $\Delta_{\text{B}} = 6 \pm 2 \text{ meV}$ for data set 3.

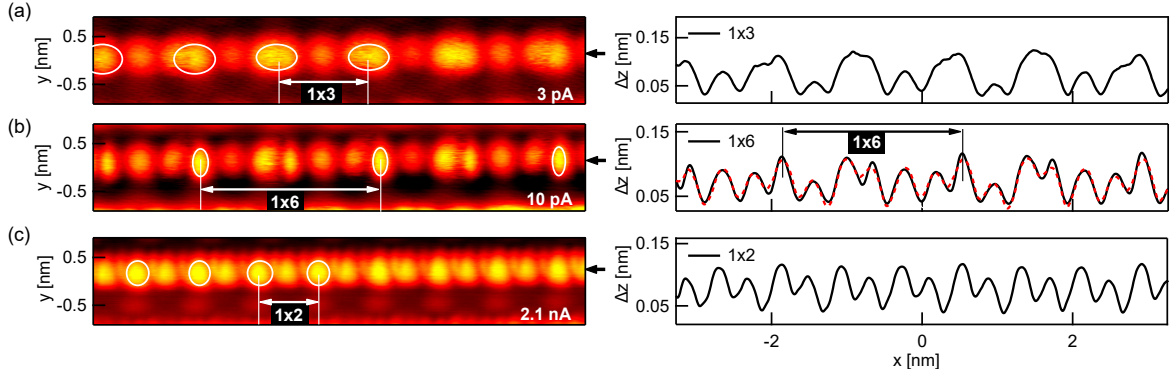


Figure 7.32: STM image at 60 K (tunneling bias of 1 V). of a single Si step edge. For every STM image there is a linescan shown on the right part of the image. The position of the linescan is highlighted by a black arrow. For 3 pA a $\times 3$ phase is observed while for 2.1 nA a $\times 2$ phase. For intermittent currents a phase with a $\times 6$ periodicity is observable. The corresponding line scan shows a red dashed curve, which highlights that the $\times 6$ structure is a (time-averaged) linear combination of the $\times 3$ and $\times 2$ phases. Images are adapted from [202].

scattering of values. Obviously, in agreement with the overall low anisotropy seen at room temperature (cf. section 7.5.1), the contribution of the Au-wire for temperatures above 120 K is extremely small. Here, in the presented case, the residual conductivity along the wires is almost identical to the conductivity measured in the perpendicular direction. Thus, the exact determination of the surface conductivity suffers from the large bulk contribution for temperatures > 120 K and has a large error. Nonetheless, the remaining conductivity below 60 K as well as the pronounced drop of the conductivity for $T < 80$ K are not influenced by details of the background subtraction and are a feature of all three data sets, which will be the focus of the following discussion.

7.5.3 Discussion of the observed structural and electronic transition

In the following, three different scenarios are proposed rationalizing the data shown in figure 7.31.

Transient doping Figure 7.32 shows that the periodicity and the occurrence of $\times 3$ and $\times 2$ measured at 60 K is strongly depending on the tunneling conditions. Thus, the potential effect of transient doping, which result in current-dependent periodicities [183, 202], should be discussed briefly. POLEI et al. [183] reported that the $\times 3$ ordered ground state get reversibly destabilized by transient electron doping and reorganizes into a $\times 2$ ordered phase. In a typical transport experiment with a probe spacing of $75 \mu\text{m}$ the probing current is passed through around 100000 wires. In the performed experiments, currents of $10 - 50 \mu\text{A}$ were used for probing of the surface which corresponds to $0.1 - 0.5 \text{ nA}$ per wire. The current used was constant for a each sample preparation shown in figures 7.29 to 7.31. Thus, an induced transition by a change of the probing current during experiment is unlikely. However, based on the previous estimation, it might be possible, that there is a transient doping of the system by transport which shifts the phase transition related to the $\times 3$.

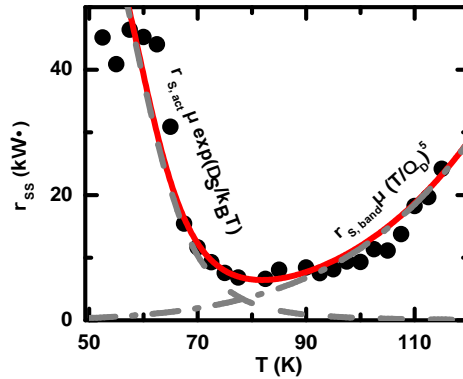


Figure 7.33: The plot shows the maximum $\rho_{SS} \equiv 1/\sigma_{SS}$ from figure 7.31(b) and the corresponding fits mentioned in the text for an activated and band-mediated transport.

Activated and band-mediated transport It will be shown in the following that the resistivity along the atomic chains can be quantitatively described by taking into account an activated ($\rho_{S, \text{act}}$) and a band-mediated ($\rho_{S, \text{band}}$) surface transport. For a detailed description of this 1D surface conductivity it is further considered that both surface channels are connected in series. The surface state conductivity is then given by

$$\sigma_{SS} \equiv 1/\rho_{SS} = 1/(\rho_{S, \text{act}} + \rho_{S, \text{band}}), \quad (7.5.5)$$

where the two separate channels are parametrized by $\rho_{S, \text{act}} \propto \exp(\Delta_S/k_B T)$ and $\rho_{S, \text{band}} \propto (T/\Theta_D)^5$ taking into account activated transport and electron-phonon scattering, respectively. The fit to the experimental data is shown in figure 7.33. This analysis reveals a well-defined surface activation energy of $\Delta_S = 50 \pm 2 \text{ meV}$. A sharp increase in the conductivity is expected if similar defects impact the conductive Au-chains. Indeed, high resolution STM measurements revealed such characteristic defects on Si(553)-Au [176]. Thereby, the Si-step edge acts predominantly as a nucleation site for adsorbates, consistent with the transport and DFT studies in section 7.4. Albeit atomistic details are still missing to date, some of the point defects act locally, while others induce similar characteristic charge redistribution patterns on the terraces along the Au-chains leaving the distribution originating from the Si-edge density of states itself intact [176]. In this context, the Au-channels undergo a MIT due to a defect-mediated effect, which is not related to the structural phase transition seen along the Si chain, though.

However, at low temperatures the system is still conductive. This means that there are channels at low temperatures which are still conductive. The residual conductivity does not fit to the proposed image, but could be explained by an interwire hopping in accordance with a former study [71].

Partial Peierls transition The transition and the residual conductivity in figure 7.31 may be explained by a partial Peierls transition. As written before in the introduction in section 7.2.2 ARPES data reveals a band filling of 0.56 and 0.51 for the $S1$ and $S2$ band [68, 81]. Notably, the first mentioned value is near perfect nesting conditions. So, it may be that there is a transition to an isolating state and an opening of a band gap in the $S2$ band while the $S1$ band remains metallic.

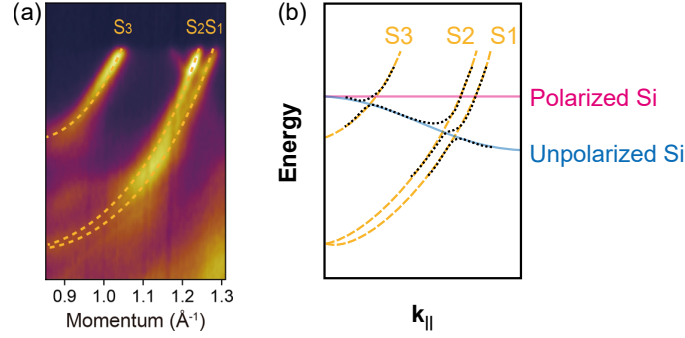


Figure 7.34: (a) Energy distribution measured by ARPES using photons with an energy of 46 eV showing the three metallic bands (S_1 , S_2 and S_3) (Spectra taken from [175]). (b) Proposed hybridization of the S bands showing the opening of a gap.

A partial Fermi nesting would result in a $\times 2$ distortion which would be hard to distinguish from the $\times 2$ of the gold chains in LEED. Furthermore, it was shown in calculations that there is always a hybridization of the gold-induced states with those of the step edges [175, 203]. However, this effect was not seen in photoemission which was attributed to thermal fluctuation. An ARPES spectra and a proposed hybridization is seen in figure 7.34 (a,b). In addition, very recent calculation of SANNA et al. [204] predict, that there is a band gap opening depending on the degree of dimerization within the Au chains which is assigned to the $\times 2$. This dimerization change would not be visible in LEED (within a kinematic approximation) and may not be observed in photoemission experiments due to poor energy resolution. A gap opening depending on the degree of dimerization fits to the STS data by SNIJDERS et al. [70]. Their STS data shows a gradual gap opening at low temperature which was attributed to successive gap opening in the S bands.

7.5.4 Summary on the phase transition of Si(553)-Au

In summary, the phase transition of Si(553)-Au was carefully investigated in a combined SPALEED and transport study. Within SPALEED measurements a structural transition was observed at $T_C = 100$ K for the $\times 3$ spot. Further it could be shown that the transition temperature T_C is strongly dependent on defect structures. E.g. defective Si(553)-Au phases, which were intentionally prepared with less than the necessary 0.48 ML Au, showed $\times 3$ characteristics even at room temperature.

However, transport studies revealed a different behavior which is not related to the transition of the $\times 3$. Notably, even below the observed structural transition temperature of 100 K, a finite conductivity was seen within the probed temperature range and the system remained metallic at least down to 30 K. Thus a MIT can not be attributed to the structural transition of the $\times 3$. Three different scenarios were proposed rationalizing the observed conductivity behavior: a transient doping which may shift the phase transition temperature, activated and band mediated transport and a partial Peierls transition. The latter seems to be likely since the first calculations show that a band gap opens and is depending on the dimerization degree of the Au chains which is related to the $\times 2$ structure. However, a complete picture describing the experimental findings could not be given and further DFT calculations at low temperature are necessary for a better understanding.

Tb silicide nanowires on Si(001)

8.1 Introduction

The previous chapters dealt with ensemble of atomic wires which are very interesting in terms of a fundamental physical point of view. In contrast single or bundled wires can be grown on silicon using rare earth (RE) forming the so-called silicide nanowires. In addition to fundamental physical questions [73, 77, 205–208], these systems are also of high interest for future applications in nanodevices as they could serve as interconnects or gate electrodes for the next generation CMOS technology due to their ideally 1D structure and strong compatibility with current techniques of the “silicon platform” [209–213].

The following chapter will first very briefly introduce silicide nanowires on silicon in general and then focus on recent results obtained within the scope of this thesis on Tb silicide wires. Here, the results were previously published in “Atomic size effects studied by transport in single silicide nanowires” [31] in 2016 by MICCOLI, EDLER and will not be cited separately.

Silicide nanowires

Silicide nanowires are binary compounds of silicon with electropositive elements like transition metals (TM) or RE elements. The deposition of monolayer amounts of TM or RE materials and additional thermal treatment leads to the formation of silicide nanowires.

Here the RE silicide nanowires are of special interests. This is because of an anisotropic lattice mismatch in respect to the silicon substrate which is about 7–8%¹ there is an uniaxial growth resulting in the growth of very long but also extremely thin nanowires on (100)-oriented or vicinal (111)-oriented Si-substrates [215–218]. In terms of possible applications mentioned in the beginning of this chapter, the concept of uniaxial strain- or step-mediated growth is highly interesting because it overcomes lithographic problems and limitations of the present techniques [209–213]. The most prominent RE silicide nanowire systems are grown on Si(100) surfaces and have a hexagonal structure [75, 219–222]. Often a bunching is observed where each individual nanowire is 2 - 3 nm wide. Depending on the substrate and preparation

¹For instance in case of the in the following treated TbSi₂ silicides, the lattice mismatch along the wires is only 0.26% while perpendicular a high mismatch of 7.47% is found [214] leading to a limited growth in the mismatched direction.

parameters, the nanowire lengths may reach several 100 nm or even in some cases exceed 1 μm length and the growth is usually only limited by substrate steps or defects. All these nanowires are characterized by a metallic band structure and there are indications for a one-dimensional dispersion [75, 220]. Moreover, the metallic wires serve as important model systems to understand the effects of electronic correlation and instabilities characteristic for 1D physics [34, 73]. As a recent example, YSi₂ nanowires with cross sections as small as 0.5 nm² were shown to reveal Van Hove singularities, a clear benchmark for a 1D electronic structure. Short-range charge order along these 1D wires was found coming along with an opening of an electronic gap. However, the Peierls model is inappropriate and details about the electron-phonon coupling are still under debate [73]. Latest temperature-dependent transport measurements on these nanowires indicate a thermally assisted tunneling of polarons showing that quantum transport suffers from atomic-scale charge trapping defects [208].

In most cases the atomic structure of silicide wires is related to known bulk silicides. However, the transport properties in such thin wires are severely influenced by atomic-scale defects [77] and finite size effects [223] resulting in electronic properties deviating from those of the bulk silicides. Thus, for a better understanding, a detailed investigation of the atomic structures in correlation with transport studies is inevitable. But up to now, only very few transport studies were performed [77, 208] on these RE silicide systems and nearly never correlated with their atomic structures. Additionally, previous approaches relied on *ex-situ* processing steps (e.g. capping with amorphous Si and fabrication of contacting pads [208]) which possibly lead to a contamination of the wires itself.

In contrast, the multi-probe scanning tunneling microscope (STM)/scanning electron microscope (SEM) setup allows to perform *in-situ* transport measurements and high resolution STM studies of the *same* nanowire which will be used for a detailed study of TbSi₂ wires in the following.

8.2 Formation of TbSi₂ wires on Si(001)

The growth process of TbSi₂ wires by adsorption of Tb on planar as well as vicinal Si(001) surfaces was recently investigated in detail by APPELFELLER et al. [224]. The self-assembly of nanometer-sized silicide wires on Si proceeds in two steps: first, Tb induces a 2×7 reconstructed isolating wetting layer on planar Si(001) for coverages of about 0.4 ML, while subunits of this reconstruction are found on vicinal Si(001) [224]. Any supplementary Tb deposition leads to the epitaxial growth of TbSi₂ nanowires preferentially along the $[\bar{1}10]$ direction, i.e. perpendicular to the Si dimer rows of the 2×1 reconstruction [224, 225], until a step edge is reached. Depending on the annealing temperatures and Tb coverage rates, the growth of single or bundled nanowires is promoted [224].

The preparation parameters were carefully chosen so that long TbSi₂ nanowire bundles are formed and can be easily seen in SEM. Single TbSi₂ nanowires were not observed in additional STM analysis. Therefore for the sake of simplicity, if not explicitly stated otherwise, the term nanowire is synonymously used for nanowire bundle structures for the rest of this chapter.

8.2.1 Sample preparation

Within this thesis, for the self-assembly of Tb silicide nanowires, Si(001) wafers with a nominal miscut of 4° towards the [110] direction and a bulk resistivity ρ of 1 – 20 Ωcm (p -doped with B) were used. The substrates were first degreased for 10 min in an ultrasonic bath of acetone and subsequently in isopropyl alcohol. Then they were rinsed in de-ionized water and dried under pure N₂. Finally, they were outgassed in ultra-high vacuum by direct-current (DC) heating at 700 °C for several hours and were treated by subsequent flash annealing cycles up to 1150 °C for around 10 s while keeping the pressure below 2×10^{-9} mbar. This cleaning procedure allows to fully desorb Si oxides and carbon contaminants from the surface yielding 2×1 reconstructed terraces [226] separated by double-atoms.

Tb silicide wires were then grown by depositing around 0.8 monolayer (ML) of Tb² using a home-built electron-beam evaporator which was calibrated before using a quartz-crystal microbalance. After the Tb deposition, the DC heating of the sample was immediately turned off in order to reduce the competitive growth of islands on the Si surface (cf. figure 8.1 in section 8.2.2), as reported before for other RE metals [76, 227].

8.2.2 Structural properties of TbSi₂ wires

Figure 8.1(a) - (c) shows SEM images demonstrating the successful growth of Tb silicide nanowires on large areas of the vicinal Si(100) substrate. The wire length typically varies between 2 and 4 μm , while their maximum width is always smaller than 30 nm (cf. also STM results exemplarily shown in figure 8.2(a)). Moreover, it is evident that the substrate miscut promotes wire growth along Si steps (cf. blue and red areas in figure 8.1(a)), corresponding to the $[\bar{1}10]$ direction, apart from a few Tb silicide islands (highlighted in yellow) and bigger TbSi₂ wires, which are oriented either along the $[\bar{1}10]$ or the [110] direction (in green). Additionally on all preparations, Tb silicide islands with an average diameter of 0.4 – 1 μm are seen. These behave as getters and show no wires in their surroundings. This effect has been already observed in various STM studies for different RE metals [74, 219, 225] and is mainly related to high diffusion lengths of Tb at high temperatures. While Tb silicide islands are always present, the density of the wires, growing perpendicularly with respect to the main growth direction, reduces drastically with increasing the flash annealing cycles before Tb deposition, resulting finally in a homogeneously covered surface with apparently smaller wires (cf. figure 8.1(a) in comparison to figure 8.1(c)). This observation is in agreement with previous studies on vicinal Si substrates [228, 229] showing that extended DC heating severely modifies the step height and density. This typically induces large or even giant step bunching which drastically hinders the nanowire growth across the steps.

A low resolution STM overview image of a wire ensemble comparable to that of a preparation as shown figure 8.1(c) is depicted in figure 8.2(a). Interestingly, the STM image does not show any step or step bunches, respectively. This is in well agreement with previous studies on silicide wires [219, 224, 227], which noticed that RE deposition promotes a step movement and flattening of the Si substrate especially pronounced in the vicinity of the silicide wires.

As it is obvious from the insets in figure 8.2(a), the silicide wires exhibit a substructure, i.e. they consist of bundles of single wires separated by atomically thin grooves in agreement with results of a recent transmission electron microscope (TEM) study [230]. The widths of the

²1 ML = Si atomic surface density of 6.8×10^{14} atoms/cm²

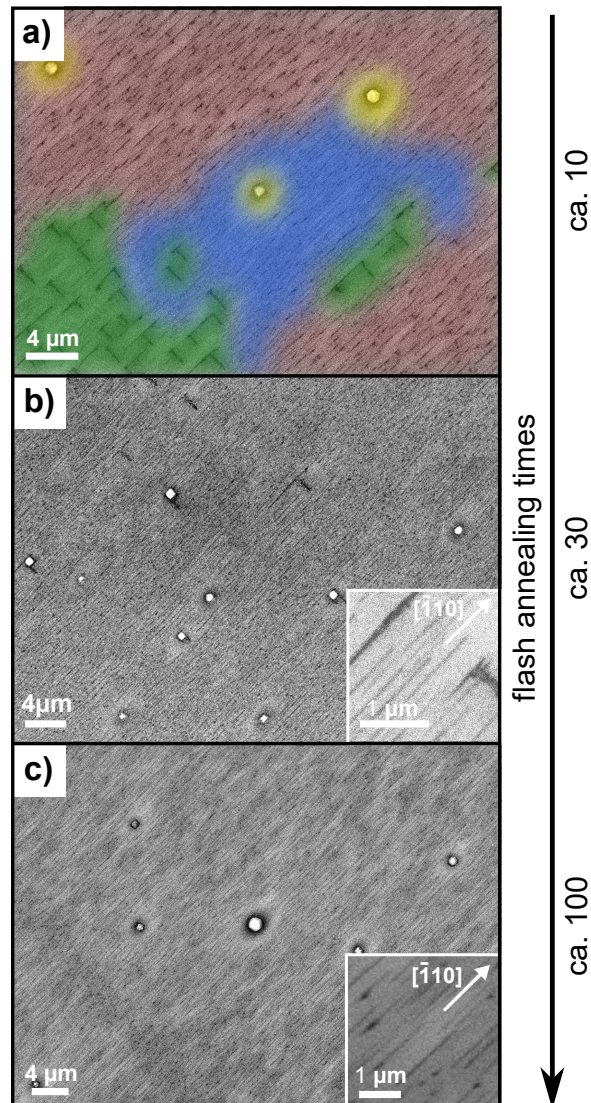


Figure 8.1: SEM images of TbSi_2 wires grown on a $\text{Si}(001)\text{-}[110]4^\circ$ for different flash annealing cycles of the Si sample. (a) Three different nanostructure types are initially visible: TbSi_2 wires aligned along the $[\bar{1}10]$ direction (highlighted in red, blue), most likely Tb silicide islands (highlighted in yellow) and apparently bigger TbSi_2 wires sometimes rotated by 90° (in green). (b), (c) Further flash annealing of the $\text{Si}(001)$ substrate (up to 100 cycles) generally results in samples that only show the thinnest wires (highlighted in blue in (a)).

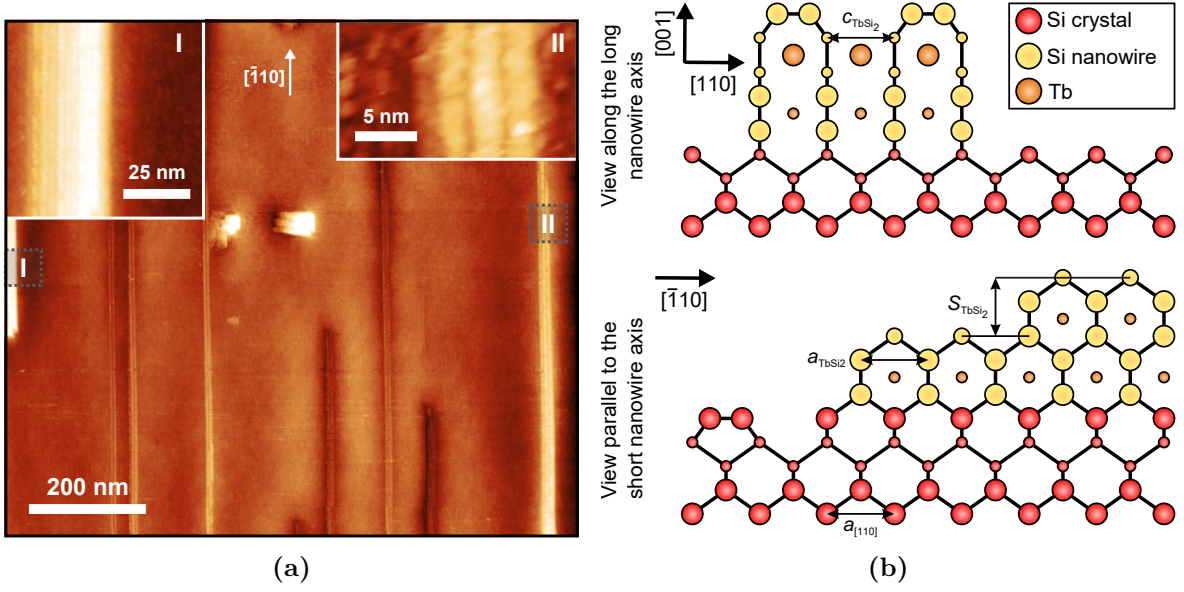


Figure 8.2: (a) STM overview image ($V_T = 2 \text{ V}$, $I_T = 100 \text{ pA}$) of TbSi_2 wires grown on $2 \times 1 \text{ Si}(001)$ substrate after many (> 50) flash-annealing cycles. The insets (I) and (II) show detailed STM images of the two TbSi_2 wire bundles labeled with I and II in the figure. (b) Schematic drawing of the structure model for the TbSi_2 nanowires. Here, smaller circles indicate lower lying atoms. The Si surface lattice constant along the $[110]$ direction is given by a_{TbSi_2} . $S_{\text{TbSi}_2} = 0.333 \text{ nm}$, $a_{\text{TbSi}_2} = 0.385 \text{ nm}$ and $c_{\text{TbSi}_2} = 0.415 \text{ nm}$ are the step height of TbSi_2 and the averaged lattice constants according to [214]. Image adopted from [224].

single wires are quantized in units of the Si surface lattice constant along $a_{[110]} = 0.384 \text{ nm}$ with the thinnest (broadest) being $3a_{[110]} = 1.15 \text{ nm}$ ($8a_{[110]} = 3.07 \text{ nm}$) wide. The majority of the wires has an average width of $(6 \pm 1)a_{[110]} = (2.2 \pm 0.4) \text{ nm}$, which is in full agreement with previous STM studies [224, 231] (cf. structure model in figure 8.2(b)).

Surface roughness of the wires

An important aspect of the growth is the roughness of the wires. Exemplarily, the STM image in figure 8.3(b) shows a wire bundle, which consists of five single wires, each with an average width of 2.5 nm . The wire bundle has a maximum height of 0.9 nm , roughly corresponding to three atomic steps (each 0.33 nm high [224]). But, only the first two layers form a compact structure, while the third one consists of an ensemble of TbSi_2 nanoislands, which is responsible for the surface roughness. As it will be discussed in section 8.2.4 this has severe consequences on the transport properties.

Therefore, the surface topography was quantified by the so called height-height correlation function (HHCF) $H(x)$ along the wire [232], which is defined as

$$H(x) \equiv \langle [h(x') - h(x + x')]^2 \rangle. \quad (8.2.1)$$

Here, $h(x)$ is the vertical position of the surface at lateral coordinate x along the nanowire direction with respect to a reference plane, while the angular brackets $\langle \cdot \rangle$ denote the averaging.

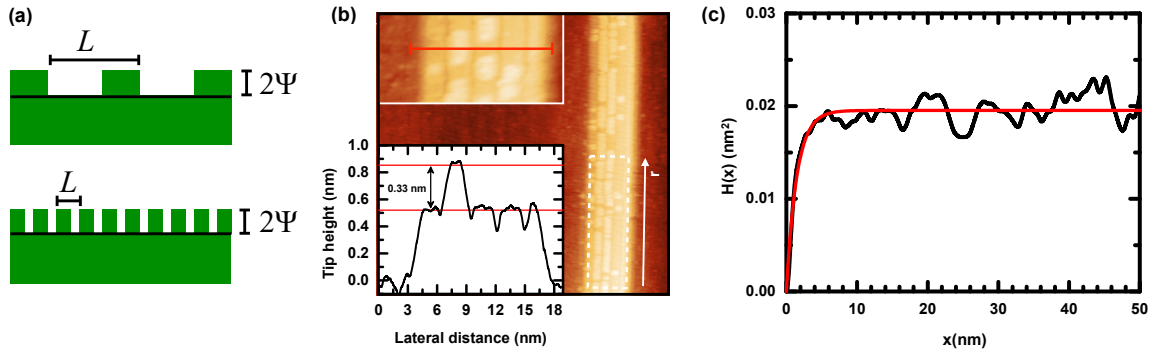


Figure 8.3: (a) Two schematics to illustrate different correlation lengths L and roughness Ψ . (b) High resolution STM image ($V_T = 2$ V, $I_T = 100$ pA) showing the formation of additional nanoislands on top of the wires. A detailed image is shown in the upper inset and analyzed quantitatively using the height contour shown in the lower inset. (c) Derived HHCF plot along the wire (black) with fit curve (red) according to equation (8.2.1).

The HHCF is usually assumed to be exponential (or Gaussian) and expressed as a function of the surface root-mean-square roughness Ψ and the lateral correlation length L of the surface [233–235] (cf. schematics of figure 8.3(a) for reference). For the analysis of the data, the exponential correlation was adopted, i.e. $H(x) = 2\Psi^2(1 - \exp(-x/L))$, which showed a better agreement to the experimental findings. From the best fit of the experimental HHCF (cf. red solid curve in figure 8.3(c) for reference), typical surface roughness values of $\Psi \approx 0.1$ nm and lateral correlation length of $L \approx 1$ nm were obtained. These values agree reasonably well with those determined from transport measurements (cf. section 8.2.4).

8.2.3 Electronic properties of TbSi_2 wires

As a consequence of the stress-mediated uniaxial growth and the silicide formation, the nanowires are in close contact with the Si surface. To see how this influences the electronic properties of the TbSi_2 wires, scanning tunneling spectroscopy (STS) was performed (cf. figure 8.4).

The spatially resolved STS spectra reveal that the central part of the wire bundle has no gap in contrast to the STS spectra taken on the host material. The dI/dV -spectra taken at a distance of about 5 nm from the wire shows basically the Si band gap. The gap is slightly larger as expected which is attributed to tip-induced band bending effects on low-doped surfaces [236]. Most importantly, the Tb induced wetting layer between the wires is insulating, thus not influencing our transport measurements due to parasitic current paths. On the contrary, the band gap vanished in the center of a five-wire wide TbSi_2 bundle. Generally, these results for TbSi_2 wires are in agreement with many studies performed to date on various RESi_2 materials [220, 237–240] using either STS or angle-resolved photoemission spectroscopy (ARPES), which corroborate the presence of metallic states at room temperature.

In order to confirm the STS findings, density functional theory (DFT) calculations were performed in cooperation with the university of Paderborn (SCHMIDT GROUP) to determine the local density of states (LDOS) in different regions of the nanowire-decorated surface. For further information about the calculations see [31]. The structural model of a stable wire

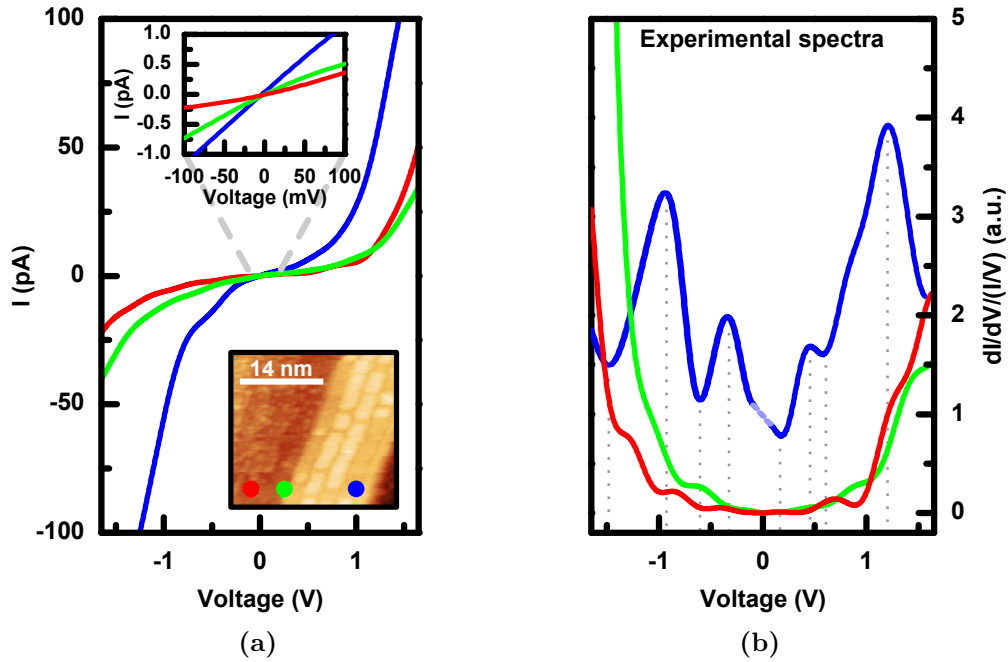


Figure 8.4: Experimental $I(V)$ (a) and normalized $(dI/dV)/(I/V)$ -spectra (b) taken at respective color-coded positions indicated in the STM image in the inset. The color code of the spectra corresponds to the one shown in the inset. The metallic behavior of the TbSi_2 wires is obvious from both the steep $I(V)$ -characteristics (see magnification in inset) and the finite $(dI/dV)/(I/V)$ signal at the Fermi energy.

geometry determined from *ab initio* thermodynamics as well as the space regions representing the sectors defined as *substrate*, *transition* and *on wire* are shown in figure 8.5.

The energy dependent LDOS, which was first derived by this approach for a clean surface, is shown in figure 8.5(a). Additionally, in order to address the origin of states found in the experiment, DFT calculations were performed for hydrogenated surfaces where the surface dangling bonds of both the silicide wire as well as the $\text{Si}(001)$ surface were saturated which is shown in figure 8.5(b). Compared to the substrate, a modification of the LDOS at the Fermi energy is observed in the *transition* region, in reasonable agreement with the experiment as explicitly shown in the inset of figure 8.5(b) comparing the peak position of the experimental spectra with the theoretical calculation. A further remarkable increase of the density of states (DOS) is observed in the *on wire* region, in close agreement with the measurements. As shown in figure 8.5, the removal of surface states due to H adsorption reduces substantially the LDOS in the *transition* region with respect to the clean surface, showing that it is largely related to surface localized states that arise from the rearrangement of the substrate due to the wire formation. H adsorption on the clean $\text{Si}(001)$ substrate region leads to a LDOS that is reminiscent of the Si bulk density of states. The metallicity of the nanowire itself, in contrast, is not affected by H adsorption. Its robustness with respect to surface termination effects is related to the existence of metallic states within the RE nanowire. The mapping of the LDOS onto the different elements (Si, Tb, H) reveals in calculations that the peaks (marked by dashed lines) reflect Tb-Si hybrid states, which are responsible for the metallicity.

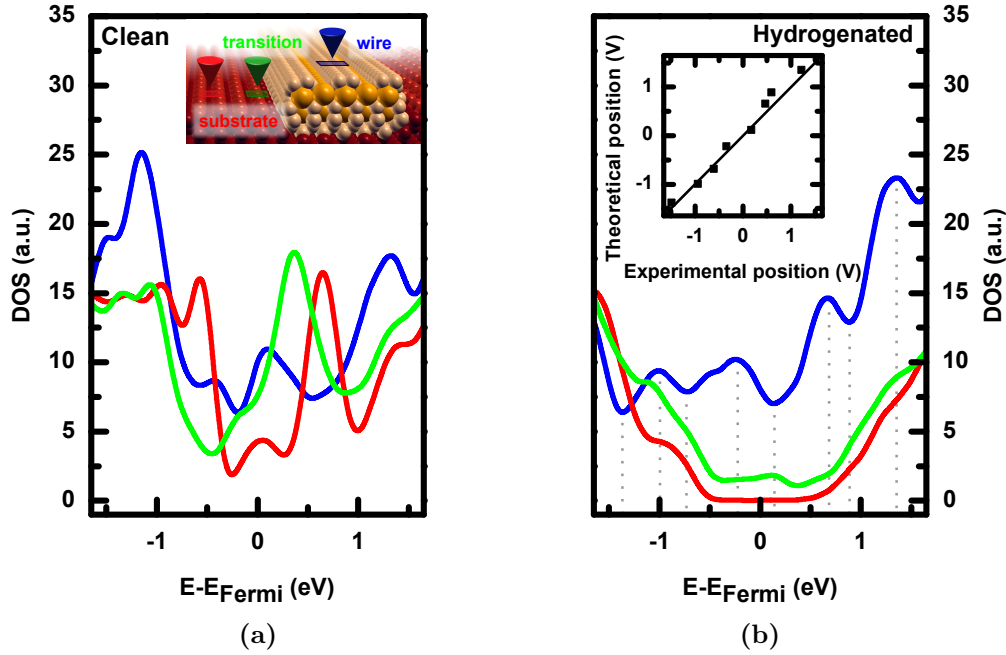


Figure 8.5: (a) The theoretical LDOS in the different space regions of the surface, labeled as *substrate*, *transition*, and *wire* as indicated in the inset. (b) The LDOS for a fully H-saturated surface structure is in excellent agreement with the experiment as indicated in the inset comparing the position of the experimental peaks with the theoretical prediction.

Moreover, the LDOS calculated for a single TbSi₂ wire is in almost perfect agreement with the dI/dV spectrum taken on bundles. This demonstrates that width-dependent strain effects are of minor importance. As shown by a recent TEM investigation, the bundle structure consists of single nanowires as a consequence of the stress developing during growth along the [110] direction [230].

8.2.4 Transport properties of TbSi₂ wires

The electrical transport properties of the TbSi₂ wires were investigated using the multi-probe capabilities of the STM system. Special attention was paid for a gentle approach of the tips in order to avoid, or at least to reduce, damages upon contacting the silicide wires. The following subsections first describe the contacting procedure which differs from the contacting used in the previous for the other material chapters. Afterwards, the results of probe distance dependent measurements as well as the correlation of transport data with the structure of the wires is discussed.

Ohmic contacts via STM tips approached onto single TbSi₂ wires

The approaching procedure is illustrated in detail by the sequence of SEM images shown in figure 8.6. First, the STM tips were brought into the tunneling regime ($V_T = -2$ V, $I_T = 500$ pA) on the free substrate in between the wires (cf. figure 8.6(a)). After turning off the STM feedback control, the tip is retracted by around 50 nm, navigated to the desired position

above the wire and then slowly lowered towards the wire surface in steps of 0.1 nm. As soon as a stable contact between a wire and the tip is reached, the wire appears darker in the SEM image (cf. figure 8.6(b)) caused by the modified negative surface potential. The homogeneity of the contrast along the wire is indicative for its conductivity, while the unchanged contrast of the surrounding substrate indicates a good insulation from the nanowire. Since the SEM contrast remains unchanged by contacting the wire with a second tip, well-defined probe distant dependent measurements become at first feasible. The precise positioning of the second tip at various lateral positions is achieved by biasing the approaching tip with respect to the first one at around 0.5 V. Finally, reliable contacts are realized as soon as the measured current jumps from 10^{-10} A (i.e. the noise level with blanked SEM beam) to about 10^{-7} A.

Despite the gentle approaching procedure, the realization of ohmic contacts deals inevitably with a mechanical impact. As evident from figure 8.6(f) by the white spots visible on top of the wires, the TbSi_2 nanowires show morphological changes upon contacting with the probes. Moreover, the wire resistance is increased if a previously contacted area is between the two contacting probes. Additionally, the same effect was observed if a probe was contacting several times the same position. Both things are an indication for a local wire damage. Therefore, the transport measurements shown in the following sections of this chapter here were all performed starting with largest probe spacings. Because of this technical limitation, collinear four-point probe (4pp) measurements, usually recommended in order to rule-out contact-resistance contributions, were not performed here in favor of two-point probe (2pp) measurements with variable probe spacings. As it will be shown in the context of figure 8.8 in the following subsection, the contact resistances in probe distance dependent measurements are sufficiently small justifying the 2pp approach for this case.

2pp analysis of TbSi_2 wires

Figure 8.7 shows exemplarily 2pp $I(V)$ -curves for a TbSi_2 wire measured at different probe spacings. All $I(V)$ -curves reveal linear characteristics as expected for ohmic contacts between the W tips and a metallic TbSi_2 wire. Moreover, the resistance clearly decreases as the probe spacing between the tips is decreased. In contrast, the inset (a) in figure 8.7 shows the $I(V)$ -curve when one of the tips accidentally contacts the substrate. Besides a Schottky-type characteristic, the current is about two orders of magnitude smaller than that on the wire for comparable voltages. As mentioned already above, this result directly confirms the insulating nature of the wetting layer covering the bare $\text{Si}(001)$ substrate between the wires as well as a sufficiently high Schottky-barrier height to the substrate, suggesting that all the current flows exclusively through the silicide wire (i.e. no significant current paths along the Si substrate). This is further corroborated by inset (b) in the same figure showing a TbSi_2 wire contacted by two STM probes before (left) and after (right) applying a voltage of 20 V. The Joule heating induced by high-current densities ($> 10^8$ A/cm²) preferentially flowing through the wire causes its complete and selective desorption as well as some modifications of the neighboring substrate surface, e.g. by electromigration or by local desorption of the wetting layer.

By fitting every single $I(V)$ -curve of a probe distance dependent measurement, the resistance profile of the nanowires is obtained. Figure 8.8 shows an exemplary 2pp resistance measurement of a TbSi_2 nanowire versus the probe spacing. As expected for a 1D diffusive transport along a wire, the impedance increases linearly with the probe spacing [30]. Inter-

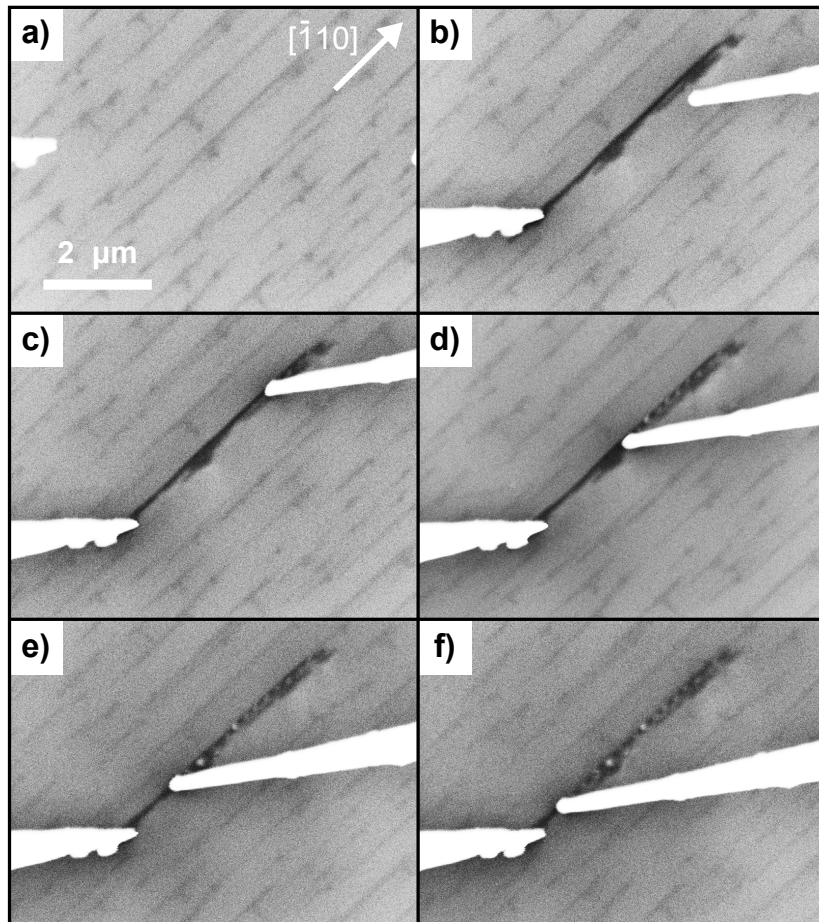


Figure 8.6: Sequence of plan-view SEM micrographs depicting the contacting procedure of a single $5\ \mu\text{m}$ long TbSi_2 wire with two STM probes. (a)-(c) First, the two tips are placed at the ends of the wire, (d)-(e) then keeping fixed the position of one tip, the second one is moved step-by-step towards the first, performing at each position an $I(V)$ measurement in order to determine the wire resistance. (f) Despite the adopted extremely gentle measurement procedure, white spots (marked by arrows) are appearing on the wire and indicate a slight local damage.

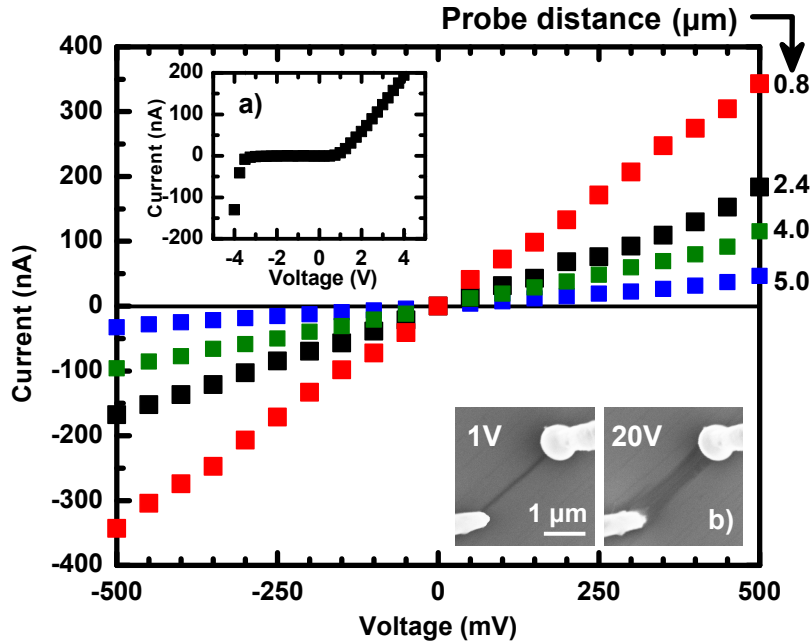


Figure 8.7: 2pp $I(V)$ curves of the same TbSi_2 wire shown in figure 8.6 for various probe spacings. The different slopes reflect the linear decrease of resistance as the two probes get closer. For sake of comparison, inset (a) shows an $I(V)$ -curve when one of the tip accidentally contacts the substrate, while inset (b) shows the wire-desorption induced by Joule heating *after* applying an extremely high voltage of 20 V.

estingly, at around $3.5 \mu\text{m}$ the slope changes drastically. Close inspection of the SEM image (see inset) reveals at this point a reduction in the wire size, which turns out to be responsible for the sudden change of the resistance. The two solid curves in figure 8.8 show therefore two linear fits of the experimental data before and after the wire size reduction, respectively. It needs to be highlighted that the solid curve fitted in the regime without the defect intercepts the origin of the axes, which indicates an almost negligible contact resistance at the wire-tip interface. The resistance per length of the silicide wire is around $26 \text{ k}\Omega/\mu\text{m}$, which increases to $300 \text{ k}\Omega/\mu\text{m}$ when the region with the reduced wire size in this particular wire is probed.

The described approach was now used to analyze the transport properties of different TbSi_2 wires. In total these kind of 2pp transport measurements were performed on almost fifty (homogeneous³) wires of different size and length on several samples, which were prepared with different numbers of initial annealing cycles (cf. figure 8.1). The outcome of such analysis is shown in figure 8.9. Classically, the resistance R of the wire as a function of the probe spacing s is

$$R(s) = \rho s A^{-1}, \quad (8.2.2)$$

where ρ is the wire resistivity and A its cross-sectional area. In a double logarithmic plot of R vs. s , as shown in figure 8.9. $R(s)$ pragmatically appears as $\log(R(s)) = \log(\frac{\rho}{A}) + \log(s)$, which yields identical slopes for different wires, while only the height of the curves varies as a function of the wire resistivity and/or cross section. Different symbols in figure 8.9

³Means only TbSi_2 wires with a constant width along their entire length were considered.

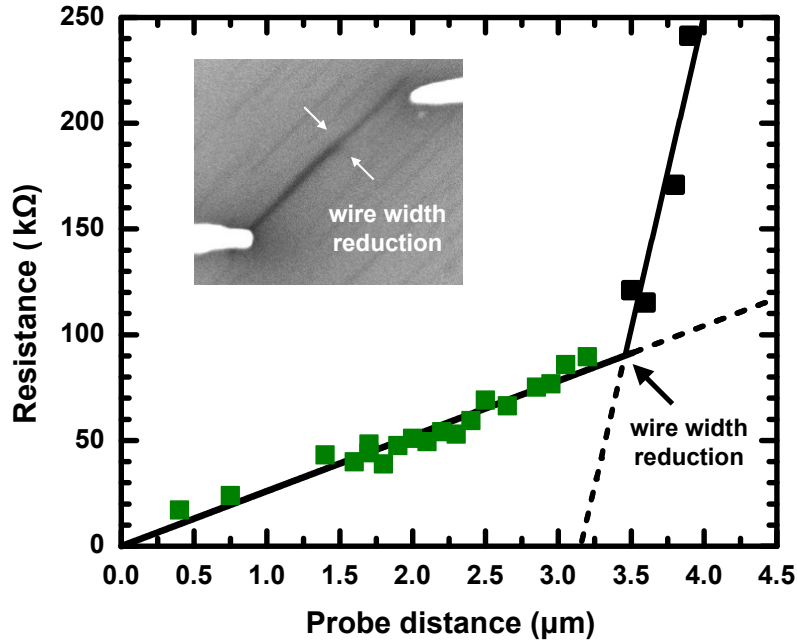


Figure 8.8: Two-point-probe resistance versus probe spacing of a TbSi_2 nanowire. The resistance increases linearly with the probe distance as expected for diffusive 1D transport. Moreover, the sudden change of the slope at around $3.5 \mu\text{m}$ can be attributed to a reduction of wire size (structural inhomogeneity) indicated in the inset.

refer to distinct wires, but same colors are used for wires with a comparable resistance per length. Roughly, three classes of wires, labeled by $w1$, $w2$ and $w3$, can be identified and are highlighted in blue, red, and green with a resistance per length of approximately 1, 0.2 and $0.03 \text{ M}\Omega/\mu\text{m}$, respectively.

Apparently, the formation of the different types of wires depends on the preparation and atomistic details of the Si substrate. For instance, wire types $w1$ and $w2$ are typically observed on samples, which were flash annealed more than 50 times (cf. figure 8.1(c)), while $w3$ refers to the big wires, visible in figure 8.1(a) - (b), that are exclusively oriented along the $[\bar{1}10]$ direction. As it will be shown below, the $w1$ - and $w2$ -type wires differ mainly with respect to their widths. Slightly modified preparation parameters should result in the formation of wires with intermediate widths (between $w1$ - and $w2$ -type). In this sense, the used nomenclature here is rather artificial and accounts only for the findings shown in figure 8.9.

The large range of measured wire resistances can be ascribed to characteristic structural motifs, e.g. to the wire cross section A . Therefore, in order to make a close connection of the transport properties with the atomic structure, for some wires high-resolution STM measurements were also performed (cf. figure 8.10). First, two low resolution STM tips were placed at the ends of a wire and the type of wire according to figure 8.9, i.e. $w1$, $w2$, or $w3$, was deduced from an $I(V)$ measurement. Thereafter, the high resolution STM tip was navigated between the probes to measure locally the topography with high resolution, as shown exemplarily for a $w1$ - and $w2$ -type wire in figure 8.10(c) and (d), respectively. Here, the SEM capability of the measurement setup is a big advantage for the correlation of transport properties with structural characteristics of the wire. This is exemplarily shown

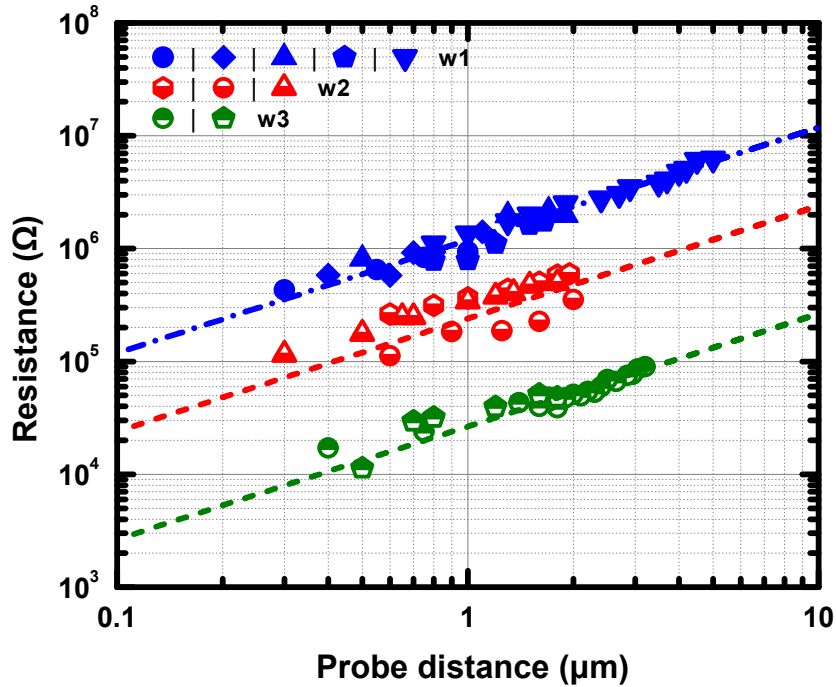


Figure 8.9: Resistance determined by a 2pp geometry for several wires of different lengths and sizes. Three wire classes, named $w1$, $w2$, and $w3$ with a resistance per length around 1, 0.2, and 0.03 $\text{M}\Omega/\mu\text{m}$, are highlighted in blue, red, and green, respectively.

in figure 8.10(a) and (b). Figure 8.10(a) shows a SEM scan, which exactly corresponds to the STM image shown in figure 8.10(b). Obviously, the four scratches (highlighted by white dashed ellipses) at the ends of the two wires marked with $w1$ and $w2$ in figure 8.10(a) and (b) result from the ohmic contacts of the low resolution STM tips. Finally after the structural characterization of the wires, the high resolution STM tip was retracted and the remaining $R(s)$ measurements along the wire profile were performed in order to further rule out the effects of wire inhomogeneities.

The wires marked by $w1$ and $w2$ in figure 8.10(a) and (b), show a resistance per length of $940 \text{ k}\Omega/\mu\text{m}$ and $480 \text{ k}\Omega/\mu\text{m}$, respectively. Both types of wires have a similar height (between two and three silicide layers, i.e. 0.66 nm and 0.99 nm). However, since only the second layer appears entirely continuous in the STM images, an effective height of 0.66 nm is assumed here (corresponding to the red lines in the line scans in figure 8.10(c) and (d)). Indeed, better resolved STM images (cf. figure 8.3 for reference) show an incomplete coverage for the third layer along the wire axis, which does not contribute to the wire current flow while it is mainly responsible for the surface roughness of the wire. The full width at half of the *effective* height of wires $w1$ and $w2$ is around 18 nm and 33 nm, respectively, as indicated by the dashed lines in the line profiles in (c) and (d). For both the $w1$ - and $w2$ -type wires the corresponding resistivity thus results to around $1100 \mu\Omega\text{cm}$, which is roughly one order of magnitude larger than the value reported for a 12 nm thick TbSi_2 film grown on a $\text{Si}(111)$ substrate [241].

As mentioned in the context of figures 8.1 and 8.9, there were also wires observed oriented along the $[\bar{1}10]$ direction, labeled previously $w3$ -type. The STM topography as well as a

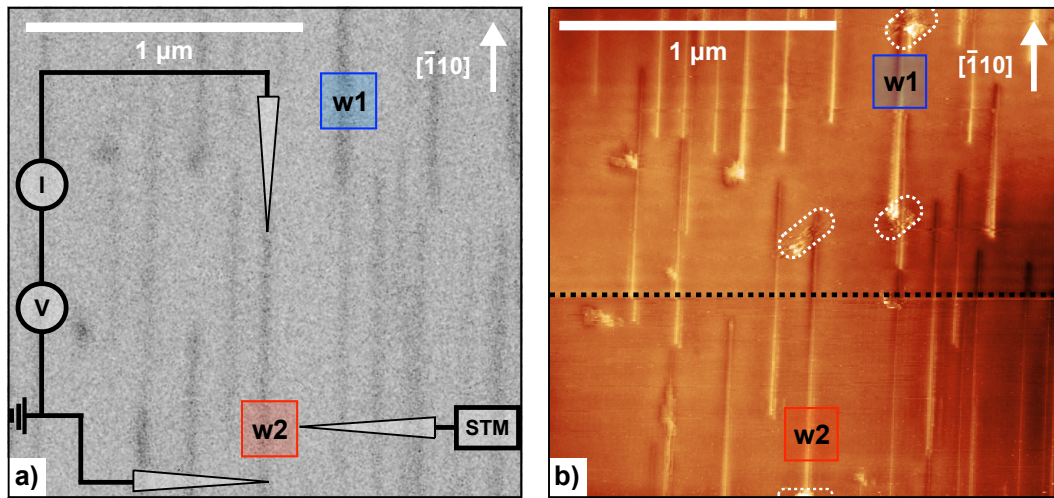


Figure 8.10: SEM (a) and STM (b) micrographs showing the *same* surface area. The schematic drawing in (a) shows how both transport studies as well as STM images of the same wire were obtained. The STM image in (b) ($V_T = 2$ V, $I_T = 100$ pA) is composed by two micrographs connected at the black dashed line. The areas marked by dashed white ellipses show defects induced by contacting procedure for transport measurements. Red and blue framed squares highlight the area shown at higher magnification in figure 8.11.

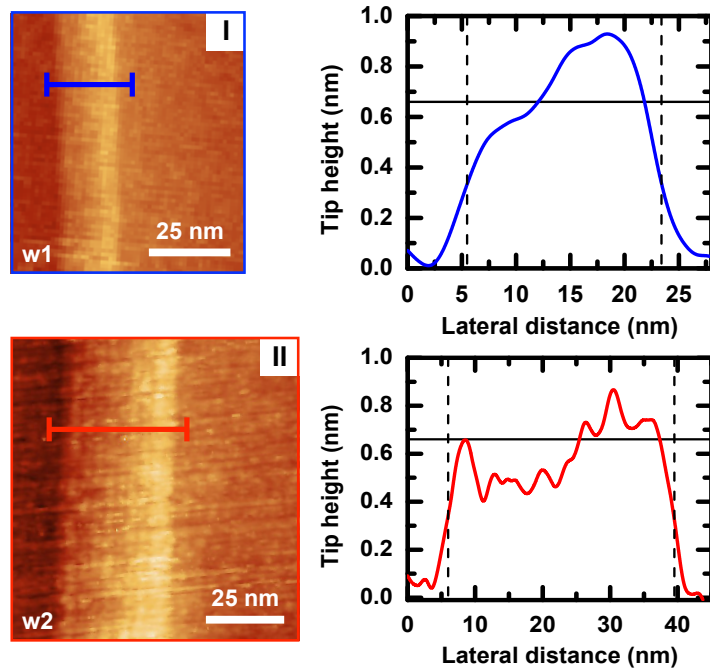


Figure 8.11: Zoomed STM images of the framed areas from figure 8.10. The position of line profiles shown at the right part of the figure is indicated by lines in the STM micrographs.

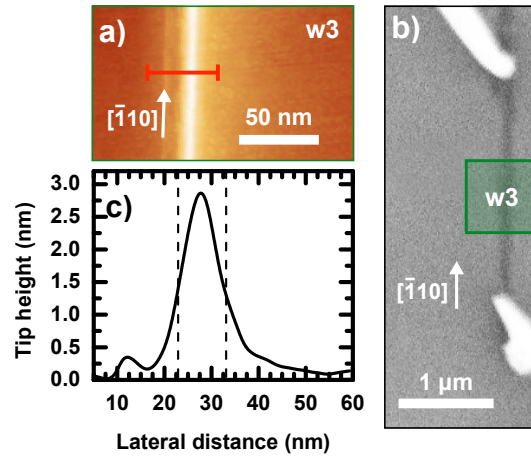


Figure 8.12: (a) STM topography ($V_T = 2\text{ V}$, $I_T = 100\text{ pA}$) of an apparently bigger wire. (b) SEM image showing the 2pp setup for such a wire. The color code corresponds to the one used in figure 8.9. (c) Height profile across the wire taken along the red line shown in (a).

height profile across such a wire is shown in figure 8.12 and yields a width of around 10 nm and height of almost 3 nm. The resistance per length of this wire amounts to $130\text{ k}\Omega/\mu\text{m}$ and refers to a resistivity of $380\text{ }\mu\Omega\text{cm}$. The latter value is closer to the one expected for a compact thick TbSi_2 film [241], suggesting a height-dependent increase for the nanowire resistivity while decreasing the wire size which will be discussed in the following section 8.2.5.

8.2.5 Resistivity size-effects in TbSi_2 wires

As shown in the previous section, the structurally different wires exhibit also different resistivities. For a quantitative treatment of this interesting phenomenon the widths and heights to the resistance per length were correlated. Therefore, seven wires were characterized in detail by STM (see table 8.1 for reference). The lateral width of the wires vary between 10 nm and 110 nm, while the apparent height ranges from 0.67 nm to 9 nm. Finally, with these structural parameters the resistivities were calculated and plotted vs. their apparent height in figure 8.13. Noteworthy, the wire resistivity has no clear dependence on the wire width or cross section, while it strongly decreases with increasing wire height. In the following, different transport models are discussed and compared quantitatively to the experimental findings.

Modeling of the resistivity in nanowires

It is well known from literature that nano-sized materials often exhibit larger electrical resistivities compared to their macroscopic counterparts. This effect is ascribed to additional scattering of the conduction electrons at the material surfaces and/or grain boundaries [242–249] and was first observed by THOMSON [242]. This effect is dominant if the electron mean free path ℓ becomes comparable to the extension of the nano-object. For instance, a free electron density and a bulk resistivity of $n = 10^{22}\text{ cm}^{-3}$ and $\rho_{\text{Bulk}} = 90\text{ }\mu\Omega\text{cm}$ for TbSi_2 at room temperature [241] yields a mean free path of around $\ell = \frac{h}{2ne^2\rho} \sqrt{3n/\pi} \approx 3\text{ nm}$ [250]. Similar

Table 8.1: Structural parameters and transport properties of seven different wires. The resistivities are plotted in figure 8.13 as a function of wire height and can be reliably modeled within the Chatterjee-Meyerovich model. The error bars of the resistivities are calculated assuming an uncertainty of one atomic step for the TbSi_2 nanowire height.

Data point	Height (nm)	Length (μm)	Width (nm)	Resistance ($\text{k}\Omega$)	Resistivity ($\times 100 \mu\Omega\text{cm}$)
1	0.67	1.4	18	1300	11.2 ± 5.6
2	0.67	1.0	34	482	10.7 ± 5.4
3	1.2	1.0	17	402	8.0 ± 2.2
4	2.0	1.0	50	52	5.2 ± 1.7
5	3.0	2.1	10	271	3.8 ± 0.8
6	4.0	3.2	25	90	2.8 ± 0.5
7	9.0	2.9	110	4	1.5 ± 0.1

values were reported for other silicides (e.g. CoSi_2 [251–253] or NiSi [254]). Qualitatively, this already explains why the measured resistivity is so sensitive to the height rather than to the width of the wires. Contributions to the material resistivity originating from grain boundaries, which are usually described in the framework of a classical theory by Mayadas, [249, 255], are not considered here further, since high-resolution TEM investigations [256, 257] reveal that the density of these bulk defects compared to the surface roughness is extremely low.

The apparent width of the investigated wires is larger than their electronic elastic mean free path. However, as mentioned above, the nanowires reveal a substructure. From a recent TEM [230] study it turns out that they consist of single wires with an average width of only 2.2 nm, which are separated from each other by atomically thin (≈ 0.3 nm) grooves. The grooves between these subunits are atomically smooth ($\Psi_{\text{lateral}} = 0$), as seen from STM. Therefore, as it will be shown below, the resistivity of the wires is not affected by their limited width. Moreover, the radius of the current probes is always larger than the apparent width of the wires, so that all nanowires in a bundle are contacted. This justifies the approach to evaluate the transport data in terms of an effective width.

Classical description of resistivity size effects

Within a classical approach the transport phenomena in nano-sized structures were described first by FUCHS [245] introducing a specular parameter p , i.e. the fraction $(1 - p)$ of electrons scatters diffusively at the surfaces and interfaces, thus reducing the mean free path and, consequently, increasing the resistivity. FUCHS [245] derived a theoretical expression for the case of a thin film solving the Boltzmann's transport equation. Since the component of electron momentum parallel to a electric field is not conserved in the case of a diffusive scattering, the related mean free path is consequently reduced. The resistivity is inversely proportional to the mean free path ℓ therefore the resistivity naturally increases if the mean free path is reduced. This effect increases as the film thickness reduces because of a larger surface to volume ratio. Analytically, the ratio of the resistivities between bulk and film of

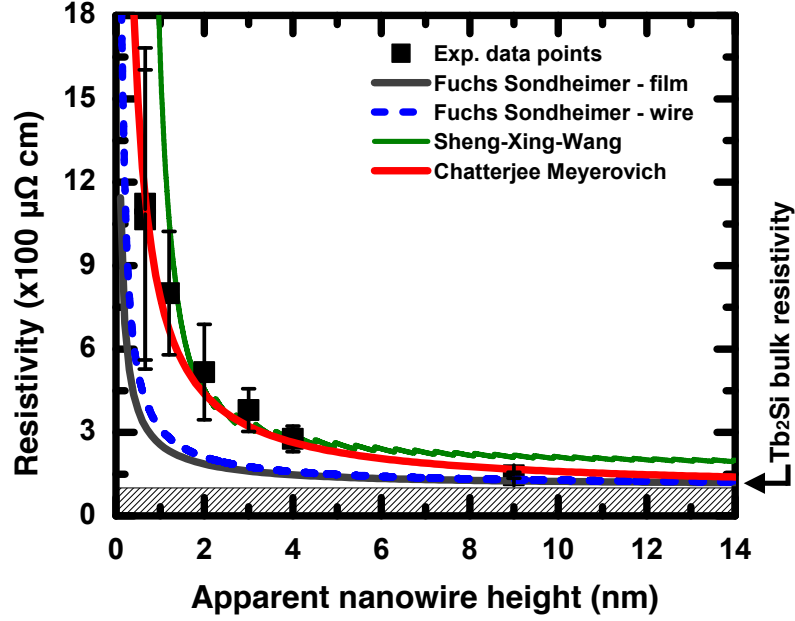


Figure 8.13: Calculated resistivity vs. the apparent height of the $TbSi_2$ nanowires revealing a strong decrease with increasing height. The solid and dashed lines are deduced from classical and quantum theories.

thickness t is expressed as [243, 245]:

$$\frac{\rho_{\text{Bulk}}}{\rho_{\text{Film}}} = 1 - \frac{3\ell}{2t}(1-p) \int_0^{\pi/2} \cos \xi \times \sin^3 \xi \frac{1 - \exp\left(-\frac{t}{\ell \cos \xi}\right)}{1 - p \exp\left(-\frac{t}{\ell \cos \xi}\right)} d\xi \quad (8.2.3)$$

The theory was revised by SONDHEIMER [250] and extended to wires of square and circular cross section by MACDONALD et al. [246] and DINGLE [247] respectively, while just lately the corresponding result for wires of rectangular cross section were published [243, 248, 258]. Although a solution for the latter case was obtained only for a perfectly diffuse scattering, since the Boltzmann's equation can not be solved for $p \neq 0$ [248]. Since the investigated $TbSi_2$ wires have an average width-to-height aspect ratio $\mu \approx 10$, tentatively both the original Fuchs model for a continuous thin film (cf. equation (8.2.3) - corresponding to the gray solid curve in figure 8.13) and the revised version for rectangular wires (corresponding to the blue dashed curve in figure 8.13 using the model by MORAGA et al. [248]) were applied. For the sake of comparison, a complete diffuse scattering at the surface ($p = 0$) for both models was assumed, while the bulk-mean-free path and resistivity for $TbSi_2$ material is taken from [241]. It is evident that the revised Fuchs model for rectangular wires predicts only a modest increase with respect to a continuous film because of relatively large wire aspect ratio $\mu \gg 1$ and both models justify only in part the observed resistivity increase.

Along the timespan of almost 80 years both the original Fuchs model and the several later revised versions often were not capable of describing the observed resistivity dependence with sample sizes. This happens systematically in the sub-50 nm thickness interval [259–264] (i.e.

in the limit of ultra-thin films), where one or more of the simplifying assumptions of the model inevitably fail. Indeed:

- (i) the Fuchs theory is based on the classical Boltzmann's equation and assumes a free-electron-like description for the metal with a spherical Fermi surface,
- (ii) it does not explicitly include the contribution coming from surface roughness, which naturally increases the effective film surface and related resistivity, and
- (iii) it simply adopts a single specularly parameter p independent of the electron energy and of the angle of incidence to the surface.

While the first assumption is probably reliable until the film thickness $t \gg 100$ nm, however it should eventually fail when the energy-level spectrum becomes discrete. On the other hand, the latter assumption was already questioned in the 1960's by ZIMAN [265], who derived in the Kirchhoff formalism an angular dependent specularly parameter (also function of surface roughness), which is expressed as:

$$p(\phi) = \exp \left[\left(-\frac{4\pi\Psi}{\lambda_F} \right)^2 \cos^2(\phi) \right], \quad (8.2.4)$$

where Ψ is surface film roughness and λ_F is the Fermi length. SOFFER [266] implemented this specularly parameter inside the original Fuchs equation [267], while SAMBLES [268] extended it to the circular wire case, and several authors applied extensively this formula to describe the thickness-dependent resistivity of sub-50 nm thick epitaxial metallic films, but usually deriving meaningless parameter values. Indeed, equation (8.2.4) predicts a specular scattering only for $\Psi \ll \lambda_F$ (where λ_F is of the order of fews Å for metals), and questionable roughness values of few tenth of Å are often reported in literature[268–272], while converges to zero (i.e. to the Fuchs equation in the fully diffusive regime) for $\Psi \gg \lambda_F$, with neither describing the additional resistivity caused by larger effective film surface and energy spectrum discreteness nor solving the discrepancy observed for the data reported in figure 8.13.

Lately, authors propose also the introduction of additional empirical parameters in order to describe the contribution coming from surface roughness and recover the experimental discrepancy in the ultra-thin film regime. Interested readers are refereed to the original papers[273, 274]. Although the latter models successfully fit the presented data, the fitting parameters are not unique, the physical meaning of phenomenological parameters is questionable and the details of scattering mechanisms are completely inaccessible.

All these factors suggests the adoption of a better theory, which uses the informations coming from the surface topography analysis as given by roughness and its correlation length, considering the discrete nature of energy spectrum in the mesoscopic range and allowing to overcome the described shortcomings.

To summarize the pitfalls of a classical approach: The Fuchs theory is based on the classical Boltzmann equation and relies on the model of a nearly free electron gas. Most severely, it does not explicitly include surface roughness and adopts a p -parameter independent of the electron energy and of the angle of incidence to the surface. It will be shown in the following that the surface morphology, parametrized by the rms-roughness Ψ and the correlation length L , indeed are the key characteristics for a quantitative description. Technically, the angular

dependency of the p -parameter can be tentatively considered [265]. However, in this system the Fermi wavelength λ_F is comparable to the surface roughness, which causes a fully diffusive scattering behavior, i.e. $p = 0$.

Quantum models for resistivity size effects including surface roughness

More realistic models are based on a quantum mechanical description considering details of the surface topography, i.e. roughness Ψ and correlation length L , as well as potential effects of electronic confinement [264, 275–279]. The limitation of these theories is that they were solved for thin films rather than for wires. However, as seen in the context of the classical description, lateral constrictions only marginally affect the resistivity values. Here, in the following theories elaborated by SHENG, XING, and WANG [276] (in the following SXW MODEL) and the CHATTERJEE and MEYEROVICH [277] model (CM MODEL) will be used to describe the data.

The SXW MODEL, based on the Kubo formalism in real space [280], considers both bulk and surface scattering. While for $t \gg \ell$ the model transforms into the Fuchs model (cf. equation (8.2.3)), it almost reproduces for $t \ll \ell$ the description of TRIVEDI et al. [264] and the resistivity of the film can be expressed by:

$$\rho_{\text{Film}}(t) = \left(\frac{2e^2}{\lambda_F \hbar k(t)} \times \sum_{n=1}^{n_c(t)} \frac{1 - n^2/k(t)^2}{\frac{2n_c(t)+1}{\frac{2\pi}{\lambda_F} \ell k(t)} + \left(\frac{2\pi^2 L \Delta}{\lambda_F t} \right)^2 \frac{S_{n_c(t)} n^2}{n_c(t)^3 k(t)}} \right)^{-1} \quad (8.2.5)$$

Here, $k(t) = 2t/\lambda_F$, $n_c(t) = \text{Int}(k(t))$ denotes the number of occupied subbands, λ_F is the Fermi wavelength, and $S_{n_c(t)} = n_c(t)(1 + n_c(t))(1 + 2n_c(t))/6$. The first term in the denominator inside the summation of equation (8.2.5) represents the bulk scattering, while the second is responsible for the surface scattering [279] and is taken into account via the Mathiessen rule approximation. For the case that the bulk contribution is negligible, equation (8.2.5) reduces to the result reported by FISHMAN et al. [279]. Besides effects of the surface roughness, equation (8.2.5) is additionally taking into account lateral correlation effects.

In the context of the quantum model from CHATTERJEE and MEYEROVICH [277], considering the rough surface by an appropriate mapping onto an equivalent bulk Hamiltonian [281], the thin film resistivity is given by [277]:

$$\rho_{\text{Film}} \approx \frac{m}{ne^2} \left[\frac{1}{\tau_{\text{tr}}^b} + \frac{16\sqrt{2\pi} E_F \Psi^2}{p_F \lambda_F L t} + \frac{10\sqrt{2} E_F \Psi^2}{\sqrt{\pi} p_F \lambda_F L t} \times \left(\frac{\hbar}{2\tau_b E_F} \frac{\lambda_F^2}{L^2} + \frac{\lambda_F^2 m}{2\tau_b^2 E_F} \right) \right] \quad (8.2.6)$$

Here τ_{tr}^b and τ_b denote the electron bulk transport and collision time, m is the electron mass, and E_F , p_F , and λ_F are the Fermi energy, momentum, and wavelength, respectively. Effectively, equation (8.2.6) should be considered as a semi-classical description, since the summation over the subbands was replaced by an integration of the density of states. The first terms represent the bulk and surface scattering, similar to the SXW MODEL. In contrast, the remaining two terms describe the effect of interference between the surface and bulk transport channels. Indeed, there is clear evidence that the Mathiessen rule is violated in the proximity of mean free path thickness [278, 282] where the bulk and surface-scattering

processes are not necessarily independent, but may strongly interfere with each other. Note that this contribution is inherently neglected in the SXW MODEL, which adopts a white noise approximation (i.e. small correlation lengths).

Both models were applied to the resistivity dependence shown in figure 8.13. It was assumed a Fermi wavelength for TbSi₂ material of $\lambda_F = (8\pi/3n)^{1/3} \approx 0.94$ nm, and an electron bulk transport time $\tau_{tr}^b = (m/e^2n\rho_{Bulk}) \approx 3 \times 10^{-15}$ sec, which is also comparable to the collision time τ_b since the Debye temperature of TbSi₂ amounts to $\Theta_D \approx 260$ K \leq 300 K [241]. The green solid curve in figure 8.13 reveals the best fit of the experimental data using equation (8.2.5) with a surface roughness of $\Psi_{SXW} \simeq 1.9 \pm 0.3$ Å and a correlation length of $L_{SXW} \simeq 2.9 \pm 0.2$ Å, while the red curve is the best fit using equation (8.2.6) and yields a roughness of $\Psi_{CM} \simeq 0.2$ nm and a correlation length of $L_{CM} \simeq 0.8$ nm.

As shown above, STM reveals roughness values of $\Psi \simeq 0.1$ nm and $L \simeq 1$ nm, which almost perfectly agree with those of the CM MODEL. Any height-dependence of Ψ and L is neglected in this discussion.

It is evident that both models nicely reproduce the resistivity increase with TbSi₂ wire height shown in figure 8.13. The trend to underestimate the correlation length in the SXW MODEL is most likely ascribable to its assumptions and certain boundary conditions. Indeed, equation (8.2.5) is valid only in the limit of small correlation lengths [264], or more precisely until $k_1L \ll 1$ [279] (where k_1 is the largest of the Fermi wave vectors k_n of subband n), which is roughly corresponding to $L < 3$ Å in the shown case and is clearly experimentally disobeyed. Moreover, FISHMAN et al. [283] showed that the surface contribution within equation (8.2.5) strongly changes when $k_1L \gg 1$ and needs to be replaced by an $n \times n$ matrix, which they explicitly evaluated for the surface scattering term only (i.e. neglecting the contribution coming from the bulk). Although incomplete, this analysis showed that the surface scattering decreases by several orders of magnitude for high quality surfaces (i.e. $L \gg 1$ nm). Thus, a pronounced decrease in the resistivity of as-grown TbSi₂ is expected, if the growth process is stopped once a complete layer is formed. This is also evident from the semi-classical description of CHATTERJEE et al. [277], where the leading terms in equation (8.2.6) reveal a $1/L$ dependence.

Finally, it needs to be pointed out that the SXW description is strictly valid only in the limit of the white-noise approximation (i.e. assuming a quasi uncorrelated surface or $L \ll 1$ nm). For a correlated surface roughness MUNOZ [284] recently derived a new modified SXW expression based on weaker constriction ($\Psi^2 k_F \ll L$), which is however typically satisfied at low temperature only.

8.3 Summary and outlook

In this chapter the growth of TbSi₂ wires on vicinal Si(001) substrates were comprehensively characterized by means of a multi-tip STM/SEM system. The experimental setup allowed to analyze the transport properties of individual Tb silicide wires and correlate the transport findings with the atomic structure. A STS analysis revealed that the wires are electronically decoupled from the Si substrate in agreement with DFT calculations performed in cooperation with the university of Paderborn (SCHMIDT GROUP). In contrast to previous studies [77, 208] on RE silicide nanowires, transport measurements were performed directly using the STM tips without any need of further supporting contacts. This is a big advantage because any

contaminations resulting from an additional *ex-situ* processing steps can be excluded by this *in-situ* approach.

In the transport experiments it was seen, that depending on the details of the preparation, several classes of wires were found with distinct resistance values per lengths. For a better understanding, the wires were additionally characterized in detail by STM. It was observed that, in contrast to their widths, the heights of the wires vary by an order of magnitude being comparable or even smaller than the characteristic electron mean free path. Most importantly, the analysis showed that the resistivity values of these wires are strongly increasing with decreasing height. Albeit the experimental parameters cannot be entirely considered by current theories, it was succeeded in a quantitative description of this finding on the basis of the CHATTERJEE and MEYEROVICH [277] model assuming coherence effects between surface and bulk transport channels, showing both the importance of surface and bulk channels as well as of the atomistic roughness on these wires. Moreover, the roughness parameters deduced from the data analysis agree very well with those determined from the STM analysis.

Decoration of TbSi₂ nanowires

Up to now, the transport properties of TbSi₂ nanowires were only studied at room temperature. As mentioned in the introduction, silicide nanowires as quasi-1D can exhibit very interesting physical properties, e.g. upon cooling van Hove type singularities [73] or a metal-insulator transition (MIT) [77]. Thus as next step, it seems logical to also probe the transport properties of the TbSi₂ nanowires by temperature dependent measurements. The current used contacting procedure has some issues if one wants to perform a temperature dependent study of the transport properties of the wires. As discussed in section 8.2.4, the nanowires are always showing a mechanical impact in terms of scratches as visible in the SEM images in figure 8.6 and STM image in figure 8.10 after contacting. Additionally, it was observed that the resistance of the wire is increased if the probes were contacting an area several times or if a probed area is in between two contacting probes. Both is indicating a local wire damages by every contacting process. This was the reason why after every transport measurement, the distance between contacting probes was decreased respectively position of the probes was changed. But, for temperature dependent measurements the position of the probes needs to be fixed.

To overcome this issue, an idea would be to adopt for the contacting of TbSi₂ wires an approach which was already utilized successfully by QIN et al. [285] on GdSi₂ silicide wires. QIN et al. [285] demonstrated that gold nano-islands deposited by a field-induced emission process from a Au-coated tungsten STM tip work as a reliable bridge between the probed silicide nanowires and transport probes. The process is illustrated in detail in figure 8.14(a) and is based upon the work of MAMIN et al. [286] who were the first reporting a field-induced material transfer process from an STM tip to a surface in general. For the fabrication of the gold droplets on TbSi₂ wires, a Au-coated STM tip is first brought into tunneling contact at the desired position on the nanowire. Afterwards, the STM feedback loop is turned off and a bias voltage of 15 V is applied (negative potential at the tip). Then the tip is lowered in 0.1 nm steps towards the nanowire while measuring the current between sample and tip. Gold deposition is observed to start for currents of $\sim 1 \cdot 10^{-7}$ A. During deposition, the measured current rapidly increases. Depending on the used cut-off current for stopping the

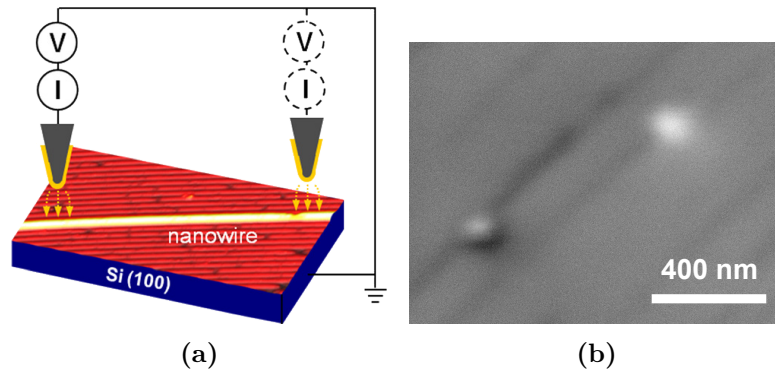


Figure 8.14: (a) Schematics illustrating the fabrication of gold droplets on silicide wires using an Au coated tungsten tip (adopted from [77, 285]). (b) SEM image illustrating two successfully fabricated gold droplets on two separate TbSi_2 nanowires. The difference in contrast of the droplets in SEM was not further analyzed and is most likely due to charging effects since also one of the contacted nanowire appears slightly darker.

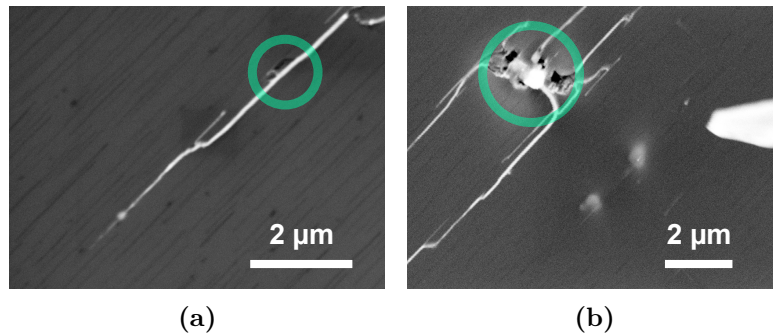


Figure 8.15: SEM images showing gold coated TbSi_2 wires in detail. Residuals of the Au-coated tungsten tip respectively defects after retracting of the tips are encircled in turquoise color.

deposition and the total deposition time, droplets of 50 - 150 nm diameter could be fabricated. Small droplets of 50 nm diameter could be achieved with a cut-off current of $\sim 1 \cdot 10^{-6}$ A and large droplets of 150 nm were observed with cut-off currents of $\sim 1 \cdot 10^{-4}$ A (cf. exemplarily figure 8.14). Since the area which was scratched by contacting is typically around 100 nm (cf. figure 8.10(b)), it was aimed to optimize the deposition parameters for getting large droplets ≥ 100 nm (cf. figure 8.14(b) illustrating the fabrication of 150 nm gold droplets on TbSi_2 wires).

While the successful fabrication of Au droplets of 150 nm diameter on TbSi_2 wires is exemplarily shown in figure 8.14(b), further optimization to increase the reliability of the used procedure is strictly necessary before temperature dependent measurements can be performed: The increase of the current from $1 \cdot 10^{-6}$ A to $1 \cdot 10^{-4}$ A is most of the time faster than the sampling time (ms range) of the used setup and often higher current above the set cut-off value were obtained.

Most interestingly, for currents $\geq 1 \cdot 10^{-3}$ A a Au coating of TbSi_2 wires was observed (cf. figure 8.15). This process could even be reliably triggered if instead of biasing a voltage

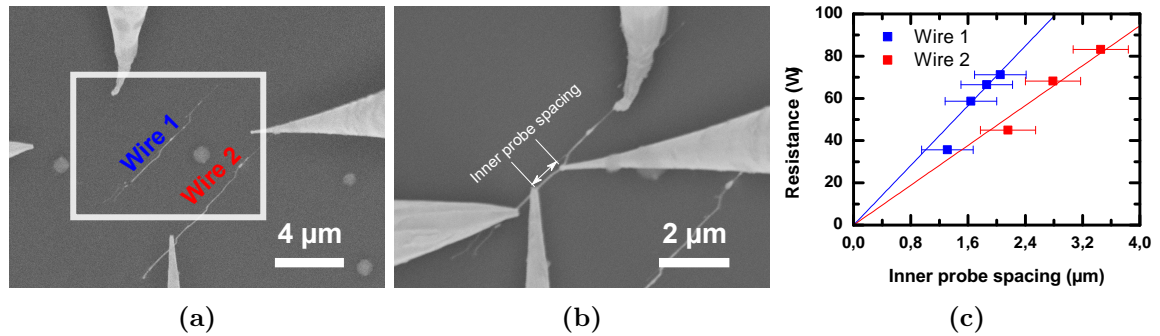


Figure 8.16: (a) SEM image of two gold coated TbSi₂ wires with different lengths (Wire 1 9 μm, wire 2 12 μm). (b) SEM image showing the contacting of the wire by a linear 4pp arrangement. (c) Resistance profile of the two wires displayed in (a). The error bar of the x -axis was estimated from tip apex as seen in SEM.

between gold coated tip and sample, the voltage was biased between a tungsten tip, which was already in ohmic contact with the TbSi₂ nanowire, and the gold coated tip. The analysis of SEM images indicates that those high currents are occurring with high probability when the deposited material is enough for forming a contact between gold coated tip and TbSi₂ wire (cf. encircled areas in figure 8.15 showing residuals of the tip after retracting). If a contact of gold coated tip and TbSi₂ wire is obtained, material is transferred along the current paths of conducting TbSi₂ wires indicating a Joule heating related effect. The resistance of these wires was roughly analyzed by means of the 4pp setup showing clearly a 1D behavior with more than three orders of resistance decrease (cf. figure 8.16) in comparison to the pristine TbSi₂ wires.

Summary

Within the scope of this thesis three different metallic atomic wire systems grown on silicon substrates by self-assembly were investigated (In/Si(111)- 4×1 , Si(hhk)-Au and TbSi₂ nanowires). The investigations focused on the transport properties and defect related effects. Measurements were performed by means of a four-point probe (4pp) scanning tunneling microscope (STM)/scanning electron microscope (SEM) system in combination with spot profile analysis low-energy electron diffraction (SPA-LEED). In addition, within a cooperation with the SCHMIDT GROUP from the university of Paderborn, multiple density functional theory (DFT) calculations were performed which further supported the findings of the experimental results.

9.1 Analyzed systems

9.1.1 In/Si(111)-(4×1) reconstruction

The In/Si(111)-(4×1) is up to now the most comprehensively studied system in literature. While the metal-insulator transition (MIT) occurring at ~ 120 – 130 K is reasonably explained by a Peierls-like first order transition, the tuning of critical temperature T_C by adsorbates is still not completely understood: A decrease of the MIT temperature is observed for many adsorbates like e.g. H, In while contrary the adsorption of O leads to an increase of T_C . In addition, the anisotropy ratio $\sigma_{\parallel}/\sigma_{\perp}$ reported for the In/Si(111)-(4×1) varies strongly from values of around 60 [83] in 2003 to 7 [129] in 2012 which was attributed to different defect density.

Thus, to increase the sensitivity toward defects, transport measurements were performed on infinite and spatially restricted areas for a better sensitivity toward defects. As predicted by theory, transport in finite areas showed more pronounced resistances compared to the unrestricted case. Using this setup, the conductivity parallel and perpendicular to the atomic chains was analyzed in detail during adsorption of molecular oxygen. Concerning the question of the influence of defect structures, it could be shown in agreement with DFT calculations that there is an effective interwire coupling which is influenced by oxygen adsorbates. Therefore, the conductivity parallel and perpendicular to the chains is described by the sum of the conductivity of the surface states as well as the contribution of conductivity of the isotropic space-charge layer (SCL). In accordance with literature [129], it has been shown in addition

that the SCL contribution is increased by elevated flash annealing temperatures. Moreover, the transport along and perpendicular to the wire was calculated in a coherent transport model. The calculated decrease of the transmittance in dependence of the adsorbed oxygen fits in good agreement the experimental data.

9.1.2 Si(hhk)-Au

In contrast to the In/Si(111)- 4×1 reconstruction, the Si(hhk)-Au system is of peculiar interest since physical properties can be altered very easily by the vicinality leading to different structural building blocks of the system (single or double Au chains, Si-adatom chain, Si-honey comb (HC) edge). Within this thesis the Si(557)-Au and Si(553)-Au surfaces were studied in detail. The Si(557)-Au consists of a single gold atom chain, an adatom chain surrounded by restatoms and a Si-HC part at the step-edge. In contrast, the Si(553)-Au consists of a double Au chain and a Si-HC structure at the step-edge.

In respect to the question how defects effect the transport in the atomic chains, a detailed study was performed regarding the stability of the surfaces against defects induced by molecular oxygen adsorption. In combination with low-energy electron diffraction (LEED), the analysis showed, that the Si(553)-Au surface is rather immune against oxidation while the Si(557)-Au surface revealed a strong decrease of the conductance which is very comparable to the behavior of the In/Si(111)- 4×1 reconstruction. This decrease was rationalized by a complete destruction of the Si-adatom ordering along the chains. In addition, the experimental findings were further backed up by DFT calculations highlighting that the cause of the metallic surface bands along the wires are of different origins.

The transport measurements on Si(hhk) also highlighted the influence of parasitic transport channels like SCL which is crucial for the understanding of transport experiments on atomic wire systems in general. It was found that the formation and width of the SCL, which was best described by a p-type layer formed by C contaminations resulting in interstitial defects, is strongly depending on the initial doping of the semiconductor. Since the formation of a SCL can not be prevented and is inherent to the sample preparation this has severe consequences. For small SCL (as in the case of high doped samples) electrons are more affected by scattering at ionized bulk donors than for the case of low doped samples with large SCL. Thus, it was observed in experiment that samples with as a high doping ($N_D \sim 10^{18} \text{ cm}^{-3}$) showed high conductivity ratios of around 15 while samples with a low doping $N_D \sim 10^{12} \text{ cm}^{-3}$ only showed ratios of around 2. In addition, this effect rationalizes the different conductivity ratios published in literature for the In/Si(111)- 4×1 .

A second focus was set on an investigation of the MIT of the Si(553)-Au since the nature of the phase transition - especially concerning an electronic phase transition - is still under current debate. The MIT of the Si(553)-Au was studied in detail in a combined 4pp and SPALEED study. In accordance to literature, a structural phase transition of the $\times 3$ reconstruction was observed for the Si(553)-Au. Notably, at the same temperature at which a structural phase transition was observed, the sample still showed a residual conductivity along the chains in the transport experiments. Thus, it was discussed that there is no formation of a charge density wave (CDW) due to the $\times 3$ phase. This finding was discussed in terms of a transient doping which shifted the $\times 3$ phase transition within transport experiments, an activated and band mediated transport, or a partial Peierls transition. However, the partial

Peierls transition seems to be the most reasonable explanation within the discussion. Further DFT calculations of the band structure in combination with the results of this thesis will help to deepen the understanding of the phase transition of the Si(553)-Au system.

9.1.3 TbSi₂ nanowires

The third part of the thesis treated TbSi₂ silicide nanowires grown on Si(001) wafers. These nanowires are in clear contrast to the previously examined systems. While the In/Si(111)-(4 × 1) and the Si(hhk) system form ensemble of atomic wires on the surface, rare earth (RE) elements form very long, thin and well separated either single or bundled nanowires depending on the used growth parameters whose atomic structure is related to bulk properties. Thus, in comparison to the In and Au system, transport experiments mainly measure bulk effects and not the surface states.

It could be shown in combination with a high resolution STM, STS and DFT study that the silicide wires are electronically decoupled from the Si template. However, the transport properties of these wires in terms of resistivity are heavily altered by their surface morphology. The transport in such wires could be qualitatively fitted by a theoretical quasi-classical transport model which is taking into account the atomic-scale surface roughness as well as the lateral surface correlation. The calculated roughness and correlation lengths match the experimentally determined values from the STM study.

9.2 Outlook

Future research objectives should concentrate further in systematic studies on how the observed effects feedback to physical properties. Thus, the following aspects should be in the focus of future transport related research on these systems:

- Systematic variation of the step density
- Adsorption of impurity atoms as well as the effect of excess coverages

Chapter 6 showed that the anisotropy ratios $\sigma_{\parallel}/\sigma_{\perp}$ vary strongly within literature for the In/Si(111)-(4 × 1) system (cf. especially table 6.1). The anisotropy measured within this thesis was around 2, i.e. a factor of 30 lower compared to the highest value reported in literature [83] but only around the half of the latest published value 7 of the same group [129]. However, there is also a deviation within the used miscut angles. Since the influence of substrate steps have not be explicitly studied within literature and was basically just used to trigger single domain structures, a systematic study of the miscut angle of the Si(111) templates will help to understand the role of Si-surface steps better and its influence on the In phases (4 × 1) ↔ (8 × 2). In addition, up to now there is also no study concerning the role of steps on the MIT of the In/Si(111)-(4 × 1) system. It is assumable that the phase transition temperature will shift due to change of stability of the phase in respect to the Si-step edges. Future transport studies with gradually varied inclination angles in combination with STM will shed light on this question.

After a better understanding of the influence of the SCL, further transport measurements on the Si(hhk)-Au concerning the phase transition are highly interesting. Up to now, the

influence of adsorbates on Si(hhk)-Au is rarely analyzed. First measurements by reflectance anisotropy spectroscopy (RAS) indicate a reversible effect on the MIT by adsorption of H atoms which shift the critical temperature T_C to higher temperatures [287]. This effect should be easily observable in transport experiments. Thus, further systematic transport measurements on Si(hhk)-Au with adsorbates will help to clarify the understanding of the nature of the MIT and the dependence on the adsorption sites and modification of inter- and intrawire couplings.

Previous transport studies on the phase transition of Si(557)-Au were reported to have only an activation-type insulating character [188]. This is intriguing since the temperature dependence observed in angle-resolved photoemission spectroscopy (ARPES) and STS for the Si(553)-Au [38, 70] is similar to the one on Si(557)-Au [165, 220]. However, the measurements published in literature [188] were only performed in a linear 4pp configuration so that the contribution of conduction along the chains can not be disentangled from bulk contribution as performed in chapter 7. Therefore, an investigation of the Si(557)-Au using the 4pp approach used in this thesis, which is sensitive to conduction along and perpendicular to the wires and allows to disentangle the contribution of the SCL, in combination with a structural analysis would be very helpful to shed light in to this intriguing inconsistency.

In addition to Si(553)-Au and Si(557)-Au, there are two other known vicinal surfaces namely the Si(335)-Au and Si(775) which are less discussed in literature. In a first glance concerning the structural motif of single Au row or double Au strand, the Si(335)-Au is similar to the Si(557)-Au while the Si(775)-Au is comparable to the Si(553)-Au. But up to now, there are no transport studies covering these two systems. Therefore, systematic studies will deepen the understanding of the structural motifs of the Si(hhk)-Au family and the interplay in respect to their physical properties.

Concerning the transport properties of TbSi_2 silicide nanowires, it would be interesting to study in more detail the role of local defects, i.e. local height variations, wire width and grain boundaries, as well as the transport in these nanowires depending on the temperature. It was very recently shown by APPELFELLER et al. [230] within a STM and transmission electron microscope (TEM) study that TbSi_2 silicide nanowires maintain their structural properties after being capping by several nanometers thick amorphous Si films. In respect to possible applications of those silicide nanowires in future devices, it would be highly interesting to get further insights in the transport properties of capped wires.

Part IV
Appendix

Calculation of the SCL conductance

As motivated in section 2.3 the space-charge layer (SCL) is described by solving the Poisson's equation.

$$\frac{d^2\Phi(z)}{dz^2} = -\frac{\rho(z)}{\epsilon_0\epsilon_B}, \quad (\text{A.0.1})$$

where ϵ_B is the relative permittivity of the semiconductor bulk and $\rho(z)$ the charge density, which is depending on the density of ionized acceptors N_A and donors N_D , and the concentration of the electrons $n(z)$ and conduction holes $p(z)$, respectively:

$$\rho(z) = e(N_D - N_A + p(z) - n(z)). \quad (\text{A.0.2})$$

Φ is the potential variation, i.e. the band bending, near the surface which is given by the deviation of the intrinsic level E_i from the Fermi energy E_F :

$$\Phi(z) = \frac{1}{e}(E_F - E_i(z)) \quad (\text{A.0.3})$$

Following the arguments outlined in [78, 80] the conductance through the SCL was numerically deduced in this thesis. It is convenient to define the dimensionless potential u

$$u(z) = e\Phi(z)/(k_B T), \quad (\text{A.0.4})$$

which allows to express the spatially varying carrier concentrations in a space charge layer by

$$n(z) = n_i \exp(u(z)) \quad (\text{A.0.5})$$

$$p(z) = n_i \exp(-u(z)) \quad (\text{A.0.6})$$

with n_i as the intrinsic carrier concentration. By defining $u_B \equiv u(z \rightarrow \infty)$ it thus follows in the deep bulk

$$N_D = n(z \rightarrow \infty) = n_i \exp(u_B), \quad N_A = p(z \rightarrow \infty) = n_i \exp(-u_B) \quad (\text{A.0.7})$$

Using equations (A.0.2), (A.0.4) and (A.0.7), the Poisson's equation (A.0.1) can be rewritten as

$$\frac{d^2\Phi(z)}{dz^2} = -\frac{2en_i}{\epsilon_0\epsilon_B}(\sinh(u_B) - \sinh(u(z))). \quad (\text{A.0.8})$$

By defining a function $F(u(z), u_B)$

$$F(u, u_b) = \sqrt{2} \sqrt{(u_b - u) \sinh(u_b) - \cosh(u_b) + \cosh(u)} \quad (\text{A.0.9})$$

the first derivative of equation (A.0.8) is analytically obtained which is equal to the electric field [78]:

$$\frac{d\Phi(z)}{dz} = \sqrt{\frac{2n_i k_B T}{\epsilon_0 \epsilon_B}} F(u(z), u_B) = \quad (\text{A.0.10})$$

The excess-electron concentration accumulated in the SCL can now be expressed as [78, eq. (32, 33)]

$$\Delta n = n_i \lambda_D \int_{u_S}^{u_B} \frac{\exp u - \exp u_B}{F(u, u_B)} du, \quad (\text{A.0.11})$$

and

$$\Delta p = p_i \lambda_D \int_{u_S}^{u_B} \frac{\exp(-u) - \exp(-u_B)}{F(u, u_B)} du, \quad (\text{A.0.12})$$

where $u_S \equiv u(z \rightarrow 0)$ and $\lambda_D = (\epsilon_0 \epsilon_B k_B T / (2e^2 n_i))$ is the Debye length.

Finally the conductance of the SCL is given by

$$\sigma = e(\mu_n \Delta n + \mu_p \Delta p), \quad (\text{A.0.13})$$

where μ_n and μ_p are the mobilities of the electrons and holes.

The temperature dependence of the SCL of equation (A.0.13) was evaluated numerically using Mathematica [288] and the electron and hole mobility temperature dependence given in [200]. In the case of a n-type Si material with a resistivity of $\rho = 1700 \Omega\text{cm}$, the SCL contribution is calculated to be below $1 \mu\text{S}$ at room temperature.

Two-step adsorption process within the Langmuir adsorption model

In the following the formula for a two-step adsorption process within the Langmuir model approach will be deduced. To simplify notation, in the following the time derivatives in equations are abbreviated by $\dot{}$. Starting from a thermodynamic approach, the impinging rate of particles on a surface is given by the so called Hertz-Knudsen equation [195]

$$\dot{N} = \frac{p}{\sqrt{2\pi m k_B T}}, \quad (\text{B.0.1})$$

where p is the ambient pressure, determining how many particles impinge on the surface, m the mass of the impinging atom or molecule, T the temperature, k_B the Boltzmann's constant. The number of adsorbed particles is proportional to the impinging rate via the so called sticking coefficient S . Therefore, the change of the relative coverage Θ (ratio of the number of occupied and available sites) is given by

$$\dot{\Theta} = S\dot{N} \quad (\text{B.0.2})$$

For an activated adsorption, the sticking coefficient can be written as [79]

$$S = cf(\Theta) \exp -E_a/(k_B T), \quad (\text{B.0.3})$$

where c is the so called condensation coefficient dependent on the degree of freedom of the adsorbed molecule evaluated by statistical theory [79], $f(\Theta)$ the occupation factor taking into account the probability for finding an adsorption site and E_a the energetic barrier for adsorption. For a non-dissociative adsorption process a site is either occupied or unoccupied resulting in the simple occupation factor of $f(\Theta) = 1 - \Theta$ [79, 194, 195].

Assuming a constant impinging rate \dot{N} due to constant pressure during the dosing experiments and combining the constant parts to the single variable C representing the sticking factor for a clean surface, one can easily get

$$\begin{aligned} \dot{\Theta} &= cf(\Theta) \exp -E_a/(k_B T) \dot{N} (1 - \Theta) \\ &= C(1 - \Theta). \end{aligned} \quad (\text{B.0.4})$$

For a multi-step adsorption process the total relative coverage is the sum of the partial coverages of the processes $\Theta = \sum_i \Theta_i$. Here Θ_0 reflects the initial relative coverage, while $\Theta_{i \geq 1}$ the relative coverage after the first, second, etc. adsorption process. Assuming the adsorption processes are dependent from each other ($\Theta_{i-1} = 1 - \Theta_i$), one can establish the following equations for a two-step adsorption process from equation (B.0.4):

$$\dot{\Theta}_1 = C_0 \Theta_0 - \dot{\Theta}_2 \quad (\text{B.0.5})$$

$$\dot{\Theta}_2 = C_1 \Theta_1 \quad (\text{B.0.6})$$

Here, the first equation (B.0.5) describes the change of relative coverage after the first adsorption process which, from apparent reasons, is dependent from the change of the initial relative coverage. After the first adsorption step, the second adsorption process can appear, reducing the change of relative coverage of $\dot{\Theta}_1$ leading to the $-\dot{\Theta}_2$ term. Similar considerations lead to equation (B.0.6).

Simple transformations of equations (B.0.5) and (B.0.6) give

$$\Theta_0 = \frac{\dot{\Theta}_1 + \dot{\Theta}_2}{C_0} = \frac{\ddot{\Theta}_2}{C_0 C_1} + \frac{\dot{\Theta}_2}{C_0}. \quad (\text{B.0.7})$$

For single layer adsorption, the sum of the relatives coverages is $\sum_i \Theta = \Theta_0 + \Theta_1 + \Theta_2 = 1$ when the system is in equilibrium [194] leading to the differential equation using equations (B.0.6) and (B.0.7)

$$\begin{aligned} \Theta_0 + \Theta_1 + \Theta_2 &= 1 \\ \frac{\ddot{\Theta}_2}{C_0 C_1} + \frac{(C_0 + C_1)\dot{\Theta}_2}{C_0 C_1} + \Theta_2 &= 1 \end{aligned} \quad (\text{B.0.8})$$

Since the second adsorption process is depending on products of the first one, equation (B.0.8) can be solved analytical using the boundary conditions $\Theta_2(0) = 0$ and $\dot{\Theta}_2(0) = 0$ by [288] to

$$\Theta_2(t) = \frac{C_0 - C_0 \exp -C_1 t + C_1 (\exp(-C_0 t) - 1)}{C_0 - C_1} \quad (\text{B.0.9})$$

Presuming the total sheet resistivity is the superposition of different oxidized surface areas, the resulting sheet resistivity can be expressed as the sum of the weighted partial sheet resistivities $\rho = \Theta_0 \rho_0 + \Theta_1 \rho_1 + \Theta_2 \rho_2$. Applying the solution in equation (B.0.9) to the previous equations the weighted sheet resistivity can be derived by [288] to equation (7.4.3). In the same way one can retrieve the conductivity by $\sigma = \rho^{-1}$.

Bibliography

- [1] G. E. MOORE: Cramming more components onto integrated circuits, Reprinted from *Electronics*, volume 38, number 8, April 19, 1965, pp.114 ff. *IEEE Solid-State Circuits Newsletter*, vol. 20(3) (Sept. 2006), pp. 33–35 (cit. on p. 3).
DOI: 10.1109/n-ssc.2006.4785860.
- [2] R. R. SCHALLER: Moore’s law: past, present and future. *IEEE Spectr.* Vol. 34(6) (June 1997), pp. 52–59. ISSN: 0018-9235 (cit. on p. 3).
DOI: 10.1109/6.591665.
- [3] IBM CORPORATION: *Intel®14 nm Technology: Ultra-fast, energy-sipping devices powered by Intel.* 2014 (cit. on p. 3).
URL: <https://www.intel.com/content/www/us/en/silicon-innovations/intel-14nm-technology.html> (visited on 07/26/2017).
- [4] B. HOEFFLINGER: “ITRS: The International Technology Roadmap for Semiconductors”. *The Frontiers Collection*. Springer Berlin Heidelberg, 2011, pp. 161–174 (cit. on p. 3).
DOI: 10.1007/978-3-642-23096-7.
- [5] W. C. O’MARA, R. B. HERRING, and L. P. HUNT: *Handbook of Semiconductor Silicon Technology*. WILLIAM ANDREW PUB, Jan. 11, 1991. 815 pp. ISBN: 0815512376 (cit. on p. 3).
URL: http://www.ebook.de/de/product/3772569/william_c_o_mara_robert_b_herring_lee_p_hunt_handbook_of_semiconductor_silicon_technology.html.
- [6] M. M. WALDROP: The chips are down for Moore’s law. *Nature*, vol. 530(7589) (Feb. 2016), pp. 144–147 (cit. on p. 3).
DOI: 10.1038/530144a.
- [7] S. ROY and A. ASENOV: Where Do the Dopants Go? *Science*, vol. 309(5733) (2005), pp. 388–390. ISSN: 0036-8075 (cit. on p. 3).
DOI: 10.1126/science.1111104.

- [8] WIKIPEDIA: *Microprocessor chronology* — *Wikipedia, The Free Encyclopedia*. 2017 (cit. on p. 4).
URL: https://en.wikipedia.org/w/index.php?title=Microprocessor_chronology&oldid=791370997 (visited on 07/26/2017).
- [9] WIKIPEDIA: *Transistor count* — *Wikipedia, The Free Encyclopedia*. 2017 (cit. on p. 4).
URL: https://en.wikipedia.org/w/index.php?title=Transistor_count&oldid=792223616 (visited on 07/26/2017).
- [10] C. JOACHIM and J. GIMZEWSKI: An electromechanical amplifier using a single molecule. *Chem. Phys. Lett.* Vol. 265(3-5) (Feb. 1997), pp. 353–357 (cit. on p. 3).
DOI: 10.1016/s0009-2614(97)00014-6.
- [11] M. ELBING et al.: A single-molecule diode. *Proceedings of the National Academy of Sciences*, vol. 102(25) (June 2005), pp. 8815–8820 (cit. on p. 3).
DOI: 10.1073/pnas.0408888102.
- [12] A. K. GEIM and K. S. NOVOSELOV: The rise of graphene. *Nat. Mater.* Vol. 6(3) (Mar. 2007), pp. 183–191 (cit. on p. 3).
DOI: 10.1038/nmat1849.
- [13] M. FUECHSLE et al.: A single-atom transistor. *Nat. Nanotechnol.* Vol. 7(4) (Feb. 2012), pp. 242–246 (cit. on p. 4).
DOI: 10.1038/nnano.2012.21.
- [14] T. GIAMARCHI: *Quantum Physics in One Dimension*. Oxford University Press, Dec. 2003 (cit. on pp. 4, 10).
DOI: 10.1093/acprof:oso/9780198525004.001.0001.
- [15] S. HASEGAWA: Quasi-one-dimensional metals on semiconductor surfaces with defects. *J. Phys.: Condens. Matter*, vol. 22(8) (Feb. 2010), p. 084026 (cit. on p. 4).
DOI: 10.1088/0953-8984/22/8/084026.
- [16] S.-i. TOMONAGA: Elementary Theory of Quantum-Mechanical Collective Motion of Particles, I. *Progress of Theoretical Physics*, vol. 13(5) (May 1955), pp. 467–481 (cit. on p. 4).
DOI: 10.1143/ptp.13.467.
- [17] J. M. LUTTINGER: An Exactly Soluble Model of a Many-Fermion System. *J. Math. Phys.* Vol. 4(9) (Sept. 1963), pp. 1154–1162 (cit. on pp. 4, 9).
DOI: 10.1063/1.1704046.
- [18] J. VOIT: One-dimensional Fermi liquids. *Rep. Prog. Phys.* Vol. 58(9) (Sept. 1995), pp. 977–1116 (cit. on p. 4).
DOI: 10.1088/0034-4885/58/9/002.

-
- [19] M. G. ZACHER, E. ARRIGONI, W. HANKE, and J. R. SCHRIEFFER: Systematic numerical study of spin-charge separation in one dimension. *Phys. Rev. B*, vol. 57(11) (Mar. 1998), pp. 6370–6375 (cit. on p. 4).
DOI: 10.1103/physrevb.57.6370.
- [20] G. D. MAHAN: Spin Shift Register from a One-Dimensional Atomic Chain. *Phys. Rev. Lett.* Vol. 102(1) (Jan. 2009) (cit. on p. 4).
DOI: 10.1103/physrevlett.102.016801.
- [21] R. BLATT and D. WINELAND: Entangled states of trapped atomic ions. *Nature*, vol. 453(7198) (June 2008), pp. 1008–1015 (cit. on p. 4).
DOI: 10.1038/nature07125.
- [22] W. PAUL: Electromagnetic traps for charged and neutral particles. *Rev. Mod. Phys.* Vol. 62(3) (July 1990), pp. 531–540 (cit. on p. 4).
DOI: 10.1103/revmodphys.62.531.
- [23] S. MURMANN et al.: Antiferromagnetic Heisenberg Spin Chain of a Few Cold Atoms in a One-Dimensional Trap. *Phys. Rev. Lett.* Vol. 115(21) (Nov. 2015) (cit. on p. 4).
DOI: 10.1103/physrevlett.115.215301.
- [24] H. OHNISHI, Y. KONDO, and K. TAKAYANAGI: Quantized conductance through individual rows of suspended gold atoms. *Nature*, vol. 395(6704) (Oct. 1998), pp. 780–783 (cit. on p. 4).
DOI: 10.1038/27399.
- [25] R. PEIERLS: Zur Theorie der elektrischen und thermischen Leitfähigkeit von Metallen. *Ann. Phys.* Vol. 396(2) (1930), pp. 121–148. ISSN: 1521-3889 (cit. on pp. 5, 9, 10).
DOI: 10.1002/andp.19303960202.
- [26] T.-H. KIM, S. CHEON, and H. W. YEOM: Switching chiral solitons for algebraic operation of topological quaternary digits. *Nat. Phys.* Vol. 13(5) (Feb. 2017), pp. 444–447 (cit. on p. 6).
DOI: 10.1038/nphys4026.
- [27] S. CHEON, T.-H. KIM, S.-H. LEE, and H. W. YEOM: Chiral solitons in a coupled double Peierls chain. *Science*, vol. 350(6257) (Oct. 2015), pp. 182–185 (cit. on pp. 6, 47).
DOI: 10.1126/science.aaa7055.
- [28] S. C. ERWIN and F. HIMPSEL: Intrinsic magnetism at silicon surfaces. *Nat. Commun.* Vol. 1 (Aug. 2010), p. 58 (cit. on pp. 6, 65, 72, 73, 77, 84).
DOI: 10.1038/ncomms1056.

- [29] F. EDLER et al.: Interwire coupling for $\text{In}(4 \times 1)/\text{Si}(111)$ probed by surface transport. *Phys. Rev. B*, vol. 92(8) (Aug. 2015) (cit. on pp. 6, 43, 52, 75).
DOI: 10.1103/physrevb.92.085426.
- [30] I. MICCOLI, F. EDLER, H. PFNÜR, and C. TEGENKAMP: The 100th anniversary of the four-point probe technique: the role of probe geometries in isotropic and anisotropic systems. *J. Phys.: Condens. Matter*, vol. 27(22) (2015), p. 223201. ISSN: 0953-8984 (cit. on pp. 6, 7, 25, 36, 38, 43, 58, 93, 113).
DOI: 10.1088/0953-8984/27/22/223201.
- [31] I. MICCOLI et al.: Atomic size effects studied by transport in single silicide nanowires. *Phys. Rev. B*, vol. 93(12) (Mar. 2016), p. 125412 (cit. on pp. 7, 105, 110).
DOI: 10.1103/PhysRevB.93.125412.
- [32] F. EDLER et al.: Tuning the conductivity along atomic chains by selective chemisorption. *Phys. Rev. B*, vol. 95(12) (Mar. 2017) (cit. on pp. 7, 65).
DOI: 10.1103/physrevb.95.125409.
- [33] G. GRÜNER: The dynamics of spin-density waves. *Rev. Mod. Phys.* Vol. 66 (Augs. 1, Jan. 1994), pp. 1–24 (cit. on p. 9).
DOI: 10.1103/RevModPhys.66.1.
- [34] G. GRÜNER: *Density Waves in Solids*. Perseus Books, Mar. 1994. ISBN: 0201626543 (cit. on pp. 10, 11, 106).
- [35] T. ARUGA: Charge-density waves on metal surfaces. *J. Phys.: Condens. Matter*, vol. 14(35) (Aug. 2002), pp. 8393–8414 (cit. on pp. 10, 11).
DOI: 10.1088/0953-8984/14/35/310.
- [36] B. MIHAILA: Lindhard function of a d-dimensional Fermi gas. Vol. (Nov. 2, 2011) (cit. on p. 10).
arXiv: 1111.5337v1 [cond-mat.quant-gas].
- [37] S. KAGOSHIMA, H. NAGASAWA, and T. SAMBONGI: *One-Dimensional Conductors*. Springer Berlin Heidelberg, 1988 (cit. on p. 11).
DOI: 10.1007/978-3-642-83179-9.
- [38] J. R. AHN, P. G. KANG, K. D. RYANG, and H. W. YEOM: Coexistence of Two Different Peierls Distortions within an Atomic Scale Wire: $\text{Si}(553)\text{-Au}$. *Phys. Rev. Lett.* Vol. 95(19) (Oct. 2005) (cit. on pp. 12, 13, 70, 72, 73, 96, 100, 132).
DOI: 10.1103/physrevlett.95.196402.
- [39] T. SHIBASAKI et al.: Phase transition temperatures determined by different experimental methods: $\text{Si}(111)4 \times 1\text{-In}$ surface with defects. *Phys. Rev. B*, vol. 81(3) (Jan. 2010), p. 035314 (cit. on pp. 12, 47, 49, 50).
DOI: 10.1103/PhysRevB.81.035314.

-
- [40] W. G. SCHMIDT et al.: Influence of Na adsorption on the quantum conductance and metal-insulator transition of the In-Si(111)(4×1)-(8×2) nanowire array. *Phys. Rev. B*, vol. 84(11) (Sept. 2011) (cit. on p. 12).
DOI: 10.1103/physrevb.84.115416.
- [41] P. C. SNIJDERS and H. H. WEITERING: Colloquium: Electronic instabilities in self-assembled atom wires. *Rev. Mod. Phys.* Vol. 82(1) (Feb. 2010), pp. 307–329 (cit. on pp. 12, 13, 43, 45, 46, 65, 67, 69, 73).
DOI: 10.1103/revmodphys.82.307.
- [42] J. WANG et al.: Structure determination of indium-induced Si(111)-In-4×1 surface by LEED Patterson inversion. *Phys. Rev. B*, vol. 72(24) (Dec. 2005) (cit. on pp. 12, 44).
DOI: 10.1103/physrevb.72.245324.
- [43] S. MIZUNO, Y. O. MIZUNO, and H. TOCHIHARA: Structural determination of indium-induced Si(111) reconstructed surfaces by LEED analysis:(3×3)R30 and (4×1). *Phys. Rev. B*, vol. 67(19) (May 2003) (cit. on pp. 12, 44).
DOI: 10.1103/physrevb.67.195410.
- [44] T. ABUKAWA et al.: Core-level photoemission study of the Si(111)4×1-In surface. *J. Electron Spectrosc. Relat. Phenom.* Vol. 80 (May 1996), pp. 233–236 (cit. on pp. 12, 44).
DOI: 10.1016/0368-2048(96)02964-7.
- [45] H. W. YEOM et al.: Instability and Charge Density Wave of Metallic Quantum Chains on a Silicon Surface. *Phys. Rev. Lett.* Vol. 82(24) (June 1999), pp. 4898–4901 (cit. on pp. 12, 44, 45, 47, 54).
DOI: 10.1103/physrevlett.82.4898.
- [46] T. TANIKAWA, I. MATSUDA, T. KANAGAWA, and S. HASEGAWA: Surface-State Electrical Conductivity at a Metal-Insulator Transition On Silicon. *Phys. Rev. Lett.* Vol. 93(1) (June 2004) (cit. on pp. 12, 44, 47–49).
DOI: 10.1103/physrevlett.93.016801.
- [47] J. R. AHN et al.: Mechanism of Gap Opening in a Triple-Band Peierls System: In Atomic Wires on Si. *Phys. Rev. Lett.* Vol. 93(10) (Aug. 2004) (cit. on pp. 12, 44–47).
DOI: 10.1103/physrevlett.93.106401.
- [48] S. J. PARK et al.: Direct Evidence of the Charge Ordered Phase Transition of Indium Nanowires on Si(111). *Phys. Rev. Lett.* Vol. 93(10) (Sept. 2004) (cit. on pp. 12, 44–46).
DOI: 10.1103/physrevlett.93.106402.
- [49] J. GUO, G. LEE, and E. W. PLUMMER: Intertwined Electronic and Structural Phase Transitions in the In/Si(111) Interface. *Phys. Rev. Lett.* Vol. 95(4) (July 2005) (cit. on pp. 12, 44, 46, 47, 49).
DOI: 10.1103/physrevlett.95.046102.

- [50] S. J. PARK, H. W. YEOM, J. R. AHN, and I.-W. LYO: Atomic-Scale Phase Coexistence and Fluctuation at the Quasi-One-Dimensional Metal-Insulator Transition. *Phys. Rev. Lett.* Vol. 95(12) (Sept. 2005) (cit. on pp. 12, 44, 46).
DOI: 10.1103/physrevlett.95.126102.
- [51] J.-H. CHO and J.-Y. LEE: First-principles calculation of the atomic structure of one-dimensional indium chains on Si(111): Convergence to a metastable structure. *Phys. Rev. B*, vol. 76(3) (July 2007) (cit. on pp. 12, 44).
DOI: 10.1103/physrevb.76.033405.
- [52] A. A. STEKOLNIKOV et al.: Hexagon versus Trimer Formation in In Nanowires on Si(111): Energetics and Quantum Conductance. *Phys. Rev. Lett.* Vol. 98(2) (Jan. 2007) (cit. on pp. 12, 44, 45, 60).
DOI: 10.1103/physrevlett.98.026105.
- [53] X. LÓPEZ-LOZANO et al.: Reconstruction of quasi-one-dimensional In/Si(111) systems: Charge- and spin-density waves versus bonding. *Phys. Rev. B*, vol. 73(3) (Jan. 2006) (cit. on pp. 12, 44).
DOI: 10.1103/physrevb.73.035430.
- [54] C. GONZÁLEZ, F. FLORES, and J. ORTEGA: Soft Phonon, Dynamical Fluctuations, and a Reversible Phase Transition: Indium Chains on Silicon. *Phys. Rev. Lett.* Vol. 96(13) (Apr. 2006) (cit. on pp. 12, 44, 47, 49).
DOI: 10.1103/physrevlett.96.136101.
- [55] S.-F. TSAY: Atomic and electronic structure of the(4×1)and(8×2)In/Si(111)surfaces. *Phys. Rev. B*, vol. 71(3) (Jan. 2005) (cit. on pp. 12, 44).
DOI: 10.1103/physrevb.71.035207.
- [56] S. GHOSE, I. ROBINSON, P. BENNETT, and F. HIMPSEL: Structure of double row quantum wires in Au/Si(553). *Surf. Sci.* Vol. 581(2-3) (May 2005), pp. 199–206 (cit. on pp. 12, 44, 72).
DOI: 10.1016/j.susc.2005.02.053.
- [57] S. WANG, W. LU, W. G. SCHMIDT, and J. BERNHOLC: Nanowire-induced optical anisotropy of the Si(111)-In surface. *Phys. Rev. B*, vol. 68(3) (July 2003) (cit. on pp. 12, 44).
DOI: 10.1103/physrevb.68.035329.
- [58] J.-H. CHO, D.-H. OH, K. S. KIM, and L. KLEINMAN: Weakly correlated one-dimensional indium chains on Si(111). *Phys. Rev. B*, vol. 64(23) (Nov. 2001) (cit. on pp. 12, 44, 45).
DOI: 10.1103/physrevb.64.235302.

-
- [59] Y. J. SUN et al.: Cooperative structural and Peierls transition of indium chains on Si(111). *Phys. Rev. B*, vol. 77(12) (Mar. 2008) (cit. on pp. 12, 45).
DOI: 10.1103/physrevb.77.125115.
- [60] S. V. RYJKOV, T. NAGAO, V. G. LIFSHITS, and S. HASEGAWA: Phase transition and stability of Si(111)- $8\times 2'$ -In surface phase at low temperatures. *Surf. Sci.* Vol. 488(1-2) (Aug. 2001), pp. 15–22 (cit. on pp. 12, 49).
DOI: 10.1016/s0039-6028(01)01145-1.
- [61] C. KUMPF et al.: Low-Temperature Structure of Indium Quantum Chains on Silicon. *Phys. Rev. Lett.* Vol. 85(23) (Dec. 2000), pp. 4916–4919 (cit. on pp. 12, 49).
DOI: 10.1103/physrevlett.85.4916.
- [62] S. CHANDOLA et al.: Structure of Si(111)-In Nanowires Determined from the Midinfrared Optical Response. *Phys. Rev. Lett.* Vol. 102(22) (June 2009), p. 226805 (cit. on pp. 12, 60).
DOI: 10.1103/PhysRevLett.102.226805.
- [63] S. WIPPERMANN and W. G. SCHMIDT: Entropy Explains Metal-Insulator Transition of the Si(111)-In Nanowire Array. *Phys. Rev. Lett.* Vol. 105(12) (Sept. 2010), p. 126102 (cit. on pp. 12, 47, 49, 60).
DOI: 10.1103/PhysRevLett.105.126102.
- [64] S.-W. KIM and J.-H. CHO: Origin of the metal-insulator transition of indium atom wires on Si(111). *Phys. Rev. B*, vol. 93(24) (June 2016) (cit. on pp. 12, 47).
DOI: 10.1103/physrevb.93.241408.
- [65] E. JECKELMANN et al.: Grand canonical Peierls transition in In/Si(111). *Phys. Rev. B*, vol. 93(24) (June 2016) (cit. on pp. 12, 49).
DOI: 10.1103/physrevb.93.241407.
- [66] S. WALL et al.: Atomistic Picture of Charge Density Wave Formation at Surfaces. *Phys. Rev. Lett.* Vol. 109(18) (Nov. 2012), p. 186101 (cit. on p. 12).
DOI: 10.1103/PhysRevLett.109.186101.
- [67] S. HATTA, T. NOMA, H. OKUYAMA, and T. ARUGA: Electrical conduction and metal-insulator transition of indium nanowires on Si(111). *Phys. Rev. B*, vol. 95(19) (May 2017) (cit. on pp. 12, 49).
DOI: 10.1103/physrevb.95.195409.
- [68] J. N. CRAIN et al.: Fractional Band Filling in an Atomic Chain Structure. *Phys. Rev. Lett.* Vol. 90 (Aug. 17, May 2003), p. 176805 (cit. on pp. 12, 67, 68, 70–73, 98, 102).
DOI: 10.1103/PhysRevLett.90.176805.
- [69] L. DUDY et al.: One-dimensional quantum matter: gold-induced nanowires on semi-

- conductor surfaces. *J. Phys.: Condens. Matter*, vol. 29(43) (Sept. 2017), p. 433001 (cit. on pp. 12, 65, 72).
DOI: 10.1088/1361-648x/aa852a.
- [70] P. C. SNIJDERS, S. ROGGE, and H. H. WEITERING: Competing Periodicities in Fractionally Filled One-Dimensional Bands. *Phys. Rev. Lett.* Vol. 96(7) (Feb. 2006), p. 076801 (cit. on pp. 13, 73, 94, 103, 132).
DOI: 10.1103/PhysRevLett.96.076801.
- [71] H. OKINO et al.: Transport in defective quasi-one-dimensional arrays of chains of gold atoms on a vicinal silicon surface. *Phys. Rev. B*, vol. 76(3) (July 2007) (cit. on pp. 13, 69, 75, 88–90, 102).
DOI: 10.1103/physrevb.76.035424.
- [72] J. AULBACH et al.: Evidence for Long-Range Spin Order Instead of a Peierls Transition in Si(553)-Au Chains. *Phys. Rev. Lett.* Vol. 111 (Aug. 13, Sept. 2013), p. 137203 (cit. on pp. 13, 73).
DOI: 10.1103/PhysRevLett.111.137203.
- [73] C. ZENG et al.: Charge-order fluctuations in one-dimensional silicides. *Nat. Mater.* Vol. 7(7) (July 2008), pp. 539–542. ISSN: 1476-1122 (cit. on pp. 13, 105, 106, 125).
DOI: 10.1038/nmat2209.
- [74] C. PREINESBERGER, S. VANDRÉ, T. KALKA, and M. DÄHNE-PRIETSCH: Formation of dysprosium silicide wires on Si(001). *J. Phys. D: Appl. Phys.* Vol. 31(12) (June 1998), p. L43. ISSN: 0022-3727 (cit. on pp. 13, 107).
DOI: 10.1088/0022-3727/31/12/001.
- [75] C. PREINESBERGER et al.: Structure and electronic properties of dysprosium-silicide nanowires on vicinal Si(001). *Appl. Phys. Lett.* Vol. 87(8) (2005), p. 083107 (cit. on pp. 13, 105, 106).
DOI: 10.1063/1.2032620.
- [76] B. Z. LIU and J. NOGAMI: Growth of parallel rare-earth silicide nanowire arrays on vicinal Si(001). *Nanotechnology*, vol. 14(8) (Aug. 2003), p. 873. ISSN: 0957-4484 (cit. on pp. 13, 107).
DOI: 10.1088/0957-4484/14/8/306.
- [77] S. QIN et al.: Correlating Electronic Transport to Atomic Structures in Self-Assembled Quantum Wires. *Nano Lett.* Vol. 12(2) (Feb. 2012), pp. 938–942. ISSN: 1530-6984 (cit. on pp. 13, 105, 106, 124–126).
DOI: 10.1021/nl204003s.
- [78] S. HASEGAWA et al.: Structures and electronic transport on silicon surfaces. *Prog. Surf. Sci.* Vol. 60(5-8) (Mar. 1999), pp. 89–257 (cit. on pp. 14, 16, 135, 136).
DOI: 10.1016/s0079-6816(99)00008-8.

-
- [79] H. LÜTH: *Solid Surfaces, Interfaces and Thin Films*. Springer Berlin Heidelberg, 2010 (cit. on pp. 14, 15, 87, 137).
DOI: 10.1007/978-3-642-13592-7.
- [80] W. MÖNCH: *Semiconductor Surfaces and Interfaces*. Springer Berlin Heidelberg, 2001 (cit. on pp. 14, 135).
DOI: 10.1007/978-3-662-04459-9.
- [81] J. N. CRAIN et al.: Chains of gold atoms with tailored electronic states. *Phys. Rev. B*, vol. 69(12) (Mar. 2004), p. 125401 (cit. on pp. 15, 65–68, 88, 98, 102).
DOI: 10.1103/PhysRevB.69.125401.
- [82] T. ABUKAWA et al.: Surface electronic structure of a single-domain Si(111)4 × 1-In surface: a synchrotron radiation photoemission study. *Surf. Sci.* Vol. 325(1-2) (Feb. 1995), pp. 33–44 (cit. on pp. 15, 44, 48).
DOI: 10.1016/0039-6028(94)00693-8.
- [83] T. KANAGAWA et al.: Anisotropy in Conductance of a Quasi-One-Dimensional Metallic Surface State Measured by a Square Micro-Four-Point Probe Method. *Phys. Rev. Lett.* Vol. 91(3) (July 2003) (cit. on pp. 15, 36, 48, 52, 56, 129, 131).
DOI: 10.1103/physrevlett.91.036805.
- [84] H. M. ZHANG, K. SAKAMOTO, G. V. HANSSON, and R. I. G. UHRBERG: High-temperature annealing and surface photovoltage shifts on Si(111)7 × 7. *Phys. Rev. B*, vol. 78(3) (July 2008) (cit. on pp. 16, 57, 90, 100).
DOI: 10.1103/physrevb.78.035318.
- [85] M. LIEHR, M. RENIER, R. A. WACHNIK, and G. S. SCILLA: Dopant redistribution at Si surfaces during vacuum anneal. *J. Appl. Phys.* Vol. 61(9) (May 1987), pp. 4619–4625. ISSN: 0021-8979, 1089-7550 (cit. on pp. 16, 90, 100).
DOI: 10.1063/1.338372.
- [86] T. HIRAHARA et al.: Direct measurement of the Hall effect in a free-electron-like surface state. *Phys. Rev. B*, vol. 73(23) (June 2006) (cit. on pp. 16, 90).
DOI: 10.1103/physrevb.73.235332.
- [87] C. SEIDEL: “Die Oberfläche von atomaren Wolframspitzen zur Anwendung in Tunnelprozessen - eine Analyse mit Feldionenmikroskopie”. MA thesis. Leibniz Universität Hannover, Dec. 2014 (cit. on p. 18).
- [88] J. A. WOOD et al.: Iridium single atom tips fabricated by field assisted reactive gas etching. *Appl. Surf. Sci.* Vol. 367 (Mar. 2016), pp. 277–280 (cit. on p. 18).
DOI: 10.1016/j.apsusc.2016.01.080.

- [89] J. P. VERMEULEN: 12 Years Zeiss Gemini® FESEM Technology. *Imaging & Microscopy*, vol. 4 (2004), pp. 34–35 (cit. on p. 20).
URL: [http://www.zeiss.de/C1256E4600307C70/EmbedTitelIntern/12years_zeiss_gemini_fesem_technology/\\$File/12years_zeiss_gemini_fesem_technology.pdf](http://www.zeiss.de/C1256E4600307C70/EmbedTitelIntern/12years_zeiss_gemini_fesem_technology/$File/12years_zeiss_gemini_fesem_technology.pdf) (visited on 04/10/2012).
- [90] OMICRON NANOTECHNOLOGY GMBH: *Ultimate Nanoprobng with Four Independent Scanning Probe Microscopes - Further Details* (cit. on p. 20).
URL: <http://www.omicron.de/en/products/uhv-nanoprobe/further-details> (visited on 04/10/2012).
- [91] J. P. IBE et al.: On the electrochemical etching of tips for scanning tunneling microscopy. *Journal of Vacuum Science & Technology A*, vol. 8(4) (July 1990), pp. 3570–3575. ISSN: 0734-2101, 1520-8559 (cit. on p. 19).
DOI: 10.1116/1.576509.
- [92] P. HIDNERT: *Thermal Expansion of Tungsten*. eng. National Bureau of Standards, 1925 (cit. on p. 21).
URL: <http://archive.org/details/thermalexpansion20483hidn>.
- [93] W. M. HAYNES, ed.: *CRC Handbook of Chemistry and Physics, 92nd Edition*. 92 edition. Boca Raton, Fla.: CRC Press, June 2011. ISBN: 978-1-4398-5511-9 (cit. on p. 21).
- [94] J. H. I. LIENHARD and J. H. V. LIENHARD: *A Heat Transfer Textbook: Fourth Edition*. Dover Publications, Mar. 11, 2011. 755 pp. ISBN: 0486479315 (cit. on p. 22).
- [95] L. M. JIJI: *Heat Conduction*. Springer Berlin Heidelberg, July 9, 2009 (cit. on p. 22).
DOI: 10.1007/978-3-642-01267-9.
- [96] L. VALDES: Resistivity Measurements on Germanium for Transistors. *Proceedings of the IRE*, vol. 42(2) (Feb. 1954), pp. 420–427 (cit. on pp. 26, 29).
DOI: 10.1109/JRPR0C.1954.274680.
- [97] J. ALBERS: An Alternative Approach to the Calculation of Four-Probe Resistances on Nonuniform Structures. *J. Electrochem. Soc.* Vol. 132(10) (1985), p. 2453 (cit. on p. 29).
DOI: 10.1149/1.2113598.
- [98] J. D. JACKSON: *Classical electrodynamics*. eng. New York ; London : John Wiley, 1962 (cit. on p. 29).
URL: <http://archive.org/details/ClassicalElectrodynamics> (visited on 02/27/2017).

-
- [99] C. S. SMITH: “Macroscopic Symmetry and Properties of Crystals”. *Advances in Research and Applications*. Vol. 6. Elsevier BV, 1958, 208ff (cit. on pp. 30, 33).
DOI: 10.1016/S0081-1947(08)60727-4.
- [100] D. E. VAUGHAN: Four-probe resistivity measurements on small circular specimens. *Br. J. Appl. Phys.* Vol. 12(8) (Aug. 1961), p. 414 (cit. on p. 30).
DOI: 10.1088/0508-3443/12/8/312.
- [101] L. J. VAN DER PAUW: A method of measuring specific resistivity and hall effect of disks of arbitrary shape. *Philips Res. Rep.* Vol. 13 (1958), pp. 1–9 (cit. on p. 31).
- [102] L. J. VAN DER PAUW: A method of measuring the resistivity and Hall coefficient on lamellae of arbitrary shape. *Philips Tech. Rev.* Vol. 20 (1958), p. 220 (cit. on p. 31).
- [103] J. D. WASSCHER: Note on four-point resistivity measurements on anisotropic conductors. *Philips Research Reports*, vol. 16 (1961), pp. 301–306 (cit. on p. 34).
- [104] D. A. BANDURIN et al.: Negative local resistance caused by viscous electron backflow in graphene. *Science*, vol. 351(6277) (Feb. 2016), pp. 1055–1058 (cit. on p. 36).
DOI: 10.1126/science.aad0201.
- [105] H. C. MONTGOMERY: Method for Measuring Electrical Resistivity of Anisotropic Materials. *J. Appl. Phys.* Vol. 42(7) (June 1971), p. 2971 (cit. on p. 36).
DOI: 10.1063/1.1660656.
- [106] J. D. WASSCHER: “Electrical transport phenomena in MnTe, an antiferromagnetic semiconductor”. PhD thesis. Technische Hogeschool Eindhoven, 1969 (cit. on pp. 36, 37).
DOI: 10.6100/IR43336.
- [107] J. J. LANDER and J. MORRISON: Surface reactions of silicon with aluminum and with indium. *Surf. Sci.* Vol. 2 (1964), pp. 553–565. ISSN: 0039-6028 (cit. on p. 43).
DOI: 10.1016/0039-6028(64)90099-8.
- [108] M. KAWAJI, S. BABA, and A. KINBARA: Superstructures of submonolayer indium films on silicon (111)7 surfaces. *Appl. Phys. Lett.* Vol. 34(11) (June 1979), pp. 748–749. ISSN: 0003-6951, 1077-3118 (cit. on p. 43).
DOI: 10.1063/1.90659.
- [109] H. HIRAYAMA, S. BABA, and A. KINBARA: Electron energy loss measurements of In/Si(111) superstructures: Correlation of the spectra with surface superstructures. *Appl. Surf. Sci.* Vol. 33-34 (Sept. 1988), pp. 193–198. ISSN: 0169-4332 (cit. on p. 43).
DOI: 10.1016/0169-4332(88)90306-6.

- [110] J. KRAFT, M. G. RAMSEY, and F. P. NETZER: Surface reconstructions of In on Si(111). *Phys. Rev. B*, vol. 55(8) (Feb. 1997), pp. 5384–5393 (cit. on p. 43). DOI: 10.1103/physrevb.55.5384.
- [111] K. JITHESH, GOVIND, U. V. WAGHMARE, and S. M. SHIVAPRASAD: Experimental deduction of In/Si(111) 2D phase diagram and ab initio DFT modeling of $2\sqrt{3}$ phase. *Appl. Surf. Sci. Physics at Surfaces and Interface*(Proceedings of 2nd International Conference on Physics at Surfaces and Interfaces, PSI2009, February 23 - 27, 2009, Puri, India), vol. 256(2) (Oct. 2009), pp. 348–352. ISSN: 0169-4332 (cit. on p. 43). DOI: 10.1016/j.apsusc.2009.04.123.
- [112] W. G. SCHMIDT et al.: In-Si(111)(4×1)/(8×2) nanowires: Electron transport, entropy, and metal-insulator transition. *physica status solidi (b)*, vol. 249(2) (Feb. 2012), pp. 343–359. ISSN: 1521-3951 (cit. on pp. 43, 49, 61). DOI: 10.1002/pssb.201100457.
- [113] G. LEE et al.: Absolute In coverage and bias-dependent STM images of the Si(111) 4×1 -In surface. *Phys. Rev. B*, vol. 67(3) (Jan. 2003) (cit. on p. 43). DOI: 10.1103/physrevb.67.035327.
- [114] J. L. STEVENS, M. S. WORTHINGTON, and I. S. T. TSONG: 4×1 reconstruction of indium deposited on vicinal Si(111) surfaces. *Phys. Rev. B*, vol. 47(3) (Jan. 1993), pp. 1453–1459 (cit. on p. 44). DOI: 10.1103/PhysRevB.47.1453.
- [115] H. OKINO et al.: Influence of defects on transport in quasi-one-dimensional arrays of chains of metal atoms on silicon. *Phys. Rev. B*, vol. 76(19) (Nov. 2007), p. 195418 (cit. on pp. 44, 52, 56, 58, 59, 63, 89, 90, 100). DOI: 10.1103/PhysRevB.76.195418.
- [116] K. FLEISCHER et al.: Atomic indium nanowires on Si(1 1 1): the (4×1) – (8×2) phase transition studied with reflectance anisotropy spectroscopy. *Appl. Surf. Sci. The Ninth International Conference on the Formation of Semiconductor Interfaces*, vol. 234(1–4) (July 2004), pp. 302–306. ISSN: 0169-4332 (cit. on p. 44). DOI: 10.1016/j.apsusc.2004.05.114.
- [117] F. KLASING et al.: Hysteresis proves that the In/Si(111)(8×2) to (4×1) phase transition is first-order. *Phys. Rev. B*, vol. 89(12) (Mar. 2014) (cit. on pp. 44, 46, 49). DOI: 10.1103/physrevb.89.121107.
- [118] J. NOGAMI, S.-i. PARK, and C. F. QUATE: Behavior of indium on the Si(111) 7×7 surface at low-metal coverage. *Journal of Vacuum Science & Technology B: Microelectronics Processing and Phenomena*, vol. 6(4) (July 1, 1988), pp. 1479–1482. ISSN: 0734-211X (cit. on p. 44). DOI: 10.1116/1.584200.

-
- [119] J. NOGAMI, S.-i. PARK, and C. F. QUATE: Indium-induced reconstructions of the Si(111) surface studied by scanning tunneling microscopy. *Phys. Rev. B*, vol. 36(11) (Oct. 15, 1987), pp. 6221–6224 (cit. on p. 44).
DOI: 10.1103/physrevb.36.6221.
- [120] O. BUNK et al.: Structure determination of the indium-induced Si(111)-(4×1) reconstruction by surface x-ray diffraction. *Phys. Rev. B*, vol. 59(19) (May 1999), pp. 12228–12231 (cit. on pp. 44, 45).
DOI: 10.1103/physrevb.59.12228.
- [121] K. IWATA, S. YAMAZAKI, A. SHIOTARI, and Y. SUGIMOTO: Mechanical properties of In/Si(111)-(8×2) investigated by atomic force microscopy. *Japanese Journal of Applied Physics*, vol. 56(1) (Nov. 2016), p. 015701 (cit. on p. 45).
DOI: 10.7567/jjap.56.015701.
- [122] J. R. AHN, J. H. BYUN, J. K. KIM, and H. W. YEOM: Absence of dynamic fluctuation in metallic In chains on Si(111): Core-level and valence-band photoemission study. *Phys. Rev. B*, vol. 75(3) (Jan. 2007) (cit. on p. 44).
DOI: 10.1103/physrevb.75.033313.
- [123] J.-H. CHO, J.-Y. LEE, and L. KLEINMAN: Electronic structure of one-dimensional indium chains on Si(111). *Phys. Rev. B*, vol. 71(8) (Feb. 2005) (cit. on p. 44).
DOI: 10.1103/physrevb.71.081310.
- [124] C. GONZÁLEZ, J. ORTEGA, and F. FLORES: Metal-insulator transition in one-dimensional In-chains on Si(111): combination of a soft shear distortion and a double-band Peierls instability. *New J. Phys.* Vol. 7 (Apr. 2005), pp. 100–100 (cit. on p. 44).
DOI: 10.1088/1367-2630/7/1/100.
- [125] G. LEE, J. GUO, and E. W. PLUMMER: Real-Space Observation of Nanoscale Inhomogeneities and Fluctuations in a Phase Transition of a Surface Quasi-One-Dimensional System: In/Si(111). *Phys. Rev. Lett.* Vol. 95(11) (Sept. 2005) (cit. on p. 46).
DOI: 10.1103/physrevlett.95.116103.
- [126] H.-J. KIM and J.-H. CHO: Driving Force of Phase Transition in Indium Nanowires on Si(111). *Phys. Rev. Lett.* Vol. 110(11) (Mar. 2013), p. 116801 (cit. on pp. 47, 60).
DOI: 10.1103/PhysRevLett.110.116801.
- [127] K. FLEISCHER et al.: Surface phonons of the Si(111): In-(4×1) and (8×2) phases. *Phys. Rev. B*, vol. 76(20) (Nov. 2007) (cit. on p. 47).
DOI: 10.1103/physrevb.76.205406.
- [128] T. UCHIHASHI and U. RAMSPERGER: Electron conduction through quasi-one-dimensional

- indium wires on silicon. *Appl. Phys. Lett.* Vol. 80(22) (June 2002), pp. 4169–4171 (cit. on p. 47).
DOI: 10.1063/1.1483929.
- [129] T. UETAKE et al.: Anisotropic conductivity of the Si(111)4 × 1-In surface: Transport mechanism determined by the temperature dependence. *Phys. Rev. B*, vol. 86(3) (July 2012), p. 035325 (cit. on pp. 47, 52, 57, 58, 63, 75, 90, 129, 131).
DOI: 10.1103/PhysRevB.86.035325.
- [130] C. GONZÁLEZ et al.: Mechanism of the Band Gap Opening across the Order-Disorder Transition of Si(111)(4×1)-In. *Phys. Rev. Lett.* Vol. 102(11) (Mar. 2009) (cit. on p. 49).
DOI: 10.1103/physrevlett.102.115501.
- [131] H. MORIKAWA, C. C. HWANG, and H. W. YEOM: Controlled electron doping into metallic atomic wires: Si(111)4×1-In. *Phys. Rev. B*, vol. 81(7) (Feb. 2010) (cit. on p. 49).
DOI: 10.1103/physrevb.81.075401.
- [132] G. LEE et al.: Roles of defects induced by hydrogen and oxygen on the structural phase transition of Si(111)4 × 1-In. *Phys. Rev. B*, vol. 80(7) (Aug. 2009), p. 075411 (cit. on p. 49).
DOI: 10.1103/PhysRevB.80.075411.
- [133] H. SHIM et al.: Control of phase transition in quasi-one-dimensional atomic wires by electron doping. *Appl. Phys. Lett.* Vol. 94(23) (June 2009), p. 231901 (cit. on p. 49).
DOI: 10.1063/1.3143719.
- [134] H. W. YEOM, D. M. OH, S. WIPPERMANN, and W. G. SCHMIDT: Impurity-Mediated Early Condensation of a Charge Density Wave in an Atomic Wire Array. *ACS Nano*, vol. 10(1) (2016). PMID: 26634634, pp. 810–814 (cit. on p. 49).
DOI: 10.1021/acsnano.5b05925.
- [135] D. M. OH, S. WIPPERMANN, W. G. SCHMIDT, and H. W. YEOM: Oxygen adsorbates on the Si(111)4 × 1-In metallic atomic wire: Scanning tunneling microscopy and density-functional theory calculations. *Phys. Rev. B*, vol. 90(15) (Oct. 2014), p. 155432 (cit. on pp. 50, 59, 60).
DOI: 10.1103/PhysRevB.90.155432.
- [136] I. MATSUDA et al.: Electrical Resistance of a Monatomic Step on a Crystal Surface. *Phys. Rev. Lett.* Vol. 93(23) (Nov. 2004), p. 236801 (cit. on p. 51).
DOI: 10.1103/PhysRevLett.93.236801.
- [137] J. HOMOTH et al.: Electronic Transport on the Nanoscale: Ballistic Transmission and Ohms Law. *Nano Lett.* Vol. 9(4) (Apr. 2009), pp. 1588–1592. ISSN: 1530-6984 (cit. on p. 51).
DOI: 10.1021/nl803783g.

-
- [138] J. P. RÖNSPIES, S. WIESSELL, and H. PFNÜR: The resistance of single atomic steps in ultrathin Pb nanowires on Si(557). *Appl. Phys. A*, vol. 100(4) (July 2010), pp. 1007–1012. ISSN: 0947-8396, 1432-0630 (cit. on p. 51).
DOI: 10.1007/s00339-010-5902-y.
- [139] G. V. SAMSONOV: “Mechanical Properties of the Elements”. *Handbook of the Physicochemical Properties of the Elements*. Springer US, 1968, pp. 387–446 (cit. on p. 52).
DOI: 10.1007/978-1-4684-6066-7.
- [140] S. DEMUTH: “Transport in anisotropen 2D Systemen mit räumlicher Begrenzung”. MA thesis. Leibniz Universität Hannover, Jan. 2015 (cit. on p. 52).
- [141] N. MIYATA, H. WATANABE, and M. ICHIKAWA: Thermal Decomposition of an Ultrathin Si Oxide Layer around a Si(001). *Phys. Rev. Lett.* Vol. 84 (Aug. 5, Jan. 2000), pp. 1043–1046 (cit. on p. 53).
DOI: 10.1103/PhysRevLett.84.1043.
- [142] M. ICHIKAWA: Observation and control of Si surface and interface processes for nanostructure formation by scanning reflection electron microscopy. *J. Phys.: Condens. Matter*, vol. 11(49) (1999), p. 9861 (cit. on p. 53).
URL: <http://stacks.iop.org/0953-8984/11/i=49/a=304>.
- [143] S. FUJITA, S. MARUNO, H. WATANABE, and M. ICHIKAWA: Nanostructure fabrication using the selective thermal desorption of SiO₂ induced by electron beams. *Appl. Phys. Lett.* Vol. 69(5) (1996), pp. 638–640 (cit. on p. 53).
DOI: 10.1063/1.117932.
- [144] W. KERN: The Evolution of Silicon Wafer Cleaning Technology. en. *J. Electrochem. Soc.* Vol. 137(6) (Jan. 1990), pp. 1887–1892. ISSN: 0013-4651, 1945-7111 (cit. on p. 53).
DOI: 10.1149/1.2086825.
- [145] D. KARASHANOVA, J. J. MÉTOIS, F. LEROY, and P. MÜLLER: Is it possible to use external stress to tune silicon surface morphology? *Mater. Sci. Semicond. Process.* 7th International Workshop on Epitaxial Semiconductors on Patterned Substrates and Novel Index Surfaces (ESPS-NIS)7th ESPS-NIS 2008, vol. 12(1–2) (Feb. 2009), pp. 12–15. ISSN: 1369-8001 (cit. on p. 55).
DOI: 10.1016/j.mssp.2009.07.002.
- [146] S. WIPPERMANN, N. KOCH, and W. G. SCHMIDT: Adatom-Induced Conductance Modification of In Nanowires: Potential-Well Scattering and Structural Effects. *Phys. Rev. Lett.* Vol. 100(10) (Mar. 2008) (cit. on pp. 56, 59–61, 84).
DOI: 10.1103/physrevlett.100.106802.
- [147] H. SHIM et al.: Initial stages of oxygen adsorption on In/Si(111)-4 × 1. *Phys. Rev. B*, vol. 90(3) (July 2014), p. 035420 (cit. on p. 59).
DOI: 10.1103/PhysRevB.90.035420.

- [148] S. H. UHM and H. W. YEOM: Metal-insulator transition on the Si(111) 4×1 -In surface with oxygen impurity. *Phys. Rev. B*, vol. 88(16) (Oct. 2013), p. 165419 (cit. on pp. 59, 60).
DOI: 10.1103/PhysRevB.88.165419.
- [149] U. GERSTMANN et al.: Rashba splitting and relativistic energy shifts in In/Si(111) nanowires. *Phys. Rev. B*, vol. 89(16) (Apr. 2014), p. 165431 (cit. on p. 60).
DOI: 10.1103/PhysRevB.89.165431.
- [150] H. JOON CHOI and J. IHM: Ab initio pseudopotential method for the calculation of conductance in quantum wires. *Phys. Rev. B*, vol. 59(3) (Jan. 1999), pp. 2267–2275 (cit. on p. 60).
DOI: 10.1103/PhysRevB.59.2267.
- [151] A. SMOGUNOV, A. DAL CORSO, and E. TOSATTI: Ballistic conductance of magnetic Co and Ni nanowires with ultrasoft pseudopotentials. *Phys. Rev. B*, vol. 70(4) (July 2004), p. 045417 (cit. on p. 60).
DOI: 10.1103/PhysRevB.70.045417.
- [152] G. SCLAUZERO, A. DAL CORSO, and A. SMOGUNOV: Interaction of CO with an Au monatomic chain at different strains: Electronic structure and ballistic transport. *Phys. Rev. B*, vol. 85(16) (Apr. 2012), p. 165411 (cit. on p. 60).
DOI: 10.1103/PhysRevB.85.165411.
- [153] P. GIANNOZZI et al.: QUANTUM ESPRESSO: a modular and open-source software project for quantum simulations of materials. *J. Phys.: Condens. Matter*, vol. 21(39) (Sept. 2009), p. 395502 (cit. on p. 60).
DOI: 10.1088/0953-8984/21/39/395502.
- [154] H. J. MONKHORST and J. D. PACK: Special points for Brillouin-zone integrations. *Phys. Rev. B*, vol. 13(12) (June 1976), pp. 5188–5192 (cit. on p. 60).
DOI: 10.1103/PhysRevB.13.5188.
- [155] M. JAŁOCHOWSKI, M. STRÓŻAK, and R. ZDYB: Gold-induced ordering on vicinal Si(111). *Surf. Sci.* Vol. 375(2-3) (Apr. 1997), pp. 203–209 (cit. on pp. 65, 66).
DOI: 10.1016/s0039-6028(97)80009-x.
- [156] B. HAFKE et al.: Two-dimensional interaction of spin chains in the Si(553)-Au nanowire system. *Phys. Rev. B*, vol. 94(16) (Oct. 2016) (cit. on pp. 65, 73, 96).
DOI: 10.1103/physrevb.94.161403.
- [157] I. BARKE et al.: Coverage-dependent faceting of Au chains on Si(557). *Phys. Rev. B*, vol. 79(15) (Apr. 2009) (cit. on p. 66).
DOI: 10.1103/physrevb.79.155301.
- [158] P.-G. KANG, J. S. SHIN, and H. W. YEOM: Point defects along metallic atomic wires

-
- on vicinal Si surfaces: Si(557)-Au and Si(553)-Au. *Surf. Sci.* Vol. 603(16) (Aug. 2009), pp. 2588–2593 (cit. on pp. 67, 68, 84).
DOI: 10.1016/j.susc.2009.06.012.
- [159] I. K. ROBINSON, P. A. BENNETT, and F. J. HIMPSEL: Structure of Quantum Wires in Au/Si(557). *Phys. Rev. Lett.* Vol. 88(9) (Feb. 15, 2002), p. 096104 (cit. on p. 66).
DOI: 10.1103/PhysRevLett.88.096104.
- [160] D. SÁNCHEZ-PORTAL, J. D. GALE, A. GARCÍA, and R. M. MARTIN: Two distinct metallic bands associated with monatomic Au wires on the Si(557)-Au surface. *Phys. Rev. B*, vol. 65(8) (Feb. 2002) (cit. on pp. 66, 69).
DOI: 10.1103/physrevb.65.081401.
- [161] D. SÁNCHEZ-PORTAL and R. M. MARTIN: First principles study of the Si(557)-Au surface. *Surf. Sci.* Proceedings of the 7th International Conference on Nanometer-Scale Science and Technology and the 21st European Conference on Surface Science, vol. 532 (June 10, 2003), pp. 655–660. ISSN: 0039-6028 (cit. on p. 66).
DOI: 10.1016/s0039-6028(03)00224-3.
- [162] D. SÁNCHEZ-PORTAL, S. RIIKONEN, and R. M. MARTIN: Role of Spin-Orbit Splitting and Dynamical Fluctuations in the Si(557)-Au Surface. *Phys. Rev. Lett.* Vol. 93(14) (Sept. 2004) (cit. on pp. 66, 69, 77).
DOI: 10.1103/physrevlett.93.146803.
- [163] S. RIIKONEN and D. SÁNCHEZ-PORTAL: Interplay between electronic and atomic structures in the Si(557)-Au reconstruction from first principles. *Phys. Rev. B*, vol. 76(3) (July 2007) (cit. on p. 66).
DOI: 10.1103/physrevb.76.035410.
- [164] R. LOSIO et al.: Band Splitting for Si(557)-Au: Is It Spin-Charge Separation? *Phys. Rev. Lett.* Vol. 86(20) (May 14, 2001), pp. 4632–4635 (cit. on pp. 66, 67).
DOI: 10.1103/PhysRevLett.86.4632.
- [165] J. R. AHN, H. W. YEOM, H. S. YOON, and I.-W. LYO: Metal-Insulator Transition in Au Atomic Chains on Si with Two Proximal Bands. *Phys. Rev. Lett.* Vol. 91 (Aug. 19, Nov. 2003), p. 196403 (cit. on pp. 66, 67, 69, 132).
DOI: 10.1103/PhysRevLett.91.196403.
- [166] M. SCHÖCK, C. SÜRGER, and H. v LÖHNEYSSEN: Atomically resolved tunneling spectroscopy on Si(557)-Au. *Europhysics Letters (EPL)*, vol. 74(3) (May 2006), pp. 473–478 (cit. on p. 66).
DOI: 10.1209/epl/i2006-10009-9.
- [167] P. SEGOVIA, D. PURDIE, M. HENGESBERGER, and Y. BAER: Observation of spin and

- charge collective modes in one-dimensional metallic chains. *Nature*, vol. 402(6761) (Dec. 1999), pp. 504–507 (cit. on pp. 67, 69).
DOI: 10.1038/990052.
- [168] K. N. ALTMANN et al.: Electronic structure of atomic chains on vicinal Si(111)-Au. *Phys. Rev. B*, vol. 64(3) (June 19, 2001), p. 035406 (cit. on pp. 67, 68).
DOI: 10.1103/PhysRevB.64.035406.
- [169] H. S. KIM et al.: Evidence of metallic nature of the surface bands of Au/Si(557). *Phys. Rev. B*, vol. 80(3) (July 29, 2009), p. 033412 (cit. on pp. 67, 69).
DOI: 10.1103/PhysRevB.80.033412.
- [170] I. BARKE, F. ZHENG, T. K. RÜGHEIMER, and F. J. HIMPSEL: Experimental Evidence for Spin-Split Bands in a One-Dimensional Chain Structure. *Phys. Rev. Lett.* Vol. 97(22) (Dec. 2006) (cit. on pp. 69, 70).
DOI: 10.1103/physrevlett.97.226405.
- [171] T. OKUDA et al.: Large out-of-plane spin polarization in a spin-splitting one-dimensional metallic surface state on Si(557)-Au. *Phys. Rev. B*, vol. 82(16) (Oct. 15, 2010), p. 161410 (cit. on p. 69).
DOI: 10.1103/PhysRevB.82.161410.
- [172] H. W. YEOM et al.: Real-space investigation of the metal-insulator transition of Si(557)-Au. *Phys. Rev. B*, vol. 72(3) (July 2005), p. 035323 (cit. on p. 69).
DOI: 10.1103/PhysRevB.72.035323.
- [173] M. SAUTER, R. HOFFMANN, C. SÜRGER, and H. v. LÖHNEYSEN: Temperature-dependent scanning tunneling spectroscopy on the Si(557)-Au surface. *Phys. Rev. B*, vol. 89(7) (Feb. 10, 2014), p. 075406 (cit. on pp. 69, 70).
DOI: 10.1103/PhysRevB.89.075406.
- [174] J.-H. HAN et al.: Direct evidence of the step-edge buckling at the Au/Si(557)- 1×2 surface. *Phys. Rev. B*, vol. 80(24) (Dec. 2009) (cit. on p. 69).
DOI: 10.1103/physrevb.80.241401.
- [175] I. SONG et al.: Realization of a Strained Atomic Wire Superlattice. *ACS Nano*, vol. 9(11) (Nov. 2015), pp. 10621–10627. ISSN: 1936-0851 (cit. on pp. 69, 74, 103).
DOI: 10.1021/acsnano.5b04377.
- [176] K.-D. RYANG, P. G. KANG, H. W. YEOM, and S. JEONG: Structures and defects of atomic wires on Si(553)-Au: An STM and theoretical study. *Phys. Rev. B*, vol. 76(20) (Nov. 2007) (cit. on pp. 71, 102).
DOI: 10.1103/physrevb.76.205325.
- [177] W. VOEGELI et al.: Structure of the quasi-one-dimensional Si(553)-Au surface: Gold

-
- dimer row and silicon honeycomb chain. *Phys. Rev. B*, vol. 82(7) (Aug. 2010) (cit. on p. 72).
DOI: 10.1103/physrevb.82.075426.
- [178] S. RIIKONEN and D. SÁNCHEZ-PORTAL: Ab initio study of the double row model of the Si(553)-Au reconstruction. *Surf. Sci.* Vol. 600(6) (Mar. 2006), pp. 1201–1206 (cit. on p. 72).
DOI: 10.1016/j.susc.2005.12.043.
- [179] M. KRAWIEC: Structural model of the Au-induced Si(553) surface: Double Au rows. *Phys. Rev. B*, vol. 81 (Augs. 11, Mar. 2010), p. 115436 (cit. on pp. 72, 77).
DOI: 10.1103/PhysRevB.81.115436.
- [180] S. C. ERWIN and P. C. SNIJDERS: Silicon spin chains at finite temperature: Dynamics of Si(553)-Au. *Phys. Rev. B*, vol. 87 (Augs. 23, June 2013), p. 235316 (cit. on pp. 72, 73, 94).
DOI: 10.1103/PhysRevB.87.235316.
- [181] T. TAKAYAMA et al.: Structural Study of the Si(553)-Au Surface. *e-J. Surf. Sci. Nanotechnol.* Vol. 7 (2009), pp. 533–536 (cit. on p. 73).
DOI: 10.1380/ejssnt.2009.533.
- [182] H. W. YEOM et al.: Direct observation of the spin polarization in Au atomic wires on Si(553). *New J. Phys.* Vol. 16(9) (2014), p. 093030 (cit. on p. 73).
DOI: 10.1088/1367-2630/16/9/093030.
- [183] S. POLEI et al.: Structural Transition in Atomic Chains Driven by Transient Doping. *Phys. Rev. Lett.* Vol. 111(15) (Oct. 2013) (cit. on pp. 73, 101).
DOI: 10.1103/physrevlett.111.156801.
- [184] M. KRAWIEC, M. KOPCIUSZYŃSKI, and R. ZDYB: Different spin textures in one-dimensional electronic bands on Si(553)-Au surface. *Appl. Surf. Sci.* Vol. 373 (June 2016), pp. 26–31 (cit. on p. 73).
DOI: 10.1016/j.apsusc.2015.09.219.
- [185] T. NAGAO, S. YAGINUMA, T. INAOKA, and T. SAKURAI: One-Dimensional Plasmon in an Atomic-Scale Metal Wire. *Phys. Rev. Lett.* Vol. 97 (Augs. 11, Sept. 2006), p. 116802 (cit. on p. 74).
DOI: 10.1103/PhysRevLett.97.116802.
- [186] T. LICHTENSTEIN, C. TEGENKAMP, and H. PFNÜR: Lateral electronic screening in quasi-one-dimensional plasmons. *J. Phys.: Condens. Matter*, vol. 28(35) (July 2016), p. 354001 (cit. on pp. 74, 77).
DOI: 10.1088/0953-8984/28/35/354001.
- [187] T. LICHTENSTEIN et al.: Two-dimensional crossover and strong coupling of plasmon

- excitations in arrays of one-dimensional atomic wires. *Phys. Rev. B*, vol. 93 (Ausg. 16, Apr. 2016), 161408(R) (cit. on p. 74).
DOI: 10.1103/PhysRevB.93.161408.
- [188] H. OKINO et al.: Nonmetallic transport of a quasi-one-dimensional metallic Si(557)-Au surface. *Phys. Rev. B*, vol. 70(11) (Sept. 2004), p. 113404 (cit. on pp. 75, 88–90, 132).
DOI: 10.1103/PhysRevB.70.113404.
- [189] J. A. LIPTON-DUFFIN, J. M. MACLEOD, and A. B. MCLEAN: Detection of a Fermi-level crossing in Si(557)-Au with inverse photoemission. *Phys. Rev. B*, vol. 73 (Ausg. 24, June 2006), p. 245418 (cit. on p. 77).
DOI: 10.1103/PhysRevB.73.245418.
- [190] J. P. PERDEW, K. BURKE, and M. ERNZERHOF: Generalized Gradient Approximation Made Simple. *Phys. Rev. Lett.* Vol. 77 (Ausg. 18, Oct. 1996), pp. 3865–3868 (cit. on p. 81).
DOI: 10.1103/PhysRevLett.77.3865.
- [191] P. E. BLÖCHL: Projector augmented-wave method. *Phys. Rev. B*, vol. 50 (Ausg. 24, Dec. 1994), pp. 17953–17979 (cit. on p. 81).
DOI: 10.1103/PhysRevB.50.17953.
- [192] G. KRESSE and J. FURTHMÜLLER: Efficient iterative schemes for ab-initio total energy calculations using a plane-wave basis set. *Phys. Rev. B*, vol. 54 (1996), p. 11169 (cit. on p. 81).
DOI: 10.1103/PhysRevB.54.11169.
- [193] P. V. C. MEDEIROS, S. STAFSTRÖM, and J. BJÖRK: Effects of extrinsic and intrinsic perturbations on the electronic structure of graphene: Retaining an effective primitive cell band structure by band unfolding. *Phys. Rev. B*, vol. 89(4) (Jan. 2014), p. 041407 (cit. on p. 85).
DOI: 10.1103/PhysRevB.89.041407.
- [194] I. LANGMUIR: The Adsorption of Gases on Plane Surfaces of Glass, Mica and Platinum. *J. Am. Chem. Soc.* Vol. 40(9) (Sept. 1918), pp. 1361–1403. ISSN: 0002-7863 (cit. on pp. 87, 137, 138).
DOI: 10.1021/ja02242a004.
- [195] K. W. KOLASINSKI: *Surface Science*. John Wiley & Sons, Ltd, Apr. 2012 (cit. on pp. 87, 137).
DOI: 10.1002/9781119941798.
- [196] S. Z. TEHRANI, W. LIM, and L. LEE: Correction factors for films resistivity measurement. *Measurement*, vol. 45(3) (Apr. 2012), p. 219 (cit. on p. 92).
DOI: 10.1016/j.measurement.2011.11.019.

-
- [197] F. van DELFT et al.: Determination of surface debye temperatures by leed. *Surf. Sci.* Vol. 189-190 (Oct. 1987), pp. 695–703 (cit. on p. 94).
DOI: 10.1016/s0039-6028(87)80502-2.
- [198] P. JENNINGS and S. THURGATE: The inner potential in LEED. *Surface Science*, vol. 104(2-3) (Mar. 1981), pp. L210–L212 (cit. on p. 94).
DOI: 10.1016/0039-6028(81)90056-x.
- [199] J. N. CRAIN and D. T. PIERCE: End States in One-Dimensional Atom Chains. *Science*, vol. 307(5710) (Feb. 2005), pp. 703–706. ISSN: 0036-8075, 1095-9203 (cit. on p. 98).
DOI: 10.1126/science.1106911.
- [200] N. ARORA, J. HAUSER, and D. ROULSTON: Electron and hole mobilities in silicon as a function of concentration and temperature. *IEEE Transactions on Electron Devices*, vol. 29(2) (Feb. 1982), pp. 292–295 (cit. on pp. 98, 136).
DOI: 10.1109/t-ed.1982.20698.
- [201] S. S. LI: The dopant density and temperature dependence of hole mobility and resistivity in boron doped silicon. *Solid-State Electron.* Vol. 21(9) (Sept. 1978), pp. 1109–1117 (cit. on p. 100).
DOI: 10.1016/0038-1101(78)90345-3.
- [202] S. POLEI, P. C. SNIJDERS, K.-H. MEIWES-BROER, and I. BARKE: Current-dependent periodicities of Si(553)-Au. *Phys. Rev. B*, vol. 89(20) (May 2014) (cit. on p. 101).
DOI: 10.1103/physrevb.89.205420.
- [203] T. LICHTENSTEIN: “Plasmons in gold-induced quantum wires”. PhD thesis. Leibniz Universität Hannover, 2017 (cit. on p. 103).
- [204] SANNA. Private communication with the group of Simone Sanna, University of Gießen, Germany (cit. on p. 103).
- [205] W. TANG et al.: Ultrashort Channel Silicon Nanowire Transistors with Nickel Silicide Source/Drain Contacts. *Nano Lett.* Vol. 12(8) (2012), pp. 3979–3985 (cit. on p. 105).
DOI: 10.1021/nl3011676.
- [206] S.-Y. CHEN et al.: Low Resistivity Metal Silicide Nanowires with Extraordinarily High Aspect Ratio for Future Nanoelectronic Devices. *ACS Nano*, vol. 5(11) (2011), pp. 9202–9207 (cit. on p. 105).
DOI: 10.1021/nn203445p.
- [207] A. L. SCHMITT, J. M. HIGGINS, J. R. SZCZECZ, and S. JIN: Synthesis and applications of metal silicide nanowires. *J. Mater. Chem.* Vol. 20 (Ausc. 2, 2010), pp. 223–235 (cit. on p. 105).
DOI: 10.1039/B910968D.

- [208] V. IANCU et al.: Polaronic Transport and Current Blockades in Epitaxial Silicide Nanowires and Nanowire Arrays. *Nano Lett.* Vol. 13(8) (Aug. 2013), pp. 3684–3689. ISSN: 1530-6984 (cit. on pp. 105, 106, 124). DOI: 10.1021/nl401574c.
- [209] L. J. CHEN, ed.: *Silicide Technology for Integrated Circuits*. Vol. 5. IET, Jan. 2004. ISBN: 978-0-86341-352-0 (cit. on p. 105). DOI: 10.1049/PBEP005E.
- [210] P. S. Y. LIM, D. Z. CHI, Q. ZHOU, and Y.-C. YEO: NiSi₂ formation through annealing of nickel and dysprosium stack on Si(100) and impact on effective Schottky barrier height. *J. Appl. Phys.* Vol. 113(1) (2013), p. 013712 (cit. on p. 105). DOI: 10.1063/1.4772710.
- [211] THE INTERNATIONAL TECHNOLOGY ROADMAP FOR SEMICONDUCTORS: *ITRS 2007 Edition*. Tech. rep. ITRS, 2007 (cit. on p. 105). URL: <http://www.itrs.net/ITRS%201999-2014%20Mtgs,%20Presentations%20&%20Links/2007ITRS/Home2007.htm> (visited on 12/16/2015).
- [212] S.-L. ZHANG and Z. ZHANG: “6 - Metal silicides in advanced complementary metal-oxide-semiconductor (CMOS) technology”. *Metallic Films for Electronic, Optical and Magnetic Applications*. Ed. by K. BARMAK and K. COFFEY. Woodhead Publishing, 2014, pp. 244–301. ISBN: 978-0-85709-057-7 (cit. on p. 105). DOI: 10.1533/9780857096296.1.244.
- [213] I.-H. HONG, T.-M. CHEN, and Y.-F. TSAI: Atomically precise self-organization of perfectly ordered gadolinium–silicide nanomeshes controlled by anisotropic electromigration-induced growth on Si(1 1 0)-16 Å—2 surfaces. *Appl. Surf. Sci.* Vol. 349 (2015), pp. 49–58. ISSN: 0169-4332 (cit. on p. 105). DOI: 10.1016/j.apsusc.2015.04.094.
- [214] M. BULANOVA et al.: Terbium-silicon system. *Zeitschrift fuer Metallkunde / Materials Research and Advanced Techniques*, vol. 90(3) (1999), pp. 216–222 (cit. on pp. 105, 109). URL: <https://www.scopus.com/inward/record.uri?eid=2-s2.0-0032634104&partnerID=40&md5=34dff591e10a4a4f52db50f76b68cd03> (visited on 02/10/2016).
- [215] L. CHEN and K. TU: Epitaxial growth of transition-metal silicides on silicon. *Materials Science Reports*, vol. 6(2–3) (1991), pp. 53–140. ISSN: 0920-2307 (cit. on p. 105). DOI: 10.1016/0920-2307(91)90004-7.
- [216] Y. CHEN, D. A. A. OHLBERG, and R. S. WILLIAMS: Nanowires of four epitaxial hexagonal silicides grown on Si(001). *J. Appl. Phys.* Vol. 91(5) (2002), pp. 3213–3218 (cit. on p. 105). DOI: 10.1063/1.1428807.

-
- [217] J. L. McCHESNEY et al.: Gd disilicide nanowires attached to Si(111) steps. *Nanotechnology*, vol. 13(4) (2002), p. 545 (cit. on p. 105).
DOI: 10.1088/0957-4484/13/4/319.
- [218] M. FRANZ, J. GROSSE, R. KOHLHAAS, and M. DÄHNE: Terbium induced nanostructures on Si(111). *Surf. Sci.* Vol. 637–638 (2015), pp. 149–155. ISSN: 0039-6028 (cit. on p. 105).
DOI: 10.1016/j.susc.2015.03.026.
- [219] Y. CHEN et al.: Growth and evolution of epitaxial erbium disilicide nanowires on Si(001). *Appl. Phys. A*, vol. 75(3) (Sept. 2002), pp. 353–361. ISSN: 0947-8396, 1432-0630 (cit. on pp. 105, 107).
DOI: 10.1007/s003390201315.
- [220] H. W. YEOM et al.: Robust One-Dimensional Metallic Band Structure of Silicide Nanowires. *Phys. Rev. Lett.* Vol. 95 (Augs. 20, Nov. 2005), p. 205504 (cit. on pp. 105, 106, 110, 132).
DOI: 10.1103/PhysRevLett.95.205504.
- [221] P. BENNETT, Z. HE, D. J. SMITH, and F. ROSS: Endotaxial silicide nanowires: A review. *Thin Solid Films*, vol. 519(24) (2011), pp. 8434–8440. ISSN: 0040-6090 (cit. on p. 105).
DOI: 10.1016/j.tsf.2011.05.034.
- [222] M. DÄHNE and M. WANKE: Metallic rare-earth silicide nanowires on silicon surfaces. *J. Phys.: Condens. Matter*, vol. 25(1) (2013), p. 014012 (cit. on p. 105).
DOI: 10.1088/0953-8984/25/1/014012.
- [223] L. ZHIGANG et al.: Resistivity measurements of self-assembled epitaxially grown erbium silicide nanowires. *J. Phys. D: Appl. Phys.* Vol. 39(13) (2006), p. 2839 (cit. on p. 106).
DOI: 10.1088/0022-3727/39/13/031.
- [224] S. APPELFELLER, S. KULS, and M. DÄHNE: Tb silicide nanowire growth on planar and vicinal Si(001) surfaces. *Surf. Sci.* Vol. 641 (Nov. 2015), pp. 180–190 (cit. on pp. 106, 107, 109).
DOI: 10.1016/j.susc.2015.07.001.
- [225] V. IANCU et al.: Structure and growth of quasi-one-dimensional YSi₂ nanophases on Si(100). *J. Phys.: Condens. Matter*, vol. 25(1) (Jan. 2013), p. 014011. ISSN: 0953-8984 (cit. on pp. 106, 107).
DOI: 10.1088/0953-8984/25/1/014011.
- [226] N. INOUE, Y. TANISHIRO, and K. YAGI: UHV-REM Study of Changes in the Step

- Structures on Clean (100) Silicon Surfaces by Annealing. *Japanese Journal of Applied Physics*, vol. 26(4A) (1987), p. L293 (cit. on p. 107).
DOI: 10.1143/JJAP.26.L293.
- [227] B. Z. LIU and J. NOGAMI: A scanning tunneling microscopy study of dysprosium silicide nanowire growth on Si(001). *J. Appl. Phys.* Vol. 93(1) (Jan. 2003), pp. 593–599. ISSN: 0021-8979, 1089-7550 (cit. on p. 107).
DOI: 10.1063/1.1516621.
- [228] M. DEGAWA et al.: Direct Current Heating Induced Giant Step Bunching and Wandering on Si(111) and (001) Vicinal Surfaces. *Japanese Journal of Applied Physics*, vol. 38(3B) (1999), p. L308 (cit. on p. 107).
DOI: 10.1143/JJAP.38.L308.
- [229] H. MINODA: Direct current heating effects on Si(111) vicinal surfaces. *J. Phys.: Condens. Matter*, vol. 15(47) (2003), S3255 (cit. on p. 107).
DOI: 10.1088/0953-8984/15/47/005.
- [230] S. APPELFELLER et al.: Capping of rare earth silicide nanowires on Si(001). *Appl. Phys. Lett.* Vol. 108(1) (Jan. 2016), p. 013109 (cit. on pp. 107, 112, 120, 132).
DOI: 10.1063/1.4939693.
- [231] Y. CUI, J. CHUNG, and J. NOGAMI: Controlling the width of self-assembled dysprosium silicide nanowires on the Si(001) surface. *J. Phys.: Condens. Matter*, vol. 24(4) (2012), p. 045003 (cit. on p. 109).
DOI: 10.1088/0953-8984/24/4/045003.
- [232] “2. Statistical nature of rough surfaces”. *Experimental Methods in the Physical Sciences*. Ed. by Y. ZHAO, G.-C. WANG, and T.-M. LU. Vol. 37. Characterization of Amorphous and Crystalline Rough Surface: Principles and Applications. Academic Press, 2001, pp. 7–32 (cit. on p. 109).
DOI: 10.1016/S1079-4042(01)80057-6.
- [233] T. GREDIG, E. A. SILVERSTEIN, and M. P. BYRNE: Height-Height Correlation Function to Determine Grain Size in Iron Phthalocyanine Thin Films. *J. Phys. Conf. Ser.* Vol. 417(1) (Mar. 2013), p. 012069. ISSN: 1742-6596 (cit. on p. 110).
DOI: 10.1088/1742-6596/417/1/012069.
- [234] J. KRIM and J. O. INDEKEU: Roughness exponents: A paradox resolved. *Physical Review E*, vol. 48(2) (Aug. 1993), pp. 1576–1578 (cit. on p. 110).
DOI: 10.1103/PhysRevE.48.1576.
- [235] S. LABAT et al.: Microstructural analysis of AU/Ni multilayers interfaces by SAXS and STM. *Appl. Surf. Sci.* E-MRS SYMPOSIUM M; STRESS AND STRAIN IN HETEROEPITAXY, vol. 188 (Mar. 2002), pp. 182–187. ISSN: 0169-4332 (cit. on p. 110).
DOI: 10.1016/S0169-4332(01)00739-5.

-
- [236] M. McELLISTREM, G. HAASE, D. CHEN, and R. J. HAMERS: Electrostatic sample-tip interactions in the scanning tunneling microscope. *Phys. Rev. Lett.* Vol. 70(16) (Apr. 1993), pp. 2471–2474 (cit. on p. 110).
DOI: 10.1103/PhysRevLett.70.2471.
- [237] C. OHBUCHI and J. NOGAMI: Holmium growth on Si(001): Surface reconstructions and nanowire formation. *Phys. Rev. B*, vol. 66 (Aug. 16, Oct. 2002), p. 165323 (cit. on p. 110).
DOI: 10.1103/PhysRevB.66.165323.
- [238] D. LEE and S. KIM: Formation of hexagonal Gd disilicide nanowires on Si(100). *Appl. Phys. Lett.* Vol. 82(16) (2003), pp. 2619–2621 (cit. on p. 110).
DOI: 10.1063/1.1569654.
- [239] V. IANCU, P. R. C. KENT, C. G. ZENG, and H. H. WEITERING: Structure of YSi₂ nanowires from scanning tunneling spectroscopy and first principles. *Appl. Phys. Lett.* Vol. 95(12) (2009), p. 123107 (cit. on p. 110).
DOI: 10.1063/1.3236778.
- [240] M. WANKE et al.: Electronic properties of self-assembled rare-earth silicide nanowires on Si(001). *Phys. Rev. B*, vol. 83 (Aug. 20, May 2011), p. 205417 (cit. on p. 110).
DOI: 10.1103/PhysRevB.83.205417.
- [241] F. H. KAATZ et al.: Anomalous magnetotransport in epitaxial TbSi_{2-x}. *Journal of Vacuum Science & Technology A*, vol. 9(3) (May 1991), pp. 426–429. ISSN: 0734-2101, 1520-8559 (cit. on pp. 117, 119, 121, 124).
DOI: 10.1116/1.577426.
- [242] J. THOMSON: “On the theory of electric conduction through thin metallic films”. *Proc. Cambridge Philos. Soc.* Vol. 11. 1901, pp. 120–123 (cit. on p. 119).
URL: <http://biodiversitylibrary.org/page/34812722>.
- [243] H. MAROM, J. MULLIN, and M. EIZENBERG: Size-dependent resistivity of nanometric copper wires. *Phys. Rev. B*, vol. 74(4) (July 2006), p. 045411 (cit. on pp. 119, 121).
DOI: 10.1103/PhysRevB.74.045411.
- [244] W. STEINHÖGL et al.: Comprehensive study of the resistivity of copper wires with lateral dimensions of 100 nm and smaller. *J. Appl. Phys.* Vol. 97(2) (Jan. 2005), p. 023706 (cit. on p. 119).
DOI: 10.1063/1.1834982.
- [245] K. FUCHS: The conductivity of thin metallic films according to the electron theory of metals. *Math. Proc. Cambridge Philos. Soc.* Vol. 34(01) (Jan. 1938), pp. 100–108. ISSN: 1469-8064 (cit. on pp. 119–121).
DOI: 10.1017/S0305004100019952.

- [246] D. K. C. MACDONALD and K. SARGINSON: Size Effect Variation of the Electrical Conductivity of Metals. *Proceedings of the Royal Society of London A: Mathematical, Physical and Engineering Sciences*, vol. 203(1073) (Sept. 1950), pp. 223–240 (cit. on pp. 119, 121).
DOI: 10.1098/rspa.1950.0136.
- [247] R. B. DINGLE: The Electrical Conductivity of Thin Wires. *Proceedings of the Royal Society of London A: Mathematical, Physical and Engineering Sciences*, vol. 201(1067) (May 1950), pp. 545–560. ISSN: 1364-5021, 1471-2946 (cit. on pp. 119, 121).
DOI: 10.1098/rspa.1950.0077.
- [248] L. MORAGA, C. ARENAS, R. HENRIQUEZ, and B. SOLIS: The effect of surface roughness and grain-boundary scattering on the electrical conductivity of thin metallic wires. *physica status solidi (b)*, vol. 252(1) (Jan. 2015), pp. 219–229. ISSN: 1521-3951 (cit. on pp. 119, 121).
DOI: 10.1002/pssb.201451202.
- [249] A. F. MAYADAS and M. SHATZKES: Electrical-Resistivity Model for Polycrystalline Films: the Case of Arbitrary Reflection at External Surfaces. *Phys. Rev. B*, vol. 1(4) (Feb. 1970), pp. 1382–1389 (cit. on pp. 119, 120).
DOI: 10.1103/PhysRevB.1.1382.
- [250] E. H. SONDHEIMER: The mean free path of electrons in metals. *Adv. Phys.* Vol. 50(6) (Sept. 2001), pp. 499–537. ISSN: 0001-8732 (cit. on pp. 119, 121).
DOI: 10.1080/00018730110102187.
- [251] G. APRILESI et al.: Electrical transport properties in Co silicides formed by thin film reactions. *J. Appl. Phys.* Vol. 60(1) (1986), pp. 310–317 (cit. on p. 120).
DOI: 10.1063/1.337645.
- [252] C. -.-D. LIEN, M. FINETTI, M.-A. NICOLET, and S. S. LAU: Electrical properties of thin Co₂Si, CoSi, and CoSi₂ layers grown on evaporated silicon. *J. Electron. Mater.* Vol. 13(1) (1984), pp. 95–105 (cit. on p. 120).
DOI: 10.1007/BF02659838.
- [253] E. COLGAN, J. GAMBINO, and Q. HONG: Formation and stability of silicides on polycrystalline silicon. *Materials Science and Engineering: R: Reports*, vol. 16(2) (1996), pp. 43–96. ISSN: 0927-796X (cit. on p. 120).
DOI: 10.1016/0927-796X(95)00186-7.
- [254] J. C. HENSEL, R. T. TUNG, J. M. POATE, and F. C. UNTERWALD: Electrical transport properties of CoSi₂ and NiSi₂ thin films. *Appl. Phys. Lett.* Vol. 44(9) (1984), pp. 913–915 (cit. on p. 120).
DOI: 10.1063/1.94932.
- [255] A. F. MAYADAS, M. SHATZKES, and J. F. JANAK: Electrical Resistivity Model for

-
- Polycrystalline Films: The Case of Specular Reflection at External Surfaces. *Appl. Phys. Lett.* Vol. 14(11) (1969), pp. 345–347 (cit. on p. 120).
DOI: 10.1063/1.1652680.
- [256] G. YE, J. NOGAMI, and M. A. CRIMP: Dysprosium disilicide nanostructures on silicon(001) studied by scanning tunneling microscopy and transmission electron microscopy. *Thin Solid Films*, vol. 497(1–2) (2006), pp. 48–52. ISSN: 0040-6090 (cit. on p. 120).
DOI: 10.1016/j.tsf.2005.09.180.
- [257] G. YE, M. A. CRIMP, and J. NOGAMI: Self-assembled Gd silicide nanostructures grown on Si(001). *J. Appl. Phys.* Vol. 105(10) (2009), p. 104304 (cit. on p. 120).
DOI: 10.1063/1.3118573.
- [258] W. STEINHÖGL, G. SCHINDLER, G. STEINLESBERGER, and M. ENGELHARDT: Size-dependent resistivity of metallic wires in the mesoscopic range. *Phys. Rev. B*, vol. 66 (Aug. 7, Aug. 2002), p. 075414 (cit. on p. 121).
DOI: 10.1103/PhysRevB.66.075414.
- [259] Y. P. TIMALSINA et al.: Effects of nanoscale surface roughness on the resistivity of ultrathin epitaxial copper films. *Nanotechnology*, vol. 26(7) (Feb. 2015), p. 075704. ISSN: 0957-4484 (cit. on p. 121).
DOI: 10.1088/0957-4484/26/7/075704.
- [260] D. DAYAL and P. WISSMANN: Observation of negative p values in adsorption experiments on thin metal films. *Thin Solid Films*, vol. 44(2) (July 1977), pp. 185–191 (cit. on p. 121).
DOI: 10.1016/0040-6090(77)90453-9.
- [261] H. -.-D. LIU et al.: Thickness dependent electrical resistivity of ultrathin (40 nm) Cu films. *Thin Solid Films*, vol. 384(1) (Mar. 2001), pp. 151–156 (cit. on p. 121).
DOI: 10.1016/S0040-6090(00)01818-6.
- [262] C. DURKAN and M. E. WELLAND: Size effects in the electrical resistivity of polycrystalline nanowires. *Phys. Rev. B*, vol. 61(20) (May 2000), pp. 14215–14218 (cit. on p. 121).
DOI: 10.1103/PhysRevB.61.14215.
- [263] M. JAŁOCHOWSKI and E. BAUER: Resistance oscillations and crossover in ultrathin gold films. *Phys. Rev. B*, vol. 37(15) (May 1988), pp. 8622–8626 (cit. on p. 121).
DOI: 10.1103/PhysRevB.37.8622.
- [264] N. TRIVEDI and N. W. ASHCROFT: Quantum size effects in transport properties of metallic films. *Phys. Rev. B*, vol. 38(17) (Dec. 1988), pp. 12298–12309 (cit. on pp. 121, 123, 124).
DOI: 10.1103/PhysRevB.38.12298.

- [265] J. ZIMAN: *Electrons and Phonons: The Theory of Transport Phenomena in Solids*. International series of monographs on physics. OUP Oxford, 1960. ISBN: 9780198507796 (cit. on pp. 122, 123).
URL: <https://books.google.de/books?id=UtEy63pjngsC>.
- [266] S. B. SOFFER: Statistical Model for the Size Effect in Electrical Conduction. *J. Appl. Phys.* Vol. 38(4) (1967), pp. 1710–1715 (cit. on p. 122).
DOI: 10.1063/1.1709746.
- [267] H. HOFFMANN and J. VANCEA: Critical assessment of thickness-dependent conductivity of thin metal films. *Thin Solid Films*, vol. 85(2) (1981), pp. 147–167 (cit. on p. 122).
DOI: 10.1016/0040-6090(81)90627-1.
- [268] J. R. SAMBLES: The resistivity of thin metal films—Some critical remarks. *Thin Solid Films*, vol. 106(4) (Aug. 1983), pp. 321–331 (cit. on p. 122).
DOI: 10.1016/0040-6090(83)90344-9.
- [269] G. KÄSTLE et al.: Size effect of the resistivity of thin epitaxial gold films. *Phys. Rev. B*, vol. 70(16) (Oct. 2004), p. 165414 (cit. on p. 122).
DOI: 10.1103/PhysRevB.70.165414.
- [270] U. JACOB, J. VANCEA, and H. HOFFMANN: Surface-roughness contributions to the electrical resistivity of polycrystalline metal films. *Phys. Rev. B*, vol. 41(17) (June 1990), pp. 11852–11857 (cit. on p. 122).
DOI: 10.1103/PhysRevB.41.11852.
- [271] J. R. SAMBLES, K. C. ELSOM, and D. J. JARVIS: The Electrical Resistivity of Gold Films. *Philosophical Transactions of the Royal Society of London A: Mathematical, Physical and Engineering Sciences*, vol. 304(1486) (Mar. 1982), pp. 365–396 (cit. on p. 122).
DOI: 10.1098/rsta.1982.0016.
- [272] J. C. HENSEL, R. T. TUNG, J. M. POATE, and F. C. UNTERWALD: Specular Boundary Scattering and Electrical Transport in Single-Crystal Thin Films of CoSi₂. *Phys. Rev. Lett.* Vol. 54 (Aug. 16, Apr. 1985), pp. 1840–1843 (cit. on p. 122).
DOI: 10.1103/PhysRevLett.54.1840.
- [273] T. S. KUAN et al.: “Fabrication and Performance Limits of Sub-0.1 μm Cu Interconnects”. *Symposium D – Materials, Technology & Reliability for Advanced Interconnects*. Vol. 612. MRS Online Proceedings Library. 2000 (cit. on p. 122).
DOI: 10.1557/PROC-612-D7.1.1.
- [274] S. M. ROSSNAGEL and T. S. KUAN: Alteration of Cu conductivity in the size effect regime. *J. Vac. Sci. Technol., B*, vol. 22(1) (2004), pp. 240–247 (cit. on p. 122).
DOI: 10.1116/1.1642639.

-
- [275] A. KASER and E. GERLACH: Scattering of conduction electrons by interface roughness in semiconductor heterostructures. *Zeitschrift für Physik B Condensed Matter*, vol. 98(2) (1995), pp. 207–213 (cit. on p. 123).
DOI: 10.1007/BF01324526.
- [276] L. SHENG, D. Y. XING, and Z. D. WANG: Transport theory in metallic films: Crossover from the classical to the quantum regime. *Phys. Rev. B*, vol. 51(11) (Mar. 1995), pp. 7325–7328 (cit. on p. 123).
DOI: 10.1103/PhysRevB.51.7325.
- [277] S. CHATTERJEE and A. E. MEYEROVICH: Interference between bulk and boundary scattering in high quality films. *Phys. Rev. B*, vol. 81(24) (June 2010), p. 245409 (cit. on pp. 123–125).
DOI: 10.1103/PhysRevB.81.245409.
- [278] R. C. MUNOZ, C. ARENAS, G. KREMER, and L. MORAGA: Surface-induced resistivity of CoSi 2 films and violations of Mathiessen’s rule. *J. Phys.: Condens. Matter*, vol. 15(10) (2003), p. L177 (cit. on p. 123).
DOI: 10.1088/0953-8984/15/10/101.
- [279] G. FISHMAN and D. CALECKI: Surface-induced resistivity of ultrathin metallic films: A limit law. *Phys. Rev. Lett.* Vol. 62 (Aug. 11, Mar. 1989), pp. 1302–1305 (cit. on pp. 123, 124).
DOI: 10.1103/PhysRevLett.62.1302.
- [280] G. MAHAN: *Many-Particle Physics*. Physics of Solids and Liquids. Springer, 2000. ISBN: 9780306463389 (cit. on p. 123).
URL: <https://books.google.de/books?id=xzSgZ4-yyMEC>.
- [281] Z. TEŠANOVIĆ, M. V. JARIĆ, and S. MAEKAWA: Quantum Transport and Surface Scattering. *Phys. Rev. Lett.* Vol. 57(21) (Nov. 1986), pp. 2760–2763 (cit. on p. 123).
DOI: 10.1103/PhysRevLett.57.2760.
- [282] S. CHATTERJEE and A. E. MEYEROVICH: Quantum size effect and the two types of interference between bulk and boundary scattering in ultrathin films. *Phys. Rev. B*, vol. 84 (Aug. 16, Oct. 2011), p. 165432 (cit. on p. 123).
DOI: 10.1103/PhysRevB.84.165432.
- [283] G. FISHMAN and D. CALECKI: Influence of surface roughness on the conductivity of metallic and semiconducting quasi-two-dimensional structures. *Phys. Rev. B*, vol. 43(14) (May 1991), pp. 11581–11585 (cit. on p. 124).
DOI: 10.1103/PhysRevB.43.11581.
- [284] R. C. MUNOZ: Resistivity induced by a rough surface of thin gold films deposited on mica. *J. Mol. Catal. A: Chem.* Vol. 228(1–2) (Mar. 2005), pp. 163–175 (cit. on p. 124).
DOI: 10.1016/j.molcata.2004.09.084.

- [285] S. QIN et al.: Contacting nanowires and nanotubes with atomic precision for electronic transport. *Appl. Phys. Lett.* Vol. 100(10) (Mar. 2012), p. 103103 (cit. on pp. 125, 126). DOI: 10.1063/1.3692585.
- [286] H. J. MAMIN, P. H. GUETHNER, and D. RUGAR: Atomic emission from a gold scanning-tunneling-microscope tip. *Phys. Rev. Lett.* Vol. 65(19) (Nov. 1990), pp. 2418–2421 (cit. on p. 125). DOI: 10.1103/physrevlett.65.2418.
- [287] C. HOGAN et al.: “Controlling the local electronic properties of Si(553)-Au through hydrogen doping”. submitted / under review (cit. on p. 132).
- [288] WOLFRAM RESEARCH INC.: *Mathematica 10.0*. Champaign, Illinois: Wolfram Research, Inc., 2014 (cit. on pp. 136, 138). URL: <http://www.wolfram.com>.

Publication list

- [P1] J. BARINGHAUS, F. EDLER, C. NEUMANN, C. STAMPFER, S. FORTI, U. STARKE, and C. TEGENKAMP: Local transport measurements on epitaxial graphene. *Applied Physics Letters*, vol. 103(11) (Sept. 2013), p. 111604. ISSN: 00036951. DOI: 10.1063/1.4821364.
- [P2] J. BARINGHAUS, F. EDLER, and C. TEGENKAMP: Edge-states in graphene nanoribbons: a combined spectroscopy and transport study. *Journal of Physics: Condensed Matter*, vol. 25(39) (Aug. 2013), p. 392001. ISSN: 0953-8984. DOI: 10.1088/0953-8984/25/39/392001.
- [P3] J. BARINGHAUS, M. RUAN, F. EDLER, A. TEJEDA, M. SICOT, A. TALEB-IBRAHIMI, A.-P. LI, Z. JIANG, E. H. CONRAD, C. BERGER, C. TEGENKAMP, and W. A. de HEER: Exceptional ballistic transport in epitaxial graphene nanoribbons. *Nature*, vol. 506(7488) (Feb. 2014), pp. 349–354. ISSN: 0028-0836. DOI: 10.1038/nature12952.
- [P4] L. BARRETO, L. KÜHNEMUND, F. EDLER, C. TEGENKAMP, J. MI, M. BREMHOLM, B. B. IVERSEN, C. FRYDENDAHL, M. BIANCHI, and P. HOFMANN: Surface-Dominated Transport on a Bulk Topological Insulator. *Nano Letters*, vol. 14(7) (June 2014), pp. 3755–3760. ISSN: 1530-6984. DOI: 10.1021/nl501489m.
- [P5] F. EDLER, I. MICCOLI, S. DEMUTH, H. PFNÜR, S. WIPPERMANN, A. LÜCKE, W. G. SCHMIDT, and C. TEGENKAMP: Interwire coupling for In(4 × 1)/Si(111) probed by surface transport. *Physical Review B*, vol. 92(8) (Aug. 2015), p. 085426. DOI: 10.1103/PhysRevB.92.085426.
- [P6] I. MICCOLI, F. EDLER, H. PFNÜR, and C. TEGENKAMP: The 100th anniversary of the four-point probe technique: the role of probe geometries in isotropic and anisotropic systems. *Journal of Physics: Condensed Matter*, vol. 27(22) (May 2015), p. 223201. DOI: 10.1088/0953-8984/27/22/223201.

- [P7] I. MICCOLI, F. EDLER, P. PRETE, N. LOVERGINE, H. PFNÜR, and C. TEGENKAMP: Surface-mediated electrical transport in single GaAs nanowires. *Proc. 1st IEEE Nanotechnology for Instrumentation and Measurement Workshop*, vol. (2015).
- [P8] I. MICCOLI, F. EDLER, H. PFNÜR, S. APPELFELLER, M. DÄHNE, K. HOLTGREWE, S. SANNA, W. G. SCHMIDT, and C. TEGENKAMP: Atomic size effects studied by transport in single silicide nanowires. *Physical Review B*, vol. 93(12) (Mar. 2016). DOI: 10.1103/physrevb.93.125412.
- [P9] F. EDLER, I. MICCOLI, J. P. STÖCKMANN, H. PFNÜR, C. BRAUN, S. NEUFELD, S. SANNA, W. G. SCHMIDT, and C. TEGENKAMP: Tuning the conductivity along atomic chains by selective chemisorption. *Physical Review B*, vol. 95(12) (Mar. 2017). DOI: 10.1103/physrevb.95.125409.
- [P10] A. CHATTERJEE, T. BAI, F. EDLER, C. TEGENKAMP, K. WEIDE-ZAAGE, and H. PFNÜR: Electromigration and morphological changes in Ag nanostructures. *Journal of Physics: Condensed Matter*, vol. (Jan. 2018). DOI: 10.1088/1361-648x/aaa80a.
- [P11] F. EDLER, I. MICCOLI, H. PFNÜR, and C. TEGENKAMP: “Electronic transport in an anisotropic 2D quantum spin liquid system”. Unpublished.

Curriculum Vitae

PERSONAL INFORMATION:

NAME Frederik Edler

DATE OF BIRTH 13.03.1988 in Hannover

EDUCATION:

Since Dec. 2012 Doctorate at Institut für Festkörperphysik, Gottfried Wilhelm Leibniz Universität Hannover

2010 – 2012 Master of Science, Physics, Gottfried Wilhelm Leibniz Universität Hannover
Thesis: *Lokale Transportmessungen an Graphen-Nanostrukturen*

2007 – 2010 Bachelor of Science, Physics, Gottfried Wilhelm Leibniz Universität Hannover
Thesis: *Aufbau eines supraleitenden Mikro-Vektormagnetens und gezielte Manipulation der Kernspins in GaAs*

2000 – 2007 General qualification for university entrance (“Abitur”), Jacobson-Gymnasium in Seesen

Danksagung

An dieser Stelle möchte ich mich bei mehreren Menschen sehr bedanken...

Mein Dank gilt **Prof. Dr. Christoph Tegenkamp** für die durchgängig engagierte, hervorragende Betreuung meiner Arbeit und die interessanten Diskussionen, die mir stets neue Motivation und Anregung gaben.

Außerdem bedanken möchte ich mich bei **Prof. Dr. Herbert Pfnür** für die Möglichkeit meine Promotion an seinem Lehrstuhl durchführen zu können und sein Interesse am Fortgang meiner Arbeit.

Ich danke **Prof. Dr. Shuji Hasegawa** sowie **Prof. Dr. Wolf Gero Schmidt** für die Übernahme des Korreferats dieser Arbeit. Bei Prof. Dr. Shuji Hasegawa bedanke ich mich zudem für die Möglichkeit im Januar 2017 Teile dieser Arbeit in Tokyo vorzustellen und seine Labore zu besichtigen.

どうもありがとうございました。¹

Ein sehr großer Dank gilt auch der **Arbeitsgruppe von Prof. Dr. Wolf Gero Schmidt** der Universität Paderborn für die vielen DFT-Berechnungen und die ergebnisreichen wissenschaftlichen Diskussionen. Im gleichen Rahmen möchte ich mich auch bei **Prof. Dr. Mario Dähne** und **Stephan Appelfeller** von der Technischen Universität Berlin, sowie **Prof. Dr. Michael Horn-von Hoegen** und **Bernd Hafke** von der Universität Duisburg-Essen für die wissenschaftlichen Diskussionen im Rahmen von Kooperationen bedanken.

Für das angenehme Arbeitsklima bedanke ich mich bei allen aktuellen und ehemaligen **Mitarbeitern der Abteilung ATMOS** am Institut für Festkörperphysik. Besonders bedanken möchte ich mir hierbei bei **Dr. Lisa Kühnemund** für die gute Zusammenarbeit im Labor am Vier-Spitzen-STM/SEM und bei der gemeinsamen Betreuung des XRD Fortgeschrittenen Praktikums. Bei **Atasi Chatterjee** und **Diana Slawig** bedanke ich mich für die

¹English translation of the paragraph:

I would like to thank Prof. Dr. Shuji Hasegawa as well as Prof. Dr. Wolf Gero Schmidt as well as for agreeing to act as an examiner of this thesis. In addition, I would like to thank Prof. Dr. Shuji Hasegawa that I had the opportunity to visit his labs and to present parts of this thesis in his group in Tokyo in January 2017. Thank you very much.

jeweils angenehme Zeit im gemeinsamen Büro und die vielen Gespräche abseits der Arbeit. Ich wünsche beiden viel Erfolg bei ihrer weiteren Promotion. Ebenso bedanken möchte ich mich bei **Dr. Doaa Abdelbarey** für die vielen freundlichen, aufmunternden Worte in den letzten Monaten vor der Fertigstellung der Arbeit.

Dr. Ilio Miccoli danke ich für die gemeinsamen Messungen, sowie wissenschaftliche (und nicht zu vergessen nicht wissenschaftliche...) Diskussionen und Aktivitäten während seines Aufenthaltes am Institut für Festkörperphysik in den letzten drei Jahren. Gerade die nicht wissenschaftlichen Diskussionen und seine stets optimistische Lebensart haben mir immer wieder neue Motivation gegeben. Ich wünsche ihm alles Gute für seine weitere berufliche Laufbahn und Familie. *Grazie amico mio!*

Ein weiterer Dank gilt meinen Kommilitonen und Freunden, die mich während des gesamten Studiums begleitet haben. Insbesondere hierbei danken möchte ich bei **Frank, Dani, Kais, Olaf, Vitali** und **Agnes**.

Zu guter Letzt gilt ein ganz besonderer Dank **meiner Familie**, weil sie immer für mich da war und mich wirklich immer unterstützt und gefördert hat.